A Compact, High-Flux Source of Cold Atoms



Sean Ravenhall

Corpus Christi College,
University of Oxford

A thesis submitted for the degree of
Doctor of Philosophy

Trinity 2018

Through and for the Lord

Abstract

The ongoing drive to transfer quantum technologies from research laboratories to practical, portable devices requires the development of multiple key enabling technologies.

The field of cold atoms, which includes high-precision metrology and quantum simulation, has various real-world applications including time-keeping and navigation. A crucial component in these systems is a cold-atom source that generates a flux of low-velocity atoms suitable for subsequent capture. A large flux enables fast repetition rates, high duty cycles, long measurement times, and resistance to long-term performance degradation with a good signal-to-noise ratio, all of which are essential to produce cold-atom devices and technologies that are capable of out-performing the classical alternatives.

This thesis presents the design, fabrication and characterisation of a novel cold-atom source using a compact pyramidal magneto-optical trap (MOT) with a unique adjustable-aperture mechanism. This allowed an investigation of the dependence of the flux characteristics on the aperture size, a parameter space that has not previously been explored. The measurements showed a strong dependence of the flux on the aperture size, with a negligible flux below 0.4 mm, then an approximately linear increase up to 1.0 mm, at which point the relationship showed possible signs of saturation. Using ^{87}Rb, a flux of $1.18(6) \times 10^{10}$ atoms/s was produced using a 1.27 mm aperture, for which the mean velocity of the atoms was 21.6(3) m/s with a FWHM of 11.2(2) m/s, and the FWHM divergence of the beam was 86(2) mrad. This is the highest recorded flux from a pyramid or $2D^+$-MOT source, and amongst the highest reported fluxes from any MOT sources, and avenues for improvement still remain. This work fulfils the aim of demonstrating a compact and robust cold-atom source generating a high flux of laser-cooled atoms for real-world quantum technology applications.

Acknowledgements

Whenever I saw acceptance speeches on TV whilst growing up, I never understood why the award winner felt the need to thank a seemingly endless list of people who I'd never heard of. I was sure that if my grown-up self ever had to give one, I'd say something funny, witty, and above all, short.

But doing a DPhil has taught me many things (including how to make glass not crack, why you shouldn't hit any red buttons you see on a wall, and the incorrect way to store a vacuum chamber), and in particular how little I can do by myself and how much I rely on other people. So firstly, as all good speeches (rightly) start, I want to thank my parents, both because they're the easiest to thank (having been around for my whole life), but they're also the hardest to adequately thank, given how much they've done for me over the years that I don't even realise. Similarly, my gran has always been nothing but supportive, particularly of my love of cricket, for which I'll ever be grateful. I can't honestly say my brothers have been equally supportive at all times, and they've been downright infuriating on many occasions, but I still wouldn't change them for the world. Not much anyway. Probably.

As wonderful as all my family are, their practical assistance with my DPhil has been understandably minimal, and for that I'm instead indebted to my supervisor Chris for his regular help, advice and willingness to let me work independently and try new approaches. I'm also incredibly grateful to the rest of the Foot group for transforming me from an incompetent undergrad to an enthusiastic and mildly capable researcher, whilst making it a fun and entertaining journey; Elliot, Ed, Ben, Tiffany, Kathryn, Adam, Leo, Shinichi, David and Peter, I'm thankful for you all. The work we all do wouldn't be possible though without the superb support from Alan, Dan and Bill in stores, from Jon, Nick and Mat in the workshop, and from the many others behind the scenes who keep the whole show running, especially Simon, Roy and Tony.

To escape from the occasionally overwhelming world of atoms and lasers, I've been blessed with so many fantastic friends in Oxford. Thanks in particular to: Peter for all the free breakfasts; the Hillview hoard for teaching me about the meaning of decadence; the Randolph rabble for the freezer food and escape prevention education; the NB for showing me the benefits and power of social media; Will for kindly following me around Monaco; Matty for explaining the subtleties of prog metal versus post rock; and all the Corpuscles who may have scattered to Banbury, Reading, Rome, Leeds, London and Sheffield, but with whom it's always awesomely easy to catch up with as though no time had passed. I can also never truly express how grateful I am to my church family, both in Corpus CU and at Ebbe's, and both past and present, for the endless encouragement, friendship, prayer and demonstration of the life-changing effects of knowing Jesus as our friend, king, lord and saviour. Without Him none of this would be possible, and above all else I'm grateful for what He's done for us all on the cross and for bringing me to Him when that seemed so unbelievably unlikely.

Thanks also to Becca, for lighting up my post-thesis life.

This is definitely now long enough to seriously bore my 8 year-old self, but without all of these people I wouldn't be the person I am today, so thanks once again to you all and I hope you enjoy learning about compact cold-atom sources, or at least that you find some pretty figures.

Contents

Introduction **1**

1 Theory of Laser Cooling **6**
1.1 Atom-Light Interaction . . . 6
1.1.1 Mean Light Force . . . 8
1.1.2 Radiation Pressure & the Dipole Force . . . 12
1.2 Doppler Cooling . . . 14
1.2.1 Optical Molasses . . . 15
1.2.2 Doppler Cooling Temperature Limit . . . 17
1.2.3 Sub-Doppler Cooling . . . 17
1.3 Magneto-Optical Trapping . . . 19
1.3.1 Zeeman Interaction . . . 20
1.3.2 One-Dimensional MOT . . . 21
1.3.3 Three-Dimensional MOT . . . 24
1.4 MOT Dynamics . . . 26
1.4.1 Capture Velocity . . . 26
1.4.2 Capture Rate . . . 28
1.4.3 Equilibrium Number . . . 29
1.5 Application of Simple Models to Reality . . . 30
1.5.1 Repumping Dark States . . . 30
1.5.2 Optical Pumping . . . 33
1.5.3 Sub-Doppler Cooling in a MOT . . . 33
1.5.4 Summary . . . 34
1.6 Practical Implementation of MOTs . . . 34
1.7 Summary . . . 36

2 Cold-Atom Source Designs **37**
2.1 Requirements of a Cold-Atom Source . . . 37
2.2 Types of Cold-Atom Sources . . . 40
2.3 MOT Sources . . . 41
2.3.1 Modelling MOT Sources . . . 41
2.3.2 MOT Source Configurations . . . 43
2.3.3 Comparison of MOT Source Configurations . . . 46
2.4 MOT Source Designs . . . 47
2.4.1 Single Beam MOT Geometries . . . 49
2.5 Previous Pyramid Designs . . . 53

3 Adjustable-Aperture Pyramid Design **56**
3.1 Aperture Size . . . 56
3.1.1 Differential Pumping . . . 56
3.1.2 Large Apertures . . . 59
3.1.3 Small Apertures . . . 60
3.2 Adjustable-Aperture Mechanism . . . 61
3.2.1 Mirrors . . . 63
3.3 Summary . . . 64

4 Prototype Fabrication & Assembly **65**
4.1 Prototype Dimensions . . . 65
4.2 Prototype Material Selection . . . 66
4.2.1 Outgassing of Materials . . . 67
4.2.2 Prototype Materials Selection . . . 68
4.2.3 Manufacturing . . . 70
4.3 Mounting the Glass Mirror Substrates . . . 71
4.3.1 Cracking of the Glass . . . 72
4.3.2 Simulated Vacuum Bakes . . . 76
4.3.3 Summary . . . 76
4.4 Mirror Coating . . . 78
4.4.1 Mirror Scatter . . . 80
4.5 Assembly & Aperture Adjustment . . . 84
4.6 Summary . . . 86

5 Experimental Apparatus **87**
5.1 Vacuum System . . . 87
5.2 MOT Light Optics . . . 90
5.2.1 Ti:sapphire Laser . . . 91
5.2.2 EOM Repumping Sidebands . . . 94
5.2.3 Frequency Stabilisation . . . 95
5.2.4 MOT Beam Optics . . . 99
5.3 Double-Pass Tapered Amplifier . . . 99
5.4 Probe Light . . . 103
5.4.1 Probe Laser . . . 104
5.4.2 Beat-Note Offset Lock . . . 104
5.4.3 AOM Optical Arrangements . . . 108
5.5 Summary . . . 109

6 Flux Characterisation Technique **110**
6.1 Required Measurements . . . 111
6.2 Atomic Density Measurement . . . 112
6.2.1 Absorption vs. Fluorescence Imaging . . . 112
6.2.2 Absorption Measurement Apparatus . . . 117
6.2.3 Atomic Density Absorption Signal Fitting . . . 123
6.3 Longitudinal Velocity Measurement . . . 126
6.4 Summary . . . 130

7 Characterisation of the Flux **132**
7.1 Flux vs. Vapour Pressure & Aperture Size . . . 133
7.2 Flux vs. MOT Beam Diameter . . . 138
7.3 Flux vs. MOT Beam Intensity . . . 140
7.4 Flux vs. MOT Position & Magnetic Field . . . 143
7.4.1 Transverse Position . . . 144
7.4.2 Axial Position . . . 145
7.5 Maximum Pyramid Source Flux . . . 147
7.6 Summary . . . 150

8 Summary & Outlook **152**
8.1 Project Summary . . . 152
8.2 Future Directions . . . 154
8.2.1 Further Characterisation . . . 154
8.2.2 Design Refinements . . . 155
8.3 Concluding Remarks . . . 156

Appendices **157**

A Adjustable-Aperture Design Technical Details **158**
A.1 Mirror Mounts . . . 158
A.2 Rotator Plate . . . 159
A.3 Base Plate . . . 159
A.4 Vacuum Fastenings . . . 160

B Standard Vacuum Component Sizes **161**

C cCAS Project **162**
C.1 Design . . . 162
C.2 Assembly & Installation . . . 165
C.3 Optimal Chamber Length . . . 166

Acronyms **167**

Bibliography **168**

List of Figures

1.1 Coupled systems in light-matter interaction . . . 7
1.2 Doppler cooling force . . . 16
1.3 Zeeman effect . . . 21
1.4 Magneto-optical trapping . . . 23
1.5 Magnetic field for a three-dimensional MOT . . . 25
1.6 Maxwell-Boltzmann distribution . . . 27
1.7 Energy structure of ^{87}Rb . . . 31
1.8 Relative scattering rates for ^{87}Rb . . . 32

2.1 Pyramid MOT & pyramid MOT source . . . 50
2.2 Grating MOT . . . 52
2.3 Pyramid MOT designs . . . 54

3.1 Differential pumping . . . 58
3.2 Adjustable-aperture mechanism . . . 61
3.3 Exploded view of the adjustable-aperture pyramid design . . . 62

4.1 Sources of outgassing . . . 67
4.2 Cracked batch of epoxied custom pieces of glass . . . 73
4.3 Cracking of custom glass compared to absence of cracking in stock piece . . . 74
4.4 Absence of cracking when epoxied on a polished instead of a rough surface . . . 75
4.5 Diffraction effects from cured epoxy . . . 77
4.6 Scatter from dielectric-coated pyramid mirrors . . . 80
4.7 Comparison of mirror scatter from old and new pyramids . . . 81
4.8 Discolouration of the pyramid . . . 82
4.9 Discolouration of the brass rotator plate . . . 85

5.1 Vacuum system . . . 88
5.2 Divergence of the Ti:sapphire beam . . . 91
5.3 MOT light optics with frequency stabilisation circuitry . . . 93
5.4 MTS error signal for frequency stabilisation . . . 98
5.5 Tapered amplifier . . . 100
5.6 Double-pass tapered amplifier optical apparatus . . . 101
5.7 Double-pass TA output powers . . . 102
5.8 Probe laser optics with beat-note offset lock . . . 105
5.9 Beat-note offset lock error signal . . . 107

6.1 Atomic column density profile . . . 116
6.2 Absorption measurement scheme using an adjustable iris . . . 117

6.3 Absorption measurement scheme using an adjustable periscope 118
6.4 Reduction in probe signal due to dark state loss 120
6.5 Absorption signal as a function of probe field 123
6.6 Typical absorption column density data 126
6.7 Linear atomic density when the source is turned off 128
6.8 Typical transit time signal 130

7.1 Possible flux dependencies on the aperture size 133
7.2 Flux dependence on the aperture size 135
7.3 Divergence & velocity dependence on the aperture size 137
7.4 Flux dependence on the MOT beam diameter 139
7.5 Flux dependence on the MOT beam intensity 142
7.6 Flux dependence on transverse changes to the MOT position 144
7.7 Flux dependence on axial changes to the MOT position 146

C.1 cCAS prototype 164

List of Tables

2.1 Summary of cold-atom sources in the literature 44

7.1 Summary of cold-atom sources in the literature, including this work 149

B.1 Standard UHV vacuum component sizes 161

Introduction

Cold atoms are highly sensitive and well-understood systems; properties which have resulted in a wide range of applications. The wave-like behaviour of atoms has been exploited to perform atom interferometry for precise measurements of rotation, acceleration, magnetic fields and gravity [1–7]. These measurements can surpass the limits of state-of-the-art classical devices [8, 9], to the extent that stringent tests of fundamental physics can be conducted [10–14]. The well-defined structure of atoms allows them to be used for precision frequency measurements and time-keeping, currently providing up to three orders of magnitude improvement over the existing caesium standard [15–17]. Isolating atoms in optical lattices also enables work towards quantum computing and simulation of condensed matter systems, while cooling gases of atoms to quantum degeneracy has allowed investigations of quantum mechanics on a macroscopic scale. This multitude of interesting applications make cold atoms extremely important systems for both fundamental and applied research.

The production of cold atoms from room temperature, or higher, is performed by laser cooling. This was first performed using the optical molasses technique, in which three orthogonal pairs of counterpropagating laser beams produce a damping force on the atoms, similar to the force experienced by particles in a viscous fluid such as molasses [18]. The beams are red-detuned from resonance with the atoms, which causes stationary atoms to experience a small force while atoms travelling towards a beam see the light Doppler-shifted towards resonance, resulting in an increased rate of photon absorption and a corresponding transfer of momentum opposing the velocity. This technique slows atoms without trapping them, but by applying a weak magnetic field, the force can be made position-dependent such that

the atoms are directed towards the zero-field region. This technique is the magneto-optical trap (MOT) [19].

A MOT is capable of collecting and cooling $\sim 10^{10}$ atoms from a room temperature vapour to below 1 mK in less than a second. Despite the wide variety of cold-atom experiments, this ability of the MOT to rapidly achieve five orders of magnitude of cooling make it almost ubiquitous in work on laser cooling of atoms. Some experiments use it as the only stage of cooling, such as atom interferometry for sensing applications, while others require further optical or magnetic cooling stages, for example to produce quantum gases. All experiments benefit from having fast loading rates and long trapped lifetimes, but a single-stage MOT is unable to provide both; the latter requires a high quality vacuum to avoid collisional heating and loss of the trapped atoms, but the loading rate is dependent on the availability of atoms to be trapped. A solution which gives the best of both worlds is the use of a two-chamber system with differential pumping.

A two-chamber system employs a cold-atom source to load a MOT with a high flux of low-velocity ($v \lesssim 50\,\mathrm{m/s}$) atoms. The MOT is operated in a low pressure chamber while the source is in a neighbouring chamber held at a high pressure to maximise the output flux. Being able to combine fast repetition rates, long lifetimes, and low signal-to-noise ratios make the two-chamber approach commonplace in cold-atom experiments. Cold-atom sources are therefore an integral part of the vast majority of cold-atom experiments.

Historically, cold-atom experiments have been confined to research laboratories due to their size and complexity, and each apparatus would have a custom designed cold-atom source. Technological improvements have however allowed the construction of increasingly compact and portable devices [1, 3, 8, 20–28], and the past decade has seen an increasing drive to take advantage of the properties of cold atoms for applications outside the laboratory including time-keeping [29, 30], gravitational sensing [4, 31], accelerometers [32], and satellite-independent navigation [33]. Companies as well as research institutions have participated in the production of such devices: AOSense (USA) has developed a gravimeter; Muquans (France) has also produced a gravimeter, as well as an atomic clock based on cold

atoms; and a complete quantum gas apparatus that has been operated in space [34] is sold by ColdQuanta (USA). The field of cold atoms, and quantum technology in general, is now at an exciting stage where the long-heralded promises of revolutionary improvements over classical devices are beginning to be realised.

In the UK this has culminated in the National Quantum Technologies Program, bringing together universities, industry, government and national laboratories with the goal of accelerating the translation of quantum technologies into the marketplace and daily life. To facilitate this, a modular approach is favoured whereby optimised sub-components can be incorporated across multiple devices and experiments, reducing cost and development time. For cold-atom physics, the cold-atom source is a key enabling technology that is integral to a wide range of devices.

The project described in this thesis has been part of the UK programme, with the goal of designing a compact, robust, high-flux source of cold atoms to enable performance enhancement of portable cold-atom devices. The focus was on the optics and fields of the source, since laser systems and vacuum technologies are being developed elsewhere [28, 35–40]. The source was aimed at the development of portable evolutions of laboratory equipment, and not the miniaturised systems being designed from the ground up to provide potentially hand-held or credit-card sized devices in the long term.

In addition to demonstrating a high flux from a compact, robust source using ^{87}Rb, this project conducted an extensive characterisation of the source to guide future developments of the design, as well as to understand how the properties of this design of source may be adjusted to meet specific user requirements.

There are two main types of cold-atom sources to be considered when selecting a design: Zeeman slowers and MOT sources. Zeeman slowers use a magnetic field to optimise the slowing of atoms in a particular direction, and provide larger fluxes but at the cost of greater size and complexity. MOT sources operate on the same principle as normal MOTs, however an intensity imbalance is introduced to push the atoms out of the trapping region as a low-velocity beam. Various optical and magnetic configurations are possible, but this project

used the 'pyramid' MOT source, which produces all the beams required from a single large input beam by using a pyramidal arrangement of mirrors [41, 42]. Requiring only a single beam greatly reduces the size of the system, and minimises the possibility of misalignments, making it robust against mechanical vibrations. The main disadvantage of the pyramid is that it requires the development of in-vacuum optics, which is a main topic of this thesis, along with the subsequent testing and characterisation of the demonstrated pyramid source.

Thesis Structure

This thesis begins with the theory of laser cooling, particularly the MOT, and outlines a simple model to provide a reasonable description of the dynamics of a MOT. The practical implementation of MOTs and the importance of cold-atom sources is discussed, including the requirements of an ideal source. The different types of sources are outlined, and the various configurations and geometries of MOT source are summarised, with particular focus on single-beam geometries that are well suited for compact sources. An overview of pyramid designs in the literature is provided, and the new design of pyramid source with an adjustable aperture is presented, including a discussion of the effects of aperture size on the performance of a cold-atom source. The fabrication of a prototype source is then detailed, including the difficulties encountered during manufacturing. The vacuum system and optical apparatus used to operate and measure the prototype source are described, and the measurement techniques used to characterise the flux from the source are explained. The results of the characterisation of the source, with a focus on the effects of the aperture size, are presented and discussed before some concluding remarks including future avenues for further characterisation and design optimisation, some of which are already under development.

Funding Acknowledgements

The primary source of funding for this project was a studentship from the Defence, Science and Technology Laboratory (Dstl), as part of the UK National Quantum Technologies Program. Oxford Innovation provided assistance with the patenting of the new design of pyramid source, and there was also support from the EPSRC Impact Acceleration Account at Oxford, the Networked Quantum Information Technologies hub, the UK Quantum Technology Hub for Sensors and Metrology, and Innovate UK (in a collaboration with M Squared Lasers).

1

Theory of Laser Cooling

This chapter outlines the theory of light-matter interaction by first deriving the mean light force, which can be considered as composed of two classes of radiation force: the radiation pressure force, and the dipole force. The application of the radiation pressure force in Doppler cooling of atoms is detailed, then extended to the magneto-optical trap (MOT) that provides cooling with trapping. Simple rate equations are produced to describe the dynamics of the MOT, and their applicability to real atomic systems is explored. Finally, the practical implementation of MOTs and the associated importance of cold-atom sources are explained.

The derivation of the mean light force broadly follows Perrin [43] and the sections on magneto-optical trapping use Foot [44] as a basis. Blundell & Blundell [45] is used for kinetic theory results.

1.1 Atom-Light Interaction

The interaction of an atom with a light field is a result of the electric field of the light inducing an atomic dipole moment in the atom, that interacts in turn with the light field. In the case of a laser, the light field contains a vast number of photons in the same mode, and the fluctuations in the photon number are small for coherent states. In this case a

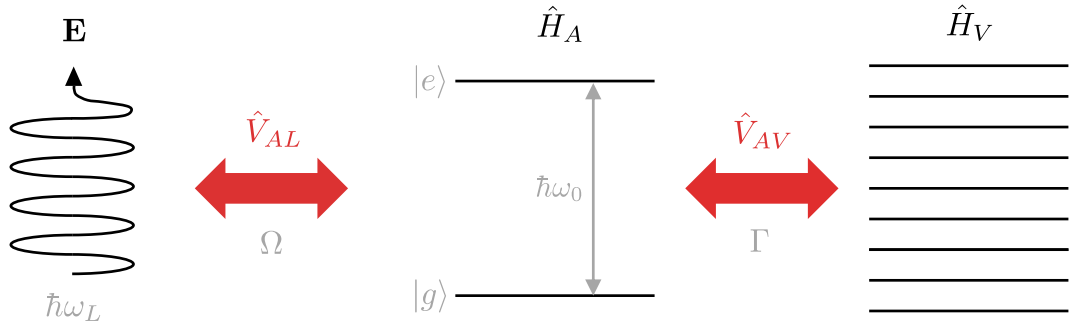


Figure 1.1: The three coupled systems involved in the interaction of light with an atom. The atom is modelled as a two-level system, and the field is treated classically.

classical treatment of the field can be applied, with the quantum fluctuations incorporated as a separate term in the total Hamiltonian of the system.

Using this approach, to examine the interaction of light with an atom requires considering three coupled systems: the light field, the atom, and the quantum field (Fig. 1.1). The total Hamiltonian of the system is a combination of four terms:

$$\hat{H}_{\text{tot}} = \hat{H}_A + \hat{H}_V + \hat{V}_{AL} + \hat{V}_{AV} \tag{1.1}$$

- $\hat{H}_A$, the atomic Hamiltonian, is the sum of the internal energy of the electronic energy structure, and the kinetic energy, from the motion of the atom. In the two-level approximation, the atom has ground $|g\rangle$ and excited $|e\rangle$ states separated by energy $\hbar\omega_0$. The two-level approximation is used for simplicity, and is broadly valid for small detunings of the laser from the atomic transition. The applicability and limitations of the two-level model are discussed in Sec. 1.5.

- $\hat{V}_{AL}$, the atom-light coupling, arises because, although an atom has no permanent dipole to interact with the light field, the electric field **E** of light with angular frequency ω_L induces an atomic dipole that in turn interacts with the light field. This interaction is responsible for stimulated emission and absorption, and is characterised by the Rabi frequency Ω.

- $\hat{H}_V$, the Hamiltonian of the quantum vacuum field, is composed of creation and anni-

hilation operators, and the coupling of the atom to the quantum vacuum field, $\hat{V}_{AV}$, is responsible for spontaneous emission (without the vacuum field this phenomenon would not be included). It is characterised by the decay rate of the excited state, Γ.

Using this Hamiltonian, an expression for the mean force experienced by an atom in a light field can be found.

1.1.1 Mean Light Force

The force operator $\hat{\mathbf{F}}$ is related to the momentum operator $\hat{\mathbf{P}}$ by $\hat{\mathbf{F}} = \mathrm{d}\hat{\mathbf{P}}/\mathrm{d}t$, which can be rewritten using the Heisenberg representation as

$$\hat{\mathbf{F}} = \frac{\mathrm{d}\hat{\mathbf{P}}}{\mathrm{d}t} = \frac{1}{i\hbar}\left[\hat{\mathbf{P}}, \hat{H}\right] \tag{1.2}$$

For the case of $\hat{H}_{\mathrm{tot}}$, $\hat{\mathbf{P}}$ commutes with $\hat{H}_A$ and $\hat{H}_V$ but not $\hat{V}_{AL}$ or $\hat{V}_{AV}$. Taking the expectation of the result to find the mean force on the atom from the light gives

$$\mathbf{F} = \left\langle \hat{\mathbf{F}} \right\rangle = -\left\langle \boldsymbol{\nabla} \hat{V}_{AL} \right\rangle - \left\langle \boldsymbol{\nabla} \hat{V}_{AV} \right\rangle \tag{1.3}$$

The $\left\langle \boldsymbol{\nabla} \hat{V}_{AV} \right\rangle$ term is zero, due to the net momentum of spontaneously emitted photons being zero.[1] Therefore only the $\hat{V}_{AL}$ interaction need be considered.

Atom-Light Coupling

The Hamiltonian for the interaction of the electric field $\mathbf{E}$ of the light with the induced atomic dipole moment $\mathbf{D}$ is

$$\hat{V}_{AL} = -\hat{\mathbf{D}} \cdot \hat{\mathbf{E}} \tag{1.4}$$

[1] Although the expectation is zero, the fluctuations from this force prevent atoms being laser cooled below the Doppler limit, as discussed in Sec. 1.2.2.

A general expression for $\mathbf{E}$, assuming monochromatic radiation, is

$$\mathbf{E}(\mathbf{r},t) = \frac{1}{2}E_0(\mathbf{r})\left[\hat{\epsilon}(\mathbf{r})e^{-i(\omega_L t+\phi(\mathbf{r}))} + \text{c.c.}\right] \tag{1.5}$$

where $E_0(\mathbf{r})$ is the amplitude, $\hat{\epsilon}(\mathbf{r})$ is the normalised polarisation vector, ω_L is the (angular) frequency of laser light, and $\phi(\mathbf{r})$ is the position-dependence of the phase.

To express the dipole moment operator $\hat{\mathbf{D}}$, it is normal to introduce the reduced dipole element, $\mathbf{d} = \langle e|\,\hat{\mathbf{D}}\,|g\rangle$, which allows $\hat{\mathbf{D}}$ to be written as

$$\hat{\mathbf{D}} = \mathbf{d}\,|e\rangle\langle g| + \mathbf{d}^*\,|g\rangle\langle e| \tag{1.6}$$

Applying these expressions produces four terms in $\hat{V}_{AL}$, that can be grouped into a 'resonant' term $\hat{V}_{AL}^{\text{res}}$ and a 'non-resonant' term $\hat{V}_{AL}^{\text{non-res}}$:

$$\begin{aligned}\hat{V}_{AL} &= -\hat{\mathbf{D}}\cdot\mathbf{E}(\hat{\mathbf{R}},t)\\ &= \hat{V}_{AL}^{\text{res}} + \hat{V}_{AL}^{\text{non-res}}\end{aligned} \tag{1.7}$$

where $\hat{\mathbf{R}}$ is the position operator. The resonant and non-resonant nature of the two contributions to $\hat{V}_{AL}$ can be understood by moving to the reference frame rotating at ω_0 due to the internal time-evolution of state $|e\rangle$ (the interaction picture). In this frame, $\hat{V}_{AL}^{\text{res}}$ evolves at frequency $\delta = \omega_L - \omega_0$ while $\hat{V}_{AL}^{\text{non-res}}$ evolves at $\omega_L + \omega_0 \gg \delta$ and is negligible compared to $\hat{V}_{AL}^{\text{res}}$ by the *rotating wave approximation*, which assumes the laser is not far-detuned from the atomic transition. In this approximation,

$$\begin{aligned}\hat{V}_{AL} &\approx \hat{V}_{AL}^{\text{res}}\\ &= -\mathbf{d}\cdot\hat{\epsilon}(\hat{\mathbf{R}})\frac{E_0(\hat{\mathbf{R}})}{2}\,|e\rangle\langle g|\,e^{-i(\omega_L t+\phi(\hat{\mathbf{R}}))} + \text{h.c.}\\ &= \frac{\hbar\Omega(\hat{\mathbf{R}})}{2}\left[|e\rangle\langle g|\,e^{-i(\omega_L t+\phi(\hat{\mathbf{R}}))} + \text{h.c.}\right]\end{aligned} \tag{1.8}$$

where the *Rabi frequency* is defined as

$$\Omega(\mathbf{r}) = -\mathbf{d} \cdot \hat{\epsilon}(\mathbf{r}) \frac{E_0(\mathbf{r})}{\hbar} \tag{1.9}$$

and is assumed to be real, which can be ensured by appropriate choice of the time origin.

Semi-Classical Approximation for the Atom

To simplify the calculation of the mean force, a semi-classical description for the atom is used: the external motion of the atom is treated as classical, while the internal dynamics remain quantum mechanical. Applying this description allows the force to be calculated with the atom at position $\mathbf{r}$ and velocity $\mathbf{v}$, and is correct if the atomic position is known better than the wavelength of laser light,

$$\Delta r \ll \lambda_L \propto \frac{1}{k_L} \tag{1.10}$$

and if the velocity, v, is known sufficiently precisely that the Doppler shift due to uncertainty in v is less than the linewidth of the transition:

$$\Delta v \, k_L \ll \Gamma \tag{1.11}$$

Inserting these requirements into the Heisenberg uncertainty principle yields (for an atom of mass M)

$$\begin{aligned} \frac{\hbar}{2} &< \Delta r \, \Delta p \\ &< \Delta r \, (M \Delta v) \\ &\ll \frac{M\Gamma}{k_L^2} \qquad \Rightarrow \quad \Gamma \gg \frac{\hbar k_L^2}{2M} = 3.8\,\text{kHz for } {}^{87}\text{Rb} \end{aligned} \tag{1.12}$$

This condition is the *broad band condition*[2] and is satisfied for the majority of practical

[2] The broad band condition means that the internal state can be considered to be in its steady state when describing the dynamics of the external state, which is the complementary view to that described in the main text. The condition can also be recast as requiring the time scales of the internal processes to be much shorter than the time scales of the external processes: $T_{\text{internal}} \gg T_{\text{external}}$.

cases of laser cooling of alkali metal atoms.[3] Applying this to the force equation gives

$$\begin{aligned}\mathbf{F} &\approx -\left\langle \boldsymbol{\nabla}\hat{V}_{AL}^{\text{res}} \right\rangle \\ &= -\left\langle \boldsymbol{\nabla}\left(\frac{\hbar\Omega(\mathbf{r})}{2}\left[|e\rangle\langle g| e^{-i(\omega_L t+\phi(\mathbf{r}))} + \text{h.c.}\right]\right)\right\rangle \\ &= -\left\langle \frac{\boldsymbol{\nabla}(\Omega(\mathbf{r}))}{\Omega(\mathbf{r})}\hat{V}_{AL}^{\text{res}} - i\boldsymbol{\nabla}(\phi(\mathbf{r}))\frac{\hbar\Omega(\mathbf{r})}{2}\left[|e\rangle\langle g| e^{-i(\omega_L t+\phi(\mathbf{r}))} - \text{h.c.}\right]\right\rangle\end{aligned} \tag{1.13}$$

To find the expectation value, the *atomic density operator* for a pure state $\hat{\rho} = |\psi\rangle\langle\psi|$ is introduced, since it has the useful property that the expectation of an operator $\hat{A}$ can be evaluated as

$$\left\langle \hat{A} \right\rangle = \text{Tr}(\hat{\rho}\hat{A}) \tag{1.14}$$

Applying this identity gives

$$\mathbf{F} = -\frac{\hbar}{2}\left\{\boldsymbol{\nabla}(\Omega(\mathbf{r}))\left[\rho_{ge}e^{-i(\omega_L t+\phi(\mathbf{r}))} + \text{c.c.}\right] + -i\boldsymbol{\nabla}(\phi(\mathbf{r}))\,\Omega(\mathbf{r})\left[\rho_{ge}e^{-i(\omega_L t+\phi(\mathbf{r}))} - \text{c.c.}\right]\right\} \tag{1.15}$$

Steady-State Solution of the Optical Bloch Equations

The elements of $\hat{\rho}$ are found by solving the *optical Bloch equations* (OBEs). The OBEs are a system of coupled differential equations, found by expanding the master equation:

$$\frac{\mathrm{d}\hat{\rho}}{\mathrm{d}t} = \frac{1}{i\hbar}\left[\hat{H}_A + \hat{V}_{AL}, \hat{\rho}\right] - \Gamma\begin{pmatrix} \rho_{ee} & \frac{1}{2}\rho_{ge} \\ \frac{1}{2}\rho_{eg} & -\rho_{ee}\end{pmatrix} \tag{1.16}$$

The master equation is the Liouville-von Neumann equation, which describes the time-evolution of the density operator, augmented by a term that accounts for the effect of spontaneous emission.[4] The mean force is found from the steady state solution of the OBEs,

[3] Special consideration is necessary for the extremely narrow transitions in some other species, such as alkaline-earth metals.

[4] This term is important for the radiation pressure force because the lifetime of the excited state limits the rate of momentum transfer; the interval between successive photon absorption events is limited by the time for spontaneous emission of the first photon.

given by

$$\rho_{ge} = \rho_{eg}^{*} = \frac{\Omega(\mathbf{r})(\delta + i\Gamma/2)}{\Omega(\mathbf{r})^2 + 2\delta^2 + \Gamma^2/2} = \frac{s(\mathbf{r})}{1 + s(\mathbf{r})}\frac{2\delta + i\Gamma}{\Omega(\mathbf{r})} \tag{1.17}$$

$$\rho_{ee} = 1 - \rho_{gg} = \frac{1}{2}\frac{\Omega(\mathbf{r})^2}{\Omega(\mathbf{r})^2 + 2\delta^2 + \Gamma^2/2} = \frac{1}{2}\frac{s(\mathbf{r})}{1 + s(\mathbf{r})} \tag{1.18}$$

where the *saturation parameter* is defined as

$$s(\mathbf{r}) = \frac{\Omega(\mathbf{r})^2/2}{\delta^2 + \Gamma^2/4} = \frac{I(\mathbf{r})/I_{\text{sat}}}{1 + 4\delta^2/\Gamma^2} \tag{1.19}$$

and the *saturation intensity* is defined by[5]

$$I_{\text{sat}} = \frac{\hbar^2 c\epsilon_0 \Gamma^2}{4|\mathbf{d}\cdot\hat{\epsilon}|^2} \tag{1.20}$$

Substituting in ρ_{ge} to $\mathbf{F}$ and averaging over one period of the laser frequency gives the total mean force on the atom as

$$\mathbf{F}(\mathbf{r}) = -\frac{s(\mathbf{r})}{1 + s(\mathbf{r})}\left(\frac{\hbar\Gamma}{2}\boldsymbol{\nabla}\phi + \hbar\delta\frac{\boldsymbol{\nabla}\Omega(\mathbf{r})}{\Omega(\mathbf{r})}\right) \tag{1.21}$$

1.1.2 Radiation Pressure & the Dipole Force

The two terms in Eq. 1.21 correspond to the two different classes of radiation force.

Radiation Pressure

The first term corresponds to the *radiation pressure force*,

$$\mathbf{F}_{\text{rp}}(\mathbf{r}) = -\frac{\hbar\Gamma}{2}\frac{s(\mathbf{r})}{1 + s(\mathbf{r})}\boldsymbol{\nabla}\phi \tag{1.22}$$

which depends on the phase gradient of the light field, and can be best understood by considering a plane wave. The phase of a plane wave with wave vector $\mathbf{k}_L$ is $\phi(\mathbf{r}) = -\mathbf{k}_L \cdot \mathbf{r}$,

[5] Using $I(\mathbf{r}) = cn_r\epsilon_0 E_0^2(\mathbf{r})/2$ where c is the speed of light, ϵ_0 is the vacuum permittivity of space, and n_r is the refractive index of the medium the light is propagating through, and which is assumed to be $n_r \approx 1$.

and the polarisation and amplitude have no spatial dependence, so $s(\mathbf{r}) = s$. The radiation pressure force then becomes

$$\mathbf{F}_{\text{rp}} = \frac{\Gamma}{2}\frac{s}{1+s}\hbar\mathbf{k}_L = \Gamma\rho_{ee}\hbar\mathbf{k}_L \tag{1.23}$$

using Eq. 1.18 for ρ_{ee}. The expression $\Gamma\rho_{ee}$ is the product of the steady state population of the excited state, and the rate of spontaneous emission for the excited state, which is the rate of spontaneous emission for the atom. To be in the steady state, an atom must be absorbing as many photons as it spontaneously emits, thus the absorption rate, R_{abs}, is equal to the rate of spontaneous emission, and is called the *scattering rate*:

$$\begin{aligned} R_{\text{scatter}} = R_{\text{abs}} &= \Gamma\rho_{ee} \\ &= \frac{\Gamma}{2}\frac{I/I_{\text{sat}}}{1+4(\delta/\Gamma)^2+I/I_{\text{sat}}} \end{aligned} \tag{1.24}$$

Since $\Gamma\rho_{ee} = R_{\text{abs}}$, the force $\mathbf{F}_{\text{rp}}$ is the product of the absorption rate and the photon momentum, $\hbar\mathbf{k}_L$. Thus the radiation pressure force comes from the momentum transfer associated with photon absorption from the light field. The spontaneously emitted photons also cause momentum transfer to the atom, but this emission has inversion symmetry and the net momentum transfer is zero.[6]

From Eq. 1.23 and Eq. 1.24, the radiation pressure force: is aligned to the direction of the laser beam; increases with intensity, tending towards a limit of $\hbar k_L\Gamma/2$; has a Lorentzian lineshape with respect to the detuning, δ; and is maximised for $\delta = 0$ (when the laser frequency is resonant with the atomic transition).

[6] The distribution of classical dipole radiation in cylindrical polar coordinates is proportional to $\hat{\mathbf{r}}\sin^2(\theta)/r^2$, therefore the distribution of radiation possesses inversion symmetry (also called point symmetry), meaning the probability of emitting a photon in one direction is equal to the probability of emitting the photon in the opposite direction. The mean total momentum transfer is therefore zero. Note that the emission is not isotropic – for instance there is zero emission along the dipole axis, and greatest emission perpendicular to the dipole axis. The radiation pattern from transitions involving higher momentum can be more complex, however by the correspondence principle must obey the same symmetries.

Dipole Force

The second term in the total mean force is the *dipole force*,

$$\mathbf{F}_{\text{dip}}(\mathbf{r}) = -\hbar\delta \frac{s(\mathbf{r})}{1+s(\mathbf{r})} \frac{\boldsymbol{\nabla}\Omega(\mathbf{r})}{\Omega(\mathbf{r})} = -\frac{\hbar\delta}{2} \frac{\boldsymbol{\nabla}s(\mathbf{r})}{1+s(\mathbf{r})} \tag{1.25}$$

The dipole force is proportional to the gradient of the intensity, and thus is zero for a plane wave. For a positive (blue) detuning, $\delta = \omega_L - \omega_0 > 0$, the force acts to repel the atom from regions of high intensity, whereas for a negative (red) detuning the atom is attracted towards high intensity regions, but this dispersive interaction is zero on resonance ($\delta = 0$).

The dipole force can be written as the gradient of a scalar potential, and is therefore a *conservative* force, unlike the radiation pressure force. A conservative force conserves energy, so the dipole force cannot be used to directly cool atoms. Instead, dipole force traps using focused red-detuned light serve as excellent mechanisms for storing cold atoms after initial cooling. The dipole trap potential scales as I/δ, whereas the scattering rate scales as I/δ^2, and therefore far-detuned intense beams provide traps of order $\lesssim 1\,\text{mK}$ with very low heating rates [46], unlike traps that use radiation pressure which have associated minimum temperatures that can be achieved (see Sec. 1.2.2).

Since the dipole force is conservative, the radiation pressure force is used to optically cool atoms from room temperatures (or higher) to temperatures at which the effects of the dipole force are significant.

1.2 Doppler Cooling

Laser cooling of atoms is accomplished by using the radiation pressure force to transfer atomic kinetic energy to radiated photons, reducing the velocity of the atom, in a process called *Doppler cooling*.

Thus far the velocity of the atom has been neglected. If the velocity $\mathbf{v}$ of the atom is

now considered, the laser frequency in the reference frame of the atom is Doppler shifted to $\omega_L - \mathbf{k}_L \cdot \mathbf{v}$. The detuning becomes $\delta \to \delta - \mathbf{k}_L \cdot \mathbf{v}$, and the radiation pressure force, assuming a plane wave, is now

$$\begin{aligned} \mathbf{F}_{\text{rp}} &= \frac{\Gamma}{2} \frac{s}{1+s} \hbar \mathbf{k}_L \\ &= \frac{\Gamma}{2} \frac{I/I_{\text{sat}}}{1 + I/I_{\text{sat}} + 4(\delta - \mathbf{k}_L \cdot \mathbf{v})^2/\Gamma^2} \hbar \mathbf{k}_L \end{aligned} \tag{1.26}$$

which is a velocity-dependent force. The force is maximised when $\mathbf{k}_L \cdot \mathbf{v} = \delta$ (when the Doppler shift brings the laser into resonance with the atomic transition).

1.2.1 Optical Molasses

Considering the one-dimensional case with two identical but counterpropagating beams (having wavevectors $+k_L$ and $-k_L$ respectively), the total force on the atom is the sum of the force from each beam:

$$\begin{aligned} F_{\text{rp}}^{\text{total}} &= F_{\text{rp}}(+k_L) + F_{\text{rp}}(-k_L) \\ &= \frac{\hbar\Gamma}{2} \frac{I}{I_{\text{sat}}} \left(\frac{+k_L}{1 + I/I_{\text{sat}} + 4(\delta - k_L v)^2/\Gamma^2} + \frac{-k_L}{1 + I/I_{\text{sat}} + 4(\delta + k_L v)^2/\Gamma^2} \right) \end{aligned} \tag{1.27}$$

The force is plotted in Fig. 1.2 for red-detuned light, and shows that the force acts against the velocity, slowing and cooling the atoms. Low velocity atoms ($|v| \lesssim 2\Gamma/k_L$) experience a relatively strong force and can be substantially slowed over a few centimetres, however high velocity atoms experience an increasingly negligible – although non-zero – cooling force, requiring a stopping distance in excess of that achievable in a practical experiment. In the range $|v| \ll \Gamma/k_L$ the force is approximately linear, and can be approximated in the low velocity limit using a first order expansion in v to be

$$F_{\text{rp}}^{\text{total}} \simeq -\alpha v \quad \text{where} \quad \alpha = 8\hbar k_L^2 \frac{I}{I_{\text{sat}}} \frac{-\delta/\Gamma}{(1 + nI/I_{\text{sat}} + 4\delta^2/\Gamma^2)^2} \tag{1.28}$$

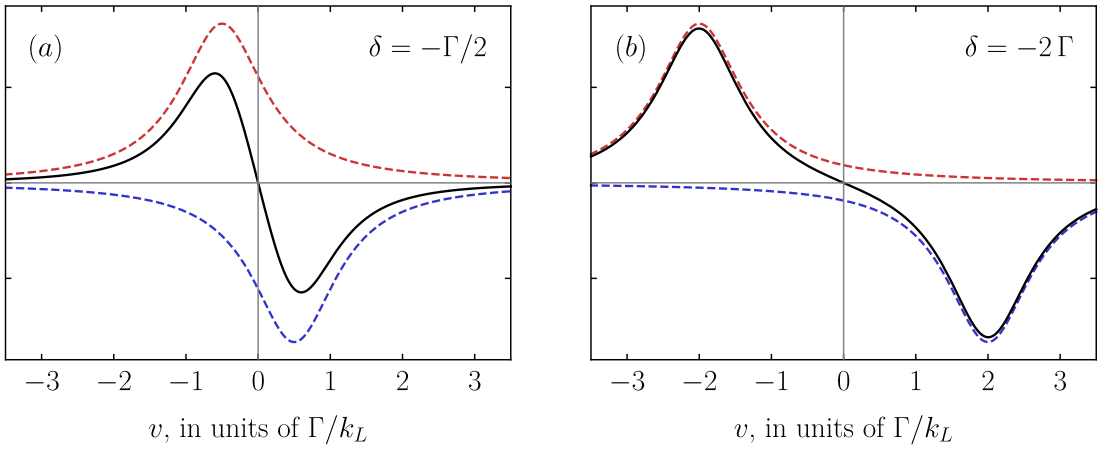


Figure 1.2: The velocity-dependent Doppler cooling force $F_{\mathrm{rp}}^{\mathrm{total}}$ on an atom in a pair of counterpropagating beams is shown (solid line) with $I = I_{\mathrm{sat}}$ for (a) $\delta = -\Gamma/2$ and (b) $\delta = -2\,\Gamma$. The individual radiation pressure forces from the right-travelling (red dotted) and left-travelling (blue dotted) are also shown.

where n is the number of beams. The addition of the factor n arises since when multiple beams interact with the atom, the excited state population ρ_{ee} is influenced by all beams. The effect of this can be approximated by replacing I/I_{sat} with nI/I_{sat} (in the expressions for ρ_{ee} and s).[7]

For red-detuned light ($\delta < 0$), $\alpha > 0$ and the atom experiences a frictional force that directly opposes the motion of the atom, analogous to the motion of a particle in viscous fluid. In light of this, the technique is called *optical molasses*, and fully three-dimensional cooling is obtained by three orthogonal pairs of counterpropagating beams, for which the total force (still in the low velocity limit) is

$$\mathbf{F}_{\mathrm{molasses}} = -\alpha \mathbf{v} \tag{1.29}$$

[7] In reality, the atom will interact with each of the n beams differently depending on the relative detuning of each beam, which depends on the velocity of the atom and the magnetic field at its position, however in the low velocity limit this approximation of replacing I with nI is reasonably justified.

1.2.2 Doppler Cooling Temperature Limit

Although the force above suggests that Doppler cooling can reduce the velocity of an atom to zero, in reality the fluctuations in the force limit the achievable temperature. In time t the atom absorbs and re-emits $R_{\text{scatter}}t$ photons, and every spontaneous emission imparts $\hbar k_L$ momentum to the atom, that changes the velocity of the atom by the *recoil velocity*

$$v_{\text{rec}} = \frac{\hbar k_L}{M} \tag{1.30}$$

where M is the mass of the atom. The fluctuations in the number of absorbed photons and the direction of the spontaneous emission cause the atom to undergo a random walk in velocity space, analogous to Brownian motion, which acts to heat the atom. Balancing this recoil heating with the Doppler cooling force for low intensities ($I \ll I_{\text{sat}}$) gives the *Doppler temperature*,

$$T_D = \frac{\hbar\Gamma}{2k_B} \tag{1.31}$$

which is the minimum expected achievable temperature[8] of the optical molasses technique in the low intensity limit for optimal detuning.[9] For ^{87}Rb, $T_D \approx 140\,\mu\text{K}$.

1.2.3 Sub-Doppler Cooling

In practice however, optical molasses can achieve temperatures below the theoretical limit T_D, which is derived for a simple two-level model interacting with independent beams. Real atoms have complicated energy structures including degenerate energy levels and hyperfine structure, and intersecting beams undergo interference, generating standing waves of varying polarisation. The complex interactions between multi-level atoms and the three-dimensional standing waves provide additional mechanisms by which atomic kinetic energy is lost, such as *Sisyphus cooling*, which is an example of polarisation-gradient cooling [47].

[8] Note that temperature is strictly only defined for an ensemble of particles, and not for a single atom, but is a useful parameter to characterise the width of the distribution of expected velocities.

[9] For a general detuning, the expected Doppler cooling temperature is $T = \frac{\hbar}{4\Gamma k_B}\left(\frac{\Gamma}{2\delta} + \frac{2\delta}{\Gamma}\right)$ which has a minimum of T_D for $\delta = -\Gamma/2$. Note that k_B is the Boltzmann constant.

Sisyphus cooling occurs because, in the one-dimensional case, two red-detuned counterpropagating beams form a standing wave of varying polarisation,[10] resulting in spatial oscillations of the light shift of the Zeeman sublevels and the optical pumping rates.[11] The effect of the periodic light shifts is that the internal energy of an atom rises and falls with position; it sees a potential energy landscape of 'hills' and 'valleys', with spacing $\lambda/4$. Climbing a hill transfers kinetic energy to internal potential energy, and vice versa when falling down into a valley, so an atom that remains in the same state will simply periodically accelerate and decelerate as its kinetic and potential energy interchange. However, an atom can change state if it absorbs a photon to transition to a higher energy electronic state, then decays by spontaneous emission back to a different Zeeman sublevel of the ground state. Crucially, the varying polarisation causes the optical pumping rates to be such that an atom has a higher probability of changing state when at the top of a hill, compared to at the bottom of a valley. As a result, an atom will repeatedly climb a hill then be transferred to a lower energy state, which corresponds to being in a valley, then will proceed to climb the next hill. In this way, kinetic energy is transferred to potential energy and then into the energy of the photons that are radiated away, cooling the atom. This works most efficiently for atoms travelling slowly enough for multiple scattering events to occur over a distance $\sim \lambda/4$.

Sub-Doppler cooling is a combination of several similar processes, and the temperature can reach a few times the *recoil temperature*,

$$T_{\mathrm{rec}} = \frac{\hbar^2 k_L^2}{m k_B} \tag{1.32}$$

which arises from the energy imparted to the atom due to absorption of a single photon. For ^{87}Rb, $T_{\mathrm{rec}} = 362\,\mathrm{nK}$, but in practice the lowest temperatures are typically a few microkelvin. Nevertheless, for a heavy alkali such as Rb, sub-Doppler cooling allows temperatures two orders of magnitude below the prediction of the two-level model. The recoil limit is not an

[10] The mechanism described here requires a red-detuned low-intensity standing wave, producing hills and valleys in the potential energy due to the varying polarisation. However, there is a similar mechanism, also called Sisyphus cooling, that requires a blue-detuned high-intensity standing wave, in which case the hills and valleys in the potential energy are due to the varying intensity, rather than the polarisation [44].

[11] Optical pumping is explained more in Sec. 1.5.2.

insurmountable barrier and can be surpassed by several techniques such as Raman cooling [48] or velocity-selective coherent population trapping [49], and, for some species with narrow linewidths, the Doppler limit is itself sufficiently low to achieve quantum degeneracy [50]. There are a considerable number of experiments that use a two-stage laser cooling process; initial cooling occurs on a broad transition for which the scattering force is strong, then cooling on a narrow transition to achieve lower temperatures, and at a faster rate than the evaporative cooling mechanisms used in most quantum degeneracy experiments. The semi-classical approximation used in this section does not apply for laser cooling using such narrow transitions (e.g. in alkaline-earth and rare-earth metals) and a substantially different treatment is necessary if the Doppler limit is comparable to, or below, the recoil limit.[12]

1.3 Magneto-Optical Trapping

Although the optical molasses technique accumulates cold atoms in the intersection region of the beams, the atoms are not confined to this region and diffuse out within a few seconds.[13] New atoms entering the region will be cooled, so the density of cold atoms in the intersection region remains higher than in the absence of optical molasses, but the lack of confinement severely limits the density that can be obtained. Extending this technique to both cool and trap atoms requires introducing a spatial dependence to the radiation pressure force, which is achieved by the addition of a weak magnetic field to cause Zeeman splitting of a multilevel transition.

[12] Such systems no longer satisfy the broad band condition of Eq. 1.12 which was required to use the semi-classical picture of the atom described in Sec. 1.

[13] From the theory of Brownian motion, the mean squared position increases at a rate $\langle x^2 \rangle = 2Dt$ where $D = \Gamma/k_L^2$ is the diffusion constant for optical molasses [43]. For rubidium $D \simeq 1\,\mathrm{mm}^2/\mathrm{s}$, so atoms will escape from beams of 1 cm diameter in 3 – 4 seconds. This assumes extremely well-balanced beams, but most experiments have intensity imbalances and imperfections that increase the rate of escape, so that tens of milliseconds is more typical.

1.3.1 Zeeman Interaction

For an atom described by Hamiltonian $\hat{H}_A$, applying a magnetic field $\mathbf{B}(\mathbf{r})$ adds an additional interaction term. The total Hamiltonian becomes $\hat{H} = \hat{H}_A - \hat{\mu} \cdot \mathbf{B}(\mathbf{r})$ where $\hat{\mu}$ is the atomic magnetic moment,[14]

$$\hat{\mu} = -\frac{\mu_B}{\hbar}\left(g_s \hat{\mathbf{S}} + \hat{\mathbf{L}}\right) \tag{1.33}$$

where μ_B is the Bohr magneton, $g_s \approx 2.002$ is the anomalous gyromagnetic ratio, $\hat{\mathbf{S}}$ is the spin angular momentum operator, and $\hat{\mathbf{L}}$ is the orbital angular momentum operator. For weak magnetic fields, the magnetic interaction is a perturbation to $\hat{H}_A$ that couples $\hat{\mathbf{S}}$ and $\hat{\mathbf{L}}$ into the total angular momentum operator $\hat{\mathbf{J}} = \hat{\mathbf{S}} + \hat{\mathbf{L}}$. This causes previously degenerate magnetic sublevels of the atomic structure to split, which is the *Zeeman effect*. The Zeeman energy shift of a state $|J, m_J\rangle$ in a magnetic field $\mathbf{B}$ is

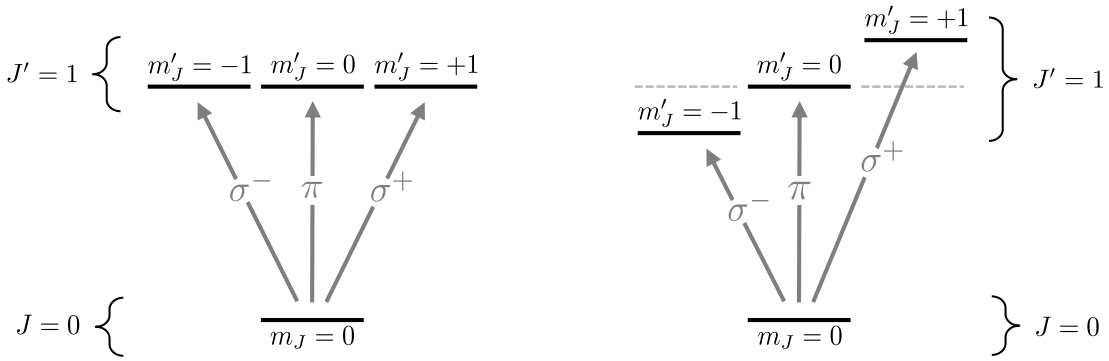
$$\Delta E_Z = g_J \mu_B m_J |\mathbf{B}| \tag{1.34}$$

where m_J is the quantum number corresponding to the projection of $\mathbf{J}$ onto the axis defined by $\mathbf{B}$, and g_J is the Landé g-factor.[15]

Figure 1.3 shows the case of a transition from a $J = 0$ ground state to a $J' = 1$ excited state. The excited state has three-fold degeneracy of its magnetic sublevels ($m_J = -1, 0, +1$), which is lifted by the application of a magnetic field. Transitions from the ground to excited states cause a change $\Delta m_J = m_{J'} - m_J$, and selection rules (that arise from angular momentum conservation) mean the different transitions are only excited by photons with particular spin projections. The $\Delta m_J = +1$ transition requires a photon with a spin projection along the quantisation axis (defined by $\mathbf{B}$) of $m_S = +1$, and is called a σ^+ transition. Similarly, the $\Delta m_J = -1$ transition requires a photon with $m_S = -1$, and is called a σ^- transition. Finally, the $\Delta m_J = 0$ transition requires a photon with $m_S = 0$ (which is not possible for a

[14] Note that the inclusion of the $1/\hbar$ term depends on defining the eigenvalues of $\hat{\mathbf{S}}^2$ as $s(s+1)\hbar$, and similarly for $\hat{\mathbf{L}}$, $\hat{\mathbf{L}}_z$, etc. If instead the eigenvalues are defined without the $\hbar$ factor, which is an alternative convention, then there is no $1/\hbar$ term in $\hat{\mu}$.

[15] $g_J = \frac{3}{2} + \frac{S(S+1)-L(L+1)}{2J(J+1)}$



(a) $B = 0$ (b) $B > 0$

Figure 1.3: The Zeeman effect for a $J = 0 \rightarrow J' = 1$ transition: (a) the three magnetic sublevels of the excited state are degenerate in the absence of a magnetic field; (b) the degeneracy is lifted for a non-zero magnetic field.

photon propagating parallel to the magnetic field), and is called a π transition.[16]

By exploiting the different photon polarisation requirements of the transitions, combined with the differences in transition frequency due to the Zeeman effect, atoms can be subjected to a position-dependent cooling force that causes them to be trapped.

1.3.2 One-Dimensional MOT

To understand how this combined cooling and trapping can be achieved, first consider the one-dimensional case where the magnetic field simply varies linearly with position, as shown in Fig. 1.4 for $B_z = bz$. If red-detuned right-hand circularly polarised light[17] of frequency ω_L is directed along the $+z$ direction, it will drive the σ^- transition in the region $z < 0$ (since the magnetic field is antiparallel to the propagation direction), with a resonance where the Zeeman splitting causes the transition frequency to be ω_L. In the $z > 0$ region, the magnetic field is parallel to the propagation direction of the beam so it drives σ^+ transition, but the

[16] σ^+, σ^- and π refer only to the atomic transitions, and the common labelling of light as such is shorthand for saying the light has the requisite polarisation to drive such transitions. Often right-hand circularly polarised light is described as σ^+-polarised because the spin projection of the photons along the direction of propagation is $m_S = +1$, however this will only drive σ^+ transitions in an atom if the quantisation axis of the atom is parallel to the propagation of the photon. If the quantisation axis of the atom is antiparallel to the propagation direction, then right-hand circularly polarised light will drive σ^- transitions instead.

[17] Using the convention of defining the polarisation from the point of view of the source, right-hand circularly polarised light has spin projection $m_S = +1$ along the direction of propagation, and left-hand circularly polarised light has spin projection $m_S = -1$.

magnetic field gradient increases the detuning, which reduces the rate that the atom absorbs photons. Similarly, identical right-hand polarised light propagating along the $-z$ direction drives the σ^- transition in the region $z > 0$, and σ^+ transition for $z < 0$, with a resonance in the $z > 0$ region when the Zeeman shift makes the σ^- transition frequency equal to ω_L. Therefore, when both beams are present, the force on the atom from the beam propagating towards $+z$ exceeds that of the counterpropagating beam in the region $z < 0$, and vice versa; the net force on the atom is always directed towards the $z = 0$ position. The result is that atoms are cooled and pushed towards the $B = 0$ position where the forces from the two beams cancel out and there is no net force.

The form of these forces is that of the radiation pressure force from Eq. 1.27, but with $\omega_0 \to \omega_0 + m_J\beta z$, where the Zeeman splitting (Eq. 1.34) has been rewritten for convenience as $\Delta E_Z = \hbar m_J \beta z$ by defining $\beta = g_J \mu_B b/\hbar$. Using $\delta = \omega_L - \omega_0$, the force for the one-dimensional case with $\sigma^\pm$ beams propagating along $\pm z$ is

$$F_{\text{rp}}^{\pm} = \pm\frac{\Gamma}{2}\frac{I/I_{\text{sat}}}{1 + I/I_{\text{sat}} + 4(\delta \mp k_L v \mp \beta z)^2/\Gamma^2}\hbar k_L \tag{1.35}$$

In the low velocity limit, and for small displacements about $z = 0$, the combined force from the two beams can be expressed as

$$F_z = -\alpha v - \kappa z \tag{1.36}$$

In addition to the one-dimensional optical molasses force in the same limit, Eq. 1.29, there is a restoring force with a spring constant given by $\kappa = \alpha\beta/k_L$ which is the effective spring constant for the restoring trap, which is maximised for $\delta = -\Gamma/2$. The atom therefore (in the linear approximation) undergoes damped harmonic motion, and typical values for α and κ satisfy the overdamped condition ($\kappa^2 \gg 4M\alpha$). Therefore atoms are pushed towards the centre with minimal oscillatory motion.

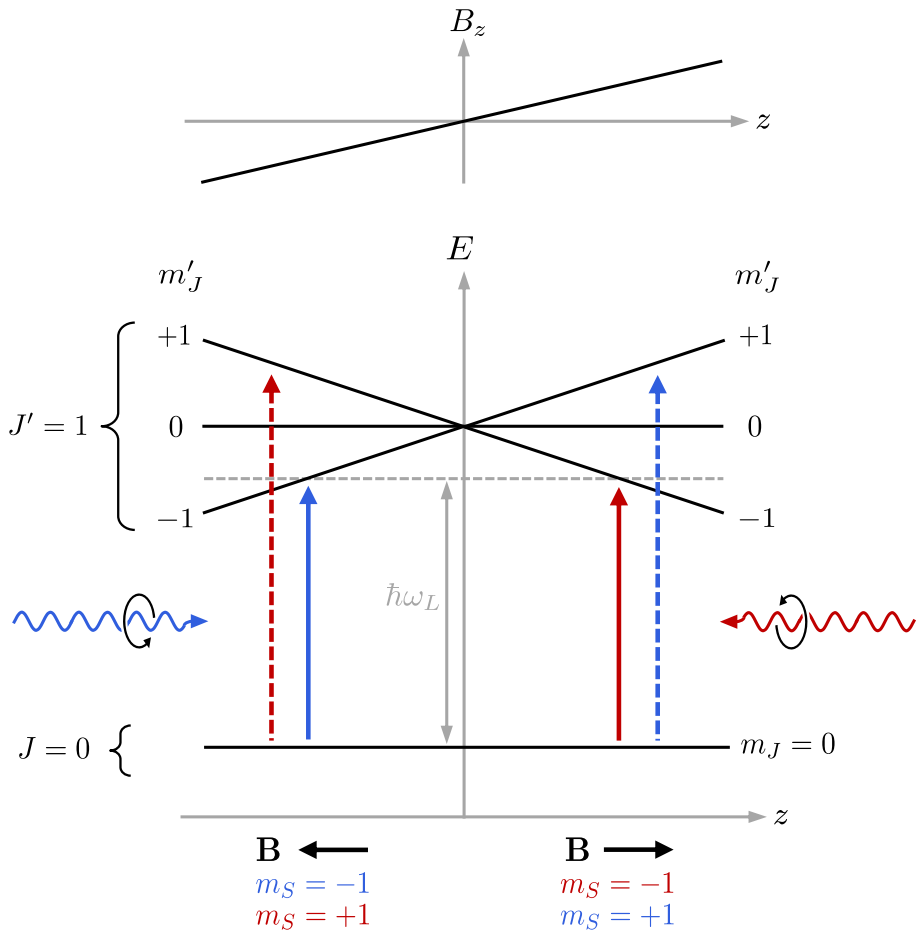


Figure 1.4: Magneto-optical trapping for a $J = 0 \rightarrow J' = 1$ transition in a magnetic field $B_z = bz$. Light of frequency $\omega_L < \omega_0$ is directed along $+z$ and circularly polarised such that it drives the σ^- transition in the $z < 0$ region (with a resonance when the Zeeman shift is equal to the detuning $\omega_0 - \omega_L$), and drives the σ^+ transition in the $z > 0$ region, for which the detuning increases due to the Zeeman effect. The force on the atom is therefore greatest for $z < 0$, and the presence of an identical counterpropagating beam (directed along $-z$) results in a net force for a stationary atom that drives it towards the $B = 0$ position (where the forces of the two beams cancel because of the absence of Zeeman splitting).

1.3.3 Three-Dimensional MOT

The extension to a three-dimensional MOT typically involves three orthogonal pairs of counterpropagating beams, like an optical molasses, with a suitable magnetic field. The most common magnetic field configuration is the spherical (or 3D) quadrupole, produced by a coaxial pair of coils in the anti-Helmholtz configuration,[18] as illustrated in Fig. 1.5. The field is directed towards the central $B = 0$ point in the transverse (x, y) plane, while the field on-axis is directed away from the $B = 0$ point, which requires beams of opposite handedness for the axial and transverse directions in order to produce the correct configuration for a MOT.[19]

Aside from requiring beams of opposite polarisation, the axial and transverse directions also differ in their respective magnetic field gradients. The gradient in the transverse (x and y) directions are equal, however the axial (z) component has opposite direction and double the magnitude:

$$\frac{\mathrm{d}B_x}{\mathrm{d}x} = \frac{\mathrm{d}B_y}{\mathrm{d}y} = -\frac{1}{2}\frac{\mathrm{d}B_z}{\mathrm{d}z} \tag{1.37}$$

which arises from the Maxwell equation $\boldsymbol{\nabla} \cdot \mathbf{B} = 0$. The opposite polarity is what requires that the beam polarisations along $\hat{\mathbf{z}}$ are reversed from those along $\hat{\mathbf{x}}$ and $\hat{\mathbf{y}}$, and the greater axial magnitude means that the restoring force is twice as large along $\hat{\mathbf{z}}$. Thus the extension

[18] Note that there is some ambiguity as to what the anti-Helmholtz configuration of two coils refers to. The Helmholtz configuration is that of two identical coils with currents in the same direction, where the separation is equal to the radius so that the first, second and third derivatives of the field are zero at the midpoint of the coils, providing a highly uniform field. The configuration where the current in one coil is reversed may be referred to as the anti-Helmholtz configuration, however the third derivative is non-zero unless the separation is $\sqrt{3}$ of the radius, in which case the second, third and fourth derivatives are all zero, providing a highly uniform field gradient. In practice, a MOT is insensitive to small variations in the separation, and the term 'anti-Helmholtz' is used for any pair of coils with opposite currents generating a spherical quadrupole field.

[19] If instead the currents in both coils are reversed from the scenario depicted in in Fig. 1.5, the field directions are reversed (directed towards the central $B = 0$ point in the axial direction and away from it in the transverse direction), requiring the axial and transverse beams to have opposite handedness to those described in the text. Both arrangements are valid to produce a MOT.

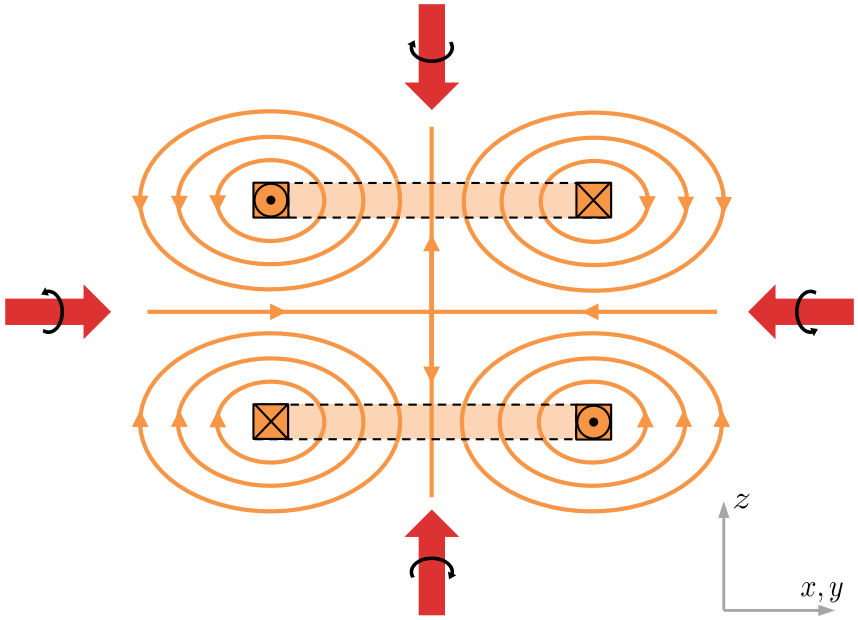


Figure 1.5: The typical magnetic field for a three-dimensional MOT, a spherical quadrupole, is produced by a pair of coils with equal and opposite currents. The coils are coaxial along the z axis, and have rotational symmetry about the z axis, as does the resultant magnetic field. At the centre of the coils is a $B = 0$ point, and the field direction is towards this point in the transverse direction (requiring the transverse MOT beams to be left-hand circularly polarised), but away from this point in the axial direction (requiring the axial MOT beams, to be right-hand circularly polarised). The third pair of counterpropagating beams are not shown for simplicity, but are directed in and out of the plane of the figure, and require the same handedness as the other pair of transverse beams, which are shown.

of the one-dimensional MOT force to three dimensions is,[20]

$$\begin{aligned} \mathbf{F}_{\text{MOT}} &= \mathbf{F}_{\text{molasses}} + \mathbf{F}_{\text{restoring}} \\ &= -\alpha \mathbf{v} - \kappa(x\,\hat{\mathbf{x}} + y\,\hat{\mathbf{y}} + 2z\,\hat{\mathbf{z}}) \end{aligned} \tag{1.38}$$

This demonstrates how the presence of a weak magnetic field causes a position-dependence of the Doppler cooling, and, with the appropriate magnetic field and light polarisations, will drive atoms to the zero of the magnetic field. It is important to note that the field is too weak to cause trapping by itself, and just has the effect of introducing the spatially-varying Zeeman splitting. A full description of the MOT is a complex endeavour, however the key MOT dynamics can be captured using some simple expressions.

[20] Just considering the region of the field near $B = 0$, for which a linear approximation of the field is valid.

1.4 MOT Dynamics

Certain key parameters are useful to provide insights into MOT behaviour. The *capture velocity* determines what proportion of atoms can be trapped and cooled, the *capture rate* defines the rate at which atoms are trapped and cooled, and the *equilibrium number* describes the total number of atoms available for the subsequent experiment. Some simple parameter estimates and rate equation models, using the results just obtained, are able to describe the basic dynamics of the MOT system.

1.4.1 Capture Velocity

To estimate the maximum velocity v_c an atom can have whilst still being trapped, consider an atom travelling along the full length of the MOT trapping volume (the region of intersecting laser beams) on-axis. An atom with v_c will travel the full width of the MOT, being decelerated to $v = 0$ at the opposite side; if instead the atom had velocity $v > v_c$, it would still have $v > 0$ after traversing the width of the MOT, and therefore escape. The maximum deceleration that a beam can exert on an atom of mass M occurs for $I \gg I_{sat}$ and zero detuning, and is given by $a_{max} = \hbar k_L \Gamma / 2M$ (from Eq. 1.35). A realistic assumption is that the atom experiences an average deceleration of $\sim a_{max}/2$ as it traverses the MOT region (the size of which can be characterised by the length d). Hence the estimated capture velocity is given by[21]

$$v_c \approx \sqrt{a_{max} d} = \sqrt{\frac{\hbar k_L \Gamma d}{2M}} \tag{1.39}$$

For ^{87}Rb, $a_{max} \approx 114\,\mathrm{km/s^2}$ and $v_c \approx 50\,\mathrm{m/s}$ for $d = 20\,\mathrm{mm}$, which is typical of measured capture velocities [51].

The capture velocity defines the proportion of a population of atoms that can be trapped. When loading a MOT from a room temperature vapour, the probability distribution of

[21] Using the classical equation of motion for constant acceleration a (over a distance s from initial velocity u to final velocity v): $v^2 = u^2 + 2as$.

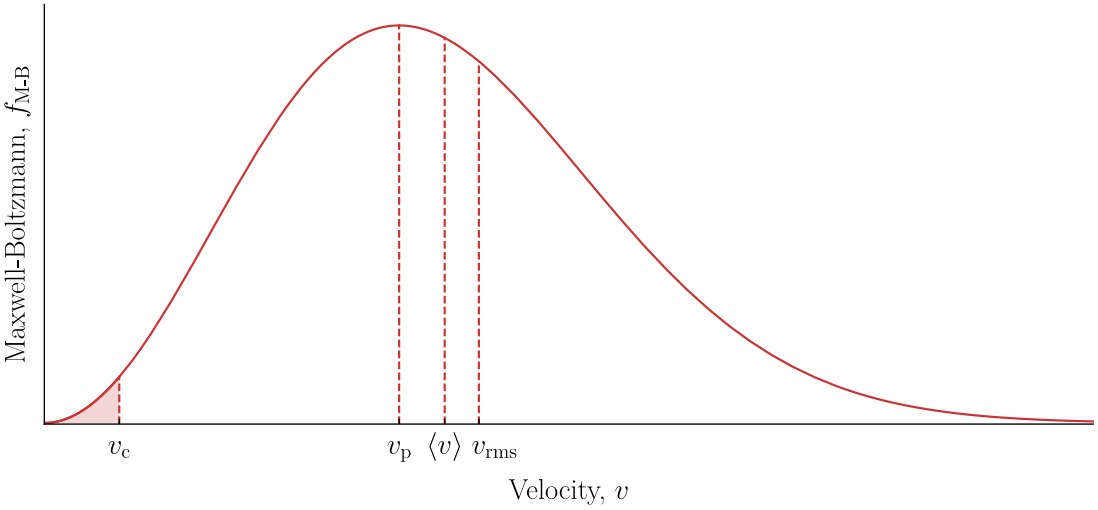


Figure 1.6: The Maxwell-Boltzmann distribution (Eq. 1.40) at room temperature, $T = 293\,\text{K}$. The most probable speed $v_p = 237\,\text{m/s}$, the mean speed $\langle v \rangle = 267\,\text{m/s}$, and the root mean square speed $v_{rms} = 290\,\text{m/s}$, of the distribution are shown, for ^{87}Rb, as well as the approximate capture velocity $v_c \approx 50\,\text{m/s}$. Only 0.7% of atoms have $v < v_c$.

atomic speeds is given by the Maxwell-Boltzmann distribution,

$$f_{\text{M-B}}(v)\,\mathrm{d}v = \frac{4}{\sqrt{\pi}}\frac{v^2}{v_p^3}e^{-v^2/v_p^2}\,\mathrm{d}v \tag{1.40}$$

where $v_p = \sqrt{2k_BT/M}$ is the most probable speed at temperature T for particles of mass M.[22] Figure 1.6 shows $f_{\text{M-B}}(v)$ at room temperature, $T = 293\,\text{K}$, and less than 1% of atoms have $v < v_c$, so when loading a MOT with a thermal population of atoms, the vast majority of atoms will fail to be slowed and instead just act as a background. For a MOT, this low fraction is compensated by the ability of the MOT to capture atoms over almost all incident angles. In contrast, laser cooling of atoms by a single counterpropagating laser beam can slow down atoms from velocities approaching the peak of the distribution, but only for a small solid angle (more details on *Zeeman slowers* are in Sec. 2.2).

[22] Note that the asymmetry of the Maxwell-Boltzmann distribution Fig. 1.6 means that the most probable speed, v_p, is different to the mean velocity, $\langle v \rangle = \sqrt{8k_BT/\pi M}$, and the rms-speed, $v_{rms} = \sqrt{3k_BT/M}$.

1.4.2 Capture Rate

From kinetic theory, the flux of particles in a gas with speeds between v and $v + \mathrm{d}v$ is

$$\Phi_{\mathrm{kin}}\,\mathrm{d}v = \frac{1}{4} n v f(v)\,\mathrm{d}v \tag{1.41}$$

where n is the number density of the gas and $f(v)$ is the speed distribution of the particles. For a room temperature vapour, $f(v)$ is the Maxwell-Boltzmann distribution from Eq. 1.40. The rate at which trappable atoms enter the MOT region is the product of Φ_{kin} and the surface area of the MOT region, S, integrated over the range of trappable speeds:

$$\begin{aligned} R &= \int_0^{v_{\mathrm{c}}} \Phi_{\mathrm{kin}} S\,\mathrm{d}v \\ &= \frac{nS}{\sqrt{\pi}} \int_0^{v_{\mathrm{c}}} \frac{v^3}{v_{\mathrm{p}}^3} e^{-v^2/v_{\mathrm{p}}^2}\,\mathrm{d}v \end{aligned} \tag{1.42}$$

Since $v_{\mathrm{c}} \ll v_{\mathrm{p}}$, $e^{-v^2/v_{\mathrm{p}}^2} \approx 1$ leaving

$$\begin{aligned} R &= \frac{nS}{\sqrt{\pi}} \left[\frac{v^4}{4v_{\mathrm{p}}^3}\right]_0^{v_{\mathrm{c}}} \\ &= \frac{nS}{4\sqrt{\pi}} \frac{v_{\mathrm{c}}^4}{v_{\mathrm{p}}^3} \end{aligned} \tag{1.43}$$

Finally, the surface area of the MOT region scales as $S = \xi d^2$, (the prefactor ξ varies on the shape of the surface area[23]). Substituting in for S, and for v_{c} using Eq. 1.39, yields the capture (or loading) rate

$$R = \frac{a_{\mathrm{max}}^2 n \xi}{4\sqrt{\pi} v_{\mathrm{p}}^3}\, d^4 \tag{1.44}$$

For a MOT loaded from a room temperature vapour of ^{87}Rb, assuming typical values of $d = 20\,\mathrm{mm}$ and $n = 10^8\,\mathrm{cm}^{-3}$,[24] the loading rate is of the order of $10^9 - 10^{10}\,\mathrm{atoms/s}$. An important result here is the very strong d^4 dependence of the loading rate on the length scale of the MOT.

[23] Modelling the MOT region as: a sphere gives $S = \pi d^2$; a cube gives $S = 6d^2$; the intersection region of three pairs of orthogonal beams (a tricylinder) gives $S = 6(2 - \sqrt{2})d^2 \approx 3.5d^2$.

[24] Which corresponds to a pressure of $4 \times 10^{-9}\,\mathrm{mbar}$ using $P = k_B n T$.

1.4.3 Equilibrium Number

The steady state number of atoms in the MOT, N, can be estimated by a simple rate equation approach. The loading rate R is balanced by a decay term due to collisional losses:

$$\frac{\mathrm{d}N}{\mathrm{d}t} = R - N\Gamma_{\mathrm{col}} \tag{1.45}$$

Kinetic theory gives the rate at which a particle undergoes collisions as $\Gamma_{\mathrm{col}} = n_{\mathrm{bg}}\sigma_{\mathrm{col}}\langle v\rangle$ where n_{bg} is the number density of background atoms and σ_{col} is the collisional cross-section.[25] Assuming that collisional losses are overwhelmingly due to collisions with atoms of the same species [52, 53], then $n_{\mathrm{bg}} \approx n$ and the collisional loss rate is[26]

$$N\Gamma_{\mathrm{col}} = \frac{\sqrt{\pi}}{2} N\sigma_{\mathrm{col}} n v_{\mathrm{p}} \tag{1.46}$$

The steady state solution for N is

$$\begin{aligned} N &= R/\Gamma \\ &= \frac{a_{\mathrm{max}}^2 \xi}{8\sigma_{\mathrm{col}} v_{\mathrm{p}}^4}\, d^4 \end{aligned} \tag{1.47}$$

There is a strong dependence on the length scale of the MOT region, but the equilibrium atom number is independent of n, and therefore does not depend on vapour pressure. Assuming the same parameters as for the estimate of R, and using $\sigma_{\mathrm{col}} = 3 \times 10^{-12}\,\mathrm{cm}^2$ [54] for ^{87}Rb, the equilibrium number of a MOT is of the order of 10^9 to 10^{10} atoms. This is in keeping with observed MOT populations for typical laser beam diameters of a few centimetres.

[25] $1/\Gamma_{\mathrm{col}}$ is the average time between collisions for a single particle.
[26] Using $\langle v\rangle = \frac{\sqrt{\pi}}{2} v_{\mathrm{p}}$.

1.5 Application of Simple Models to Reality

These models provide useful insights into the characteristics of MOTs, but they are based on simple models of the atoms, so it is reasonable to question how applicable they are to more complicated multi-level systems, such as alkali metals. It transpires that these models work surprisingly well.

1.5.1 Repumping Dark States

One of the key assumptions in the models presented is that of a closed transition; there are no states other than those of the ground and excited manifolds available to the atom. The reality of a complex multi-level electronic structure allows an atom undergoing laser cooling to decay into states that do not interact with the light. Such 'dark' states no longer undergo cooling, and the atom is lost. The key to laser cooling is therefore to find transitions that have minimal leakage to dark states, or to drive atoms back into the states of the cooling cycle. Alkali atoms are particularly popular candidates for laser cooling because their comparatively simple energy structure, arising from a single valence electron, features nearly-closed transitions suitable for laser cooling. For example, Fig. 1.7 shows the D2 transition in ^{87}Rb from the $5s\,^2S_{1/2}$ ground state to the $5p\,^2P_{3/2}$ excited state. Laser cooling occurs on the $F = 2 \rightarrow F' = 3$ transition, for which electric dipole selection rules forbid any transitions except back to the $F = 2$ ground state.[27] However, the atom can also be off-resonantly excited on the $F = 2 \rightarrow F' = 2$ transition then decay to the dark $F = 1$ hyperfine ground state.

To understand the importance of decay to the dark states requires examining the number of photon scattering events that typically occur before off-resonant loss to the dark state, relative to how many scattering events are required for cooling. The frequency difference between the $F = 2 \rightarrow F' = 2$ and $F = 2 \rightarrow F' = 3$ is $\Delta = 267\,\mathrm{MHz}$, which is much greater

[27] The selection rule $\Delta F = 0, \pm 1$ (but not $0 \rightarrow 0$) prevents atoms in the $F' = 3$ state from decaying to the dark hyperfine ground state, but all other excited F' states are allowed.

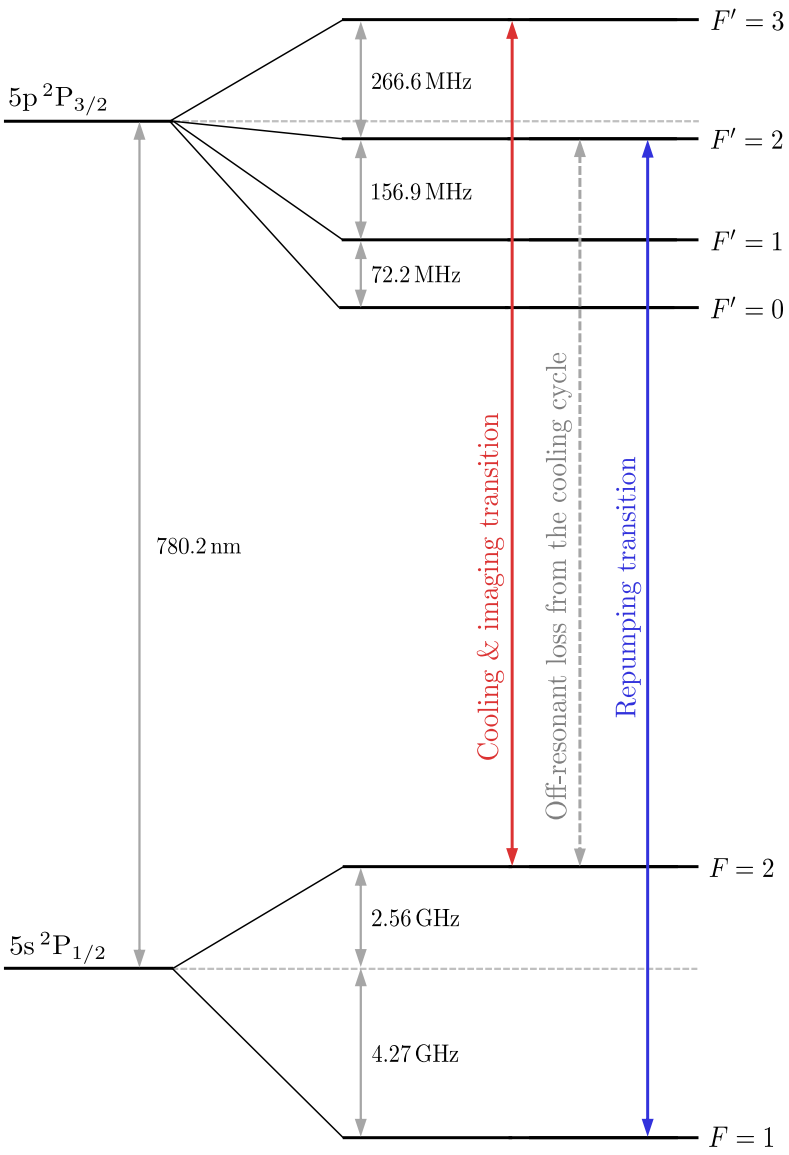


Figure 1.7: The energy structure of the D2 line of ^{87}Rb, with the cooling and repumping transitions indicated, as well as the off-resonant transition responsible for losses of atoms to the dark hyperfine state. All numerical values are from Steck [55], from which the frequency difference between the cooling and repumping transitions is 6.568 GHz.

than the typical detuning $|\delta| \sim 2-4\,\Gamma \approx 10-25\,\mathrm{MHz}$ of the cooling light.[28] Using Eq. 1.24 then gives the relative scattering rate as

$$\frac{R_{\mathrm{scatter}}^{\mathrm{cooling}}}{R_{\mathrm{scatter}}^{\mathrm{off\text{-}res}}} = \frac{1 + 4((\Delta+\delta)/\Gamma)^2 + I/I_{\mathrm{sat}}}{1 + 4(\delta/\Gamma)^2 + I/I_{\mathrm{sat}}} \tag{1.48}$$

The relative scattering rate is plotted in Fig. 1.8 as a function of intensity for different

[28] The cooling light is red-detuned, so the sign of δ is negative.

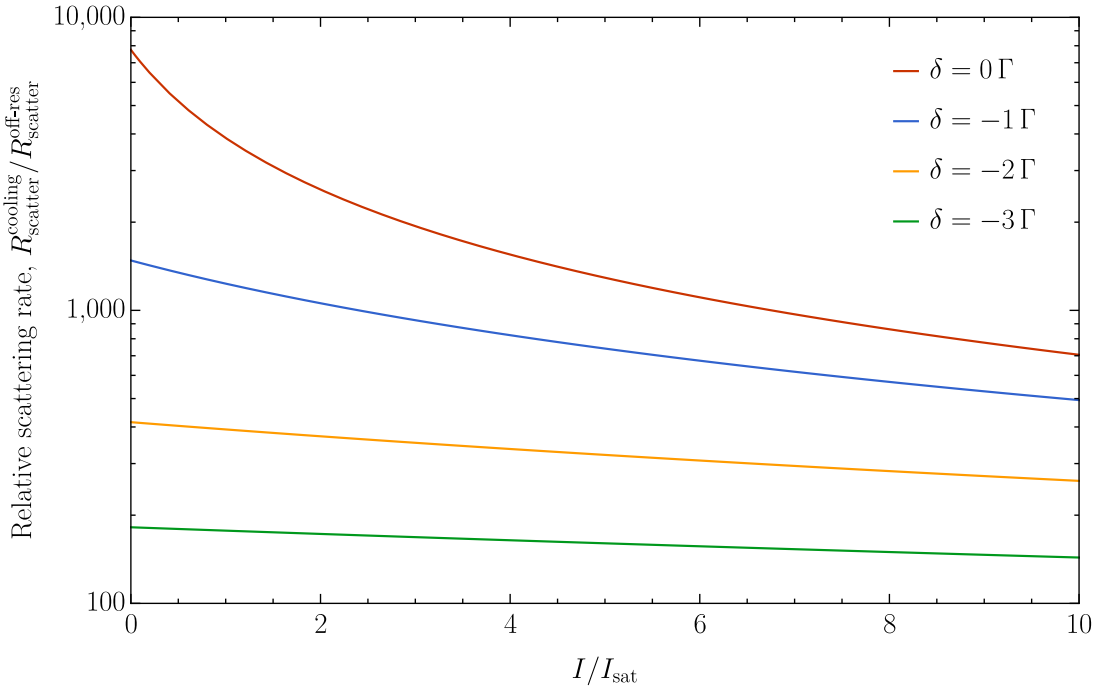


Figure 1.8: The relative scattering rates, as a function of intensity I and for various detunings δ, for ^{87}Rb atoms in the $F = 2$ ground state to the $F' = 3$ and $F' = 2$ excited states, which correspond to near-resonant excitation on the cooling cycle and off-resonant loss to the dark state, respectively.

detunings. A typical MOT operates with $\delta \sim 2-3\,\Gamma$, for which the relative scattering rate is approximately 200. A ^{87}Rb atom with velocity $v_c \approx 50\,\text{m/s}$ has momentum Mv_c and absorbs $\hbar k_L$ momentum per photon, so it requires on the order of $Mv_c/\hbar k_L \approx 8{,}300$ photons to be absorbed in order to be fully slowed. Therefore the vast majority of atoms would fall out of the cooling cycle before being fully slowed, greatly reducing the capture rate and equilibrium atom number of the MOT.

To prevent atoms accumulating in the dark state, an additional frequency of light is applied to depopulate the dark state by 'repumping' the atoms on the $F = 1 \rightarrow F' = 2$ transition. Some atoms without hyperfine structure such as ^{88}Sr can be laser-cooled without requiring repumping light if the decay rate to dark states is small compared to the cooling transition rate [56]. In contrast, molecules have very complicated electronic structures with many possible decay paths, generally requiring several repumping frequencies even for the best choice of cooling transition.

1.5.2 Optical Pumping

Even with a closed cooling transition, the number of magnetic sublevels of the excited state is often much greater than the three assumed in the $J = 0 \rightarrow J' = 1$ example used to illustrate the MOT mechanism. In the case of ^{87}Rb, the $F = 2$ ground state has five sublevels ($m_F = 0, \pm 1, \pm 2$) and the $F' = 3$ excited state has seven ($m_{F'} = 0, \pm 1, \pm 2, \pm 3$). However, when the atom interacts with σ^+ polarised light, every photon absorption results in $\Delta m_F = +1$, while every spontaneous emission can be $\Delta m_F = 0, \pm 1$. In this way the atom is driven towards the $m_F = F$ sublevel within a few scattering events. Similarly, when the atom interacts predominantly with σ^- polarised light, it is driven to the $m_F = -F$. This is *optical pumping* and serves to make the model used (with one ground state and three upper states) a reasonable approximation despite the multi-level reality.[29]

This optical pumping to the extremities would be expected to occur during the capture process when the atoms are far from the centre and tuned to be close to resonance with the beam opposing the motion. Atoms at the centre of the MOT feel the effect of all the laser beams and are distributed over many m_F states. This must be taken into account to calculate the expected scattering rate and trap spring constant, as described by Townsend et al. [57].

1.5.3 Sub-Doppler Cooling in a MOT

In Sec. 1.2.3, it was noted that the effect of multi-level atoms and light interference on optical molasses was to allow sub-Doppler cooling. The addition of a magnetic field prevents the same cooling mechanisms occurring when the Zeeman energy shifts exceed the polarisation-induced light shifts that are required for sub-Doppler temperatures. Therefore sub-Doppler cooling only occurs very close to the $B = 0$ position in a MOT. Trapped atoms will undergo some sub-Doppler cooling if the intensities are balanced [58], however the temperature limit

[29] Note that the atom is not always in the fully stretched state ($|m_F| = F$) because even when the interaction with σ^+ light dominates, there is a non-zero probability of absorbing a photon from the σ^- light, temporarily placing the atom in the $m_F = F - 1$.

of a MOT is higher than for optical molasses because of the magnetic field and increased atomic density.

1.5.4 Summary

It transpires that the two-level model for atom-light interaction, with the addition of magnetic sublevels in the excited state, is a better model than might be expected for complex real atoms. It assumes a closed cooling transition, and a close approximation to such a transition can effectively be achieved either by repumping from dark states or careful selection of the atom and transition. The model has been experimentally verified as correctly describing the general behaviour of optical molasses and MOTs, and to provide order-of-magnitude correct parameter values [59, 60]. More detailed modelling refines some of the relationships found via the simple model – for example, the d^4 dependence of R and N is adjusted to a $d^{3.6}$ relationship, that fits with experimentally observed data [60, 61]. All models of magneto-optical trapping however tend to require a scaling factor to produce quantitative agreement, due to the difficulty in accurately accounting for light field inhomogeneity, saturation, the position and angle-dependence of the capture velocity, etc. The presented model does not describe the sub-Doppler cooling mechanisms in optical molasses, which are also present, albeit to a lesser degree, at the low-field region close to the centre of a MOT. The behaviour of the MOT at high atom densities is also not included in the model, since it assumes non-interacting independent atoms. Overall though, the model and its predictions provide useful guidance for the design and optimisation of laser cooling apparatus.

1.6 Practical Implementation of MOTs

A MOT is able to cool of order 10^{10} atoms in about a second and confine them to clouds a few millimetres in size, which makes it an excellent starting point for the study of cold matter, to the extent that it has become the default tool for accumulating cold atoms. However, the achievable temperature in a MOT is insufficient for many cold-atom applications. Optical

molasses typically achieve temperatures an order of magnitude lower by sub-Doppler cooling (see Sec. 1.2.3), which can be used directly in atom interferometry. To reach the regime of quantum gases, including Bose-Einstein and fermionic condensates, a further increase in phase-space density is necessary to reach quantum degeneracy. This is commonly achieved by evaporative cooling in magnetic traps, dipole-force traps, or combinations of the two, and corresponds to approximately another order of magnitude decrease in temperature. The MOT therefore serves as an important first step in cold-atom experiments, before subsequent alternative cooling methods are performed to achieve the desired temperatures. A typical experimental sequence would involve loading a MOT, sweeping the MOT parameters towards an optical molasses to increase sub-Doppler cooling, then transfer of the atoms into a dipole or magnetic trap for evaporative cooling.[30]

An ideal cold-atom apparatus would be able to quickly collect atoms, before keeping them cold for as long as possible with minimal losses to perform investigations. This would allow fast repetition rates and high duty cycles, while permitting long interrogation times and strong signal-to-noise ratios. However, both the loading rate of a MOT and the collisional losses from background collisions are directly proportional to the vapour pressure (see Eq. 1.44 and Eq. 1.46). Therefore, despite the equilibrium number of a MOT being pressure independent (Eq. 1.47), the experimentalist is faced with a choice of a high vapour pressure to achieve rapid loading, at the cost of a short lifetime of the trapped atoms, or a low vapour pressure to permit long interaction times but with protracted experimental cycles.

The solution to achieving the best of both worlds is to use a two-chamber system: the MOT, and all subsequent cooling and probing, occurs in a low pressure 'science' chamber to keep the atoms isolated from background gases; but the MOT is initially loaded by a low-velocity ($v < v_c$) atomic flux generated in a neighbouring 'source' chamber. The source of low-velocity atoms can be operated at a much higher pressure to maximise the flux, and hence the MOT loading rate, without significantly contaminating the environment of the atoms in the science chamber. Attaining two markedly different pressures in a single system

[30] Magnetic traps, like dipole traps, are conservative, which means that atoms trapped in them conserve energy, however external stimuli are used to cool the atoms or to preferentially extract the atoms with highest kinetic energy, reducing the overall temperature.

can be achieved by having a small exit aperture in the source to produce differential pumping, which is outlined in Sec. 3.1.1. An alternative approach to a low-velocity source is to form a MOT in the source chamber, then to transport the atoms while they are trapped, either in a magnetic or dipole-force trap [62, 63]. This approach has the benefit of not requiring a MOT stage in the science chamber, which can be a benefit if optical access is limited, however the transport is slower and causes heating that then requires additional cooling in the science chamber.[31] The two-chamber approach with a cold-atom source is widely favoured.

The two-chamber arrangement is particularly important for quantum gas experiments, where the trap depths are low enough for background collisions to rapidly reduce the trapped population, and the speed of the evaporative cooling process is limited by the rate of rethermalisation. The use of a two-chamber system increases the lifetime of the quantum gas, and a higher initial population allows faster evaporative cooling.

1.7 Summary

The MOT is an effective method to laser cool atoms to sub-millikelvin temperatures, and is the workhorse of cold-atom experiments for initial cooling and trapping. The majority of cold-atom experiments greatly benefit from a two-chamber approach where the MOT is loaded by a cold-atom source, instead of directly from a thermal vapour. This makes a robust and compact cold-atom source a vital enabling part of practical quantum devices that utilise the sensitivity of cold atoms for real-life applications, particularly given the current rapid expansion of such markets. In the next chapter, the various types and designs of cold-atom sources are outlined and compared.

[31] In principle, moving the magnetic or optical trap adiabatically would cause no heating, but in reality there is a trade-off between fast transport and increased heating.

2

Cold-Atom Source Designs

A cold-atom source is a key component of devices using the two-chamber arrangement for cold-atom experiments, and a wide range of designs can be implemented. This chapter outlines the important requirements for a source, then summarises the two main types: MOT sources and Zeeman slowers.[1] A simple model of the MOT source is developed by adapting the MOT model from the previous chapter, then the possible configurations of optical and magnetic fields, and the various geometries possible to produce the required fields, are detailed and compared.

2.1 Requirements of a Cold-Atom Source

Before discussing the different principles and designs of cold-atom sources, it is important to set out the key requirements of a cold-atom source used to load a MOT:

1. High flux of low-velocity atoms

   A high flux is the critical characteristic for loading a subsequent MOT, since a high loading rate allows improvements to the repetition rate, signal-to-noise ratio,

[1] Alternative approaches include bichromatic slowers, in which two frequencies of light are used to cause momentum transfer via purely stimulated processes, thereby avoiding the rate limitation of spontaneous emission [64–70]. However, these methods introduce several complications for the experimental setup (including high optical power requirements), which have prevented their widespread adoption.

duty cycle, trap lifetime, and resistance to long-term performance degradation of the cold-atom device. However, only atoms with a velocity below the capture velocity v_c of the MOT are able to be utilised to load the MOT. This velocity will vary between devices and is typically in the range $30-50\,\mathrm{m/s}$ depending on trapping volume and optical intensities (as shown in Sec. 1.4.1).

2. Low divergence of the atomic beam

   A low divergence allows loading of a MOT to occur far from the source, which may be a requirement of the vacuum system, or a design feature to minimise the effect of stray magnetic fields and thermal background (see below) from the source at the MOT. For a compact device where the separation between the source and the MOT being loaded is minimal, it allows the MOT trapping region (perpendicular to the source axis) to be small.

3. Low thermal background

   The thermal background is the flux of high-velocity atoms that propagates collinear with the low-velocity flux. Some experiments are very sensitive to a high thermal background, particularly quantum gases, for which any source of heating or loss is significant.

4. Efficient use of optical power

   Compact, portable laser systems have limited available optical power that should be used as efficiently as possible, unlike laboratory experiments where optical power is often not a limiting factor.

5. Compact

   Compact can refer to the absolute size of the device, but also the efficient use of space. The cold-atom source designed in this thesis is focused on the latter while still generating a high flux, whereas a source intended to occupy minimal volume at the cost of a lower flux would likely have a different design.

6. Robust

   The source should be resistant to mechanical vibrations, variations in the local magnetic field, and optical misalignments, so that it is suitable for operation in real-world scenarios.

Different designs of cold-atom sources satisfy these requirements to different extents, and the precise application will dictate their relative importance. Cold-atom sources fall into two main types: MOT sources and Zeeman slowers.[2]

Before detailing these two approaches, it is first important to note that the sources considered here are *continuous sources*; sources that are able to produce a continuous flux.[3] In addition, there exist *pulsed sources* in which a standard MOT is loaded, forming a static cloud of cold atoms, and is subsequently launched towards another MOT which recaptures them. Whereas continuous sources can be partially classified by the magnetic field employed, all pulsed sources use a 3D quadrupole in order to trap atoms. Pulsed sources are instead classified by the mechanism employed to launch and transfer the atoms, including push beams [73–76], plug beams [42], moving molasses[4] [77], magnetic confinement [78–80] and 2D MOT stages [81]. In some investigations, operating a source continuously has outperformed a pulsed operation [80], while the opposite has been found in other cases [74, 75]. The advantage of pulsed sources is that the atoms are colder when they are launched, which can allow very efficient transfer of the atoms due to their low initial velocity,[5] however the disadvantages are in their additional complexity (requiring precise timing, additional beams, transfer stages), which make them less attractive for a compact source. As a result, continuous sources are the focus of this thesis, although investigating pulsed operation of the cold-atom source developed in this project may present opportunities to increase the flux.

[2] Hybrid options combining both types have also been implemented [71, 72].
[3] Such 'continuous' sources may still be operated in a pulsed mode by switching the flux on and off by magnetic, optical or mechanical means.
[4] Moving molasses are explained in Sec. 2.3.2.
[5] Transfer efficiencies of 80 – 90% can be achieved [79, 81].

2.2 Types of Cold-Atom Sources

A *MOT source* operates identically to a traditional MOT, except that atoms escape along an exit channel in a particular direction, usually by introducing an intensity imbalance at the MOT centre.[6] Atoms entering the trapping region with $v < v_c$ are cooled and directed towards the centre, where the intensity imbalance in the exit channel accelerates them, forming a cold atomic beam. The source may be loaded from either a directional source of thermal atoms or a background vapour. In either case, the transverse cooling of the MOT results in a small divergence of the beam.

A *Zeeman slower* utilises the same radiation pressure force as a MOT, however is arranged to optimise deceleration for a particular direction of the atomic motion. A cooling beam counterpropagates with a directional source of thermal atoms, and the magnetic field is arranged to vary with the axial position such that the Zeeman shift compensates for the changing Doppler shift as the atoms are slowed. This arrangement exerts a strong radiation force on atoms with velocities in a small solid angle but over a long distance, so that atoms with a much larger initially velocity can be slowed than in a MOT source, and higher fluxes can be produced (generally by one to two orders of magnitude). The disadvantages of Zeeman slowers compared to MOT sources are their large size (typically about a metre long,[7] although a commercially available compact version is $\sim 30\,\text{cm}$ in length[8]), stray magnetic fields, high thermal background, large beam divergence, and general complexity. In a research laboratory setting, without significant space restrictions, a Zeeman slower is an excellent high flux cold atom source, particularly when incorporating transverse cooling stages, beam deflection, shutters and other additions to circumvent the inherent drawbacks (including loading a

[6] Alternatively, instead of an axial intensity imbalance there may be simply an absence of light along an axis, in which case the absence of cooling leaves the atoms with a significant residual velocity in that direction with which they exit the MOT along the axis [51].

[7] The theoretical length of a Zeeman slower is a function of the selected initial and final velocities (since the deceleration is constant by design), however practical considerations (e.g. the implemented magnetic field being only an approximation to the ideal, imperfect polarisation of the light reducing the acceleration, etc.) require an actual length generally 2 to 2.5 times the theoretical length [82, 83].

[8] AOSense Beam-RevC – a Zeeman slower with integrated 2D cooling to reduce divergence and thermal background; available for calcium, strontium and ytterbium.

MOT source with a Zeeman slower in a dual-stage source [71, 72]), however these all add bulk, complexity and cost. For compact practical devices, MOT sources are substantially better suited than Zeeman slowers for many atomic species.[9]

2.3 MOT Sources

2.3.1 Modelling MOT Sources

The model used in the previous chapter to provide useful insights into the dynamics of the MOT can be extended to the MOT source. Previously, the main quantity of interest was the equilibrium trapped population, however for a source the key parameter is the flux. The maximum possible flux is equal to the loading rate R of the MOT from Eq. 1.44 if all atoms loaded into the MOT are transferred into the output beam. In reality there are two sources of loss:

1. Funnelling Efficiency, χ

   When atoms enter the exit channel of the source (either from an intensity imbalance or absence), they have a finite transverse velocity. Those with a sufficiently large transverse velocity will cross to the other side of the exit channel before reaching the aperture of the source, and therefore do not form part of the output flux. Similarly, the aperture of the source has a finite length, and atoms that enter it with a sufficient transverse velocity (dependent on position in the aperture) will impact on the sides and be lost from the flux. This is particularly important when the aperture length exceeds the diameter, which is usually the case in systems requiring differential pumping (see Sec. 3.1.1). The fraction of atoms successfully funnelled through the aperture can be described by χ, which is a function of:

[9] For atomic species with low vapour pressures, a MOT source requires loading from an oven instead of from a background vapour. For higher oven temperatures, the fraction of atoms with $v < v_c$ decreases, so that for species requiring very high oven temperatures to produce a sufficient hot flux, a MOT source traps an impractically small fraction of atoms, and a Zeeman slower is required instead.

- aperture size
- aperture length
- transverse velocity of the atoms entering the exit channel
- length of the exit channel
- transit time from the $B \approx 0$ region of the source to the aperture, which in turn depends on the intensity and detuning of the axial beam, and the magnetic field gradient

The rate that atoms are lost this way is then $(1 - \chi)R$.

2. Collisional Loss

Collisions with background gas particles will transfer kinetic energy to the cooled atoms and remove them from the flux. In the previous chapter the loss rate was the product of the trapped population with the rate of collisions $\Gamma_{\text{col}} = n\sigma_{\text{col}} \langle v \rangle$ from kinetic theory (Eq. 1.46).[10] However this assumed that all atoms will eventually undergo collisions, by virtue of having no other means of escaping the MOT. For a MOT source, collisional losses may only occur before the atoms reach the aperture, after which it is assumed that collisional losses in the low-pressure science chamber are negligible. The fraction of atoms lost due to background collisions before exiting the source is[11] $1 - e^{-\Gamma_{\text{col}}\tau}$, where τ is the transit time for an atom to be cooled, directed into the exit channel, and pushed out through the aperture. Like χ, τ depends on many parameters of the source:

- initial velocity of the atom entering the trapping volume
- characteristic size d of the trapping volume
- deceleration during cooling
- acceleration through the exit channel

[10] To recap: n is the number density of the background vapour; σ_{col} is the collisional cross-section; and $\langle v \rangle$ is the mean velocity of atoms in the background vapour.

[11] This comes from Γ_{col} being the fractional rate of loss, so the rate of change in atom number N is $\mathrm{d}N/\mathrm{d}t = -N\Gamma_{\text{col}}$, then integrating gives the exponential decay form.

Combining these gives a simple model of the flux from a MOT source as

$$\Phi = R\chi e^{-n\sigma_{\mathrm{col}}\langle v\rangle\tau} \tag{2.1}$$

In some respects the modelling of a MOT source is simpler than a MOT, because the atoms spend little time near the $B \approx 0$ region so the effects of sub-Doppler cooling, optical pumping of the multi-level electronic structure, and inter-atom interactions for high atomic densities have largely negligible impacts on the flux. On the other hand, calculating the loss rates of atoms requires a knowledge of the time scales of atomic motion within the MOT source – which depends on the magnetic field gradient, cooling light intensity and detuning, and initial velocity of the atoms – whereas in modelling a MOT it is sufficient to calculate the rate that atoms entered the trapping region and assume that they eventually become trapped, without detailed knowledge of the time scale of that process.

The characteristics of a wide variety of MOT sources from the literature are compiled in Table 2.1, with several Zeeman slowers for comparison, and two hybrid Zeeman-MOT sources. Note that direct comparison of different sources is complicated by the dependence of the flux on the laser beam intensities, trapping volume and geometry, detunings, and background pressure (as indicated by Eq. 2.1), however Table 2.1 serves as a useful guide to typical characteristics and provides a concise summary of the various examples from the literature which will be discussed in the following.

2.3.2 MOT Source Configurations

MOT sources can be broadly grouped first by the configuration of optical and magnetic fields they use, and secondly by the geometries employed to generate the optical fields. There are three different configurations: 2D, 2D$^+$, and 3D.

A 2D-MOT source combines a 2D quadrupole magnetic field with transverse cooling. The magnetic field is zero along the axis of the field, and atoms are cooled and directed towards this region, along which they propagate with their initial axial velocity. A ‘pure’

Source Type	Institution	Year	Species	Flux (atoms/s)	Velocity (m/s) Mean	Velocity (m/s) FWHM	Divergence, Full Angle (mrad)	Cooling Intensity (mW/cm^2)	Cooling Intensity (I_{sat})	Detuning ($\Gamma/2\pi$)	B-Field Gradient (G/cm)	Aperture Size (mm)	Reference
Zeeman Slower	Havard	2005	^{87}Rb	3.2×10^{12}	45	25	24	–	–	–	3	–	[84]
		2005	^{87}Rb	1.7×10^{12}	120	25	24	–	–	–	3	–	[84]
	Nottingham	2014	^{133}Cs	1×10^{8}	–	–	–	–	–	–	–	–	[85]
		2014	^{6}Li	7×10^{7}	40	–	–	–	–	–	–	–	[85]
	AOSense	2018*	Sr/Ca/Yb	1×10^{11}	40	–	–	–	–	-2	–	–	[86]
Pure 2D-MOT	FOM, Amsterdam	1998	^{87}Rb	6×10^{9}	12	15	46	3	1.8	-1.7	17.7	0.8	[54]
	Stuttgart	2002	^{87}Rb	6×10^{10}	50	75	32	11.2	6.7	-1.9	17	6	[51]
	NPL, London	2005	^{87}Rb	2×10^{8}	–	–	<74	2.5	1.5	-3	6	2	[87]
	JPL, Pasadena	2006	^{133}Cs	1.5×10^{10}	38	22	–	2.1	1.9	-1.4	15	4	[88]
2D-MOT	LKB, Paris	2002	^{87}Rb	1×10^{9}	0.3-3	–	–	4.2	2.5	-3	10	–	[89]
	JPL, Pasadena	2012	^{133}Cs	8×10^{9}	–	–	–	2.3	2.1	-1.4	15	4	[90]
	KRISS, Daejeon	2012	^{87}Rb	4.5×10^{10}	39	2	12	–	–	-2	14	4	[91]
	USTC, Shanghai	2017	^{88}Sr	1×10^{9}	33	15	60	42.5	1.0	-1.5	–	2	[92]
2D$^+$-MOT	FOM, Amsterdam	1998	^{87}Rb	9×10^{9}	8	3.3	43	3	1.8	-3	12.6	0.8	[54]
	Strathclyde	2000	^{85}Rb	7.3×10^{8}	2-8	–	23	5	3.0	–	–	–	[93]
	Harvard	2003	^{87}Rb	8×10^{9}	15	3	12.5	11	6.5	-5	21.5	1.25	[94]
	NPL, London	2005	^{87}Rb	8×10^{9}	11	5	<74	2.5	1.5	-3	6	2	[87]
	TIFR, Mumbai	2006	^{85}Rb	1.9×10^{10}	15	3.5	26	–	–	-2	15	2	[95]
		2006	^{87}Rb	2×10^{10}	17	5	26	–	–	-2	15	2	[95]
	ColdQuanta	2018*	Rb/Cs	1×10^{9}	–	–	–	–	–	–	–	0.75	[96]
3D-MOT	CNRS, Paris	1997	^{133}Cs	1×10^{6}	1.9-5	–	–	–	–	–	–	–	[97]
	INFN, Napoli	2001	^{87}Rb	7×10^{7}	14	–	–	5	3.0	-2.5	15	–	[80]
	LKB, Paris	2001	^{87}Rb	1.3×10^{8}	14	9	20	–	–	-3	15	5	[98]
LVIS	JILA, Boulder	1996	^{87}Rb	5×10^{9}	14	2.7	30	13.2	7.9	-5	5	~ 1	[99]
	FOM, Amsterdam	1998	^{87}Rb	3.2×10^{8}	26	6.3	27	6.8	4.1	-3.3	13.6	0.8	[54]
	NIST, Boulder	2005	^{133}Cs	1×10^{10}	–	–	–	10	9.1	-1.7	7	0.5	[100]
	NPL, London	2005	^{87}Rb	8×10^{9}	8.5	4	<74	2.5	1.5	-3	8	2	[87]
Pyramid MOT	Oxford	1998	^{133}Cs	1.1×10^{9}	11.3	2-3	40	6	5.4	-2	10	1×2	[42]
	Wisconsin	1998	^{39}K	5.3×10^{3}	–	–	–	12.5	7.1	-7	4	2	[101]
		1998	^{40}K	3×10^{-1}	–	–	–	12.5	7.1	-7	4	2	[101]
	Pisa	2001	^{133}Cs	4×10^{9}	10	1.5	26	10	9.1	-2.7	12	1×2	[102]
	JPL, Pasadena	2003	^{133}Cs	2.2×10^{9}	15	–	15	3	2.7	-2.1	–	1	[103]
		2004	^{87}Rb	1×10^{8}	10	–	15	1.2	0.7	-2.3	–	1	[104]
		2004	^{133}Cs	2×10^{8}	–	–	15	0.99	0.9	-2.1	–	1	[104]
	Durham	2008	^{87}Rb	1.8×10^{7}	–	–	–	4.0	2.4	-2.8	10.1	2.4×3.0	[105]
		2008	^{133}Cs	1.3×10^{7}	–	–	–	4.0	3.6	-3.0	8.5	2.4×3.0	[105]
Grating MOT	AFRL, New Mexico	2017	^{87}Rb	4×10^{8}	16.5	8	–	11	6.5	–	20	1	[106]

Table 2.1: A summary of cold atom sources from the literature, sorted by source type, including the source characteristics (total flux, velocity and divergence) and some important parameters (intensity of each cooling beam, detuning of the cooling light, and magnetic field gradient). For 3D quadrupole magnetic fields, the gradient shown is the axial gradient. *The ColdQuanta and AOSense sources are commercially available from the respective companies.

2D-MOT has no light in the axial direction, thus the atoms have no preferred axial direction of travel. In some cases, a narrow push beam is applied along the axis to push the atoms in one direction, which also accelerates slow atoms and alters the velocity distribution of the resulting flux [72, 91].[12]

A 2D$^+$-MOT source adds axial molasses cooling to the 2D-MOT source configuration. Transverse MOT beams still cool and push atoms towards the central axis where $B = 0$, however the longitudinal cooling produces a much narrower velocity distribution. The atoms are channelled into a flux by an axial intensity imbalance, or by applying axial beams of different detunings. The former is achieved either with axial beams of different intensities, or by using beams with identical intensity but with a 'hole' in one beam; in both these cases the intensity imbalance creates an exit channel to accelerate the atoms out of the MOT trapping region. This acceleration causes transverse heating of the atoms, which can be avoided by the latter method of using different detunings. By careful choice of the detunings, a *moving molasses* can be implemented, in which the atoms are cooled towards a velocity at which the axial detunings are identical in the reference frame of the atoms, thereby subjecting the atoms to an optical molasses in their rest frame [97, 107]. This approach can produce a slower atomic flux with a smaller velocity spread than using an intensity imbalance, however it adds complexity to the system and the velocity reduction is at the cost of a reduced flux [94]; a slower velocity increases τ and hence increases collisional losses. Certain applications, such as loading magnetic guides, require these extra-low velocity ($< 5\,\mathrm{m/s}$) sources [89, 108], but for loading a MOT as the initial step in a cold-atom experiment, a velocity below the MOT capture velocity $v_c \approx 30-50\,\mathrm{m/s}$ is sufficient, and intensity imbalances are preferred.

A 3D-MOT source uses a 3D (spherical) quadrupole magnetic field, with cooling and trapping occurring in all directions and a single $B = 0$ point. This is the configuration of standard MOTs used for trapping atoms, with a pair of anti-Helmholtz coils generating the magnetic field, and three orthogonal pairs of counterpropagating beams providing the

[12] A notable alternative implementation of the 2D-MOT source was that of Kellogg et al. [90], whereby the transverse beams were tilted by 4° to provide a small but significant axial force that accelerated the atoms without the need of a separate push beam, while not reaching a fully 2D$^+$-MOT source with axial molasses cooling.

cooling light (although a 4- or 5- beam geometry is also possible [26, 109, 110]). Extracting the atoms to generate a flux is achieved in one of two ways: adding an extra push beam through the MOT origin,[13] or making a 'hole' in one of the existing beams to produce an intensity imbalance, as with the 2D$^+$-MOT. Adding a push beam allows fine control of the velocity distribution of the flux [108], particularly if using multiple push beams to perform a moving molasses [76, 107], however, for the purposes of loading a MOT, the fine control of the velocity distribution is not required and including a push beam is just an additional complication. As a result, the widespread approach is to make a 'hole' in one beam, which is referred to as a low-velocity intense source (LVIS) [99].

2.3.3 Comparison of MOT Source Configurations

The lack of axial cooling in the 2D-MOT source results in a high mean velocity with broad velocity distribution that limits the fraction that can be collected in a subsequent MOT. Schoser et al. [51], for example, measured the velocity distribution of a 2D-MOT to have a mean of 50 m/s and a FWHM of 75 m/s, which meant that only a third of the total flux was able to be captured by a subsequent MOT (which had $v_c = 50$ m/s). 2D-MOTs also produce lower fluxes than 2D$^+$ and 3D-MOT sources by up to an order of magnitude [87, 91, 95] (for the same optical intensities and trapping volume[14]) because the lack of axial cooling limits the axial velocities for which atoms will enter the flux, and reduces the time atoms spend undergoing radial cooling, resulting in higher transverse velocities and more atoms being filtered out of the flux at the exit aperture of the source (corresponding to a lower χ for 2D-MOT sources). In addition, half the atoms in a pure 2D-MOT source travel in the wrong direction. As a result, pure 2D-MOT sources are uncommon, with the slower and narrower velocity distributions of LVIS and 2D$^+$-MOT sources preferred.

LVIS and 2D$^+$-MOT sources produce very similar fluxes for identical optical intensities

[13] This approach is sometimes referred to as an 'atom faucet' [98].

[14] Dieckmann et al. [54] compared a 2D-MOT, 2D$^+$-MOT and LVIS, but the trapping volume for the LVIS was smaller by a factor of 3.4, and gave an order of magnitude lower flux as a result. A better direct comparison of the types of MOT sources is Ovchinnikov [87] where similar settings were used for the three types of MOT source.

and geometries [87], and are both in widespread use. $2D^+$ sources have the advantage of easy scalability, since the axial independence of the magnetic field allows the trapping volume to be extended in the axial direction.[15] This increases the flux by capturing faster atoms ($R \propto v_c^4$ from Eq. 1.43),[16] although reduces the radial momentum transfer sufficient to push slower atoms out of the beam, so that χ reduces for slow atoms, resulting in a higher mean velocity of the flux [51, 88]. In contrast the 3D quadrupole of the LVIS restricts the effective trapping volume to have a 2:1 radial-to-axial length ratio due to the axial magnetic gradient being twice the radial gradient (as discussed in Sec. 1.3); extending the source axially would have an increasingly negligible impact due to the large detuning caused by the axial field, without also increasing the radial extent. The axial trapping of the LVIS does however produce a lower mean velocity with narrower distribution compared to an identical $2D^+$ source. This is the case since the atoms reach the exit channel with a smaller spread of velocities and positions, reducing the spread of final velocities, and the axial field detunes the atoms out of resonance with the pushing beam as they travel along the exit channel.

The comparable performance of the LVIS and $2D^+$-MOT source configurations of optical and magnetic fields has made them both popular choices for cold-atom sources. The implementation of their optical fields varies however, with some designs better suited to use in laboratories, and others for compact devices.

2.4 MOT Source Designs

Generating the multiple beams for both MOTs and MOT sources alike adds substantial complexity and size to the apparatus. The original MOT [19] used six independent laser beams to form the standard configuration of three orthogonal pairs of beams, which requires numerous optical elements to independently control the polarisation, intensity and direction of each beam. The advantage of independent beams is that the optical forces can be finely balanced, which maximises the lifetime of atoms in an optical molasses. This is important

[15] Note that the axial scalability and the impacts on flux and velocity also apply to the 2D-MOT source.
[16] The increase of flux with axial length saturates when the trap length exceeds the mean free path due to collisions with background atoms.

for experiments that trap cold atoms in a MOT then transition to an optical molasses to perform sub-Doppler cooling on the atoms. For a MOT, or MOT source, that does not involve an optical molasses stage, small intensity imbalances are compensated for by the trapping force, and the laser beam intensities are not so critical.

The most common simplification is to reflect one beam to form another. Reflectors may be placed outside or inside the vacuum system, the latter of which reduces the required optical access to the vacuum, but is more complicated to implement. Usually beams are retroreflected to form the counterpropagating partner to the original, however an elegant alternative for trapping close to a surface is the mirror MOT, in which the six-beam configuration is formed from four beams reflected off a mirror surface [111].[17] Retroreflection halves the required number of independent beams, and is particularly popular for MOT sources since retroreflection off a mirror with an aperture will form a dark region or 'hole' in the retroreflected beam, along which atoms are accelerated by the intensity imbalance, exiting through the aperture in the mirror. Many laboratory-based sources use retroreflection of three beams to form a six-beam geometry, which requires both axial and transverse optical access. Vacuum chambers with multiple optical feedthroughs are sometimes used [76, 80, 102, 113], but the size and weight issues make glass cells the normal choice [51, 54, 89–91, 93–95, 98, 106, 108].

Even with retroreflection, requiring three initial beams (and optical access for each) results in an extensive system with many possible sources of misalignment. The ideal arrangement uses a single laser beam, for which there are two possible implementations: the pyramid MOT and the grating MOT. By using a single beam, they minimise the number of optical elements, forming compact systems with few misalignment possibilities, providing the robustness desired in portable practical devices.

[17] The mirror MOT is particularly popular in conjunction with atom chips, where atoms are trapped first by a MOT, then transferred to a magnetic trap formed within a few millimetres of a micro-electronically patterned surface [112].

2.4.1 Single Beam MOT Geometries

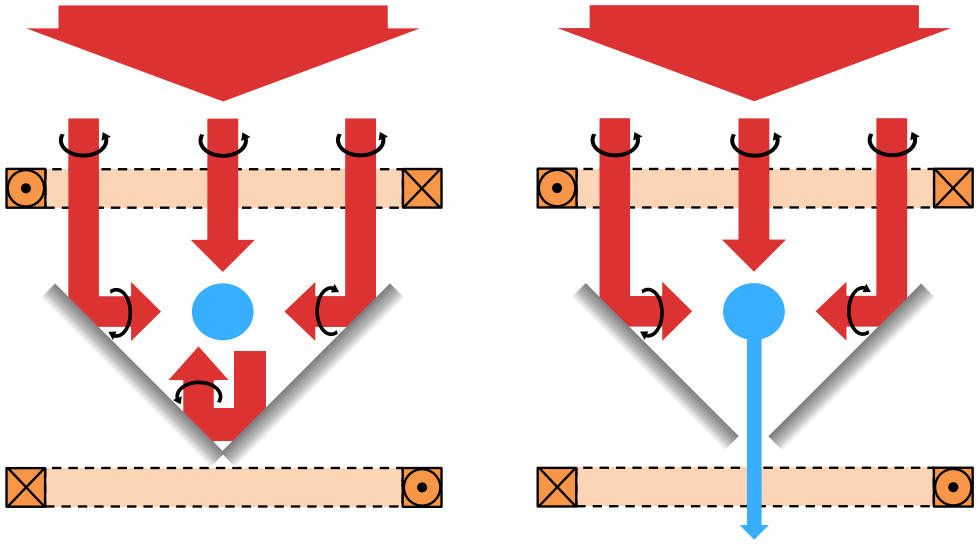
Pyramid MOT

The pyramid MOT uses a pyramidal arrangement of mirrors to reflect a single on-axis beam into an optical configuration compatible with a spherical quadrupole magnetic field to produce a MOT [41]. Generally a square-based pyramid is used to form the standard six-beam configuration (although triangular-based [114] and conical pyramids [115–117] have also been implemented) as shown in Fig. 2.1(a). A large circularly polarised beam propagates along the pyramid axis and fills the pyramid. The left portion of the beam (in the figure) is reflected by a mirror with an incident angle of 45°, upon which the p-component of the light field undergoes a 180° phase shift relative to the s-component (assuming ideal mirrors[18]) to reverse the handedness of the polarisation. This beam then counterpropagates with the reflected right portion of the beam to form a pair of beams with opposite polarisation to the initial beam. The same occurs in the direction normal to the plane of the figure to form a second beam pair, again with opposite handedness to the initial light. When the light is reflected for a second time, the 180° phase shift returns the polarisation to the original handedness, and the 45° mirror angle causes the light to counterpropagate with the initial beam, creating a third beam pair. The result is that the pyramid produces one beam pair along its axis, and two beam pairs in the transverse direction that are of the opposite polarisation to the axial pair. This is precisely the optical configuration that produces a MOT when combined with the spherical quadrupole field detailed in Sec. 1.3.3 and illustrated in Fig. 1.5.[19]

The use of a square-based pyramid to produce the optical configuration for a MOT has several benefits. The intensity balances at all points (assuming perfectly reflecting mirrors and an axially symmetric incident beam, such as a Gaussian-profile beam), and all phase and intensity noise (including polarisation-induced intensity noise) is common-mode between

[18] The case of non-ideal mirrors is considered in Sec. 4.4.

[19] A pyramid cannot be used with a 2D quadrupole magnetic field because the transverse field is not symmetrical (see Eq. 1.37), and therefore requires a different configuration of polarisations than that generated by a pyramidal reflector.



(a) (b)

Figure 2.1: A pyramid MOT (a) is formed by illuminating a (usually square-based) pyramidal assembly of mirrors with circularly polarised light. A 180° phase shift upon reflection produces the optical configuration required for a MOT when combined with the spherical quadrupole field produced by an anti-Helmholtz coil pair (orange), forming a cold cloud of atoms (blue). If the apex of the pyramid is truncated to form an aperture, the absence of retroreflected light along that direction produces an exit channel through which the atoms are directed by the intensity imbalance, forming a pyramid MOT source (b). The magnetic field lines are not shown here for simplicity, but are identical to those of Fig. 1.5.

beam pairs [21]. Also, the light returns along the same axis, requiring only a single optical feedthrough for the vacuum system. The pyramid geometry therefore greatly reduces the size and complexity of the vacuum and optical systems, providing a robust and compact system. The stability and simplicity is obtained by sacrificing the ability to fine tune individual beams, making it difficult to achieve very low temperatures without near-identical mirrors, although the common-mode phase and intensity noise assists sub-Doppler cooling. The pyramid geometry also has the disadvantages of limited optical access to the atoms,[20] and substantial complexity in designing and assembling in-vacuum components.

The pyramid MOT can be straightforwardly adapted to produce a source of atoms by the presence of an aperture at the apex, forming the LVIS configuration [42, 101]. As shown in Fig. 2.1(b), the transverse cooling beams are unchanged, however the absence of retrore-

[20] For the square-based pyramid in Fig. 2.1, with a 90° internal angle, the trapping volume is entirely inside the pyramid, however by angling the mirrors to increase the internal angle, the trapping volume can be extended outside the interior of the pyramid, thus improving the optical access [114].

flected light along the pyramid axis creates a dark region that forms an exit channel, through which the trapped atoms are accelerated by the intensity imbalance. When operated as a source, the pyramid design's limited optical access and difficulty in obtaining sub-Doppler temperatures are not issues, and the only major drawback is the difficulty of producing the in-vacuum optics.

Grating MOT

The grating MOT is a more recent development that redirects a single beam using diffraction gratings [26, 118], as illustrated in Fig. 2.2. The incident beam is diffracted to form a 'tripod-style' geometry; the incident beam along $-z$ is balanced by multiple beams with a component along $+z$, whose radial components provide axial cooling and trapping. The grating MOT geometry can be used as a grating MOT source [106], using two parallel diffraction gratings to produce a 2D-MOT configuration with three radial beams (the same arrangement as shown in Fig. 2.2). The planar optical element gives the grating geometry the benefits of superior compactness and optical access compared to the pyramid geometry, as well as the simplicity and stability inherent to a single-beam MOT geometry. Manufacturing the required gratings can utilise standard semiconductor processing techniques, and a master grating approach enables mass manufacture. Although only a single grating MOT source has been demonstrated so far, grating MOTs have been incorporated into atom chips [119], used in ultracold electron sources [120], and investigated with the intention of developing compact quantum sensors [121].

However, the use of a planar optical element also has fundamental drawbacks, since all possible optical configurations (4-beam and 5-beam MOTs have been demonstrated [26]) are of the tripod-style. The beams therefore no longer travel parallel to the magnetic field, and if the incident beam drives σ^+ transitions, the diffracted beams will drive a combination of σ^+, σ^- and π transitions, depending on their projection along the local magnetic field, reducing the trapping force. The polarisation of the diffracted beams is also complicated by the variation of the diffraction efficiencies of s- and p- polarised light with wavelength and

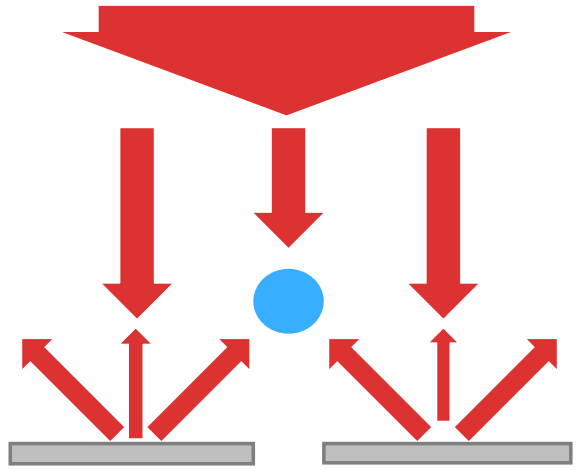


Figure 2.2: The grating MOT uses a planar diffraction grating to diffract a large incident beam such that the first order diffracted beams combine to balance the incident intensity and produce a MOT geometry to trap atoms (blue). The magnetic fields are not shown. In a grating MOT source, a push beam directs atoms perpendicular to the plane of this figure.

polarisation.[21] This wavelength dependence is a difficulty for multi-species grating MOT sources, whereas broadband mirror coatings allow more flexibility for a single pyramid to be used for multiple species [113, 122]. Another consequence of the tripod-style geometry is that the diffraction efficiency must be less than unity for the axial intensity to balance between the incident beam and the diffracted beams.[22] This results in optical power being wasted, unlike the square-based pyramid geometry, and in any case the intensities do not balance at all points (for a non-uniform beam), reducing the trapping volume and hence the loading rate. Large diameter laser beams are used to give approximately uniform intensity over the central region. Finally, since the light does not return along the axis of the incident beam, provisions are required to allow the diffracted light to escape from the vacuum chamber to prevent light scattering and heating the atoms. This would likely require additional optical access to the vacuum chamber, compared to the single viewport required for the pyramid MOT.

[21] The s- and p- diffraction efficiencies are difficult to design to perfectly match what is ideally required, and grating MOTs essentially rely on the robustness of magneto-optical trapping; the process seems to work unless the polarisation is so far off that it has the wrong handedness.

[22] Following [123], the requirement to attenuate the beams travelling along $+z$ can be seen as follows: an incident beam of intensity I_0 is diffracted with efficiency η at angle α to z; the diffracted beam has intensity $I_{\text{dif}} = I_0\eta/\cos\alpha$; for m diffracted beams, the intensities are balanced along z for $I_0 = mI_{\text{dif}}\cos\alpha$; and combining these two results yields $\eta = 1/m$. $m > 3$ for 3D cooling, so $\eta < 1$.

Overall, both the grating and pyramid MOT geometries provide substantial improvements to the size, complexity and robustness of cold-atom sources. Grating MOTs present the current ultimate in compact MOT geometries, and are ideal for ultra-compact devices. However, for a cold-atom source intended for high-flux loading of MOTs, the pyramid geometry provides far more efficient use of the available optical power, balanced intensities at all points, simpler extension to multi-species sources, and requires only one optical feedthrough, at the cost of a more challenging implementation of the vacuum optics. The basis for the cold-atom source design of this thesis was therefore chosen to be a square-based pyramid MOT source.

2.5 Previous Pyramid Designs

Designs of pyramids used for both MOTs and MOT sources have tended to fall into one of two forms. The original pyramid MOT [41] was constructed from four triangular mirrors, forming a square profile in the transverse plane. Of the first two pyramid MOT sources,[23] Williamson et al. [101] used a similar geometry (four triangular mirrors with a circular profile), while Arlt et al. [42] instead placed two triangular glass prisms in a valley formed by two rectangular mirrors at 90°. With small variations, these two geometries have been the dominant design of pyramid MOTs and sources. In particular, square-based glass structures are overwhelmingly preferred [21, 102, 113, 122, 124–126] because polishing techniques to achieve optical quality (flat to at least $\lambda/2$, typically $\leq \lambda/10$) are well-established for glass, and square-based profiles are simpler to construct than circular profiles.

A square-based pyramid profile is akin to putting a round peg in a square hole, and is therefore not suitable for compact devices. Without complicated beam shaping, a circular laser beam of diameter d requires a square-based pyramid with outer diameter $\sqrt{2}d$, as shown in Fig. 2.3(a). This translates to a 100% increase in radial cross-section and a 182% greater volume for a square profile pyramid compared to a circular profile (assuming the pyramid is

[23] Note that some early publications referred to the pyramid MOT source as a "pyramid funnel" [101–103].

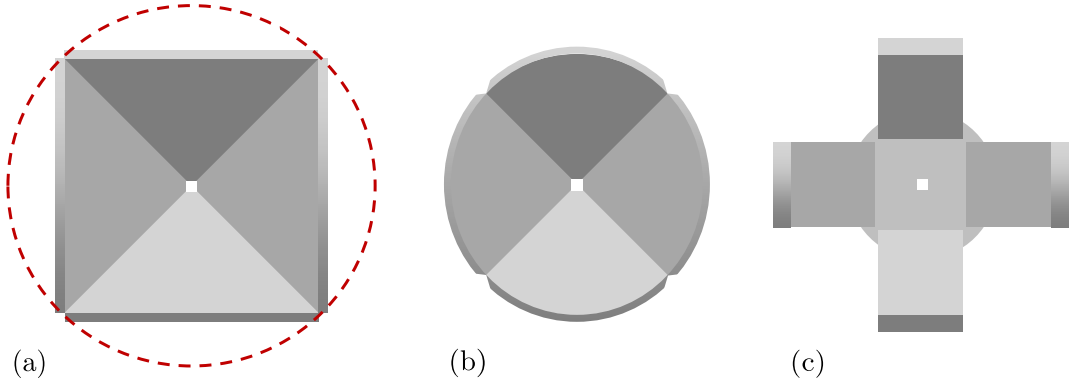


Figure 2.3: Different pyramid MOT designs. The common square profile design (a) has a radial footprint (red dashed line) double that of a circular profile pyramid (b). The design in (c) is made from off-the-shelf right angle prism mirrors [21], for which 40% of incident light is unused for a single circular beam.

chosen to minimise unused optical power[24]). In a laboratory setting, such size concerns are of limited importance, unlike for a portable device. Some pyramids have been built using glass mirrors in a circular profile, however they have significant gaps of several millimetres between mirrors [103, 127, 128].

Gaps between mirrors are an important issue in pyramid designs, partly because they reduce the trapping volume (and hence the capture velocity and loading rate R), but primarily due to the scatter from the mirror edges. Scatter has been widely observed to cause heating (corresponding in the simple model to a decrease in χ) and reduce MOT performance [42, 99, 103], to the extent that it can be impossible to form a MOT directly above the pyramid apex [41, 126], and machined mirror edges are the main source of scatter. Overlapping the mirrors reduces the number of visible edges and hence the amount of scatter, which is why pyramids made of two prisms between two rectangular mirrors are highly popular [102, 113, 122, 124, 125], while truncating the pyramid and using a flat retroreflector (with a $\lambda/4$ coating to enforce the correct polarisation) at the apex is another common adaptation to avoid the performance degradation due to scatter [21, 103, 128].[25] The presence of in-vacuum optics is both the key to the inherent compactness and robustness of the pyramid design,

[24] If instead the beam diameter is chosen to illuminate the entire pyramid, 36% of the beam is not utilised for a square pyramid.

[25] For a pyramid MOT source, the retroreflector has a hole through which the flux exits. Using such a retro-optic can allow a higher quality aperture compared to using truncated mirrors, minimising the scattered light [103].

and the reason for the scatter, lack of adjustability and the manufacturing complexity that makes $2D^+$-MOT sources more common in research environments without significant size restrictions.

Some more recent pyramid designs have used off-the-shelf optics to avoid the time and material cost of bespoke pieces [21, 114]. One typical example is shown in Fig. 2.3(c) where four right angle prism mirrors are arranged around a central retroreflector, however 40% of the incident light is wasted by the large gaps between components. Although using off-the-shelf components greatly reduces development time, the resultant pyramids are inefficient and far from optimal.

A carefully devised and tested compact pyramid source could therefore find widespread use as an enabling component to improve the performance of cold-atom devices, out-performing existing designs with regard to size, optical power efficiency, and performance. Therefore a unique design incorporating all these considerations has been developed, and is presented in the following chapter.

3

Adjustable-Aperture Pyramid Design

The pyramid MOT geometry provides a compact and robust approach to producing a MOT source from a single laser beam, and was used as the basis for the cold-atom source of this thesis. The new design is presented here, and the process of fabricating a prototype is described in the subsequent chapter.

3.1 Aperture Size

When considering the design of a cold-atom source, the aperture size is a key design parameter. As well as providing an exit for the atomic flux, it allows differential pumping between the high pressure source region and the low pressure science chamber, which controls the relative pressures.

3.1.1 Differential Pumping

A vacuum pump with pumping speed S (in litres/sec) will achieve a pressure P at the entrance to the pump given by

$$P = \frac{Q}{S} \tag{3.1}$$

where Q is the *throughput*; the quantity of gas passing a plane in unit time. The minimum throughput of the system is set by the outgassing rate (see Sec. 4.2.1 for more details), and increases if gases are deliberately added to the system.[1] Away from the pump entrance, P will increase because any finite pipe size will limit the movement of particles. To calculate P at any point, the *conductance* of a section of a chamber is defined as the ratio of the throughput to the pressure differential across the section:

$$C = \frac{Q}{P_{\text{high}} - P_{\text{low}}} \tag{3.2}$$

Substituting in to Eq. 3.1 to eliminate Q yields the differential pumping ratio

$$\frac{P_{\text{high}}}{P_{\text{low}}} = 1 + \frac{S}{C} \tag{3.3}$$

The conductance of a section of chamber depends on the flow dynamics of the system. In the high vacuum (HV) and ultra-high vacuum (UHV) regimes[2] in which cold-atom experiments operate, the mean free path length is significantly greater than the dimensions of the chamber. Molecular interactions are virtually non-existent and the dynamics of the particles are described by *free molecular flow*.[3] In this regime, the conductance of an orifice of cross-sectional area A is

$$C_{\text{orifice}} = A\frac{\langle v \rangle}{4} \tag{3.4}$$

where $\langle v \rangle = \sqrt{8k_BT/\pi M}$ is the mean velocity for a Maxwell-Boltzmann distribution of particles with mass M at temperature T.[4] This assumes that the gas in the chamber is in thermal equilibrium. The conductance of a pipe is the product of C_{orifice} with the probability of passing through the pipe, P_{pipe}. For a long round pipe of length l and diameter d (where

[1] Gases may be intentionally introduced for material deposition, to load a MOT, etc.

[2] High vacuum is generally defined as below 10^{-3} mbar, and ultra-high vacuum as below 10^{-7} mbar.

[3] Technically, this flow is true for systems where the ratio of the mean free path to the chamber dimensions (a ratio defined as the Knudsen number) is greater than 1, so a small chamber will enter the molecular flow regime for a lower pressure than a very large chamber. However, given the size of typical cold-atom vacuum systems, mean molecular flow is true for all pressures below 10^{-3} mbar at room temperature, so the regime of free molecular flow is often stated as a pressure range.

[4] At room temperature, this gives $C^{\text{air}}_{\text{orifice}} = 11.6A$ for air and $C^{\text{Rb}}_{\text{orifice}} = 6.7A$ for ^{87}Rb, where A is in cm^2 and C is in litres/sec.

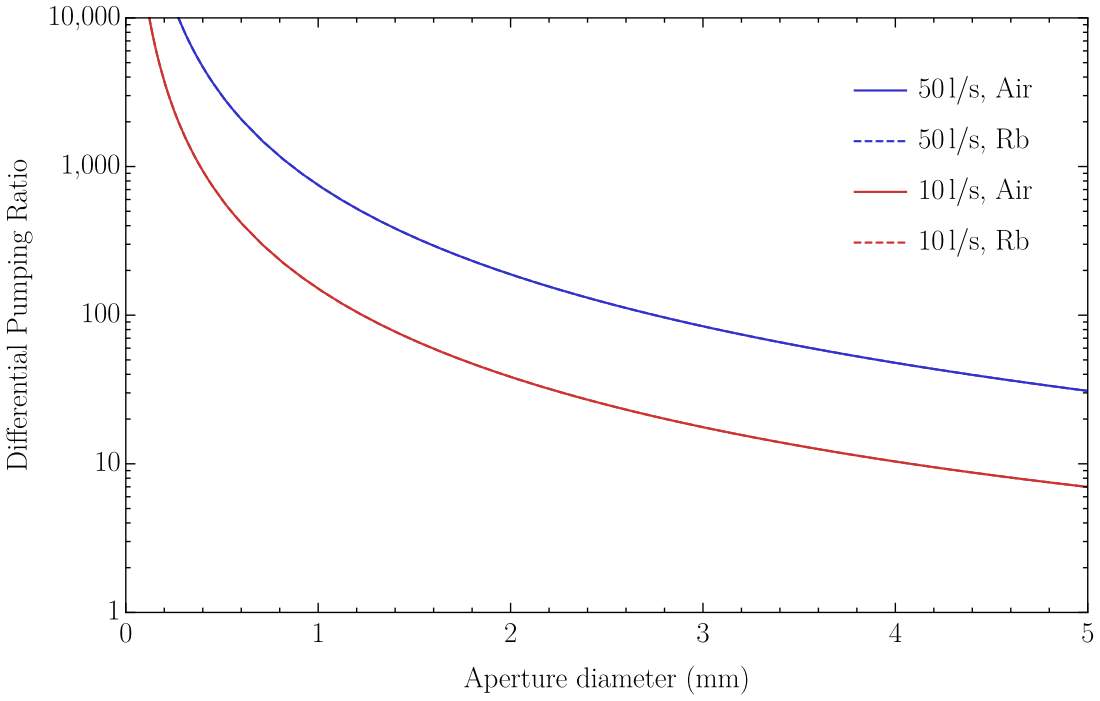


Figure 3.1: The differential pumping ratio due to a circular aperture, shown for $S = 55\,\mathrm{l/s}$ (blue) and $S = 10\,\mathrm{l/s}$ (red) vacuum pumps. The greater mass of rubidium (dashed line) increases the obtained differential pumping compared to air (solid line).

$l \gg d$), the conductance is given by

$$C_{\mathrm{pipe}} = C_{\mathrm{orifice}} \cdot P_{\mathrm{pipe}} = C_{\mathrm{orifice}} \frac{4d}{3l} \tag{3.5}$$

Using this result, the differential pumping ratio of Eq. 3.3 is plotted in Fig. 3.1 for rubidium and air,[5] and for both a high $50\,\mathrm{l/s}$ pumping speed typical of a laboratory-based experiment and a low $10\,\mathrm{l/s}$ pumping speed, which is achievable by compact pumps. The conductance of more complex passages must be calculated numerically. It is desirable to make the pressures of the source and science chamber differ by at least two orders of magnitude to balance fast MOT loading with long trap lifetimes, e.g. by using a 1 mm to 2 mm aperture with a $50\,\mathrm{l/s}$ pump. Using smaller capacity pumps or larger apertures reduces the differential

[5] Note that when rubidium is introduced to an initially clean system, a monolayer film is formed on the chamber surfaces due to the high adsorption [38]. After this layer is formed, the adsorption energy drops substantially and the rate that rubidium atoms hit the surfaces is in balance with the rate they leave, instead of atoms 'sticking'. The differential pumping theory above assumes the surfaces are coated and that these rates are in balance.

pumping obtained by just an aperture, in which case a high differential pressure can still be achieved by placing a narrow tube after the aperture. Conductances in series are combined as reciprocals,

$$\frac{1}{C_{\text{total}}} = \frac{1}{C_1} + \frac{1}{C_2} + ... \tag{3.6}$$

and therefore the total conductance of an aperture in series with a tube will tend towards the conductance of the tube as the aperture size increases.

The differential pumping also controls the thermal background emitted by the source. Some atoms that are travelling too quickly to be cooled are able to travel from the source chamber to the science chamber, and this fraction of the flux depends on the geometry of the differential pumping.

The aperture size therefore plays an important role in both defining the relative pressures and controlling the thermal background of the source. It appears from the literature that these have been the overriding considerations in deciding the aperture size in previous work, without much consideration of the impact on the characteristics of the flux. The ways the aperture size impacts the flux can be seen by considering the two extremes of very large and very small apertures.

3.1.2 Large Apertures

As atoms are trapped and cooled in a MOT source, they travel towards the $B = 0$ region until they reach the central exit channel where the aperture causes an absence of retroreflected light and the intensity imbalance accelerates the atoms along this region. Transverse cooling occurs throughout, since there are still the appropriate transverse beams for optical cooling, but the amount of cooling is limited by the time τ it takes for the atoms to be accelerated through the aperture. In addition, as atoms move further from the $B = 0$ point, the magnetic field change detunes the atoms to make transverse cooling less effective. As the aperture size increases, atoms reach the dark region with a higher transverse velocity, $v_\perp$, which corresponds to a flux with higher divergence. If $v_\perp$ is sufficient for atoms to traverse the

dark region within τ, they will be filtered out by the aperture and not contribute to the flux; χ reduces due to the increased transverse velocities of the atoms.

3.1.3 Small Apertures

Evidently, without an aperture a MOT source would have no exit channel for atoms and produce no flux. If ray optics were valid, then for any finite aperture, a region without retroreflected light would extend along the source axis and provide an exit channel for the atoms, generating a flux. However, diffraction of the retroreflected light occurs due to the aperture, and this places a limit on the minimum aperture size below which the exit channel is closed to the atoms. This occurs when the retroreflected on-axis intensity reduces the intensity imbalance experienced by the atoms such that the net force is insufficient to direct them through the aperture.

For diffraction of light with wavelength λ from a circular aperture of width w, the region for which far-field diffraction can be assumed is for distances $r \gg w^2/\lambda$ from the aperture, which is the *Fraunhofer condition* [129, 130]. For 780 nm light and $r \approx 20$ mm (typical of the distance from the aperture to the centre of the trapping region in a MOT source), the Fraunhofer condition is only valid for $w \gg \sqrt{D\lambda} = 0.12$ mm. Therefore, far-field diffraction can only be assumed for aperture sizes an order of magnitude smaller than those used in cold atoms sources (see Table 2.1), and to accurately estimate the minimum aperture would instead require solving Kirchoff's diffraction formula in the intermediate regime between the Fraunhofer and Fresnel cases. A theoretical evaluation of the minimum aperture is outside the scope of this thesis, however an estimate based on experimental results is presented in Chapter 7.

As far as we are aware, there has been no systematic study of the impact of the aperture size on the flux of a MOT source, either theoretically or experimentally. The cold-atom source of this thesis was therefore designed to conduct this investigation, in addition to demonstrating a compact and robust source of cold atoms.

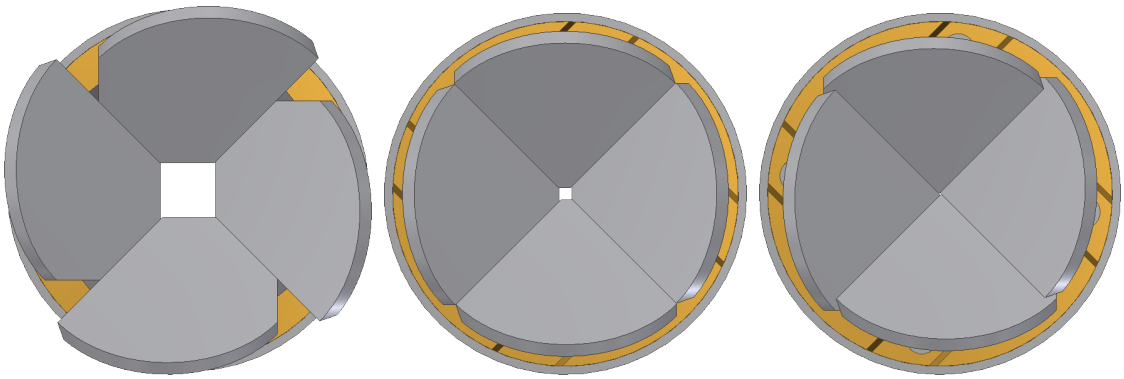


Figure 3.2: The adjustable-aperture mechanism: (a) opened up to form a large aperture; (b) set so that the profile presented to the laser is fully circular; (c) fully closed.

3.2 Adjustable-Aperture Mechanism

In order to explore this important parameter space for cold-atom sources, a pyramid MOT source was designed with an adjustable aperture. Examples of the source set to different apertures are given in Fig. 3.2 and an exploded view of the source is shown in Fig. 3.3. Four mirrors form the square-based pyramid geometry (albeit with a circular profile for compactness), and are located in linear grooves in the upper of two plates, referred to as the *rotator plate*. Each groove has a narrower collinear through-slot (that passes completely through to the rear of the plate), and slots of identical width are present in the lower plate, referred to as the *base plate*. Each mirror is secured by a bolt that passes through one slot in both the rotator and base plates. When the rotator plate is rotated, the base plate slots force the bolts attached to the mirrors to move, and the rotator plate constrains the resulting motion to be linear. The effect is that the mirrors slide past each other to vary the central aperture size – a feature unique to this cold atom source.[6] The symmetry of the design optimises the ease and cost of manufacturing by minimising the number of different pieces. The overlap of the mirrors minimises the gaps and reduces the scatter from the machined mirror edges, unlike previous circular-profile pyramids using glass mirror substrates.[7]

[6] It was noted after constructing the pyramid that the same idea (a symmetrical mechanism of linearly sliding components to create an adjustable aperture) was employed as part of the retractable roof for the Mercedes-Benz Stadium in Atlanta, Georgia, albeit with an 8-fold rotational symmetry.

[7] A clearance of 0.20 mm between the mirrors was sufficient to avoid them contacting one another.

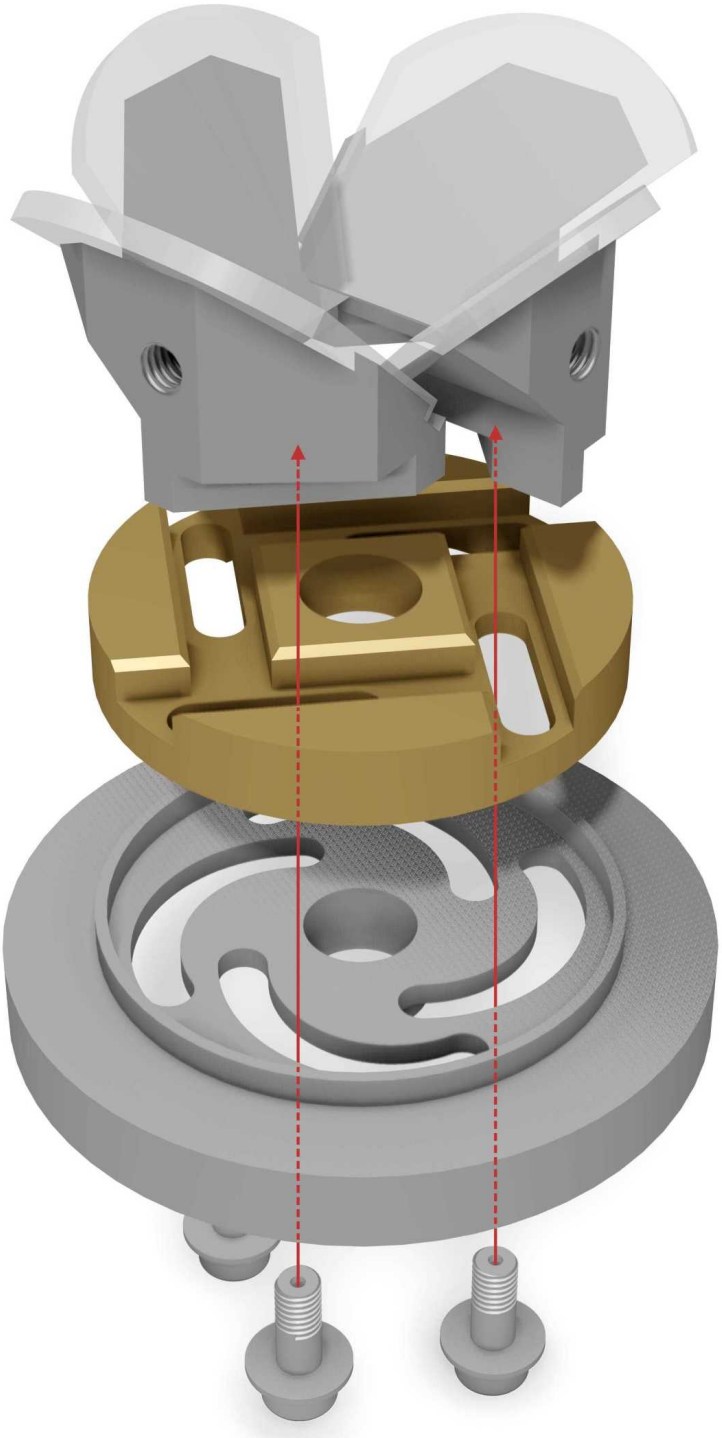


Figure 3.3: An exploded view of the adjustable-aperture pyramid design. Four mirrors on metal mounts are secured by bolts that pass through a base plate (bottom, grey) and a rotator plate (middle, gold), which each have slots which combine to adjust the relative position of the mirrors when one plate is rotated (the red lines show the path of two of the bolts). This allows the aperture size at the pyramid apex to be varied.

In the details of the design, care was given to avoid *virtual leaks*[8] either from enclosed regions or large areas of surface-to-surface contact. Consideration was also given to minimise the risk of the mechanism seizing, by both choosing the shape of the base plate slots to limit the impact of slack in the mechanism on the positioning of the mirrors, and by placing the bolts in line with the centre-of-mass of the mirror mounts.[9]

The design is currently subject to an ongoing international patent application, and additional technical details (including a fuller description of some of the considerations mentioned above) can be found in Appendix A. The details of the material choice, dimensions and fabrication methods used for the first prototype are specified in the following chapter, and first some specifics of the mirror design are described below.

3.2.1 Mirrors

Feedback from manufacturers was that forming the four sections of the pyramid from single glass prisms would be prohibitively complicated and expensive, so the pyramid mirrors were formed by coated plates of glass supported by metal mounts. To present a perfectly circular profile to the incident laser beam would have required a non-trivial mirror shape, so the ideal curve was approximated by the arc of a circle. This allowed the mirrors to be cut from circular blanks, greatly reducing the complexity and cost of manufacturing, while reducing the cross-sectional area of the pyramid by just 3.7% from the circular ideal.

The mirror coating was a multilayer dielectric stack. Metal-coated mirrors have been used in previous sources [41, 101, 103, 115] but they provide lower reflectivities than multilayer dielectric coatings, which both wastes optical power and increases the risk of intensity imbalances that reduce the performance of the source.[10] It was also important to avoid materials that would corrode in a rubidium atmosphere; rubidium is highly reactive, e.g. it

[8] Trapped pockets of air in a vacuum system, with a low conductance channel to the main volume, will gradually leak and limit the achievable pressure. Such trapped pockets are called *virtual leaks*.

[9] This avoids applying rotational torque (parallel to the pyramid axis) to the mounts when operating the mechanism, which would have increased the friction of the mounts with the rotator plate grooves.

[10] In [87] a 5% imbalance was sufficient to cause a 10% decrease in flux, and a 10% imbalance reduced the flux by 50%.

is known to alloy with unprotected gold [84, 131].

Securing the mirrors to their mounts is often done with metal clips [105, 125], however the tight tolerances of the adjustable mechanism were not compatible with this approach. Similarly, indium is a UHV-compatible low-temperature solder, but the requirement to compress the indium to form the seal by diffusion bonding would have made it difficult to obtain repeatable positioning accurate enough to be compatible with the mechanism tolerances, as well as requiring careful application of stress to the glass. In addition, indium softens above 110 °C, limiting the maximum temperature of the system, and reacts with rubidium at as low as 65 °C [132]. More involved methods that could have been used included optical contacting or anodic bonding, which both create leak-tight seals but require the mating surfaces to be flat to within $\lambda/5$ to $\lambda/50$. Instead, UHV-compatible epoxy was selected as the best option for precise locating and strong bonding of the mirrors (more details in Sec. 4.3), as had been used previously by the cold-atom and ion-trapping research groups in Oxford.

3.3 Summary

All cold-atom source designs in the literature have a common feature – a fixed aperture. The aperture size affects not only the pressure differential and the thermal background, but also the flux of the source. For this reason, a pyramid MOT source with an adjustable aperture was designed and is the subject of an international patent application. Throughout the design, focus was given to minimising the complexity of manufacturing while avoiding unnecessary virtual leaks, friction, and risks of seizing. The design is also readily scalable to fill any size of chamber. Following the completion of the design, a prototype source was fabricated to characterise the source, particularly the influence of aperture size.

4

Prototype Fabrication & Assembly

To characterise the performance of the new design of cold-atom source, a prototype pyramid source was manufactured. Exploring how the flux depends on aperture size was an important focus. Having the ability to adjust the aperture while the system was under vacuum would have greatly accelerated the characterisation of the source, however the additional complexity and lack of a custom chamber made this impractical for the initial prototype. The aperture size was instead varied by removing the pyramid from vacuum and manually adjusting it.

This chapter outlines the design specifications for the prototype (dimensions and material selections), the fabrication of the mounted mirrors, the properties of the multilayer dielectric coating, the assembly and installation of the pyramid in the vacuum chamber, and the procedure of changing the aperture size.

4.1 Prototype Dimensions

The pyramid chamber of the vacuum system used for testing and characterising the prototype was DN100CF (the system is described in Sec. 5.1), however the only access to the mounting points (two blind tapped holes) at the rear of the chamber was via the viewport flange, so the prototype pyramid could not be designed to fill a DN100CF tube. Instead the pyramid was designed to fill a DN63CF tube; the next smallest standard size (standard vacuum

component sizes are listed for reference in Appendix B). A radial clearance of 0.5 mm was allowed, resulting in an outer pyramid diameter of 59.5 mm, while the base plate was 88 mm in diameter to extend to the mounting holes in the rear of the pyramid chamber. If the manufactured mirrors were to be placed in a compact DN63CF chamber, a more compact base plate would be fabricated (as was done as part of an industry collaboration that is described in Appendix C).

The choice of thickness of the mirror substrate was a balance between having a very thin substrate to minimise the additional radial footprint,[1] and requiring sufficiently thick glass to enable polishing to a high quality surface finish of about $\lambda/10$ flatness. The compromise thickness selected was 3 mm, resulting in an inner pyramid diameter of 55 mm (the mirror surface presented to the laser beam). Note that these dimensions are for a particular aperture size (chosen to be 2 mm), and mechanically varying the aperture size adjusted the relative positions of the mirrors, causing small changes to these dimensions.

4.2 Prototype Material Selection

To operate a MOT source, HV pressures are normally sufficient because the vapour pressure of the species of interest is usually relatively high to maximise the output flux. However, in order to accurately characterise the pyramid source for different aperture sizes, the effect of the background pressure needed to be kept the same despite the chamber being brought up to air and pumped back down each time the aperture was changed. This was achieved by designing the entire system for UHV conditions, since minimising the base pressure minimised the effect of small pressure variations between different aperture sizes. Ensuring UHV compatibility required careful consideration of materials.

[1] For thickness t, the outer diameter of the pyramid is increased by $\sqrt{2}t$, without chamfering of the outer edges.

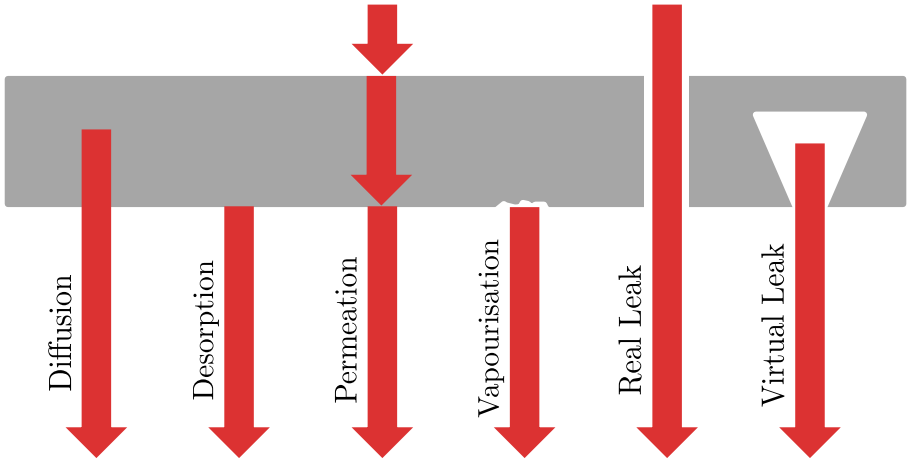


Figure 4.1: The sources of outgassing in vacuum systems that limit the achievable pressure.

4.2.1 Outgassing of Materials

To achieve UHV pressures requires a system that generates minimal gas-phase particles, in addition to providing sufficient pumping. Such particles are produced by several mechanisms [133–135]:

1. *Diffusion:* transport of gas from within a material to the surface
2. *Desorption:* release of previously adsorbed gas from the surface
3. *Permeation:* a three-step process whereby gas adsorbs onto an exterior (air-side) surface, diffuses through the material and desorbs from the inner (vacuum-side) surface
4. *Vapourisation:* thermally stimulated entry of particles of a material into the gas-phase; the partial pressure of these particles is the vapour pressure of the material

These processes are collectively called *outgassing*, and, combined with real and virtual leaks, limit the achievable base pressure (Fig. 4.1).

Diffusion and desorption can be substantially reduced through performing a 'bake-out' of the vacuum system, whereby the system is heated to 100 – 400 °C during initial pumping,

in order to increase the release rate of the absorbed and adsorbed gases.[2] Permeation and the vapour pressure are properties of the material, making the material choice critical to successfully achieving low base pressures.

4.2.2 Prototype Materials Selection

The choice of materials for the prototype source required balancing two factors:

1. Low outgassing, to achieve a low base pressure
2. Low friction, for the adjustable-aperture mechanism

Many metals are structurally stable at high temperatures in excess of the typical bake-out temperatures, therefore diffusion and desorption contributions to outgassing can be made negligible by baking. Permeation through metals is minimal for most gases because of the absence of voids, and hydrogen is one of the few gases with an appreciable permeation rate.[3] Hydrogen has low permeability through aluminium, which, combined with the low cost, good machinability and low vapour pressure, makes aluminium suitable for UHV applications. Aluminium naturally oxidises to form a porous surface layer of Al_2O_3 that increases outgassing, although this can be chemically removed and a dense Al_2O_3 layer allowed to form that actually reduces diffusion and desorption [133, 136–138].

Similarly, stainless steel has a low vapour pressure, low permeability for all gases, and naturally forms an oxide layer (Cr_2O_3) that reduces diffusion and desorption. Unlike aluminium, the natural oxide layer is not porous and requires no special chemical cleaning beyond standard UHV preparation. Grades of stainless steel with high chromium content are preferable for UHV, with the use of the 304 and 316 series being dominant.

Historically, stainless steel was favoured because aluminium was difficult to weld and softer, making reliable vacuum-tight seals more difficult (particularly the ConFlat-type seals

[2] The rate of desorption increases exponentially with temperature, as does the rate of diffusion (described by the Arrhenius equation and Fick's Law).

[3] Hydrogen dissociates upon adsorption, permeates in atomic form, then recombines on the inner surface and desorbs as molecular hydrogen.

that require a hard knife edge). However, technological advances mean that aluminium components are now widespread and similarly priced to equivalent stainless steel parts, reaching similar or lower levels of outgassing after baking [137] while being lighter and less magnetic.[4]

A recent alternative choice is titanium, which is particularly popular for compact devices [21, 116, 139–143] because it is stronger and lighter than stainless steel, and completely non-magnetic [144]. As with aluminium and stainless steel, titanium forms a surface oxide layer that reduces outgassing [145, 146], but it is expensive and more difficult to machine and weld. UHV chambers have also been made from copper [147] and beryllium [148] but these are rare and only used for specific design requirements.

For the pyramid prototype, the ease of cleaning and preparing stainless steel compared to aluminium, and the high cost of titanium, made stainless steel a good material choice. Different grades of stainless steel have different properties, with 316 having lower magnetic permeability and better corrosion resistance compared to 304, while low-carbon versions (denoted 'L') offer improved corrosion resistance and high-nitrogen versions (denoted 'N') offer lower magnetic permeability. For the prototype, 316LN was used for minimal magnetic permeability, although a MOT source does not require particularly low magnetic permeability, so any standard UHV-grade stainless steel should be suitable.

The pyramid contains moving parts, so the prototype was not made entirely of stainless steel. The friction between sliding stainless steel parts would be substantial, and it is undesirable to use greases or oil in UHV conditions. UHV-compatible lubrication is available, e.g. molybdenum disulphide powder or tungsten disulphide coatings, however the simplest approach was to select a low-friction material. Phosphor bronze was chosen, which is a copper alloy of tin and phosphorous (the presence of the latter increases the wear resistance) that is self-lubricating[5] and which has an acceptable vapour pressure for UHV [149].[6]

[4] Note that a potential issue to consider with aluminium is the presence of eddy currents if the chamber is subjected to varying magnetic fields, which are much more significant than for a stainless steel or titanium chamber due to the low resistivity of aluminium.

[5] A self-lubricating material is one that transfers microscopic amounts to the mating surface, forming a thin layer that acts as lubrication.

[6] Beryllium copper is an alternative that is also self-lubricating with a UHV-compatible vapour pressure.

The material chosen for the pyramid mirrors was BK7 borosilicate glass, which is widely used for optical components. The strong covalent bonds in the glass mean a negligible vapour pressure, and the material can be baked up to 550 °C [150]. The mirrors were in vacuum, so permeation was not an issue. If glass were to be used as part of a vacuum chamber, the permeation becomes relevant since it will contribute to the outgassing of the system. In particular, standard optical glasses are highly permeable to helium, which is difficult to pump passively, and instead glasses should be used that have a high ($\gtrsim 4\%$) aluminium oxide (also called alumina) content, or coatings should be applied to the glass (of aluminium oxide or graphene, for example) to reduce the permeability [38, 151].

4.2.3 Manufacturing

The custom pieces of glass were externally machined and polished to $\lambda/10$ flatness with 60/40 scratch-dig by SP3 Plus, while the metal components were CNC-machined by the Oxford University Department of Physics Mechanical Workshop. Unfortunately the rotator plate was incorrectly machined from brass instead of phosphor bronze, and this was only realised after assembling and characterising the source. Brass is a copper-zinc alloy considered incompatible with UHV due to the high vapour pressure of zinc [133, 149, 152, 153], so it could be surprising that the pressure was low enough for the pyramid source to work at all. Two factors may explain why this was not the case. Firstly, Raoult's Law states the vapour pressure of a component in a liquid or solid mixture is equal to the product of the vapour pressure of a pure sample of that component with the molar fraction of that component in the mixture. Therefore brass (which is $20-40\%$ zinc) is substantially better than pure zinc, and the brass alloy mistakenly used may have been a comparatively low-zinc alloy. Secondly, the surface area of the rotator plate exposed to the main section of the pyramid chamber was only about 28% of the total surface area, while the rest was either in contact with stainless steel (and thus not exposed to vacuum), or separated from the main section of the pyramid chamber via the pyramid aperture. As a result, the surface area of exposed brass that could contaminate the main pyramid MOT region was small. However, the presence of zinc in the

brass would still have degraded the vacuum system and is a manufacturing fault that should be avoided in future.

4.3 Mounting the Glass Mirror Substrates

To mount the glass mirror substrates to the metal mounts, conventional adhesives were unsuitable because of their high outgassing rates [154]. This arises from a combination of the open nature of their structure,[7] giving them a higher gas content and gas mobility compared to metals [155], and their use of solvents or moisture to cure,[8] which have unacceptably high vapour pressures; in theory the liquid should be entirely consumed during the cure, but in practice the curing process will not consume all the solvent or moisture, leaving a small remainder that will cause substantial outgassing.

The adhesive selected was EPO-TEK 353ND, which is a low-outgassing two-part epoxy [158] that has been successfully used in many UHV systems [128, 159–163], including in Oxford [126], and which passes the NASA low outgassing standard (ASTM E595) [164].[9] It is a 100% solids system, meaning no vapour comes off the material,[10] and undergoes a heat-activated cure when baked above 80 °C (typically 150 °C for one hour). The high temperature cure is unlike the majority of conventional epoxies, for which the cure process can occur at room temperature, and this aids low outgassing since heating causes an increased cross-linkage density [156, 166]. For 353ND the cure is accompanied by a colour change from pale yellow to dark brown (depending on the cure temperature), and subsequent exposure to higher temperatures causes a further darkening of the colour.[11]

[7] Gases diffuse through voids in the intertwined polymer chains by a thermally activated process [133].

[8] Curing is the process in which a liquid adhesive undergoes a chemical reaction to become solid. Under the appropriate conditions polymer chains undergo cross-linkage, which determines the rigidity and strength of the cured adhesive [156, 157].

[9] EPO-TEK 353ND has been used not only within UHV chambers, but also to form external hermetic seals to assemble UHV chambers [106, 165], albeit with mixed results.

[10] Specifically, a 100% solids system is one for which the thickness of a wet layer of the substance is equal to the thickness after it has dried.

[11] The colour cannot be calibrated to give an absolute temperature value since the colour also depends on the thickness of the glue layer, but is useful as an indicator of exposure to temperatures higher than the initial cure temperature.

Mixing the epoxy generates air bubbles in the epoxy, which if not removed could cause outgassing and reduce the adhesive strength. These can be removed by placing the mixture under vacuum or in a centrifuge, but gentle heating was sufficient; 10 minutes in a watch glass (to maximise surface area) on a hot plate at 40 °C removed all visible bubbles. A scalpel was then used to transfer a small quantity ($\lesssim 20\,\mu l$) of epoxy to the centre of the gluing area and the glass then pressed down firmly. The metal and glass surfaces to be epoxied were wiped with acetone and isopropyl alcohol (IPA) to remove contaminants. Initial testing with microscope slides found that spreading the epoxy before affixing the glass tended to result in air bubbles in the glue, so the glue was left in the uneven droplets formed by deposition from the scalpel.

4.3.1 Cracking of the Glass

Twelve of the custom-shaped pieces of glass were cured in two separate batches, one at 160 °C for 2 hours and one at 130 °C for 1h 40m, and all except two pieces ended up cracked (see Fig. 4.2). The cracks appeared only several hours after the pieces had reached room temperature, and occurred at the edge of the epoxy, particularly where the boundary of the epoxy changed direction due to a corner in the underlying metal mount. All cracks began on the epoxied bottom surface of the glass, and many did not reach the top surface.

The cause of the cracking was the differential thermal expansion of the glass and metal. The coefficient of thermal expansion (CTE) of BK7 glass is $7.1-8.3\times10^{-6}$/K at room temperature,[12] compared to $15.9-16.2\times10^{-6}$/K for 316L stainless steel.[13] As the materials were heated during the cure: the steel expanded twice as far as the glass; the epoxy cured at the elevated temperature and affixed the glass to the metal; then as the materials cooled, the glass was subjected to increasing stress as the steel attempted to contract twice as far as the glass.

[12] The CTE of BK7 is 7.1×10^{-6}/K in the range −30 to 70 °C, and 8.3×10^{-6}/K in the range 20 – 300 °C [150, 167, 168].

[13] The CTE of 316L stainless steel is 15.9×10^{-6}/K in the range 0 – 100 °C, and 16.2×10^{-6}/K in the range 0 – 315 °C [167–169].

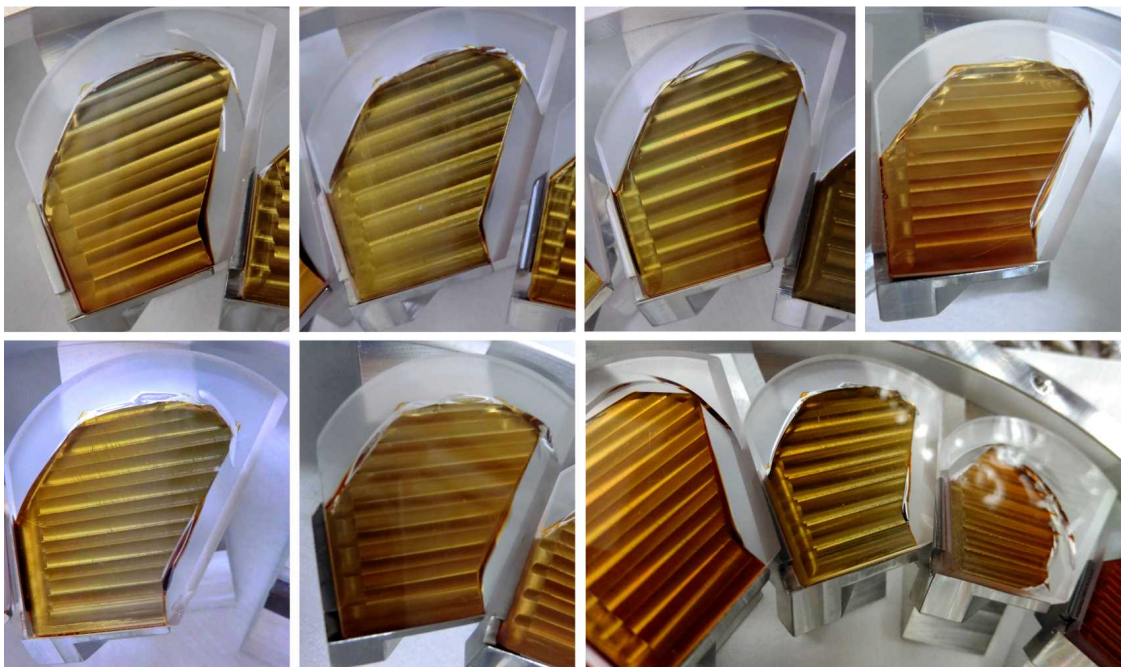


Figure 4.2: A selection of the custom pieces of glass that cracked after the curing of the epoxy. The glass cracked at the edges of the glue boundary, particularly where there was a sudden change in direction of the boundary, due to differential thermal expansion between the glass and stainless steel.

Following the cracking of the custom glass pieces, extensive testing was done to attempt to repeatedly reproduce the cracking and then to change the epoxying procedure. To replicate the conditions as closely as possible, test pieces of the same material and thickness of glass were used,[14] while blocks of machined 316LN stainless steel were used to replicate the properties of the metal mounts. Some testing was also conducted using the metal mounts themselves, but throughout all this there was no repeatable cracking; Fig. 4.3 shows a cracked piece of custom glass, and a non-cracked test piece of glass that was subject to the same epoxy procedure and cure. Repeatable cracking could not be achieved despite: using increasing cure temperatures to increase the stress on the glass; varying the amount of epoxy; varying the position of the epoxy on the glass; using shorter and longer cure times; varying the force used to press the glass into position; and replacing the stainless steel with aluminium to increase the stress on the glass (aluminium has a 50% higher CTE[15]).

[14] The test pieces were BK7 Grade 2 Experimental Grade Windows from Edmund Optics, 21×46×3 mm (stock #02-099) and 15×25×3 mm (stock #30-968).

[15] The CTE of aluminium is $22-27\times10^{-6}$/K, varying with temperature and the particular alloy [167, 168, 170, 171].



Figure 4.3: Two pieces of 3 mm thick BK7 glass epoxied to 316LN stainless steel mounts using 353ND. Left: a custom-shaped piece with extensive cracking. Right: a stock piece with no cracking despite identical cure conditions.

The issue was that the pieces of glass using for testing were polished on both sides, whereas the custom pieces of glass were polished on just the mirror side. Figure 4.4 shows how the reverse side has a frosted appearance as a result, and despite feeling smooth to the touch it has a surface roughness of 1.0 µm compared to just 0.5 nm for the polished surface.[16] This is significant because although glass has an extremely high theoretical strength >10 GPa,[17] the practical strength is greatly reduced to nearer 70 MPa by defects, usually on the surface [173–175]. Tiny chips and cracks generate critical stress concentrations at their tips, resulting in the formation of macroscopic cracks. This only applies to tensile stress however; surface defects are insignificant for compressive stress [173]. This was why the cracks in the custom pieces of glass (Fig. 4.2) were located at the edges of the epoxied region: in the central region the steel was compressing the glass but the high compressive strength of the glass was not overcome; whereas at the edge of the epoxy, there is a transition from compressive stress to zero stress, resulting in an intermediate region of tensile stress. The high surface roughness provided plenty of nucleation sites for cracks to begin, causing the glass to crack.

[16] Surface roughness, R_A, is the arithmetic average of the absolute values of the amplitudes of the surface deviations, although there are several roughness parameters that are used to quantify surface quality.

[17] For comparison, typical values for strength are: aluminium 40 – 50 MPa, copper 209 MPa, titanium 235 MPa, diamond 9 – 16 GPa [168, 172].

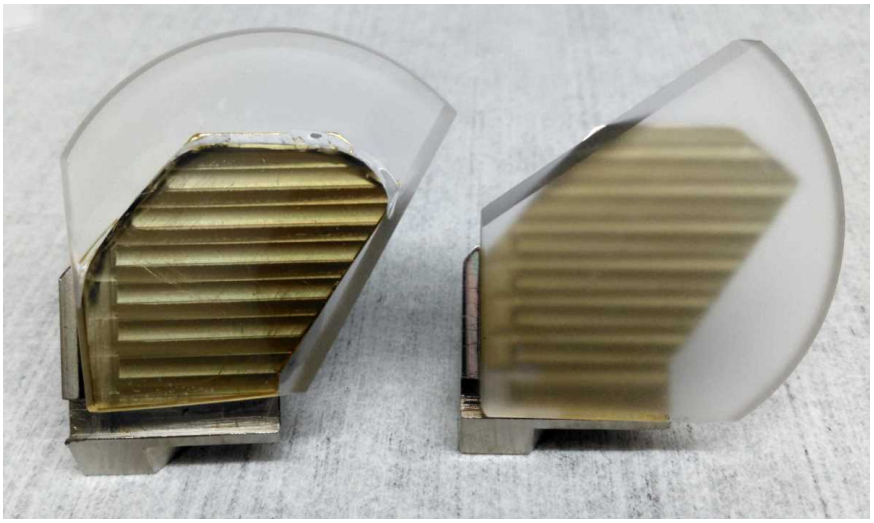


Figure 4.4: Cracking of a custom glass piece epoxied on its rough surface (left), compared to an identical piece epoxied on its polished surface (right). The latter was entirely free of cracks because of the lack of surface defects that allow the nucleation and propagation of cracks. The frosted appearance of the latter is due to the rough front surface.

This was confirmed by simply sanding the test pieces of glass to create the chips and scratches akin to the custom pieces.[18] These pieces routinely cracked in the same way as the custom pieces, while other non-sanded test pieces cured identically at the same time did not crack. Figure 4.4 shows the results of curing one custom piece of glass with the non-polished side against the metal (as designed) alongside another piece with the polished side against the metal; the former had extensive cracking while the latter had no cracking because of the absence of surface defects to allow crack nucleation. Even for very low temperature cures (87 – 90 °C) just above the cure threshold temperature (80 °C), cracking still occurred reproducibly for glass with surface defects. By taking time-lapse videos, the cracks were seen to take up to 8 hours to initially appear, and propagated on time scales from 5 minutes to 3 hours.

Having identified the surface defects as the cause of the cracking, a second batch of custom pieces of glass was produced with the rear face also polished. The dual-polished pieces were baked in small batches to monitor for any cracking. The cure conditions were: 130 °C for 2 hours, 147 °C for 3 hours, and 145 °C for 4 hours. In all cases no cracking occurred. The curing used a bench-top fan oven instead of a hotplate to provide more uniform temperatures.

[18] Initially 120 grit was used, then 240 grit; both caused repeatable cracking of the glass after curing.

4.3.2 Simulated Vacuum Bakes

When baking a vacuum system to reduce outgassing, the exponential dependence of diffusion and desorption results in significantly shorter bake times at higher temperatures, so determining the maximum temperature for the epoxied glass was important. 353ND has previously been baked at 170 °C in vacuum without issues [159], and to investigate higher temperatures, test pieces were baked at 200 °C for 11 hours, after which there were no cracks or signs of weakening of the adhesive bond. The epoxy is rated up to 250 °C [158] and passes the NASA outgassing test at this temperature [164], and the glass remained securely affixed even after baking at 265 °C, although the epoxy turned almost black. Baking to 350 – 400 °C was repeatedly sufficient to remove the glass from the metal mounts. Overall, bake-outs up to 250 °C should be possible but will be accompanied by irreversible darkening of the epoxy, while bake-outs of up to around 150 °C will produce no changes in adhesion or appearance since these conditions match the cure conditions.

4.3.3 Summary

An epoxying method was developed to mount the glass mirror substrates to the stainless steel mounts, which worked consistently on dual-polished pieces of glass. It benefited from the strength[19] and chemical stability[20] of 353ND epoxy, and was suitable for bake-out temperatures of over 200 °C. The 353ND also underwent capillary action at typical cure temperatures, filling the entire surface between glass and metal and leaving no space for small air pockets that could form virtual leaks.[21] Indeed, the epoxy filled the microscopic features of the surfaces so completely that after removing the metal mount, diffraction effects from the tooling marks on the metal could be seen in the glue (Fig. 4.5).

[19] Even repeated high force impacts from a hammer onto the glass did not cause the glass to separate away from the epoxy.

[20] No sign of weakening of the bonding was observed after 15 minutes in an ultrasonic bath of acetone at 35 °C (which would be a typical UHV-cleaning procedure), or 12 hours in acetone at room temperature.

[21] Adhesives are often designed to undergo capillary flow in order to penetrate voids, provide contact between tight clearances, and allow control of the adhesive thickness; the optimum adhesive bond strength depends on the uniformity and thickness of the adhesive, with thinner layers generally providing the strongest bond [176, 177].

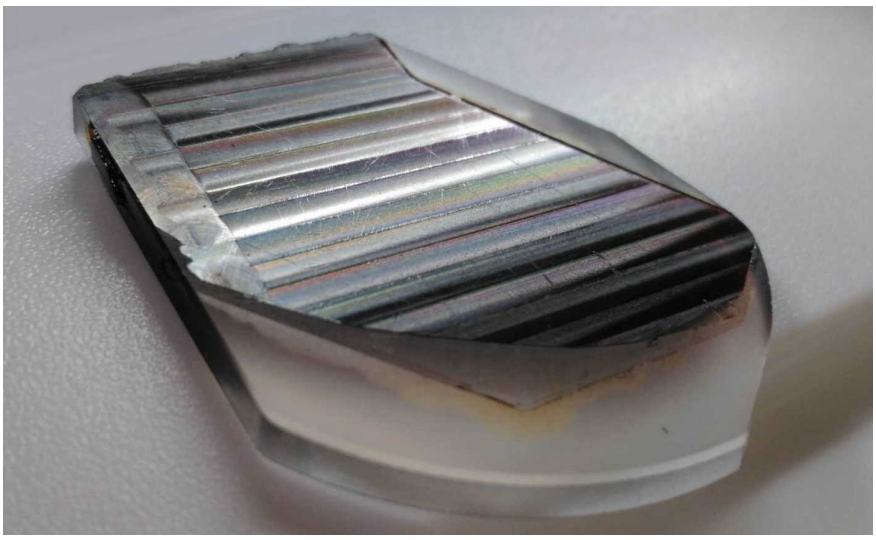


Figure 4.5: Diffraction effects could be seen from the surface of the epoxy after it was removed from metal due to the epoxy filling the microscopic tooling marks on the surface of the metal. This also means that the epoxy left no air pockets between the glass and metal surfaces to act as virtual leaks.

There was however still stress on the glass due to the differential thermal expansion, which could be observed through a polarising filter while the glass was illuminated by a polarised light source, and the nature of the cracking process had an inherent randomness to it, so this is not a method that can entirely guarantee no cracking. Extensions to this method to even further minimise the possibility of cracking (apart from changing the mounting method to one of the alternatives mentioned in Sec. 3.2.1) include: using metal mounts that cover the entire glass surface so all stress is compressive; using a more flexible UHV-compatible adhesive to reduce the stress on the glass;[22] and matching the CTE of the metal and glass to eliminate the stress entirely. Regarding the latter, titanium is a good candidate to replace the stainless steel since it has a CTE of $8.4-9.3\times10^{-6}$/K [167, 168, 171, 178] being within 5 – 15% of BK7 glass, although the material and manufacturing costs are higher than for steel.

An interesting side note is that throughout all the testing mentioned above, some microscope slides were also used as test pieces but never cracked, even when heavily sanded.[23] The reason for this is that they had a higher sodium content than the BK7 glass, which alters

[22] For example, EPO-TEK 310M.

[23] The microscope slides used were made by Menzel-Gläser of soda-lime based raw material (hydrolytic class 3): dimensions 76×26 mm; thickness 1.0 – 1.2 mm; mean CTE 9.06×10^{-6}/K (20 – 300 °C).

the CTE to be nearer that of stainless steel. Therefore, a different choice of glass material in the future would further reduce the likelihood of cracking.

4.4 Mirror Coating

The mounted glass mirror substrates were coated with a multilayer dielectric coating by the in-house Department of Physics Thin Film Facility, which also designed and produced the coating for a previous pyramid MOT [126] and provides external companies with coating services. Prior to coating, the glass substrate surfaces were cleaned with acetone then IPA, and dried with compressed argon, having already undergone cleaning prior to application of the epoxy. The mounted substrates were arranged with twelve-fold rotational symmetry using a custom aluminium mount. By arranging them in this fashion, instead of in a grid formation or similar, variations in the coatings between mirrors were minimised, since the axis of rotation was the axis about which the assembly was rotated during the coating.[24]

The coating was designed for high reflectivity for 45° angle of incidence (AOI) at both 780 nm and 767 nm, corresponding to rubidium and potassium respectively, using 29 alternating layers of SiO_2 and TiO_2, with the outer layer formed of the latter. This replicated the previous coating used successfully in our group, and avoided using different materials that risked being damaged by the reactive rubidium vapour in the pyramid chamber. In order for the mirrors to produce the correct polarisation for the MOT source the phase shift between the s- and p- components should be 180° (as described in Sec. 2.4.1), and this was measured by two separate approaches: placing a Babinet-Soleil compensator (a variable wave plate) and a mirror between crossed linear polarisers and adjusting the former to account for the phase shift due to the mirror coating; and looking at the transmission of circularly polarised light reflected from a mirror through a polarising beam splitter (PBS) as a function of ro-

[24] Deposition is typically performed by heating a small piece of material that then emits towards the sample to be coated, but the thickness of material deposited is determined by an inverse square law [130]. For planar samples, the coating would then not be uniform, so the sample is rotated during coating to even out the applied thickness. By arranging the samples with rotational symmetry as done here, it ensures that any variation in thickness that occurs (despite the physical rotation of the sample reducing such variations) will be common to all mirrors and hence minimises the variations in reflectivities of the mirrors.

tation angle of half-wave plate after the mirror. Both measurements gave the phase shift between s- and p- polarisations, modulo 180°, as 23°. For comparison, the same measurements were conducted on a simple gold-coated mirror and two broadband dielectric-coated mirrors from different brands, and the phase shifts were 19° and 7° respectively. The custom pyramid coating therefore gave a notably larger phase shift, however a previous pyramid in our group also had a 23° phase shift [42] which was sufficiently small to produce a MOT. This can be seen by considering the expression for a circularly polarised beam of amplitude E_0 in the $|x\rangle, |y\rangle$ basis:

$$E = \frac{E_0}{\sqrt{2}}(|x\rangle \pm i\,|y\rangle) \tag{4.1}$$

where $\pm$ is for left- and right-circularly polarised light. Reflection of left-circularly polarised light from a mirror with amplitude reflectivity coefficients $\sqrt{r_x}$ and $\sqrt{r_y}$, and which changes the phase of the x and y components by ϕ_x and ϕ_y respectively produces the output

$$E_{\text{refl}} = \frac{E_0}{\sqrt{2}}(\sqrt{r_x}\,e^{i\phi_x}\,|x\rangle + i\sqrt{r_y}\,e^{i\phi_y}\,|y\rangle) \tag{4.2}$$

Projecting into the right-circularly polarised basis and taking the square of the absolute value gives the fraction of the reflected power in the opposite polarisation to the incident light,

$$P_{\text{RH}} = \frac{E_0^2}{2}\left[\frac{r_x + r_y}{2} - \sqrt{r_x r_y}\sin\left(\delta + \frac{\pi}{2}\right)\right] \tag{4.3}$$

where $\delta = \phi_y - \phi_x$ is the relative phase shift between the x and y components, which can be chosen to correspond to the s- and p- components of the light incident on the mirror. When $\delta = 180°$, $P_{\text{RH}} = E_0^2$ for perfectly reflecting mirrors ($r_x = r_y = 1$), and thus all the reflected light has reversed handedness, which is the ideal case for a MOT. If instead $\delta = 180 \pm 23°$, P_{RH} is reduced but only by 4.0%, and the impact on the MOT is small.

The s- and p- reflectivities for 45° AOI were measured to be 97.6% and 94.8% respectively, which were lower than the $>99\%$ of standard broadband dielectric mirrors, but a slight improvement on the 95% of gold mirrors and sufficient for a MOT. The combination of the relative phase shift and reflectivities of the s- and p- polarisations meant that for cir-

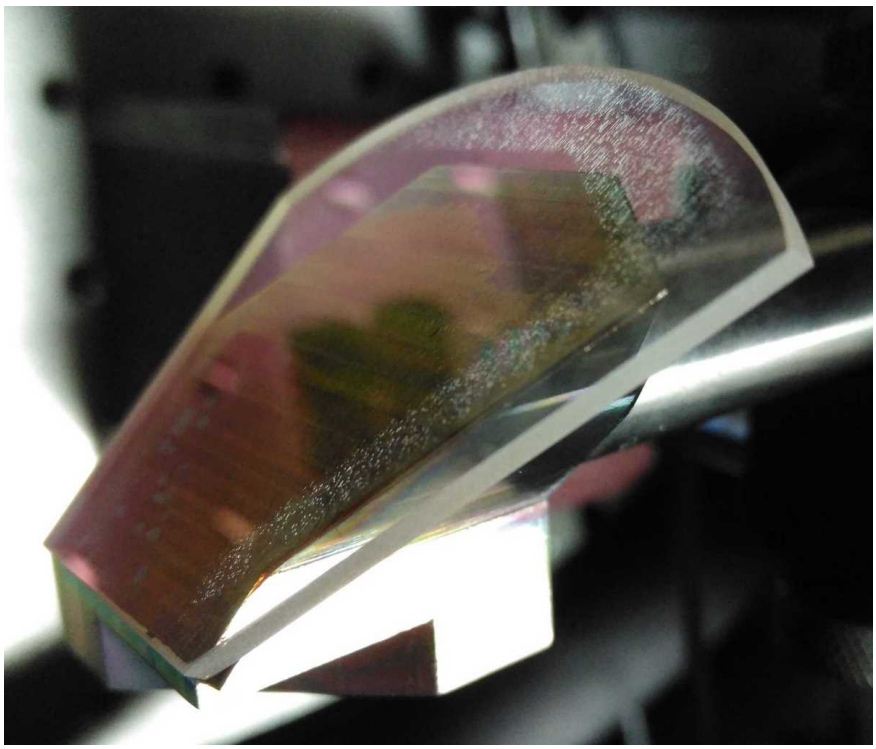


Figure 4.6: Scattered light was visible from the dielectric mirror coating of a mirror (which had not been under vacuum or exposed to rubidium) when illuminated from the rear by a white LED – the scatter covered the entire mirror surface, but the rear metal mount blocked the LED light from illuminating the central and lower regions. Subjecting dielectric coated mirrors from previous experiments and commercial providers to the same illumination showed no such scatter.

cularly polarised incident light at 45° AOI, 92.4% of the reflected power was of the opposite polarisation, 3.8% was in the incorrect polarisation, and 3.8% was lost.

4.4.1 Mirror Scatter

However, despite testing of the mirrors showing the reflectivity and phase shift to be acceptable, when the mirrors were first illuminated in vacuum with near-resonant light, it was observed on an infra-red sensitive camera that scattered light from a pronounced speckle pattern was visible across the mirrors. The scatter could also be seen when the mirrors were illuminated by bright white light, as shown in Fig. 4.6, but uncoated pieces of the same custom glass showed no speckle pattern, and nor did standard commercial mirrors. Subjecting the pyramid in vacuum to a rubidium atmosphere made no difference to the scatter,

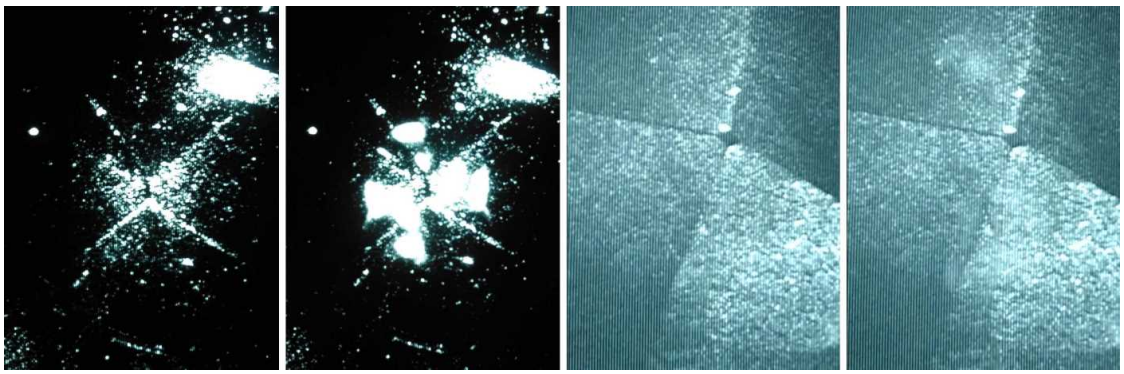


Figure 4.7: Pictures from an infrared-sensitive camera of the central region of (left pair) an old pyramid and (right pair) the new pyramid prototype. Within each pair of images, the left hand image is in the absence of a MOT, while the right hand image shows a MOT, along with reflections of the MOT in the mirrors. The signal was attenuated for the prototype pyramid due to the high amount of scatter, so the MOT signal appears weaker despite being comparable to that of the old pyramid. The bright patch in the top right of the images of the old pyramid is due to a reflection of an external light source, and not scatter from the pyramid.

however an order of magnitude increase in the scattering was observed after the pyramid had been removed from vacuum (to change the aperture size) and returned to vacuum. Subsequently, the observed scattering remained unchanged throughout repeated cycles of exposure to rubidium and temporary removal from vacuum.

Figure 4.7 shows a comparison of the observed scatter for an old pyramid that was used initially for testing the optical setup, and the new pyramid. For the old pyramid, scatter could be observed around the edges of the pyramid mirrors, as to be expected, however the majority of the mirror surfaces had very low levels of scatter compared to that of the MOT. In contrast, the scatter from the mirrors of the new pyramid was such that the camera required a pair of crossed polarisers to attenuate the light below the saturation limit. As a result, the detected fluorescence of the MOT cloud in the new pyramid was attenuated by two to three orders of magnitude, however the scatter from the mirrors was far greater than from the old pyramid. The scatter from the mirrors was in fact within an order of magnitude of the MOT fluorescence, such that it could be seen by eye, and this significantly complicated the process of initially optimising the apparatus to produce a MOT. It was also observed that the appearance of the pyramid mirrors changed so that a faint dark tint was uniformly present across the mirrors (Fig. 4.8), however the regions of the mirrors in close

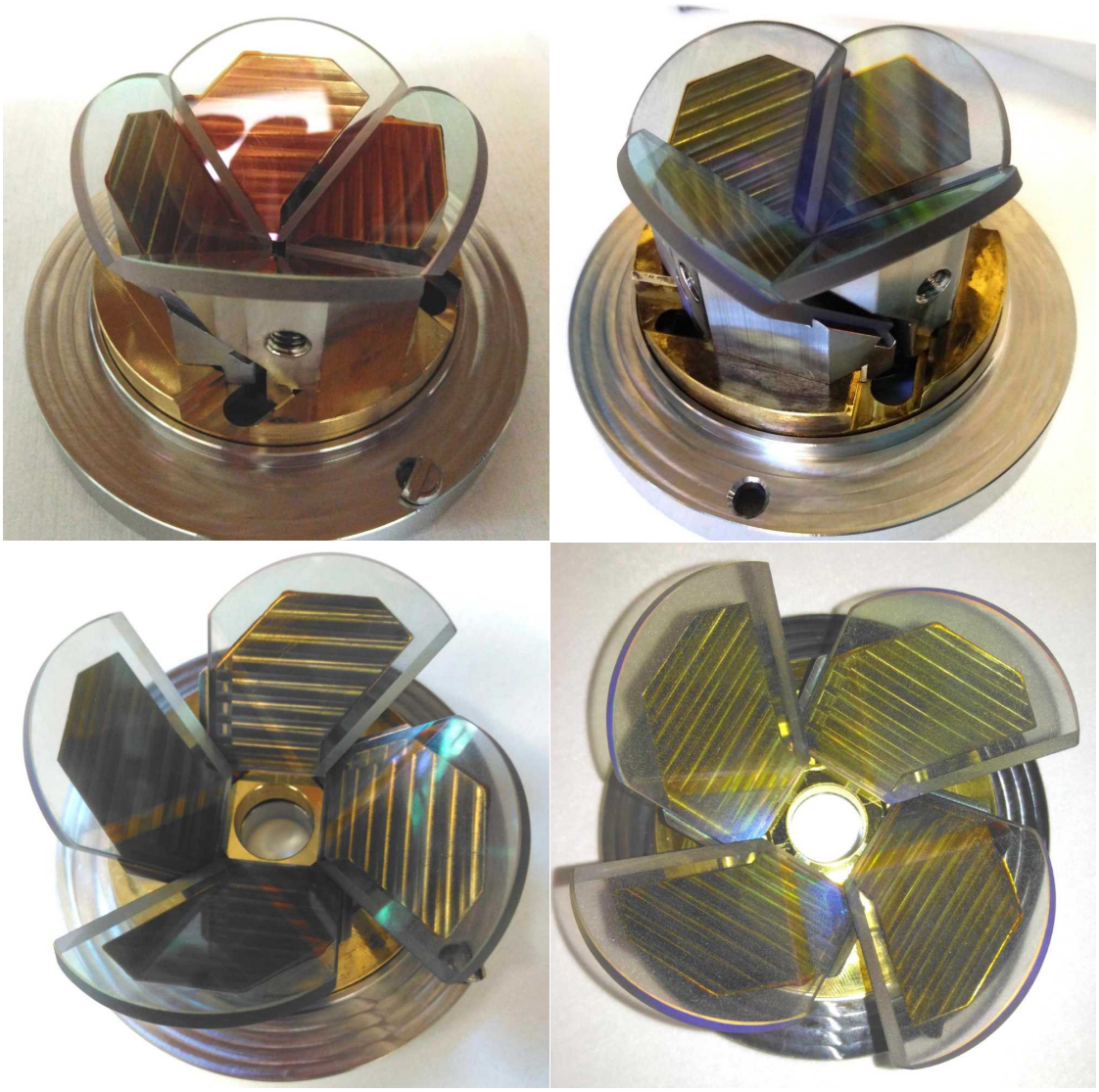


Figure 4.8: Discolouration of the pyramid mirrors after exposure to rubidium and removal from vacuum. Top row: the pyramid before (left) and after (right) being exposed to rubidium vapour, showing both a uniform darkening of the mirror surfaces, and a non-uniform darkening of the brass rotator plate. Bottom row: the pyramid after rubidium exposure, with the aperture opened up to reveal striped features where the mirrors did not discolour, corresponding to where the mirrors were in close proximity to the neighbouring mirrors; left was under standard room lights, and right was using bright illumination.

proximity ($< 0.2\,\text{mm}$) to the neighbouring mirrors did not darken, forming stripe patterns that were visible when the aperture size was opened up.

It transpired that although the in-house coating facility had produced near-identical coatings for our group several years previously, the vacuum condition of the coating chamber had deteriorated to the point where the ion gun used for ion beam assisted deposition (IBAD) would not activate. IBAD uses an ion gun to direct high energy ($100-200\,\text{eV}$) ions at the surface being coated, which provides surface atoms with sufficient energy to relocate, resulting in a denser coating. IBAD both increases the refractive index of the dielectric layer, reducing the number of layers required, and reduces the gaps available for water and other gases to occupy.

It is suspected that the initial scatter from the mirrors was due to contaminants in the dielectric coating arising from the abnormally high pressure in the coating chamber. The reflectivity measurements showed larger loss than expected for a multilayer dielectric coating (typically over 99% is achievable) but not substantially. Then, upon being exposed to a rubidium atmosphere during initial testing, the rubidium was able to penetrate one or more layers of the porous coating, which then oxidised when exposed to air while the pyramid aperture size was manually adjusted. This caused the observed order of magnitude increase in scatter, and changed the effective refractive index of the penetrated layers, causing the dark tint to appear on the mirrors. This hypothesis was supported by the presence of the striped features, since these areas were in close proximity to the neighbouring mirrors and would therefore not have been exposed to or penetrated by rubidium to the same extent.

The result of the coating issues was a significant amount of scattered light, comparable to the MOT fluorescence. This made observing the MOT difficult, and, since scattered light does not have the correct direction or polarisation for a MOT, it acts to heat the atoms. All characterisation of the pyramid source prototype is subject to the caveat of the atoms experiencing this additional heating, corresponding to an increase in transverse temperature and limiting the absolute performance of the source.

4.5 Assembly & Aperture Adjustment

After machining the rotator and base plates, and coating the mirrors, the pyramid prototype was assembled in a ISO Class 7 cleanroom to minimise contamination, and all parts and fastenings were re-cleaned in acetone at 35 °C for 5 minutes, then IPA at 35 °C for 5 minutes, and dried with highly filtered compressed air. The mechanism worked smoothly without requiring additional lubrication. An additional benefit of the adjustable-aperture mechanism was simplification of assembling the pyramid mirrors; the mirrors were able to be inserted and secured with the mechanism fully opened (for which the mirrors do not overlap) then slid into position by closing up the aperture. The adjustable-aperture mechanism is therefore useful in manufacturing as it minimises the risk of damaging mirrors during assembly. Finally, the mirrors were secured in place with the required aperture size by tightening the mounting bolts. The assembled pyramid was installed with its axis horizontal in the vacuum chamber using two slot-vented screws, then the system was pumped and baked in situ, as will be described in Sec. 5.1.

To alter the aperture size, the vacuum system was baked again to 120 – 140 °C in order to remove all the dispensed rubidium. Without this step, the rubidium would oxidise upon exposure to air, forming a white powder that, although straightforwardly wiped away, would have complicated and protracted the aperture change procedure. The chamber was cooled to room temperature still under vacuum, then vented with argon so that the majority of the vacuum system avoided exposure to contaminants and moisture in the air, which would otherwise be absorbed and adsorbed by the internal surfaces and elongate the subsequent required bake-out. With the chamber vented, the pyramid was extracted via the viewport flange, and the aperture size manually adjusted. The mirrors were cleaned with IPA on each occasion, but never showed signs of white rubidium oxide or any other contaminants. The pyramid and viewport were reinstalled and the pumping and bake-out process was repeated. This procedure was repeated every time the aperture size was changed; on occasion, the rubidium dispensers were replaced if they showed signs of being exhausted.

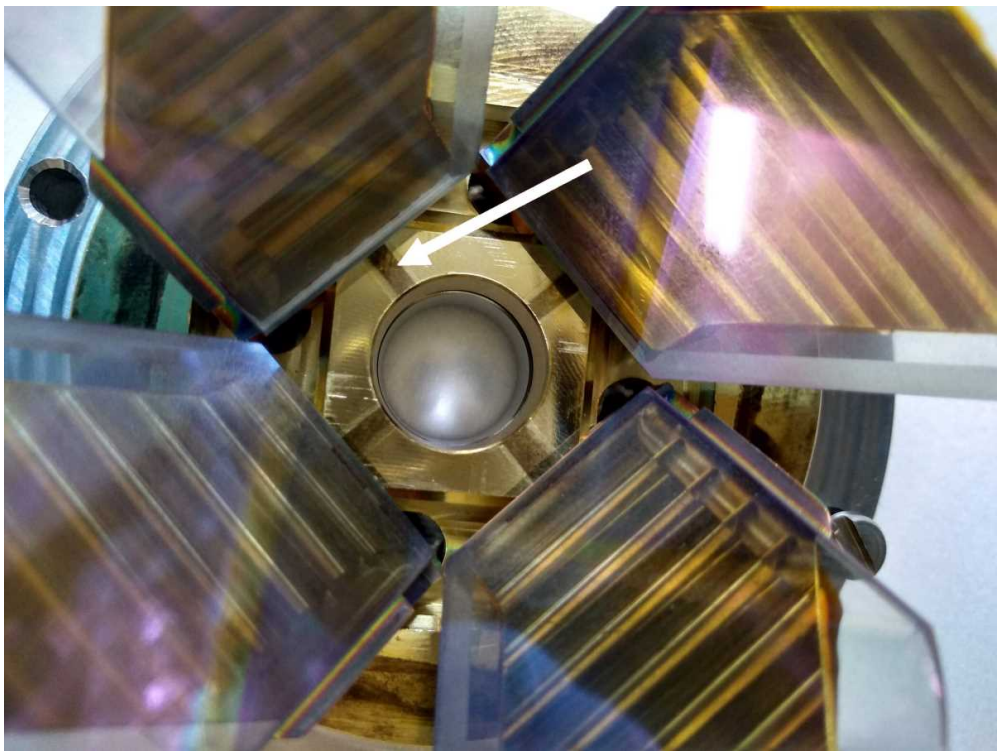


Figure 4.9: Discolouration of the central region of the brass rotator plate in a dark brown cross pattern (approximately along the diagonals of the picture, with the top-left-most piece of the cross identified by a white arrow), corresponding to the surface area not covered by the metal mirror mounts when the aperture was closed up. Also visible are the stripe patterns on the mirrors, described in Sec. 4.4.1.

Throughout all repetitions of this procedure, the pyramid mechanism operated smoothly without seizing when oriented vertically.[25] This was despite the brass rotator plate undergoing discolouration; in the top row of Fig. 4.8, it can be seen how the originally unblemished surface of the brass gained a dark non-uniform pattern, which became increasingly apparent over time. The discolouration only affected the surface area exposed to rubidium; Fig. 4.9 shows a cross pattern due to darkening where the brass was exposed but no discolouration where the stainless steel mirror mounts were in contact with the brass. The discolouration was not improved by cleaning with acetone or IPA, but gentle application of a sharp edge revealed the unblemished brass underneath. It appears the rubidium reacted with the brass, or a surface layer of tarnish on the brass, but without affecting the motion of the mechanism. No other materials within the vacuum chamber showed this discolouration.

[25] When the pyramid axis was near-horizontal, any slack in the tightness of the bolts allowed the upper mirrors to tilt downwards slightly, enough to make the mechanism prone to jamming.

4.6 Summary

The fabrication and assembly of the pyramid resulted in a well-tested method for epoxying the glass mirrors to their stainless steel mounts while avoiding cracking, and the adjustable-aperture mechanism functioned smoothly. The mistaken use of brass was not realised until after characterisation of the source, but did not prevent the source performing well (as will be described in Chapter 7). Of greater consequence was the exceptionally high scatter from the pyramid mirrors, which is likely to have limited the performance of the source by causing heating of the atoms, and some effects due to the scatter were apparent in the analysis of the flux characterisation data (see Sec. 7.3). The primary cause of the scatter was identified as the vacuum quality of the mirror coating facility, and that has since been remedied and new mirrors are currently being prepared that will not have the same issues with scatter.

To form a cold-atom source, the pyramid was housed in the vacuum system described in the following chapter, which also outlines the optical apparatus used to generate the MOT light and the probe light (for characterising the flux of the prototype source).

5

Experimental Apparatus

Characterising the prototype pyramid source required a vacuum system to house the pyramid and allow optical access to the produced flux, magnetic coils to produce the MOT field, and an optical system to produce the light for both the MOT and probing the flux. This chapter describes the apparatus built for testing the source. First the vacuum system is outlined, then the optical setup to produce the MOT light from a titanium-doped sapphire (Ti:sapphire) laser is detailed, as well as a double-pass tapered amplifier system that provided an alternative low-cost method for producing the high optical powers required, but which was replaced by the Ti:sapphire system. Finally, a separate optical system for producing light to probe the flux is reported, including a beat-note offset lock with a wide capture range.

5.1 Vacuum System

The vacuum chamber used to test and characterise the new design of pyramid source was that of a previous cold-atom apparatus [125, 179, 180], which used an old design of pyramid source to load a MOT in a glass cell 30 cm after the pyramid aperture. The vacuum system is shown in Fig. 5.1. The original intention was to use the system for preliminary testing of the external optics with the old pyramid, while building another system to house the new design of pyramid, however that second chamber had a leak that prevented the pressure

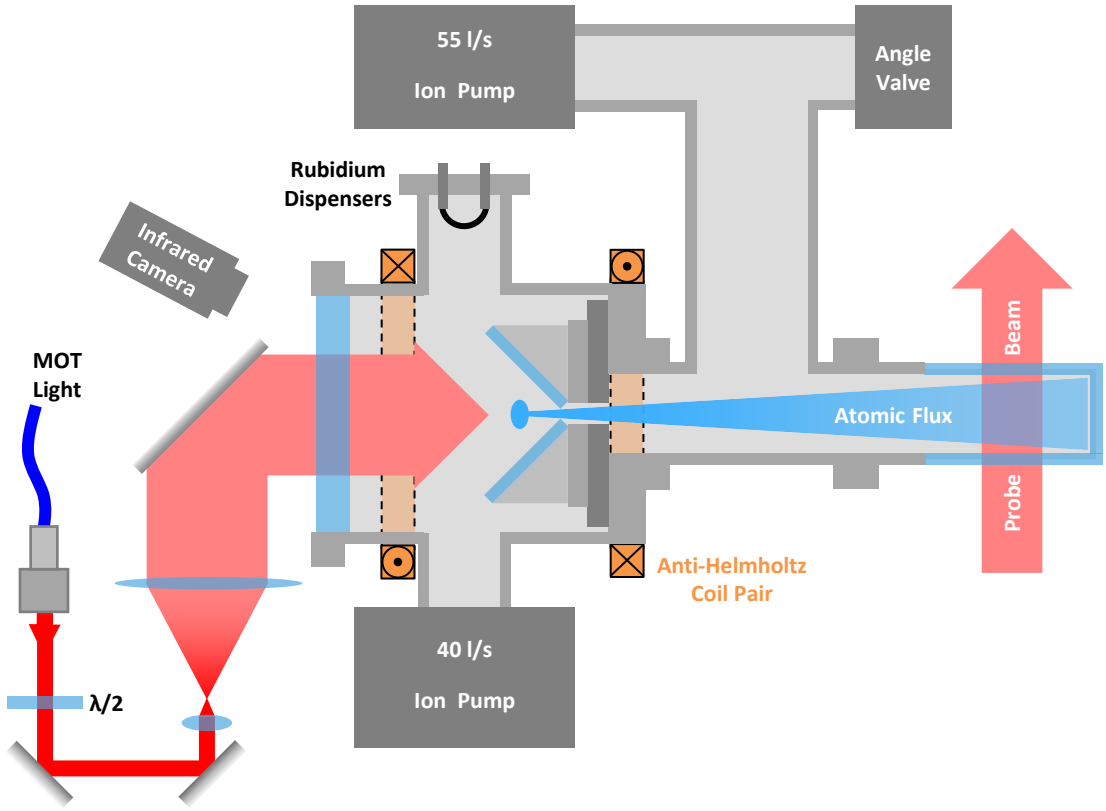


Figure 5.1: The vacuum system used to test and characterise the prototype pyramid source. The rubidium dispensers are shown in black and the anti-Helmholtz coil pair in orange, producing the field shown in Fig. 1.5. An infrared-sensitive camera was used to observe fluorescence from the pyramid MOT.

going below 10^{-9} mbar and which could not be found, so the old pyramid was removed and replaced with the new prototype.

The pyramid was housed in a 90 mm long DN100CF chamber with a 40 l/s ion pump[1] and an uncoated viewport. Rubidium was introduced into the pyramid chamber using thermally-activated dispensers, heated by applying a current of 3.5 – 6.5 A, to give a controllable partial pressure of rubidium.[2] Characterising the pyramid source at high vapour pressures quickly exhausted the dispensers, so five dispensers were installed using barrel connectors[3] in the chamber and replaced after two to three different pyramid aperture sizes were tested. The

[1] Varian VacIon Plus Starcell 55 l/s (model 919-0255)

[2] The dispensers were SAES Getters RB/NF/4.8/17 FT10+10 5G08078 – the dispensers contain rubidium chromate which reacts with a reducing agent to produce pure rubidium vapour when heated to 500 – 800 °C. Such temperatures are achievable for a small device with comparably low currents since the absence of convective heating in a vacuum environment greatly reduces the rate of heat transfer.

[3] Kurt J. Lesker FTAIBC120 – previous experiments in this group have used spot-welding to secure the dispensers in place, but operating at higher vapour pressures required the dispensers to be easily replaceable, so that the vacuum system was open to air for the minimum time required (to avoid contamination).

pyramid chamber was connected via a differential pumping tube (5 mm diameter and 17 mm long) to a DN63CF science chamber with a glass cell in line-of-sight of the pyramid, with no optical access prior to the glass cell. The science chamber was pumped by a 55 l/s ion pump[4] and the pressure was consistently below the 10^{-9} mbar minimum registered by the ion pump.

To evacuate the system from atmospheric pressure, a turbo pumping station[5] was connected to the system through an angle valve, and used to reach $\sim 10^{-6} - 10^{-7}$ mbar over the course of a day. The system was then baked in situ using heater tape[6] to 125 – 145 °C over $\sim$ 12 h while maintaining the temperature rise below 2 °C/min to avoid leaks occurring at the glass-metal seals. After the pressure had stabilised, ion pumps were turned on then the valve to the turbo pump closed. After two to three days of baking, the chamber was cooled over $\sim$ 12 h to room temperature. The only pressure gauge was on the turbo pump side of the gate valve, and the pressure obtained when fully baked was below the 5×10^{-9} mbar limit of the gauge. The current output of the ion pumps was monitored, however the pressure was below the noise level, and only pressures above 10^{-9} mbar were detectable. It is possible to use the lifetime of a MOT to infer the background pressure [181, 182], however the high intensity of the scatter from the mirrors limited the detection accuracy of the MOT fluorescence. As part of characterising the prototype pyramid source, the background pressure of rubidium had to be determined, and this was done by measuring the attenuation of the MOT light that passed through the pyramid aperture and out of the glass cell, then converting that to an atomic density using the Beer-Lambert Law (see Sec. 139).

The spherical quadrupole field for the MOT source was produced by a pair of anti-Helmholtz coils with radius 56 mm, separation 50 mm, and 15 turns each of 3 mm diameter annealed copper tubing with an inner diameter of 1.5 mm. The maximum available current

[4] Varian VacIon Plus Starcell 55 l/s (model 919-0255)

[5] Pfeiffer HiCube 80 Eco (PM S75 100 00) – a HiPace 80 Eco turbo pump backed by a MVP 015-2 diaphragm pump, and which allowed venting of the chamber with argon to avoid exposing the vacuum chamber interior to air (when opening it to change the aperture size).

[6] Four independent heater tapes (OMEGA Engineering, FGH series) were used with separate variac supplies so that a temperature gradient could be generated across the vacuum system to drive gases from the pyramid chamber towards the valve and turbo pump. The temperature was monitored using thermocouples logged via an Arduino microcontroller, in a set-up developed within our research group.

was 35.7 A, which generated an axial gradient of 18.2 G/cm, and when characterising the flux it was consistently found that the highest flux was found for this maximum gradient. The relatively high current required a new water cooling system to be designed and installed, which gave a flow rate through each coil of 0.9 l/s; the water temperature rose by 2 °C after passing through the coils. In addition to the MOT coils, three circular bias coils were arranged orthogonally around the pyramid chamber to provide fine tuning of the magnetic field centre. Each bias coil had 100 turns of 1 mm diameter enamelled copper wire, a total resistance of 1.7 Ω and an inner diameter of 150 mm. The bias coils were particularly important because the centre of the new pyramid design was at a different axial position to the old pyramid, for which the MOT coils were optimally positioned, so a significant axial bias field was required to move the quadrupole field centre. In addition, the presence of two large ion pumps nearby with their associated permanent magnets required a non-zero transverse bias field to compensate.

5.2 MOT Light Optics

To operate the pyramid prototype as a cold-atom source required a source of MOT light, consisting of light red-detuned from the $F = 2 \rightarrow F' = 3$ cooling resonance of ^{87}Rb, combined with repumping light (resonant with the $F = 1 \rightarrow F' = 2$ transition, as shown in Fig. 1.7), and which is stable to less than the linewidth of the transition.[7]. This was produced using a Ti:sapphire laser locked using modulation transfer spectroscopy, with a prototype EOM generating the repumping light as a sideband. This is described in the following, as well as an alternative low-cost system for producing high optical powers (using a double-pass tapered amplifier), but which was replaced by the Ti:sapphire system due to the better stability and mode quality.

[7] The natural linewidth of the D2 transition of ^{87}Rb is 6.0666(18) MHz [55].

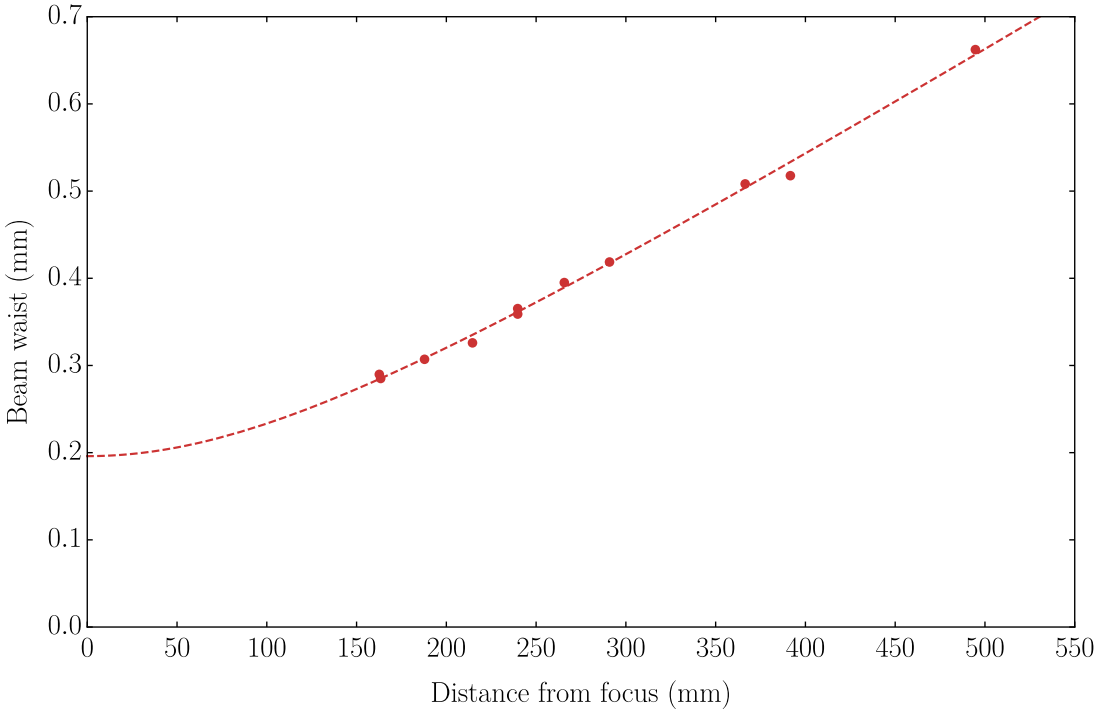


Figure 5.2: The divergence of the Ti:sapphire beam. The beam waists were measured by knife-edge measurements, and the fit is for a Gaussian beam of beam waist 196(3) µm and a divergence of 1.27(2) mrad (half-angle).

5.2.1 Ti:sapphire Laser

The scalable nature of the source design was intended to allow larger diameter pyramid sources to be produced, generating high fluxes ideal for improving the performance of cold-atom devices. Larger sources require correspondingly larger MOT beams of the same intensity, necessitating hundreds of milliwatts of optical power. This is outside the range of conventional single-frequency diode lasers without additional amplification (such a system was developed and tested; see Sec. 5.3), and instead an Innovate UK collaborative project with M Squared Lasers (MSL) provided the use of a tunable high-power continuous-wave Ti:sapphire laser.[8] The Ti:sapphire was pumped by a single-frequency 532 nm laser providing up to 18 W,[9] although only 5.5 – 6.0 W was required for the prototype source. The Ti:sapphire was also used for a separate strontium MOT and dipole trap experiments.

The Ti:sapphire output beam was divergent (see Fig. 5.2), so was expanded and colli-

[8] MSL SolsTiS SA PSX F
[9] Coherent Verdi 18W – a solid-state, diode-pumped, frequency-doubled Nd:Vanadate (Nd:YVO_4) laser.

mated by a telescope[10] before passing through a polarising beam splitter (PBS). A gravity-operated shutter[11] allowed the beam to be safely blocked but was not suitable for accurate, repeatable beam control due to the variable shutter lag and rise/fall times. The transmitted light had repumping light added as sidebands using an electro-optic modulator (EOM) and was fibre-coupled to the pyramid source, while the reflected light was fibre-coupled for frequency-stabilisation of the Ti:sapphire (Sec. 5.2.3). A PBS after the EOM allowed MOT light to be redirected either to a beam dump, a spectrum analyser, or to be used for imaging. The optical setup is shown in Fig. 5.3.

For all these optics, careful consideration was taken to avoid the risk of damage from the high optical power. The Ti:sapphire could produce up to 7 W of 780 nm light, which can be above the damage threshold for standard optical components. The greatest risk was the fibre coupling to the pyramid source, since although optical fibres can handle very high intensities, the adhesive at the fibre tip has a much lower threshold at which it burns or produces a residue.[12] The risk increases when the incident beam is misaligned, because more light fails to be coupled into the fibre and instead scatters into the adhesive and cladding. Typically 400 mW was fibre-coupled in this apparatus, and to avoid damage from drifts in the beam alignment only two mirrors were placed in the high-power beam path; all other components were at fixed heights on custom stainless steel posts. Damage can still occur, even when using stable optics and high damage threshold components, if dust is present on optical surfaces, so the entire beam path was shielded using a combination of cage optics and lens tubes.

Ideally the beam would have been expanded, thus reducing the optical intensity below the damage thresholds for standard optical components, however the high optical power restricted the choice of EOM to a single option which had a 2 mm diameter aperture. This limited the maximum beam size (without requiring additional beam expanding optics) and the $1/e^2$ beam diameter used was 1.5 mm.

[10] The telescope consisted of a pair of $f = 35$ mm (Thorlabs LA1027-B) and $f = 40$ mm (Thorlabs LA1422-B) lenses.
[11] LaserMet LS-10-12
[12] Standard fibres typically have a recommended limit of 200 – 300 mW.

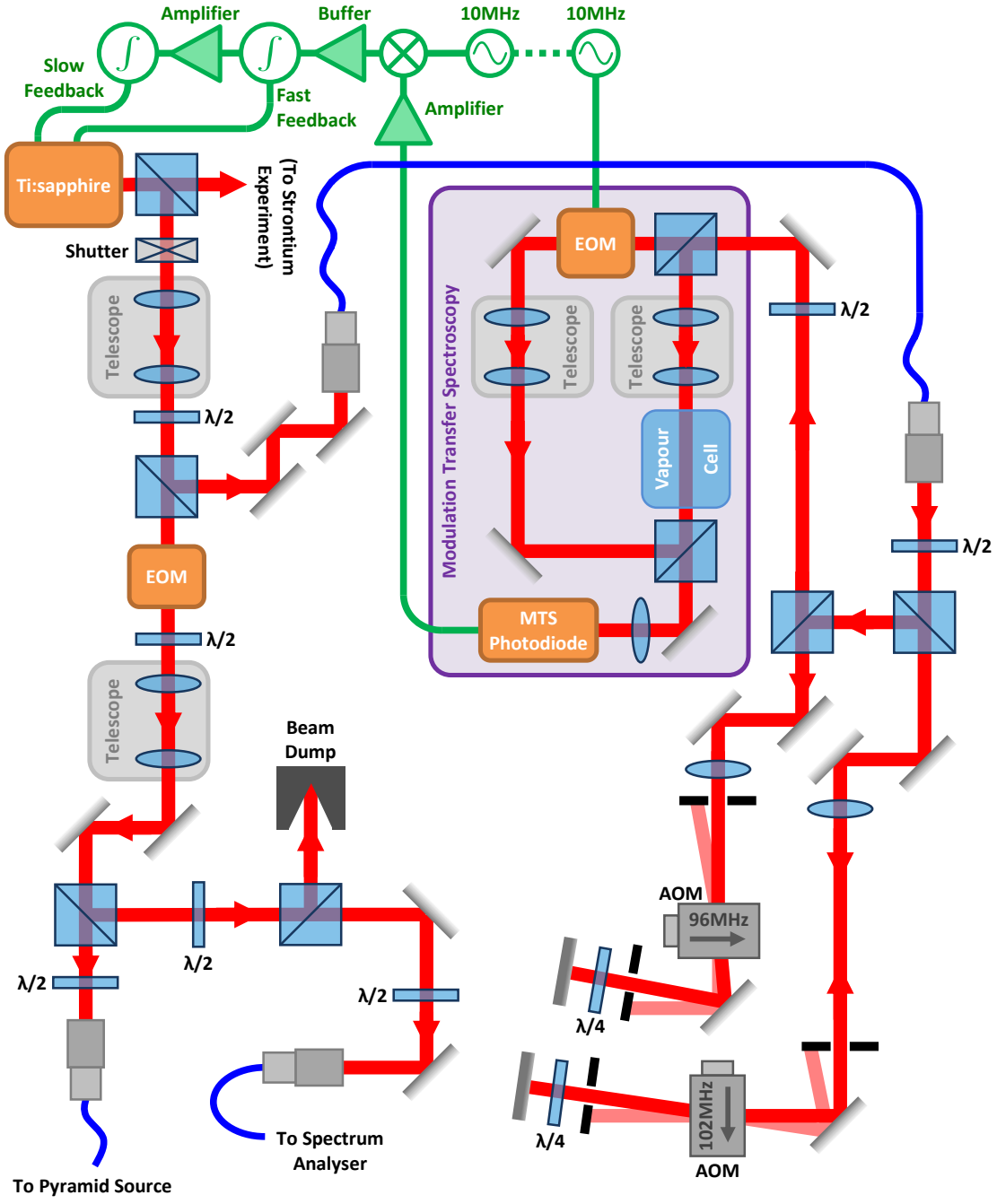


Figure 5.3: The optics for generating and frequency-stabilising the light for the pyramid MOT source. All fibres were single-mode polarisation-maintaining fibres, hence the half-wave plates to set the correct polarisation. Not shown are the cage mount and lens tubes used to shield the high-power beam path, which are used both to avoid dust and for user safety.

5.2.2 EOM Repumping Sidebands

The combination of requiring a high optical damage threshold and a resonant frequency of[13] $\sim 6.5\,\mathrm{GHz}$ resulted in no commercially available EOMs being suitable.[14] Instead a prototype EOM developed by Qubig GmbH was used,[15] which had a mechanically-adjustable resonant frequency range of $6{,}550 - 6{,}691\,\mathrm{MHz}$ and a limit of $5\,\mathrm{W/mm^2}$ to avoid thermal lensing effects (although the AR-coated MLN crystal[16] had a damage threshold of $10\,\mathrm{W/mm^2}$). The prototype was an adaptation of an existing 6.8 GHz EOM using a different crystal geometry, and, following testing of the prototype for the prototype pyramid source experiment, is commercially available with a housing and microwave driver interface redesigned based on feedback from this project.

A limitation of the EOM was its 2 mm diameter aperture, which restricted the maximum beam size. For a Gaussian beam with a 1.5 mm $1/e^2$ radius, 2.9% of the power falls outside the inner 2 mm diameter region. This loss is acceptable, but truncation of the initially Gaussian beam (transverse mode $\mathrm{TEM_{00}}$) by the aperture means that its profile is no longer fully described by the $\mathrm{TEM_{00}}$ Gaussian mode (higher order modes are present). This reduced the coupling efficiency of the laser light into a single-mode fibre, making the power loss caused by the EOM aperture higher than just the fraction of the light that was blocked.[17] Using a beam with 1.5 mm $1/e^2$ radius limited the maximum optical power to 4 W, which exceeded any commercially available alternative by an order of magnitude and will allow the testing of pyramids with diameters of up to about 18 cm.

A consequence of using a prototype EOM instead of a commercially available option was that the crystal was misplaced due to a new cavity design, which meant the crystal did not fully fill the aperture of the EOM. This did not appear to affect the performance of the

[13] See Fig. 1.7 for the origin of this value.
[14] The only possibility was a fibre-coupled option from AdvR Inc. with a 6 GHz tuning range that had a maximum optical power input of 300 mW, although up to 500 mW for a free space version.
[15] Qubig Rb87-6.6G
[16] Higher optical power limits could be possible using a $\mathrm{KTiOPO_4}$ (KTP) crystal instead of MgO-doped $\mathrm{LiNbO_3}$ (MLN).
[17] The fibre-coupling transmission decreased by 30% (from 86% to 60%) with the addition of the EOM, although was improved to 72% by inserting a 1:1 telescope after the EOM (consisting of a pair of Thorlabs LA1951-B $f = 25.4\,\mathrm{mm}$ lenses).

source, but may have contributed to the reduced fibre coupling efficiency by distorting part of the beam shape.

A spherical-mirror Fabry-Perot interferometer (optical spectrum analyser) was used to observe the frequency stability and amplitude of the EOM sidebands. The amplitudes of the first-order sidebands were 6% of the carrier peak height, corresponding to a 1:16 ratio between repumping and cooling light. Higher order sidebands were not detectable, although became noticeable for higher microwave drive powers. The repumping power could be lowered to just $1-2\%$ of the cooling power before the MOT fluorescence in the source began to reduce, however the EOM was operated significantly above this level so that the intensity of repumping light remained sufficiently high, even when the optical power was reduced during characterisation of the flux.

5.2.3 Frequency Stabilisation

Locking Electronics

The Ti:sapphire output frequency could be controlled by three components located inside the cavity: a narrow-band birefringent filter provided coarse tuning from $400-900\,\text{nm}$, accurate to $<250\,\text{GHz}$; an etalon allowed finer tuning over a range of $250-300\,\text{GHz}$ and restricted the laser to operating on a single longitudinal mode; and a piezo-mounted mirror gave fine control over the frequency by varying the cavity length. The latter was actually mounted on a pair of piezos: a small fast piezo that varied the laser frequency by $\pm 40\,\text{MHz}$, with a frequency response of $\text{DC}-50\,\text{kHz}$; and a large slow piezo that covered $\pm 15\,\text{GHz}$, with a lower frequency response of $\text{DC}-50\,\text{Hz}$. The fast piezo was used for stabilising the laser against high frequency noise, while the slow piezo was suitable for opposing long term drifts; the Ti:sapphire typically drifted outside the range of the fast piezo within 30 minutes, but daily drifts were well within the range of the slow piezo.[18]

[18] The laboratory had a domestic air-conditioning unit which was not fully adequate for the large room and there were temperature changes of the order of a few degrees.

To provide the required feedback separately to the fast and slow piezos, an op-amp circuit was designed, tested and fabricated as a PCB. An input error signal was buffered by a non-inverting near-unity gain amplifier, then integrated by a 'fast' integrator (time constant $RC = 1.2\,\mu s$, and 133 kHz crossover frequency) and attenuated by a variable potential divider. This signal was used as the feedback to the fast piezo, and was also separately attenuated by an inverting amplifier (gain $= -4 \times 10^{-3}$) and integrated by a 'slow' integrator ($RC = 2.1$ ms, 74 Hz crossover frequency) to produce the feedback signal for the slow piezo.

MTS Spectroscopy

The error signal for the piezo-feedback circuit was generated by modulation transfer spectroscopy (MTS) [183–185]. In MTS, the modulation of a pump beam is transferred to a counterpropagating, unmodulated probe beam by four-wave mixing.[19] The resulting sidebands on the probe beam, combined with the original probe frequency, produce a signal on the photodiode at the modulation frequency that can be extracted using phase-sensitive detection. This dispersion-shaped signal is suitable as an error signal for laser locking. A great advantage of MTS as compared to frequency modulation is that MTS produces a strong signal for only some of the allowed transitions; this simplification of the spectrum makes it easy to find the correct transition, such as when relocking the servo-control system.

The light used for the MTS was first frequency-shifted using acousto-optic modulators (AOMs) to control the detuning of the cooling light from resonance. Light picked-off prior to the EOM was double-passed twice through AOMs; the first AOM red-shifted the frequency by 96 MHz each pass, and the second AOM blue-shifted the light by 102 MHz each pass, resulting in an overall frequency shift of 12 MHz (to the blue). When the resulting light was locked on resonance with the cooling transition, the MOT cooling light was red-shifted by 12 MHz ($2\,\Gamma$) from resonance. The AOM frequencies could be adjusted to vary the frequency detuning of the MOT cooling light, however $2\,\Gamma$ was found to be optimal for the

[19] In the four-wave mixing process, the probe frequency and two frequencies in the pump light (e.g. the carrier and one sideband) interact via the third order non-linear susceptibility of the medium (in this case the rubidium vapour), producing a fourth frequency as a sideband on the probe light.

pyramid source. The light was focused by long focal-length lenses through the AOMs and retroreflected using concave mirrors of radius r placed $f + r$ from the lenses so that the beam was refocused at the same point and returned collimated.[20] This system is more robust to changes of the AOM frequency than a collimated beam reflected by flat mirrors, since the change in diffraction angle is accounted for by the concave mirrors.

The blue-shifted light then entered a standard MTS arrangement: the beam was split at a PBS into a pump and probe beam; the probe beam passed through a rubidium vapour cell and a second PBS onto a photodiode;[21] the pump beam first had 10 MHz sidebands added to the carrier frequency by phase-modulation using an EOM,[22] then was directed to counterpropagate with the probe beam through the vapour cell.

The photodiode signal was amplified[23] before being combined with the modulation frequency in a mixer,[24] the output of which was low-pass filtered and used as the input signal to the servo-control electronics. The modulation frequency for the mixer was produced by a separate (but synchronised) signal generator to that used to drive the EOM, so that their relative phase could be adjusted to optimise the error signal.

Lock Characteristics

The MTS error signal, along with the initial signal from the photodiode that shows both the unsaturated (Doppler-broadened) and saturated absorption spectrum of the D2 line of ^{87}Rb, is shown in Fig. 5.4. The gradient of the MTS signal at the $F = 2 \rightarrow F' = 3$ cooling transition was 14 – 18 mV/MHz (depending on the optical power into the MTS optics) and the capture range was ± 7.5 MHz. The lock was stable to less than $\lesssim 0.5$ MHz, limited by the noise on the MTS signal. This was much smaller than the 6 MHz linewidth of the transition

[20] Long focal lengths were used because optimum diffraction efficiency requires collimated light. For a Gaussian beam of wavelength λ, with its waist w at the surface of a lens of focal length f, it is collimated in a region about its focus on the order of the Rayleigh length, $z_R = \pi w_0^2/\lambda$ where $w_0 = \lambda f/\pi w$ is the beam waist at the focus. As f increases, so does z_R, allowing for a greater length of the beam within the AOM to be collimated, which increases the overall diffraction efficiency [130, 186].

[21] Thorlabs PDA36A-EC

[22] Photonics Technologies EOM-01-10-001

[23] Mini-Circuits ZFL-500LN

[24] Mini-Circuits ZP-3H+

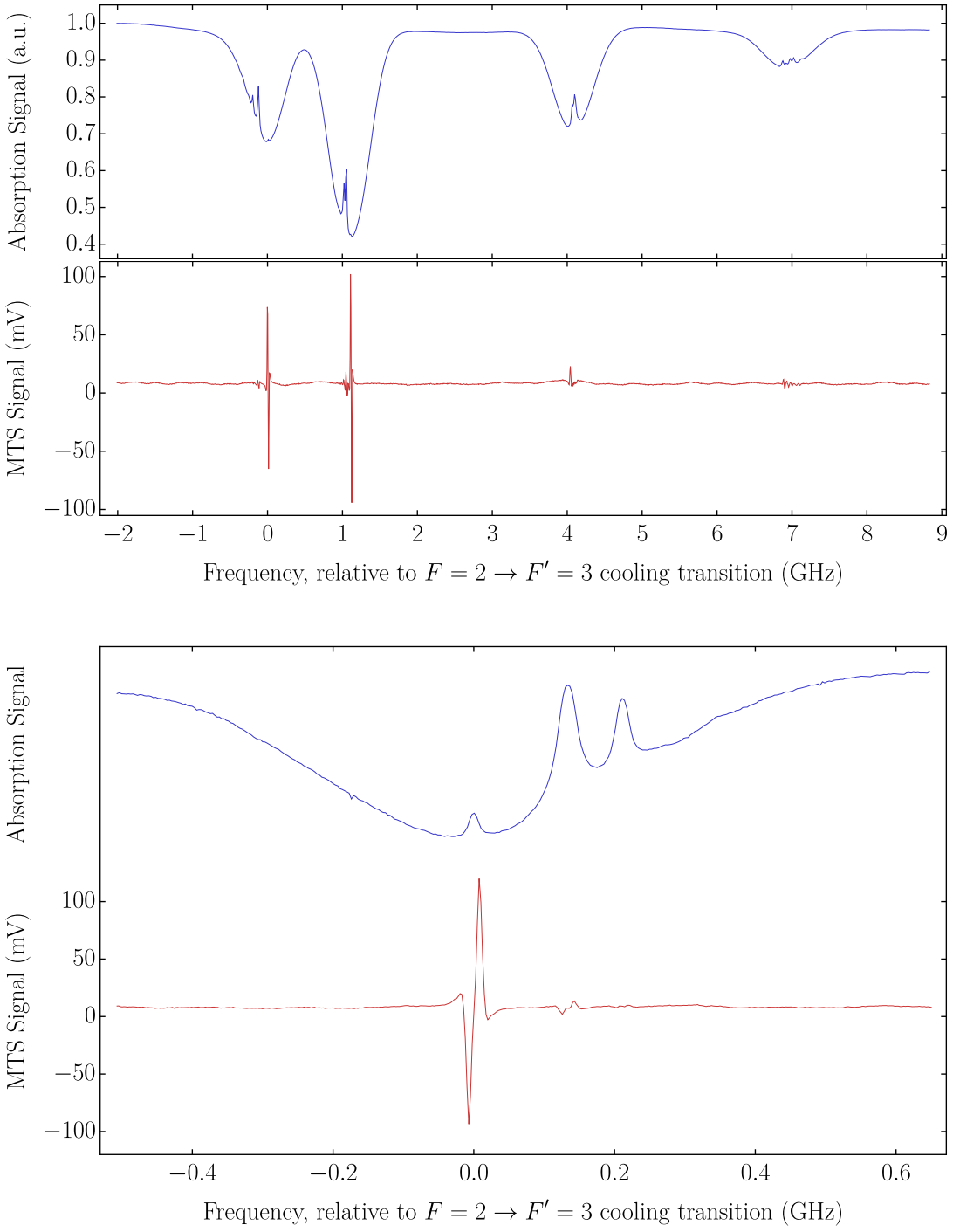


Figure 5.4: The absorption spectrum of ^{87}Rb and the MTS error signal used for frequency stabilisation. Top: all transitions of the ^{87}Rb D2 line. Bottom: the $F = 2 \rightarrow F' = 3$ cooling transition.

so more than sufficient for stable MOT behaviour, and the Ti:sapphire laser stayed locked for multiple days at a time.

5.2.4 MOT Beam Optics

The MOT beam, containing red-detuned cooling light and resonant repumping light, was conducted through an optical fibre to an elevated breadboard in front of the pyramid chamber. The beam passed through a PBS to define the polarisation and a quarter-wave plate converted the light to be circularly-polarised with the correct handedness for the MOT quadrupole field. A telescope composed of a $f = 4.5\,\text{mm}$ and $f = 200\,\text{mm}$ pair of spherical singlet lenses expanded the beam from a $1/e^2$ radius of 1.5 mm to 66.7 mm. A large iris was placed immediately behind the first lens to block light retroreflected by the pyramid. A 10 cm diameter mirror guided the expanded MOT beam into the pyramid chamber. A photodiode facing the pyramid chamber was used to detect the MOT fluorescence.[25] The optics are outlined in Fig. 5.1.

The MOT beam $1/e^2$ diameter was made larger than the pyramid (66.7 mm compared to 55 mm) to provide a more uniform intensity across the pyramid; if the MOT beam were 55 mm, the intensity at the edge of the pyramid would be 13.5% of the on-axis intensity, whereas for 66.7 mm the intensity falls to only 25.7%.[26]

The optics to generate the MOT light were not optimised for compactness, but rather for cost and ease of use in a laboratory setting. For a compact source integrated into a portable device, the apparatus would be very different, but that was outside the scope of this project.

5.3 Double-Pass Tapered Amplifier

Prior to the commencement of the Innovate UK project with M Squared Lasers, which made available the high-power Ti:sapphire laser, an alternative diode laser system was built

[25] A $f = 35\,\text{mm}$ lens focused light from the approximate position of the MOT centre.
[26] Using $I(r) = I_0 e^{-2r^2/w_0^2}$ where w_0 is the $1/e^2$ radius [129].

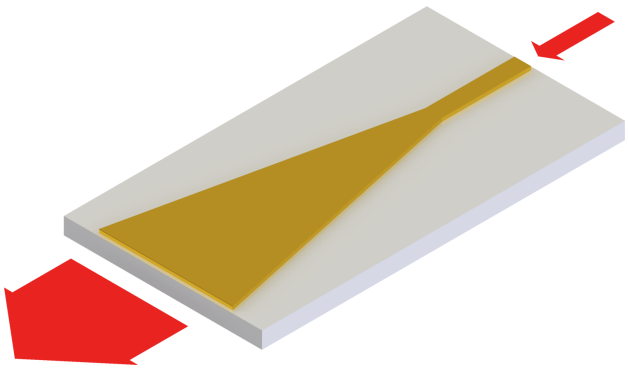


Figure 5.5: A tapered amplifier (TA) chip. Conventionally, low-power seed light enters via the narrow rear face of the chip (forward-seeding) and is amplified while remaining single mode. A current is applied to the chip to create a population inversion in the electronic bands of the semiconductor. The typical length of the tapered region is 2 – 4 mm, and the input aperture of ∼1 µm expands to about ∼ 200 µm.

and tested to generate the hundreds of milliwatts required for the pyramid source. Since conventional diode lasers do not generate sufficient optical power, tapered amplifiers (TAs) are used.

TAs enable output powers of up to 4 W by amplifying a small amount of seed light (typically 10 – 30 mW) in a tapered gain region (see Fig. 5.5). The amplification is generated by applying a current to create a population inversion in the gain medium. The transverse dimension of the gain region in conventional diode lasers is of the order of the optical wavelength in order to achieve single mode output [187]. This limits the power due to heating of the gain region which imposes a maximum intensity at the output facet, above which damage will occur [188]. A TA retains single mode operation at high power by tapering the width of the gain region along the chip axis. Seed light enters at the narrow rear end (forward-seeding) – which has similar dimensions to a conventional laser diode – then diffracts to fill the widening gain region while remaining single mode and retaining the spectral properties of the seed light.

TAs are notoriously susceptible to damage from optical back-reflections, since they are amplified and concentrated on the 'narrow' input facet of the waveguide, which can exceed its damage threshold [187, 189]. However, a double-passed TA (originally demonstrated by

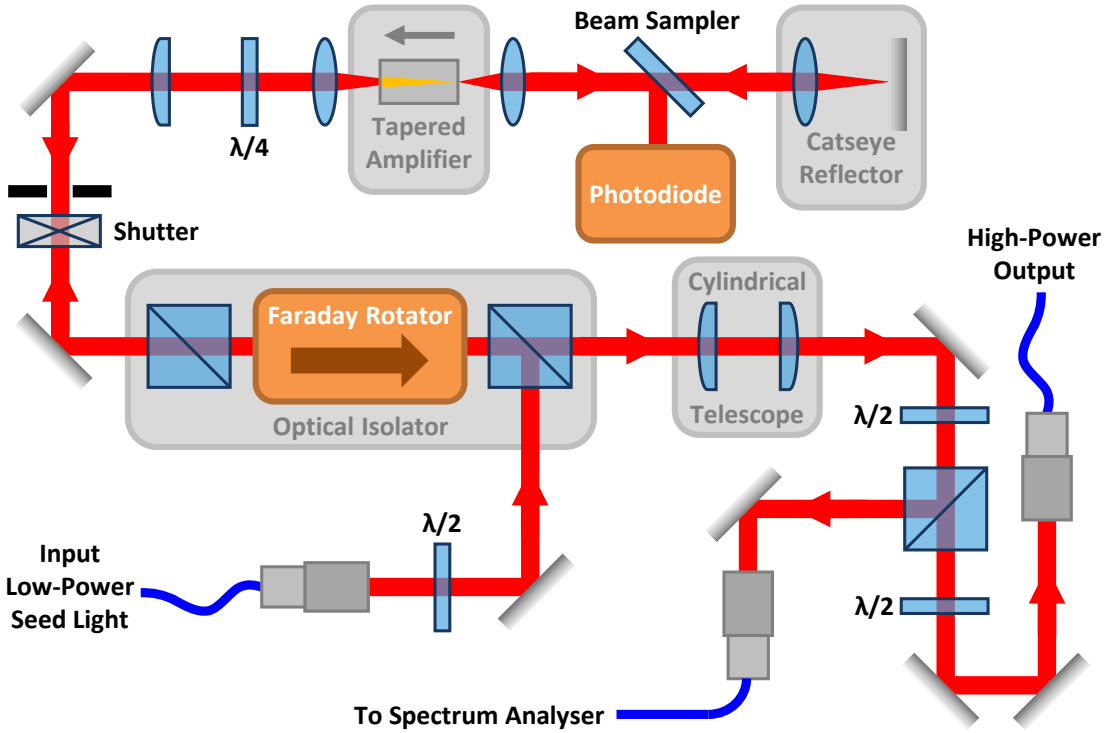


Figure 5.6: The optical layout used to implement a double-pass tapered amplifier. Low-power seed light reverse-seeded a TA chip from the wide facet, then was retroreflected by a catseye reflector to conventionally forward-seed the TA. The resulting high-power beam was highly divergent and required both an aspheric and cylindrical lens to be collimated, after which it passed through an isolator to protect the chip from backreflections and was reshaped with a rotatable cylindrical telescope to optimise the coupling into an optical fibre. The isolator was used to insert the seed light via the second PBS.

Bolpasi & von Klitzing [190] and subsequently used elsewhere [191, 192]) greatly reduces the required seed power by a factor of ~ 250. The seed light initially enters the wide end of the TA (reverse-seeding), is amplified (by a factor of $\sim$125) at the rear, then retroreflected to forward-seed the TA, generating an overall gain of several thousand.

A double-passed TA arrangement[27] to amplify seed light containing cooling and repumping light was implemented as shown in Fig. 5.6. It was successfully used to amplify 200 µW of red-detuned cooling light, combined with 50 µW of repumping light, to produce a MOT in the old pyramid. The performance of the double-pass TA was investigated (Fig. 5.7) as a function of seed power and current. Fig. 5.7(a) shows that over 800 mW could be produced from a 200 µW seed beam (a gain of 4,000), and the results closely agree with those of the

[27] The active TA chip used was an Eagleyard EYP-TPA-780 (serial number DA-02103) mounted in a custom housing detailed in [193] with current provided by a Thorlabs LDC 8040, and temperature control provided by a Thorlabs TED 8040 - the TA requires active heating by a Peltier cooler to prevent overheating.

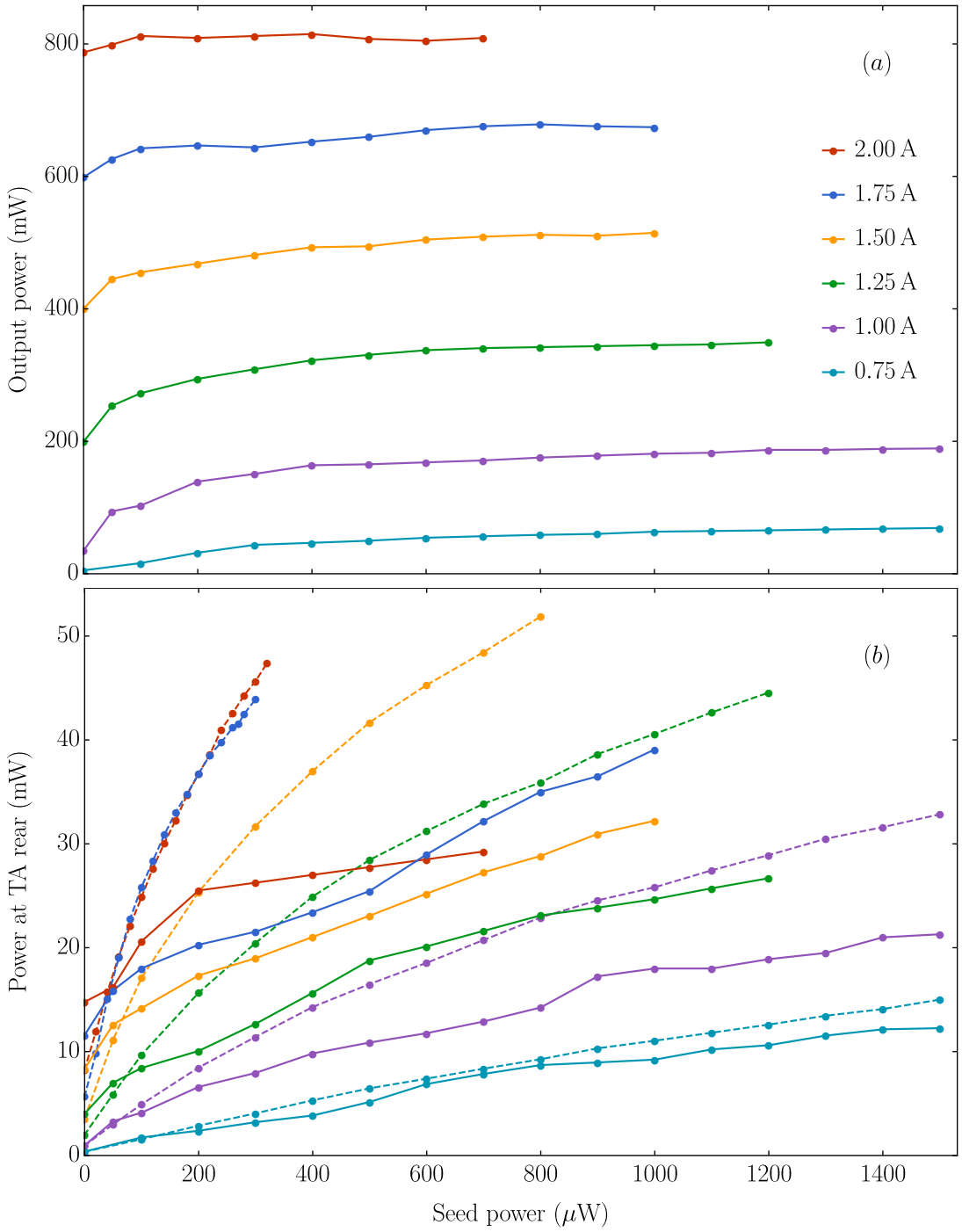


Figure 5.7: Performance characteristics of the double-passed TA for a range of TA currents (the plot colours are the same for both plots). Top (a): the total output power as a function of seed power. Bottom (b): the power at the rear of the TA after a single pass as a function of seed power, for the cases of the light being blocked at the rear (solid) and the light being retroreflected to forward-seed the TA (dashed).

original double-pass TA experiment [190]. Figure 5.7(b) shows how the power at the rear of the TA reduced when the light was retroreflected to forward-seed the TA, because the amplification of the forward-seeding light reduces the population inversion available to the reverse-seeding light. Care must therefore be taken to avoid blocking the retroreflection while the TA is being double-passed, since this would allow the power at the narrow end of the taper to exceed the damage threshold of the TA chip (50 mW in this case).

Note how in Fig. 5.7(a) the output power was substantial even for no seed power. This was because, as with any diode laser, a TA generates spontaneous emission as well as the intended stimulated emission. The high gain of a TA means that the amplified spontaneous emission (ASE) can become significant, and in the double pass configuration can be retroreflected and seed the TA. Inserting seed light quickly dominates the ASE: 70 µW of seed light was required at 1 A, which rose to 120 µW for 1.5 A, since higher currents generate more ASE, requiring a higher seed power to out-compete the retroreflected ASE.[28]

It is also important to note that the small aspect ratio of the output face of a TA results in a highly ellipsoidal beam that is difficult to fibre-couple. Coupling efficiencies of 55 – 60% were achieved using a telescope comprised of rotatable cylindrical lenses, compared to $> 80\%$ for the Ti:sapphire laser. Therefore the usable power is substantially lower than the output powers in Fig. 5.7(a) if the light is transmitted through an optical fibre, which is usually necessary for TAs since their mode structure can change with time.

5.4 Probe Light

The probe light used to characterise the cold-atom source required only a low optical power, so originally some light was picked-off from the high-power MOT beam and passed through AOMs to allow the frequency of the light to be scanned. This was unsatisfactory, because

[28] Preliminary testing of the double-pass configuration used a damaged TA chip with a hole in the output beam. Multiple frequencies were present in the output beam, even for high seed powers, because the damage to the chip (either the front facet or the gain medium itself) prevented the seed light out-competing the ASE throughout the entire gain region. This allowed enough amplification of the ASE (which has no well-defined frequency aside from being constrained by the gain bandwidth of the gain medium) for it to comprise a significant proportion of the output beam power.

the variation of diffraction efficiency and direction with frequency made the probe power noisy. Therefore a separate diode laser system had to be implemented, which also allowed a wider range of detunings. This section outlines the optical setup and frequency stabilisation using an analogue beat-note offset lock. The use of the probe light to detect and measure the flux is described in the following chapter.

5.4.1 Probe Laser

An external-cavity diode laser[29] (ECDL) in the Littrow configuration produced the probe light as shown in Fig. 5.8, with an optical isolator to block back-reflections.[30] An anamorphic prism pair was used to reduce the ellipticity of the beam profile before it was fibre-coupled. A fraction of the light was picked-off by a PBS and used for saturated absorption spectroscopy to monitor the frequency output. The spectroscopy used a quarter-wave plate and plane mirror after the vapour cell to retroreflect the beam back through the cell and onto a photodiode; this arrangement was chosen due to space restrictions, despite the disadvantage that the relative pump and probe beam powers cannot be easily varied.

5.4.2 Beat-Note Offset Lock

Frequency stabilisation of the probe laser near the cooling transition was provided by a beat-note offset lock based on the design of Ritt et al. [194]. A small fraction of the probe light (with frequency f_{probe}) was picked-off and mixed on a photodiode[31] with light from a 'master' diode laser[32] (frequency f_{master}) locked to the ^{87}Rb cooling resonance using MTS. A sufficiently strong beat-note ($f_{\text{beat}} = |f_{\text{probe}} - f_{\text{master}}|$) was obtained for $\geq 300\,\mu\text{W}$ of each

[29] Toptica DL 100

[30] Unlike a Ti:sapphire laser, a diode laser is highly susceptible to damage from back reflections from optical components, generally due to damage to the front facet. This arises because a diode laser cavity is formed by a diffraction grating that reflects typically 15 – 30% of light back towards the laser medium, therefore the output power is comparable to the power in the cavity, and back-reflections are sufficient to impact on the gain medium. In contrast, the cavity in a Ti:sapphire is formed of highly reflecting mirrors with output couplings of $< 1\%$, therefore back-reflected light is negligible compared to the optical power already circulating in the cavity. Hence only the diode laser used for probe light required an isolator.

[31] Thorlabs PDA10A-EC

[32] Toptica DL Pro

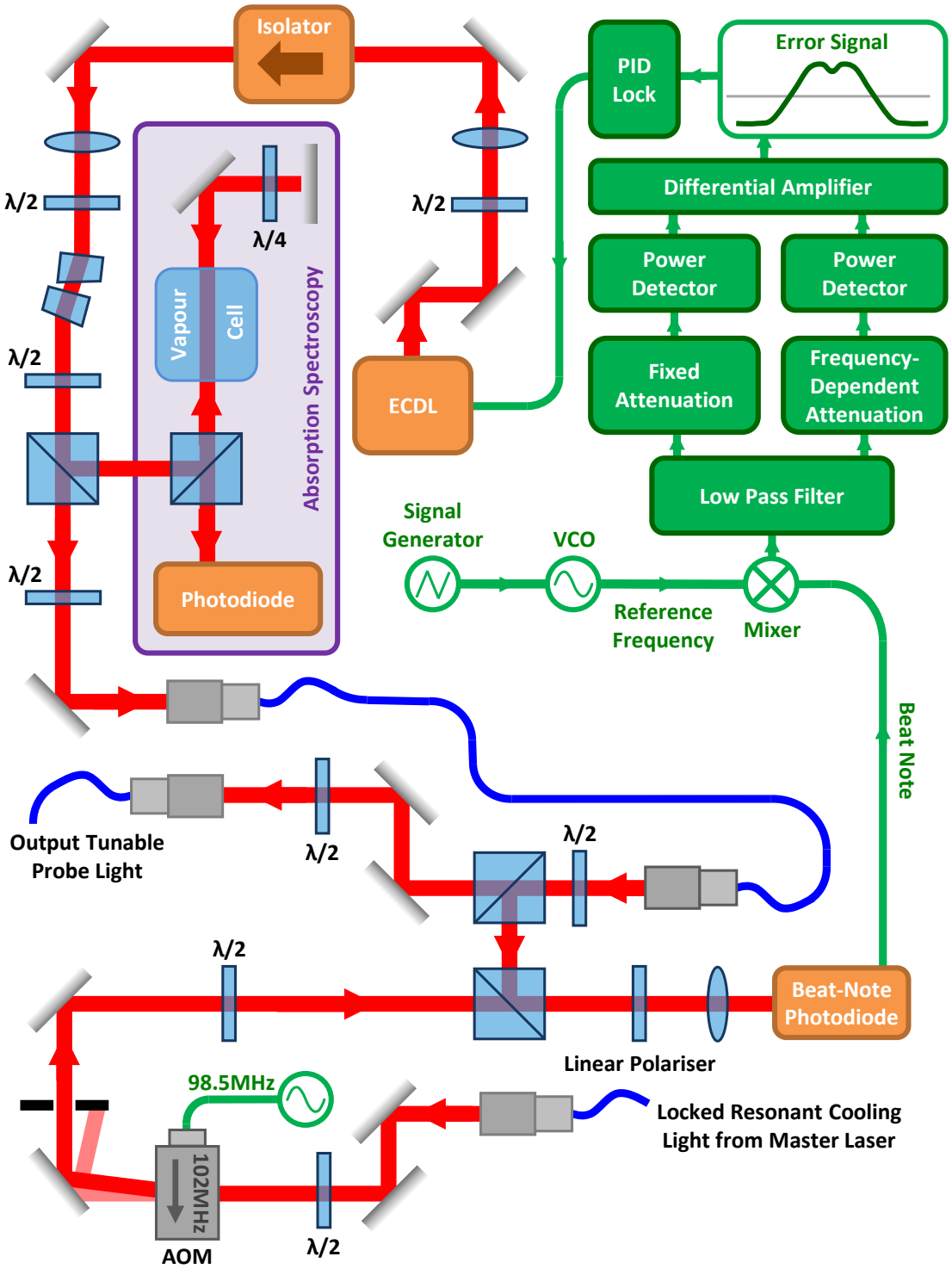


Figure 5.8: The probe laser optics and beat-note offset lock system. All fibres were single-mode polarisation-maintaining fibres, hence the half-wave plates to set the correct polarisation. The half-wave plate before the anamorphic prism pair was to maximise transmission. The light was focused onto the beat-note photodiode since a small-area sensor was required to provide the ∼100 MHz bandwidth required to detect the beat-note.

frequency. The resulting beat-note signal was locked to a reference frequency, produced by a voltage-controlled oscillator (VCO), by analogue circuitry:

1. The beat-note, f_{beat}, and the reference VCO frequency, f_{ref}, were combined by a mixer[33] to produce the sum and difference frequencies, $f_{\text{ref}} + f_{\text{beat}}$ and $|f_{\text{ref}} - f_{\text{beat}}|$

2. A low pass filter[34] removed the sum frequency and retained the difference frequency

3. The difference frequency signal was split into two identical outputs by a power splitter[35]

4. One of the identical outputs was attenuated by a fixed amount[36] while linearly frequency-dependent attenuation was applied to the other[37]

5. Both signals were converted from powers to voltages by power detectors[38] and the voltage difference was used as the input error signal to a PID controller[39] that provided feedback to the probe laser[40]

The resulting error signal (shown in Fig. 5.9) was composed of two peaks symmetrical about f_{master} since the beat-note was identical for the probe light being $f_{\text{probe}} = f_{\text{master}} \pm \Delta f$. Each mirror peak had two zero-crossings at $f_{\text{ref}} - f_{\text{beat}} \simeq \pm 14\,\text{MHz}$ suitable for frequency stabilisation (14 MHz was the frequency at which the frequency-dependent attenuation matched the fixed attenuation, producing identical voltages from the power detectors that cancelled out in the differential amplifier).[41] Varying f_{ref} caused f_{probe} to vary concurrently in order to keep $f_{\text{beat}} = |f_{\text{probe}} - f_{\text{master}}|$ detuned by 14 MHz from f_{ref}, hence allowing f_{probe} to be scanned by ramping the reference VCO frequency f_{ref}. The VCO used to generate f_{ref} had

[33] Mini-Circuits XZ05-1L-S+
[34] Mini-Circuits SLP-100+ – low passed frequencies from DC to 98 MHz.
[35] Mini-Circuits ZA2CS-251-20WS+
[36] Mini-Circuits FW-4+ and FW-10+ in series, to provide 14 dB of fixed attenuation.
[37] Commercial high/low-pass filters were found to generate roll-offs that were too steep to lock the laser, so a simple RC high-pass filter with a cutoff frequency of 17 MHz and an order-of-magnitude smaller roll-off was built.
[38] Mini-Circuits ZX47-50LN+ (the output voltage is inversely proportional to the input power)
[39] Toptica PID 110
[40] The use of a pair of power detectors differs from the error circuit used by Ritt et al. [194], and produces an error signal 20 – 50 times larger with the drawback of a higher components cost.
[41] In addition, below 2 MHz was outside the operating range of the power splitter, which caused a sharp downward spike towards 0 V because the output powers of the splitter dropped towards zero.

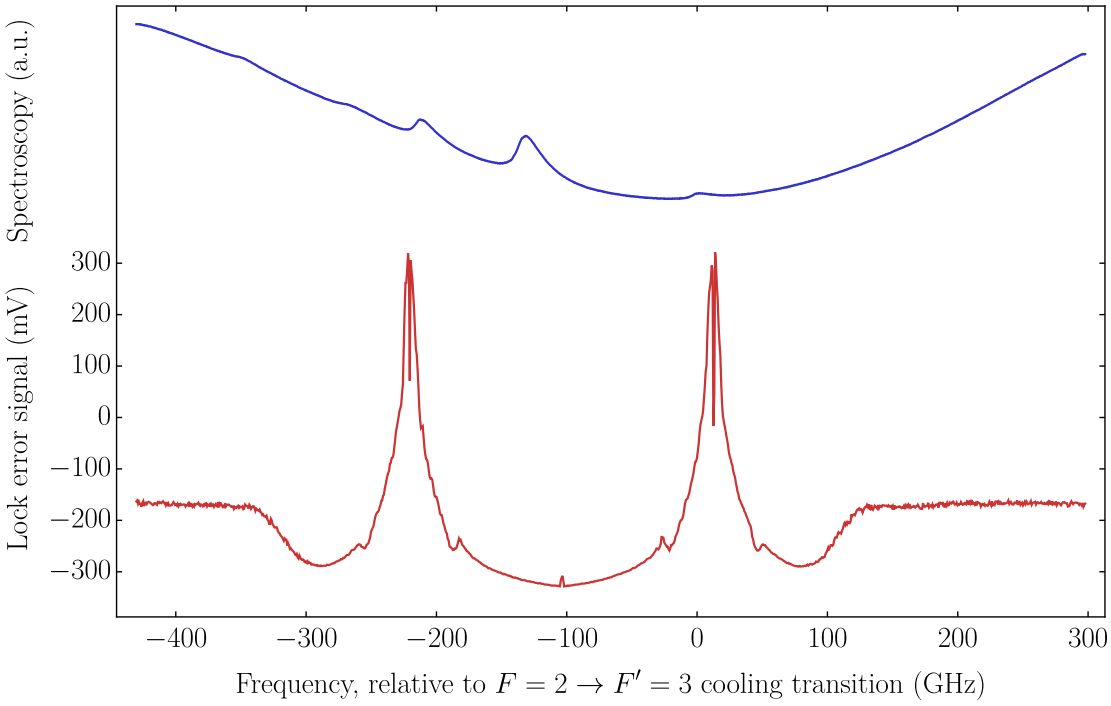


Figure 5.9: The error signal produced by the beat-note offset lock (bottom, red), with the corresponding absorption spectroscopy of the ^{87}Rb cooling transition (top, blue).

a range of 75 – 150 MHz,[42] so f_{master} was red-detuned[43] by 98.5 MHz (from the cooling resonance, to which the master laser was locked) by an AOM[44] to set f_{probe} equal to the cooling resonance when f_{ref} was in the middle of its range. The probe frequency f_{probe} could then be detuned by ±37.5 MHz. The frequency when locked was stable to 0.4 MHz (less than 10% of the linewidth), corresponding to a 2% variation in the absorption signal, which was sufficiently small to pose no issues in the characterisation of the flux. The presence of the mirror peak limited the capture range of the lock to 220 MHz (to avoid locking to the slope of the mirror peak) however this was still sufficient to keep the laser locked for days at a time, and the primary cause of unlocking was the master laser becoming unlocked.

Originally the ECDL was used to provide resonant repumping light for use with the double-pass TA system (of Sec. 5.3). The same beat-note offset lock was suitable, except

[42] Mini-Circuits POS-150+

[43] By choosing f_{master} to be red-detuned meant that increasing f_{ref} caused f_{probe} to increase to maintain $f_{\text{beat}} = f_{\text{probe}} - f_{\text{master}} = 14$ MHz, so f_{ref} and f_{probe} were directly proportional. If instead f_{master} was blue-detuned then $f_{\text{beat}} = f_{\text{master}} - f_{\text{probe}} = 14$ MHz and increasing f_{ref} would have caused f_{probe} to decrease to maintain f_{beat}, and thus f_{ref} and f_{probe} would be inversely proportional, making the frequency calibrations less intuitive.

[44] Crystal Technology 3110-140 (centre frequency 110 MHz)

f_{master} was not shifted by an AOM and the beat-note was detected by a high-speed digital photodiode[45] then digitally divided down[46] to compare to the ∼100 MHz reference frequency.

5.4.3 AOM Optical Arrangements

It may be noted that the AOM used in the beat-note optics had the light passed through collimated, whereas the AOMs used in the MOT light optics for detuning prior to MTS had the light focused through them. The reason for the different approaches is because the diffraction efficiency of an AOM depends on the beam size [196]. For small beam sizes (< 0.5 mm diameter) diffraction efficiency is limited because a smaller part of the acoustic field interacts with the beam. Above about 0.5 mm the diffraction efficiency levels off until the beam size exceeds the active aperture of the crystal. The active aperture is smaller than the crystal itself because the acoustic wave is distorted and weaker near the crystal surfaces. If the beam diameter exceeds the active aperture, the sections of the beam missing the active aperture will undergo reduced diffraction efficiency, which both reduces the overall diffraction efficiency of the beam, and alters the profile of the beam because of the position-dependence of the diffraction efficiency.

For the two cases here of the probe and MOT optics, the particular AOMs used had different optimal beam sizes due to differences in the crystal sizes. Smaller beam sizes have the advantage of faster switching times, which are set by the time required for the acoustic wave to traverse the beam width. However, this was not a concern in this work, and the important parameter was the diffraction efficiency, which was optimised in the two cases by using collimated and focused light respectively.

[45] Vescent D2-160 (9 GHz bandwidth)

[46] More details, as well as an all-digital alternative beat-note offset lock scheme, can be found in [195]. Note also that dividing down the error signal reduces the gradient of the error signal as well as the frequency, so that the use of power detectors to produce a 20 – 50 times larger error signal than the design of Ritt et al. [194] becomes particularly advantageous for a divided down beat-note offset lock.

5.5 Summary

The vacuum and optical systems described above proved effective for operating the prototype pyramid design as a cold-atom source, and for generating the probe light required to measure the flux produced. In particular, the double-pass tapered amplifier system offered a greatly cheaper alternative to the Ti:sapphire system, but with poorer mode quality and fibre coupling, and the beat-note offset lock developed for the probe light provided a stable lock with a very wide capture range. The following chapter details the methods employed to characterise the flux, and the results are presented and interpreted in the subsequent chapter.

6

Flux Characterisation Technique

The key application for cold-atom sources is to load a MOT in a high quality vacuum environment, simultaneously allowing fast loading rates and long lifetimes for the trapped atoms (see Sec. 1.6). As a result, cold-atom sources are commonly characterised by inferring the flux from the loading rate of a MOT [72, 80, 85, 87, 88, 90, 104, 106, 113, 122]. This is a pragmatic approach when the experiment already requires a MOT to be installed, however measuring just the loading rate gives limited information on the divergence and spatial profile, and is dependent on the capture velocity of the particular MOT. The full characterisation of a cold-atom source requires the more detailed method described in this chapter.

In particular, full characterisation requires measurements of the atomic density and velocity distribution to be taken for a single axial position after the source. This chapter compares absorption and fluorescence imaging as the measurement method, before describing the absorption measurement technique implemented (including: the optical apparatus; probe beam size and power; electronics for extracting the absorption signal; optical power stabilisation; and magnetic fields) and the models fitted to the raw data to extract the atomic density and velocity information. The results of this characterisation allow the performance of a source for any particular MOT setup to be predicted.

6.1 Required Measurements

The important characteristics of the flux from a cold-atom source are: the atomic velocity distribution; the beam divergence; and the total flux of atoms. These can be determined by taking and combining two measurements:

1. The spatial variation of the atomic column density, ρ_A

2. The longitudinal velocity distribution of the atoms, $f(v_z)$

The atomic density at a point in the beam is $\rho_V(x, y, z)$, and by measuring the column density $\rho_A(y, z) = \int \rho_V(x, y, z)\,\mathrm{d}x$ for a range of y positions at a given axial position z, the spatial profile of $\rho_A(y, z)$ can be estimated. The width of this profile allows the divergence to be inferred, and the integral over all y yields $\int \rho_A(y, z)\,\mathrm{d}y = \int \rho_V(x, y, z)\,\mathrm{d}x\,\mathrm{d}y = \rho_L(z)$, which is the number of atoms per unit length along the source axis; the linear atomic density. This is constant when assuming no losses as the atomic beam propagates, so $\rho_L(z) = \rho_L$, and enables the total flux to be determined as follows.

If Φ_0 is the total flux of atoms (in atoms/s), then the flux of atoms with longitudinal velocity v_z is $\Phi(v_z) = \Phi_0 f(v_z)$ where $f(v_z)$ is the normalised distribution of longitudinal velocities. The number of atoms per unit length with velocity v_z is then $\Phi(v_z)/v_z$, thus the total number of atoms per unit length, the linear atomic density ρ_L, is

$$\begin{aligned}\rho_L &= \int_{-\infty}^{\infty} \frac{\Phi(v_z)}{v_z}\,\mathrm{d}v_z \\ &= \Phi_0 \int_{-\infty}^{\infty} \frac{f(v_z)}{v_z}\,\mathrm{d}v_z \\ &= \Phi_0 \left\langle \frac{1}{v_z} \right\rangle\end{aligned} \tag{6.1}$$

By determining ρ_L from integrating the transverse atomic density distribution, the total flux Φ_0 is found by dividing by the expectation value of $1/v_z$. In general $\langle 1/v_z \rangle \neq 1/\langle v_z \rangle$,

however, using the Taylor expansion of $\langle 1/v_z \rangle$ about the mean velocity $\langle v_z \rangle$,

$$\left\langle \frac{1}{v_z} \right\rangle = \left\langle \frac{1}{\langle v_z \rangle} - \frac{v_z - \langle v_z \rangle}{v_z^2} + \frac{(v_z - \langle v_z \rangle)^2}{v_z^3} - \cdots \right\rangle \tag{6.2}$$

then if $f(v_z)$ has a narrow distribution around a non-zero mean, all higher order terms are small compared to the first, and $\langle 1/v_z \rangle \simeq 1/\langle v_z \rangle$ is a reasonable approximation. For a Gaussian velocity distribution with standard deviation σ_v, this is satisfied for $\langle v_z \rangle / \sigma_v \gg 1$, which is the case for the velocity distribution from a typical cold-atom source.[1] Therefore the total flux is found by

$$\Phi_0 = \rho_L \langle v_z \rangle \tag{6.3}$$

In this chapter, the methods used to obtain these measurements are described, focusing first on the atomic density profile, and then on the longitudinal velocity distribution.

6.2 Atomic Density Measurement

6.2.1 Absorption vs. Fluorescence Imaging

Observation and measurement of atoms can be done in several ways, which can be grouped into the categories of absorption, fluorescence, and dispersive imaging.[2] Absorption and fluorescence both rely on atoms resonantly scattering light from a probe beam, whereas dispersive imaging uses off-resonant light and depends on the phase shift of the light, rather than the change in intensity. This avoids heating the atoms and is less perturbative, which can be useful to probe dynamics in a less destructive fashion. For measuring the flux of a cold-atom source there is no need to avoid heating of the atoms, and dispersive techniques typically have weaker signals because the atom-photon interaction is weakened by the detuning, so they were not considered. Absorption and fluorescence imaging have advantages

[1] When $\sigma_v \leq \langle v_z \rangle / 5$, which was typical of the measured values, then $1/\langle v_z \rangle$ is within 5% of $\langle 1/v_z \rangle$.

[2] Absorption and fluorescence arise from the absorptive properties of the atoms, determined by the complex component of the refractive index, while dispersive techniques derive from the real component of the refractive index.

and drawbacks that make them suitable in different circumstances, and for the specific application of measuring the flux produced by the prototype pyramid source, depth of field limitations dictated the method of imaging to be absorption, as explained in the following.

Absorption Imaging

Absorption imaging measures the atomic density by attenuation of a probe beam caused by stimulated absorption and rescattering. The Beer-Lambert law states that a probe beam of initial intensity $I_0(x, y)$, propagating along the z direction through a region of density $\rho_V(x, y, z)$, has an intensity given by

$$I(x, y) = I_0(x, y)\, e^{-\rho_A(x,y)\,\sigma(x,y)} \tag{6.4}$$

where $\sigma(x, y)$ is the *scattering cross-section*, $\rho_A(x, y)$ is the column density of atoms given by $\int_0^Z \rho_V(x, y, z)\,\mathrm{d}z$, and Z is the distance the light propagates through the medium. The product $\rho_A\sigma$ is defined as the *optical depth*. The scattering cross-section is defined as the power radiated by an atom as a fraction of the incident intensity I. The radiated power is the product of the photon energy and the scattering rate from Eq. 1.24, which yields

$$\sigma = \frac{\hbar\omega R_{\text{scatter}}}{I} = \frac{\sigma_0}{1 + 4(\delta/\Gamma)^2 + I/I_{\text{sat}}} \tag{6.5}$$

where $\sigma_0 = \hbar\omega\Gamma/2I_{\text{sat}}$ is the *peak cross-section*.[3]

The signal measured in absorption imaging is the absorption ratio

$$\frac{I_0(x, y) - I(x, y)}{I_0(x, y)} = 1 - e^{-\rho_A(x,y)\,\sigma(x,y)} \tag{6.6}$$

which can then be used to determine the column density ρ_A. The signal is measured from the normalised response of a photodetector, and is maximised by having a large scattering cross-section σ and column density ρ_A. The former is maximised by operating on resonance ($\delta = 0$)

[3] σ_0 is the maximum value of σ, and occurs as $\delta, I \to 0$.

with low intensity ($I \lesssim I_{\text{sat}}$). Maximising the latter for the case of a diverging atomic flux would require imaging close to the exit aperture of the source, however the inherited vacuum system did not have optical access before the glass cell; probing was limited to at least 30 cm downstream from the pyramid aperture.[4] For a typical flux of 10^9 atoms/s diverging with a full-angle of 30 mrad and an average velocity of 15 m/s (using typical values from Table 2.1), the density at the measurement position is $\sim 10^6$ atoms/cm^3 and the absorption signal is around 0.1%.[5] This limited the size of the absorption signal, and to accurately measure the column density (in order to determine the transverse profile of the beam) a sensitivity of at least one part in 10^4 was required.

Fluorescence Imaging

In fluorescence imaging the light scattered by the atoms is detected, and is in that sense the opposite to absorption imaging in which the *absence* of those scattered photons is detected. The advantage of fluorescence imaging is that it has less noise than absorption imaging, because it avoids noise from power fluctuations of the laser beam (shot noise). However, this advantage is offset by a reduced signal, since the fluorescence is emitted in all directions and only a small fraction is able to be collected by the imaging lens. The signal strength can be increased by detecting atoms over a longer time period, provided the sample does not change during the exposure, which makes fluorescence imaging suitable for many weak signal applications, with limitations imposed by dark currents in the detector.

[4] The divergence increases the beam radius linearly with distance, Z, thus the cross-sectional area increases as $\propto Z^2$ and the atomic density decreases at the same rate. However the column density is the atomic density integrated over the beam diameter, which is $\propto Z$, so the column density (and hence the optical depth) decreases linearly with Z.

[5] A 30 mrad divergence produces a 4.5 mm radius at the 30 cm measurement position, thus the product of the cross-sectional area and the velocity is 0.001 m^3, which is the volume swept out by the atoms per second. Dividing the flux Φ by this gives the atomic density and the signal strength (assuming circularly polarised light, for which $\sigma_0 = 2.9 \times 10^{-9}$ cm^2, and $I = I_{\text{sat}}/10$) is $\approx 2 \times 10^{-12}\Phi$.

Depth of Field

Whether using absorption or fluorescence imaging, the ideal approach to acquire spatially-resolved information of the atomic density is to illuminate and image the entire region of interest. This generates the atomic density profile in a single shot, but requires the imaging optical system to have a depth of field greater than the width of the sample being imaged. In cold-atom experiments this is rarely an issue, since the objects of interest are small and dense,[6] allowing imaging with high resolution and shallow depths of field. In the case of this project however, the flux diverged to a diameter of about 2 cm at the measurement position (30 cm from the pyramid aperture), producing unusual imaging requirements.

The depth of field of an imaging system with numerical aperture NA is approximately given by [197]

$$\mathrm{DOF} = \frac{\lambda\sqrt{n_0^2 - (\mathrm{NA})^2}}{(\mathrm{NA})^2} \tag{6.7}$$

where λ is the wavelength of the probe light, and n_0 is the refractive index of the medium the light travels in. For a single lens of focal length f and an aperture of diameter D, the NA is

$$\mathrm{NA} = n_0 \frac{D}{2f} \tag{6.8}$$

To achieve a depth of field of 2 cm in air ($n_0 \simeq 1$) at $\lambda = 780$ nm means NA ~ 0.006, which requires a long focal length and/or a small aperture. For a standard 25 mm diameter lens, this corresponds to a focal length of 2 m. Placing the lens 2 m from the flux, in order for the focus to be at the atoms, would result in only 0.001% of scattered light being collected in the case of fluorescence imaging, rendering it impractical for measuring the atomic flux, and similarly for absorption imaging.[7]

[6] A typical MOT is a few millimetres wide with a density of 10^{10} atoms/cm^3, and a BEC is of the order of 10 µm with a density of 10^{14} atoms/cm^3, compared to the flux in this study which is of the order of 10 mm and 10^6 atoms/cm^3.

[7] In a single-shot absorption imaging setup, probe light would illuminate the entire width of the atomic flux, and the shadow cast by the atoms would be imaged by a (often two-lens) optical system. The resolution and sensitivity increase with the fraction of the shadow that is collected by the objective lens, but to have the entire width of the atomic flux in focus would require a small NA that would limit the signal strength. In addition, in order to detect the small absorption signal, the detector would need to be sensitive to one part in 10^5, corresponding to a digital sensor with 16 to 18 bit resolution, which is on the limit of commercially

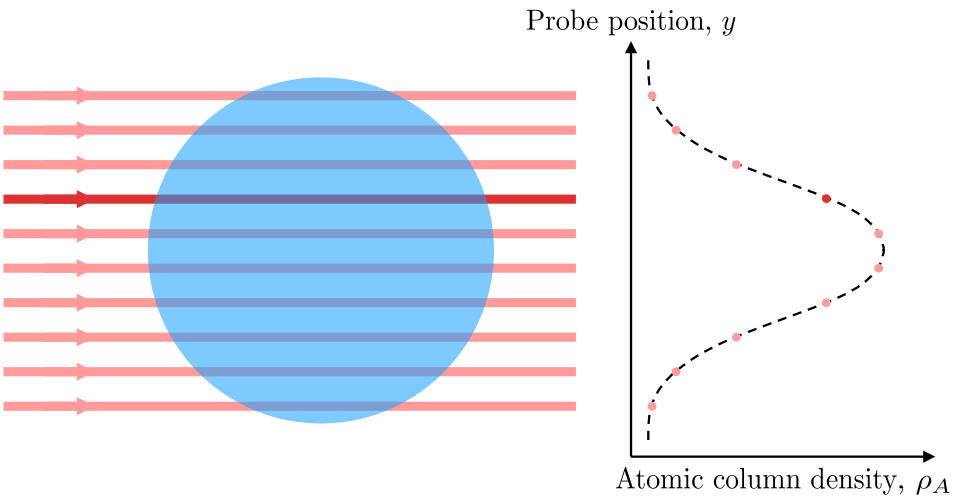


Figure 6.1: By passing a narrow probe beam (dark red) through the atomic flux (blue), transverse to the direction of the flux (in/out of the plane of the figure), the measured absorption of the probe light gives the number of atoms in the illuminated region, and hence the column density parallel to the probe beam for that probe position can be calculated (using the known size of the probe beam). By repeating this measurement for different heights of the probe beam (light red), the profile of the atomic column density can be fitted (black dashed line). The apparatus used to perform these measurements is depicted in Fig. 6.3, and example data is shown in Fig. 6.6.

Spatially-Resolved Measurements of the Density

Because the depth of field requirement prevented spatially-resolved imaging of the atomic density in a single shot, the spatial resolution was instead acquired by taking data for multiple positions of a narrow probe beam that interacted with only a small portion of the atomic flux. When measuring the total absorption experienced by the probe beam passing through the flux, there are no depth of field concerns and multiple measurements at different positions allow the profile of the atomic column density to be constructed, as shown in Fig. 6.1.

For fluorescence measurements on the other hand, this approach (scanning a probe beam through the flux and detecting the fluorescence) still has depth of field issues. Scanning the probe beam would change the distance from the detector, necessitating a large depth of field to keep the atoms in focus. Detecting directly without any optics would have no depth of field issues, but the solid angle over which photons could be detected would be limited by the size of the sensor. A solution could have been to adjust the height of the fluorescence

available devices.

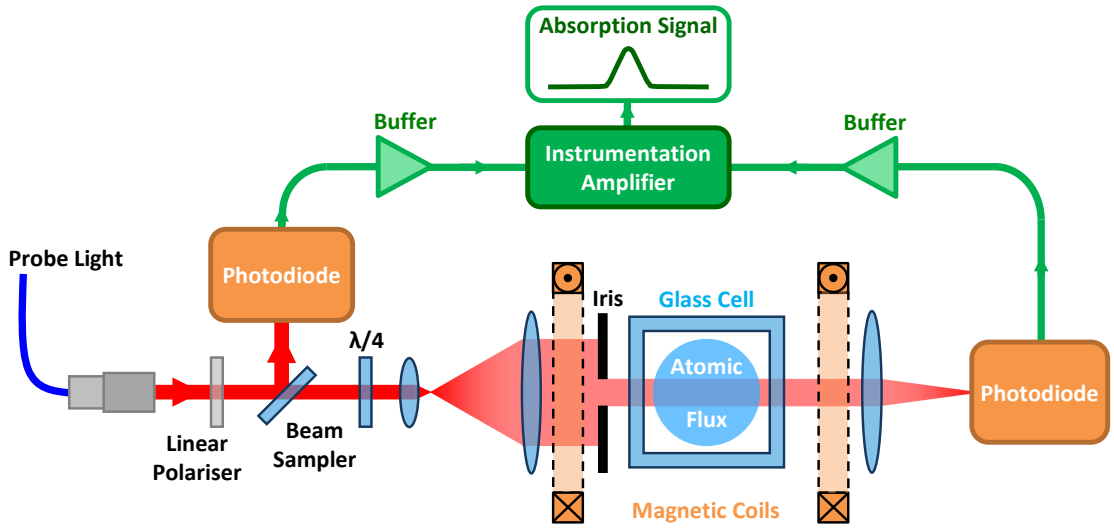


Figure 6.2: Absorption spectroscopy scheme for measuring the atomic density of the flux of cold atoms. A probe beam was expanded and passed through a micrometer-adjustable iris, allowing spatial resolution of the atomic density to be achieved by taking measurements for various iris positions.

detection system, however this would require a complicated optical arrangement, introduce mechanical instability, and force the optics further from the atoms to allow room for the motion, reducing the solid angle subtended.

Since depth of field issues prevented fluorescence measurements being practical, absorption measurements were used to determine the atomic density profile of the flux, with the apparatus described in the following section.

6.2.2 Absorption Measurement Apparatus

The initial approach to taking the absorption measurements was to scan an iris through an expanded beam to vary the position of the resultant probe beam, while the attenuated beam (after passing through the flux) was focused onto a photodiode independently of the position of the iris (see Fig. 6.2). This was successfully used to observe and measure the flux, however scanning the iris changed the probe intensity due to the non-uniformity of the Gaussian probe beam, complicating the measurement process.

The adjustable iris was replaced by an adjustable periscope, without any beam expansion,

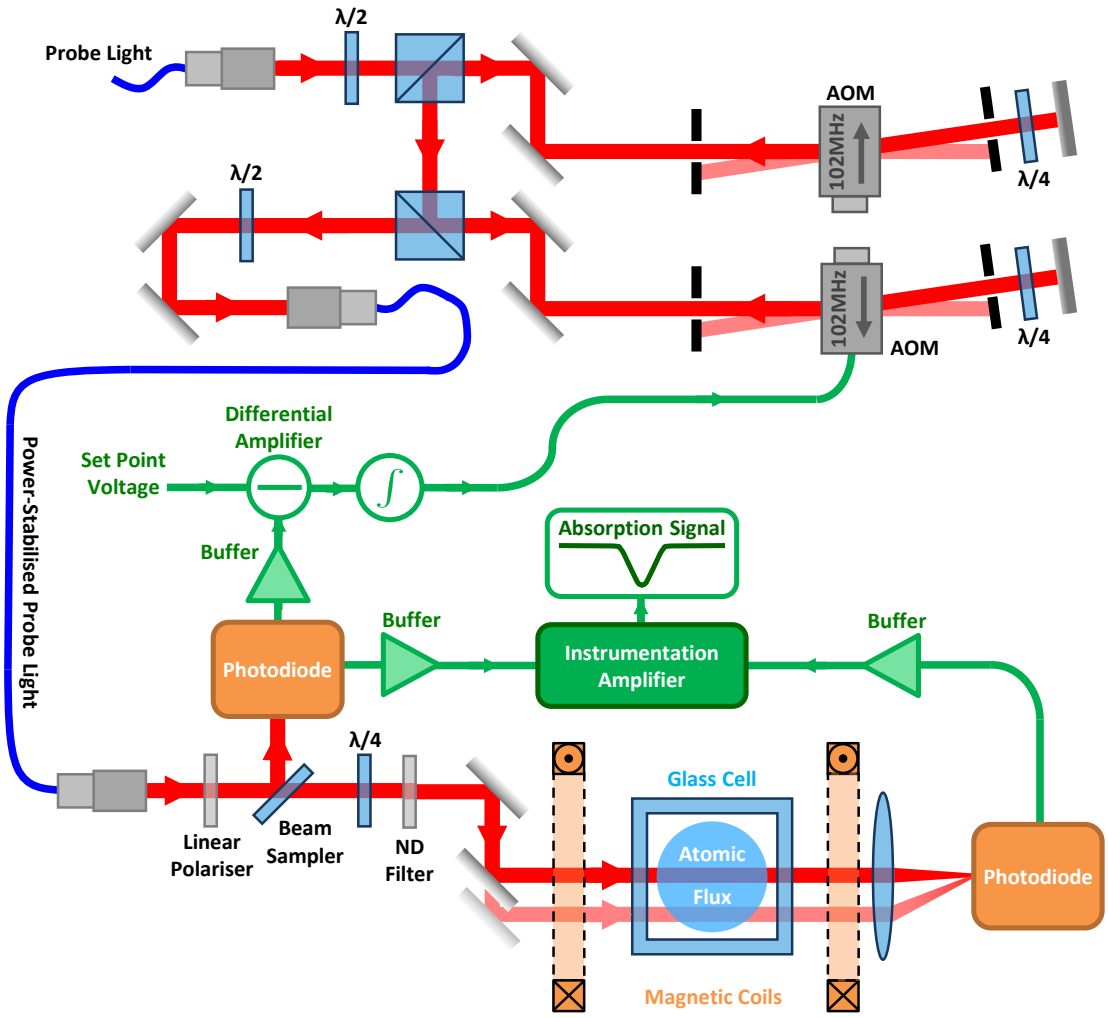


Figure 6.3: The absorption spectroscopy scheme used for measuring the atomic density of the flux of cold atoms. A collimated probe beam was passed via an adjustable periscope through the glass cell and focused onto a photodiode. By varying the periscope the atomic density at a range of heights could be taken, from which the density profile was inferred. The optical power of the probe light was attenuated by a neutral density filter to I_{sat} and stabilised by passing it through a pair of AOMs to which feedback was applied.

to avoid this problem. The final measurement system is shown in Fig. 6.3. Probe light was passed collimated through the glass cell and focused onto a photodiode, with the vertical probe position varied by an adjustable periscope formed of a fixed upper mirror and a micrometer-adjustable lower mirror. A portion of light was picked-off onto a photodiode before the glass cell to produce a background reference signal, and which was also used to provide feedback to stabilise the probe power. A uniform magnetic field applied across the glass cell maximised the absorption signal. This apparatus is detailed below.

Probe Beam

The probe beam was collimated and passed through the atomic flux to measure the atomic column density at a particular vertical position. A laser beam does not remain collimated however; all beams undergo diffraction. A Gaussian beam is collimated at its focus, at which the beam waist (the $1/e^2$ radius) is w_0, and the beam expands to $w = \sqrt{2}w_0$ after a distance equal to the Rayleigh range $z_R = \pi w_0^2/\lambda$. The path length of the probe light through the imaging setup was approximately 1 m, limiting the minimum beam waist to $\gtrsim 0.5$ mm, for which $z_R = 1.00$ m.

The probe beam size is also important in determining whether repumping light is required for absorption measurements. For a larger beam diameter, atoms spend longer interacting with the probe light, and a greater proportion of them are optically pumped into the dark hyperfine ground state. Atoms in the dark state no longer absorb the probe light, causing an underestimate of the density compared to the expected signal for a closed transition. The branching ratio to the dark state is ∼1:4,000 for resonant light with $I = I_{\text{sat}}$ (from Sec. 1.5.1), and an atom travelling with speed v a distance L through resonant light can undergo a maximum of $N_{\text{max}} = R_{\text{scatter}}L/v$ scattering events. Each scattering event has a probability $P_{\text{loss}} \approx 2.5 \times 10^{-4}$ of pumping the atom to the dark state, so the likelihood of the atom not being in the dark state, and instead still being in the cooling cycle, after n scattering events is $(1 - P_{\text{loss}})^n$. Summing over N_{max} scattering events gives the absorption, relative to the absorption if there were no loss, as

$$A_{\text{rel}} = \sum_{n=1}^{N_{\text{max}}} (1 - P_{\text{loss}})^n \tag{6.9}$$

This can then be evaluated using the formula for a finite sum of a geometric series.[8] For a circular probe beam incident orthogonal to a flux of atoms, the length L of the region over which atoms interact with the light varies for atomic trajectories that transit the probe beam at different heights y (with respect to the centreline of the probe beam.) For a beam

[8] $\sum_{k=m}^{n} ar^k = \frac{a(r^m - r^{n+1})}{1-r}$

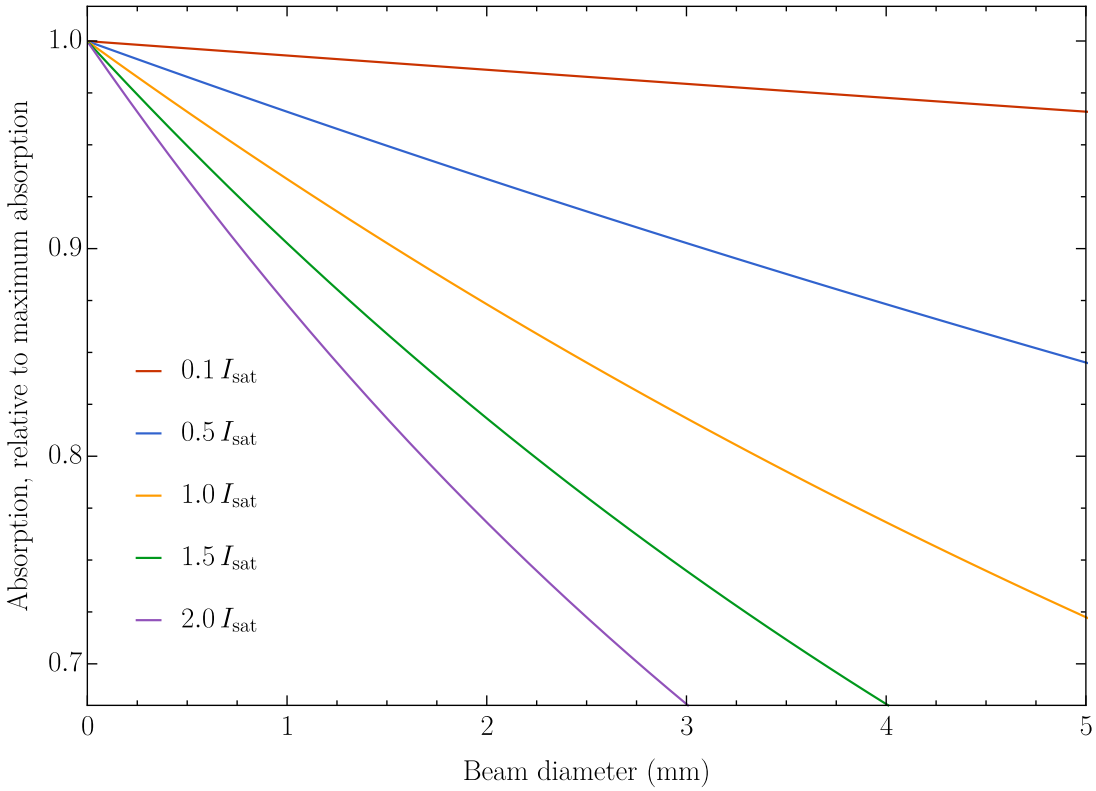


Figure 6.4: The reduced absorption of atoms in the probe beam due to pumping to the dark state, relative to the absorption without dark state loss, plotted as a function of beam diameter for different probe beam intensities. Atoms are assumed to be travelling with $v = 15\,\mathrm{m/s}$. The lines shown correspond to Eq. 6.9 after correcting to account for the fact that the diameter of the probe beam varying as a function of height, as described in the text.

of radius r, $L = 2\sqrt{r^2 - y^2}$ and the total absorption is found by $\int_{-r}^{+r} A_{\mathrm{rel}}\,\mathrm{d}y$. The reduction in absorption due to dark state loss is shown in Fig. 6.4 as a function of beam diameter $d = 2r$. The reduction is minimised for a small beam diameter and low intensity. However, the power in the probe beam should be sufficient to nearly saturate the photodiode in order to minimise electronic noise.

As a balance of all these factors, the probe beam was chosen to have a power of 30 µW and a $1/e^2$ diameter of 1.5 mm, corresponding to an average intensity of $1.0\,I_{\mathrm{sat}}$. The reduction in the absorption signal from dark state loss was less than 10%, which justified not requiring repumping light in the probe beam.

Photodiode Subtraction & Circuitry

The signal photodiode and background photodiode were the same battery-powered model[9] to avoid ground loop noise from mains supplies, with matching load resistances to provide identical frequency responses. Both signals were buffered with variable gain and differentially amplified to remove the majority of DC background from the absorption signal – the DC background varied with probe height by up to 20% due to changes in the transmission of the glass cell, which could not be calibrated for by subtracting the background signal. The amplification and subtraction were performed using instrumentation amplifiers[10] which have better common-mode rejection and smaller tolerances than standard op-amps. The final signal was recorded in the absence of artificial light on a digital oscilloscope using an 8 kHz digital low-pass filter and averaging over between 16 and 64 traces to further reduce noise – without these additional steps the signal was not above the noise floor. The sensitivity of the final signal was 210 mV/µW, compared to a noise floor of 0.2 mV. The dominant noise had a frequency of 50 Hz, and a 50 Hz component was therefore included in the models fitted to the data (as described below) in order to account for this noise.

Power Stabilisation

The typical absorption signals of one part in 10^4 corresponded to just a few nanowatts, therefore drifts in the probe power posed a major problem. Relying just on passive stability using polarisation-maintaining fibres gave power drifts that moved the signal out of the measurement range of the digital scope over tens of seconds, which prevented automatic data acquisition over long time scales. To avoid this issue, the power was stabilised by passing the probe light through AOMs and adjusting the amplitude of the driving frequency using feedback derived from the background signal. Figure 6.3 shows how the probe light (coming from the optics described in Sec. 5.4 and Fig. 5.8) was double-passed through two

[9] Thorlabs DET36A-M
[10] Texas Instruments INA129P

AOMs[11] (blue-detuned by the first then red-detuned an opposite amount by the second, so there was no overall frequency change) then fibre-coupled to the absorption measurement optics.

The feedback signal controlling the attenuation was produced by the circuit shown in Fig. 6.3. The signal from the background photodiode was buffered to avoid affecting the background signal at the absorption signal processing circuit, then differentially amplified relative to a variable set point voltage that determined the stabilised probe power. The resultant error signal was integrated and used as the tuning voltage for the voltage variable attenuator of the second AOM. The feedback system reduced 1 – 100 Hz noise below observable levels, and gave a ∼20-fold reduction of 1 kHz noise.[12] The power was measured to be stable to ±0.16% over a three hour period[13] – although the feedback system suppressed DC noise, drifts in the DC output can occur due to effects such as drifts in the set voltage due to thermal effects.

It was important that the probe light incident on the beam sampler, which was used to pick-off light for the background photodiode, had a well-defined polarisation, set by a linear polariser. In general, the reflectivity differs for s-polarised and p-polarised light, therefore a polarisation drift of the light incident on the beam sampler results in a change to the ratio of reflected and transmitted light. This would convert polarisation drifts into drifts in the transmitted power.

Magnetic fields

From Eq. 1.20, the saturation intensity depends on the optical polarisation and orientation of the atomic moment, as does the scattering cross-section according to Eq. 6.5. The signal

[11] Both AOMs were IntraAction ATM-2901A2, operating at 290.0 MHz. The driving signals for both were generated by ZX95-400-S+ VCOs and attenuated by ZX73-2500-S+ voltage variable attenuators, then amplified by ZHL-1-2W amplifiers (all components from Mini-Circuits).

[12] The integrating time constant was $RC = 560\,\text{ns}$, using $R = 560\,\Omega$ and $C = 1\,\text{nF}$, and the frequency-dependent attenuation was determined by applying noise using the first AOM while observing the background photodiode signal.

[13] The average power during the three hour period was 29.96 µW with a standard deviation of 49 nW, where the sampling rate was 0.5 Hz.

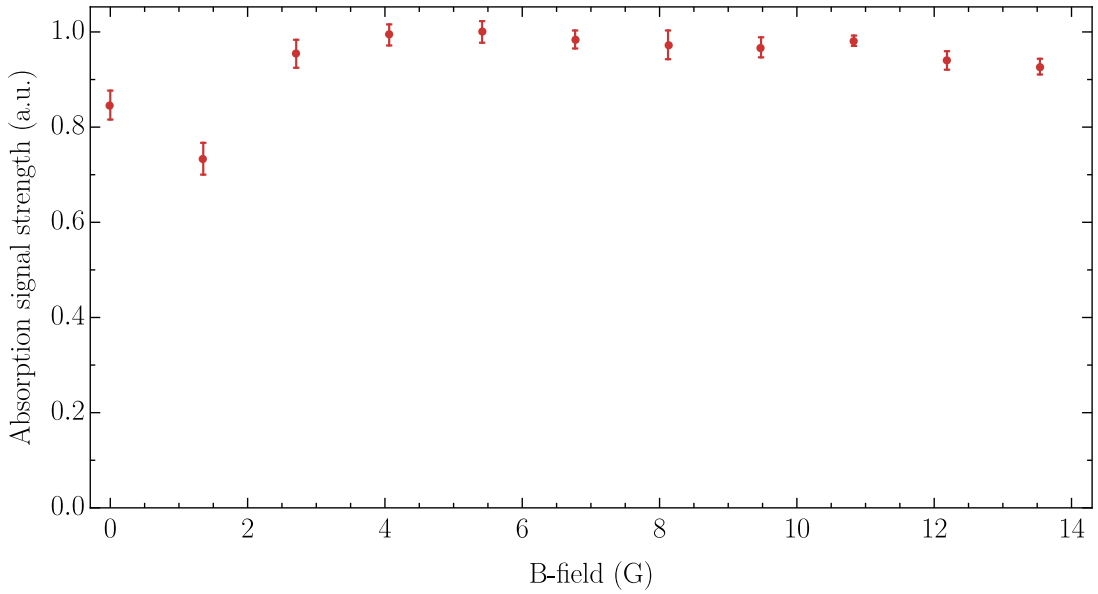


Figure 6.5: The absorption signal measured for various magnetic fields. The B-field was applied parallel to the direction of the circularly-polarised probe beam.

strength was therefore optimised by using circularly-polarised probe light with a weak uniform magnetic field applied to orient the atoms for maximal absorption. A pair of 18×18 cm square coils, with 35 turns each and separated by 12.5 cm, produced the uniform magnetic field and the effect on the absorption signal is shown in Fig. 6.5. Only a weak magnetic field is required to align the atoms, and increasing the field provides no benefit.[14] It would be expected that at $B = 0$ the atoms have no preferred orientation and the absorption would be lowest, and the reason this is not the case is believed to be residual magnetic fields from the nearby ion pump magnets. Despite this anomalous result, a clear range of fields with a flat response was clearly identified, and a field of 5.4 G was used for all absorption measurements of the atomic density.

6.2.3 Atomic Density Absorption Signal Fitting

The lineshape of the absorption signal is a Voigt lineshape; a convolution of the Lorentzian lineshape due to the natural linewidth of the transition, with the Gaussian lineshape arising

[14] Not shown in the figure is that increasing the field shifts the centre frequency because of the Zeeman shift.

from the inhomogeneous Doppler broadening due to the transverse velocity spread of the atoms. In practice however, fitting a simple Lorentzian was found to be sufficient to accurately extract the height of the absorption signal; the transverse velocities were sufficiently low that the natural lineshape dominated the contribution from the Doppler broadening.[15]

The absorption signals extracted from the data at each probe height were converted to column densities using Eq. 6.6, and the resulting data fitted to find an expression for the transverse atomic density profile, from which the width was used to calculate the divergence, and the integral over all probe heights gave the linear atomic density along the axis. The velocity distribution arises from the random walk in velocity space that the atoms undergo due to recoil from spontaneous emission of photons as the atoms are accelerated through the exit channel. Therefore the transverse atomic density is expected to have a Gaussian distribution by the central limit theorem.[16] Assuming the transverse atomic density is radially symmetric, the atomic density in Cartesian coordinates is the product of two normal distributions in the x and y directions, both with the same standard deviation $\sigma_\perp = \sigma_\perp(z)$ that varies with axial position z, multiplied by the total linear density ρ_L, which is independent of longitudinal position:

$$\rho_V(x,y,z) = \rho_L \cdot \frac{e^{-(x-x_0)^2/2\sigma_\perp^2}}{\sqrt{2\pi}\sigma_\perp} \cdot \frac{e^{-(y-y_0)^2/2\sigma_\perp^2}}{\sqrt{2\pi}\sigma_\perp} \tag{6.10}$$

Absorption imaging of the atomic density integrates the atomic density along the x direction, and measurements were taken at a range of y positions to obtain the spatial dependence of the atomic density at the measurement z position. However, the glass cell has a finite width and so cuts out a fraction of the flux if the flux has a width greater than that of the glass cell. Therefore, for a glass cell of width W along the x direction, the atomic density imaged is that integrated from $x = -W/2$ to $x = +W/2$. Assuming the flux is positioned centrally

[15] For a transverse velocity spread characterised by the Doppler limit T_D, the width of the Doppler lineshape is $\Delta\omega_\mathrm{D} = 2\omega_0\sqrt{2k_BT\ln 2/Mc^2} \approx \Gamma/10$.

[16] One formulation of the central limit theorem is: for a large sum of independent random variables, each with finite mean and standard deviation, the value of the sum will tend to be normally distributed, regardless of the distribution function of the random variables [198].

in the glass cell, then $x_0 = 0$ and the column density available for imaging is

$$\rho_V(y,z) = \rho_L \cdot \int_{-W/2}^{+W/2} \frac{e^{-x^2/2\sigma_\perp^2}}{\sqrt{2\pi}\sigma_\perp}\,\mathrm{d}x \cdot \frac{e^{-(y-y_0)^2/2\sigma_\perp^2}}{\sqrt{2\pi}\sigma_\perp} \tag{6.11}$$

By the substitution $\eta = x/2\sigma_\perp$, this integral of a Gaussian, with zero mean, becomes

$$\begin{aligned}\rho_V(y,z) &= \rho_L \cdot \int_{-\frac{W}{2\sqrt{2}\sigma_\perp}}^{+\frac{W}{2\sqrt{2}\sigma_\perp}} \frac{e^{-\eta^2}}{\sqrt{\pi}}\,\mathrm{d}\eta \cdot \frac{e^{-(y-y_0)^2/2\sigma_\perp^2}}{\sqrt{2\pi}\sigma_\perp} \\ &= \rho_L \cdot 2\int_0^{+\frac{W}{2\sqrt{2}\sigma_\perp}} \frac{e^{-\eta^2}}{\sqrt{\pi}}\,\mathrm{d}\eta \cdot \frac{e^{-(y-y_0)^2/2\sigma_\perp^2}}{\sqrt{2\pi}\sigma_\perp} \\ &= \rho_L \,\mathrm{erf}\left(\frac{W}{2\sqrt{2}\sigma_\perp}\right) \frac{e^{-(y-y_0)^2/2\sigma_\perp^2}}{\sqrt{2\pi}\sigma_\perp}\end{aligned} \tag{6.12}$$

Thus the detected column density was reduced from the total column density of the flux by this factor due to the glass cell clipping the flux. The linear atomic density was therefore found by fitting a scaled Gaussian distribution to the measured transverse profile of column densities, with the scaling factor given by

$$\rho_L \,\mathrm{erf}\left(\frac{W}{2\sqrt{2}\,\sigma_\perp}\right) \tag{6.13}$$

A typical example of the atomic density profile is shown in Fig. 6.6. At each probe height, six absorption signals were recorded and fitted to using a Lorentzian function, which also included a DC offset and a 50 Hz component to account for the dominant source of noise. The fits provided a range of values for the column density, the mean and standard error of which were plotted as in Fig. 6.6 to show the density profile. The expression of Eq. 6.12 was fitted to the density profile data, from which the divergence of the beam and the linear atomic density at the measurement position were found. The standard errors associated with the fitted column densities tended to be smaller than statistically expected; the reduced χ^2 statistic was often significantly greater than one, and the uncertainty in the fit parameters was underestimated as a result. Since a Gaussian distribution was a justified assumption as described above, and was generally observed to provide a good estimate to the shape of the density profiles, it was assumed that a Gaussian was an appropriate function to use and the

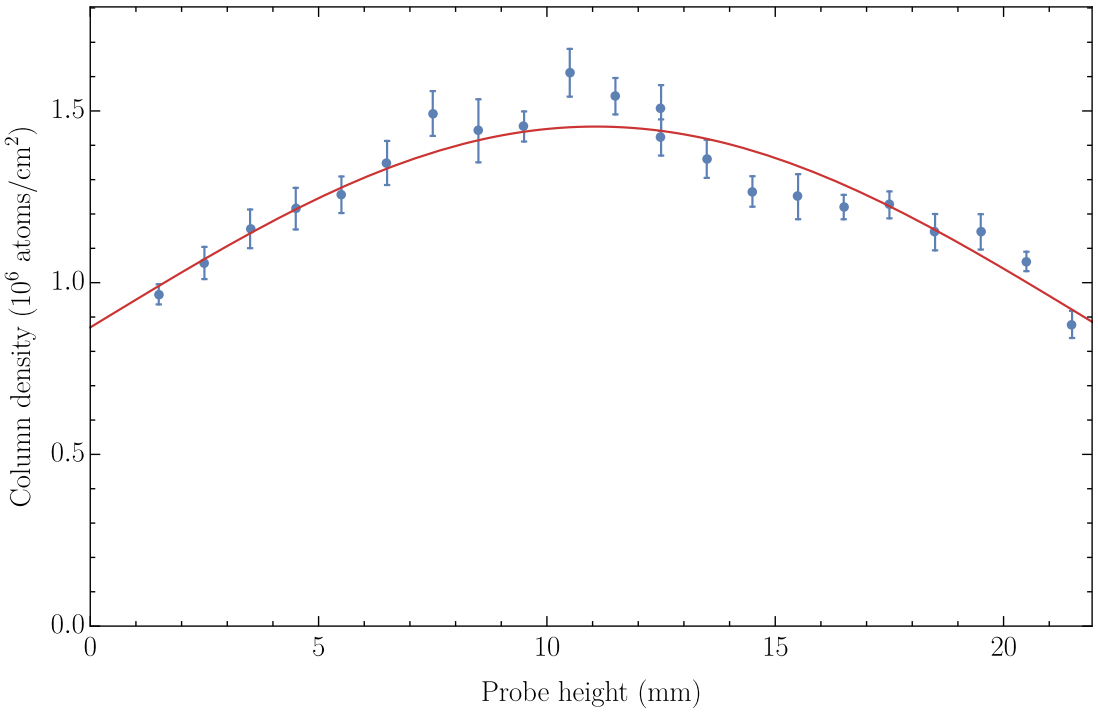


Figure 6.6: An example of a typical atomic column density profile, and the fit (red) of Eq. 6.12 to it. For each probe height, six absorption signals were recorded and fitted with a Lorentzian lineshape to estimate the column density, then the mean and standard error of those results produced the density profile shown here.

errors were scaled using the reduced χ^2 parameter [198], the effect of which was to assume and account for a systematic uncertainty common to all data points. This adjustment of the errors does not change the fitted parameters, but did alter the associated errors to better reflect the accuracy of the fits.

6.3 Longitudinal Velocity Measurement

The longitudinal velocity distribution of the atomic flux could be measured by observing the Doppler shift of the centre frequency of the absorption (or fluorescence) signal due to the longitudinal velocity, which requires changing the setup so that the probe beam is not orthogonal to this direction of motion [84, 95, 102, 103]. However, the combination of the probe board length and the layout of the vacuum system prevented the beam being angled

by more than ±15° from perpendicular to the flux.[17] Some initial data was taken but found to be too noisy to extract an accurate velocity measurement.

Instead, the longitudinal velocity profile was measured using a transit time approach: the MOT was abruptly turned off by switching off the EOM producing the repumping light, while the on-resonance absorption signal of the flux was observed. This allowed the longitudinal velocity distribution to be determined, because atoms in each velocity class took a different amount of time to propagate to the measurement region, and laser-cooling of all velocity classes was ceased at once. The velocity distribution of the atoms was therefore converted into a time-varying absorption signal.

The evolution of the time-vary signal is derived by considering the axial linear atomic density of atoms at position z with longitudinal velocity v_z and at time t, $\rho_L(z, v_z, t)$. The density of atoms with v_z at position $z, t = 0$ propagates a distance $v_z t$ in time t such that

$$\rho_L(z, v_z, 0) = \rho_L(z + v_z t, v_z, t) \tag{6.14}$$

If at $t = 0$ the flux is turned off at $z = 0$, then the density of laser-cooled atoms at that time is

$$\rho_L(z, v_z, 0) = f(v_z)\, \Psi(z) \tag{6.15}$$

where $f(v_z)$ is the probability distribution of velocities, and $\Psi(z)$ is the spatial distribution at $t = 0$ given by a step function centred at $z = 0$, as shown in Fig. 6.7: for $t < 0$ the source has always been on, so there is a constant stream of atoms at $z > 0$; for $t \geq 0$ the source is off and no more atoms are produced. The longitudinal velocities in the flux are produced by repeated photon scattering events, and by the central limit theorem the velocity distribution can be expected to be Gaussian [71, 72, 89, 91, 98, 102], with mean $\langle v \rangle$ and standard deviation σ_v.

[17] 15° corresponds to a frequency shift of 1.1 natural linewidths.

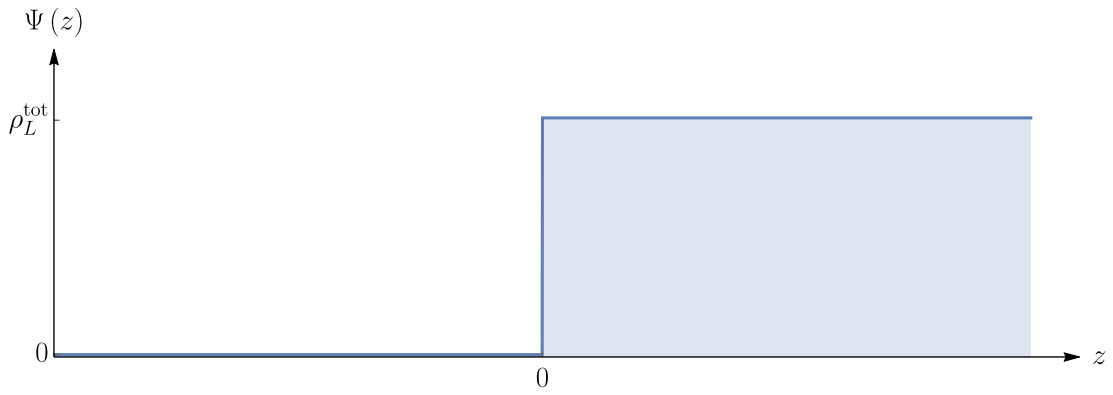


Figure 6.7: The linear atomic density at the point $t = 0$ when the source, assumed to be at $z = 0$, is turned off (this is in a simple 1D picture of the source).

The linear density of all atoms at position $z = z_0$ is given by

$$\begin{aligned}\rho_L(t) &= \int_{-\infty}^{\infty} \rho_L(z_0, v_z, t)\,\mathrm{d}v_z \\ &= \int_{-\infty}^{\infty} \rho_L(z_0 - v_z t, v_z, 0)\,\mathrm{d}v_z \\ &= \int_{-\infty}^{\infty} f(v_z)\,\Psi(z_0 - v_z t)\,\mathrm{d}v_z\end{aligned} \tag{6.16}$$

where Eq. 6.14 and Eq. 6.15 have been applied. Substituting in $\Psi(z)$ and the normal distribution form of $f(v_z)$ yields

$$\begin{aligned}\rho_L(t) &= \frac{\rho_L^{\text{tot}}}{\sqrt{2\pi}\sigma_v} \int_{-\infty}^{z_0/t} e^{-\left(\frac{v_z - \langle v\rangle}{\sqrt{2}\sigma_v}\right)^2}\,\mathrm{d}v_z \\ &= \frac{\rho_L^{\text{tot}}}{\sqrt{\pi}} \int_{-\infty}^{\gamma_0} e^{-\gamma^2}\,\mathrm{d}\gamma \\ &= \frac{\rho_L^{\text{tot}}}{2}\left[1 + \mathrm{erf}(\gamma_0)\right]\end{aligned} \tag{6.17}$$

using the substitutions $\gamma = (v_z - \langle v\rangle)/\sqrt{2}\sigma_v$ and $\gamma_0 = (z_0 - \langle v\rangle\, t)/\sqrt{2}\sigma_v t$, and the identities $\mathrm{erf}(x) = \frac{2}{\sqrt{\pi}}\int_0^x e^{-x^2}\,\mathrm{d}x$ and $\int_{-\infty}^0 e^{-x^2}\,\mathrm{d}x = \frac{\sqrt{\pi}}{2}$.

The signal recorded is the absorption given by Eq. 6.4, where the column density ρ_A is proportional to the linear density $\rho_L(t)$:

$$\frac{I(t)}{I_{\max}} = e^{-\alpha\rho_L(t)\sigma} \simeq 1 - \alpha\rho_L(t)\sigma \tag{6.18}$$

where $I_{\max}$ is the signal with no absorption, $I(t \to \infty)$, α is a constant of proportionality, and the first order expansion of the exponential is valid for $\alpha\rho_L\sigma = \rho_A\sigma \ll 1$. Typical values of the optical depth $\rho_A\sigma$ are 10^{-3} to 10^{-2} (using values from Sec. 139), so this expansion is justified. Ignoring the constant offset on the signal, the functional form to fit to the time-of-flight data is

$$f(t) \propto \operatorname{erf}\left(\frac{\langle v\rangle\, t - z_0}{\sqrt{2}\sigma_v t}\right) \tag{6.19}$$

This function has a discontinuity at $t = 0$ and changes sign for $t < 0$, which makes it difficult to fit because if the data does not extend far below $t = 0$, then it is difficult to estimate the steady-state signal before the flux is turned off. To circumvent this issue, the full data was first fitted with a simple $\operatorname{erf}(t)$ signal, from which the amplitude and offset of the fit were used to fit the correct form of the signal from Eq. 6.19. Figure 6.8 shows how the simple $\operatorname{erf}(t)$ model is a good approximation to the data, but does not capture the behaviour as well as the full model. As with fitting to the atomic density data, the model fitted to the data included a 50 Hz sinusoidal component to account for the dominant noise.

Similar approaches have been used to characterise cold-atom sources [54, 87, 98, 99], however the drawback is that atoms are assumed to have constant velocity, when in reality they are accelerated through the exit channel of the source. Since the final velocity is greater than the average velocity, this measurement approach tends to underestimate the velocities at the measurement position, which results in a corresponding underestimate of the flux from Eq. 6.3. To attempt to avoid this underestimate, transit time measurements were taken at (typically three) axial positions between 300 mm and 350 mm after the source aperture. The transit times were then combined to determine the transit time of the atoms over that region, for which the velocity actually is constant due to the absence of a push beam. In practice however, the uncertainty in the transit times made this velocity estimate an inconsistent approach, particularly for small fluxes where the signal-to-noise ratio was poor. In general, the underestimate of the approach using a transit time measurement at a single position was 10 – 20% compared to using measurements at multiple axial positions, but the variation in accuracy of the latter complicated analysis of the trends in the data (see the following

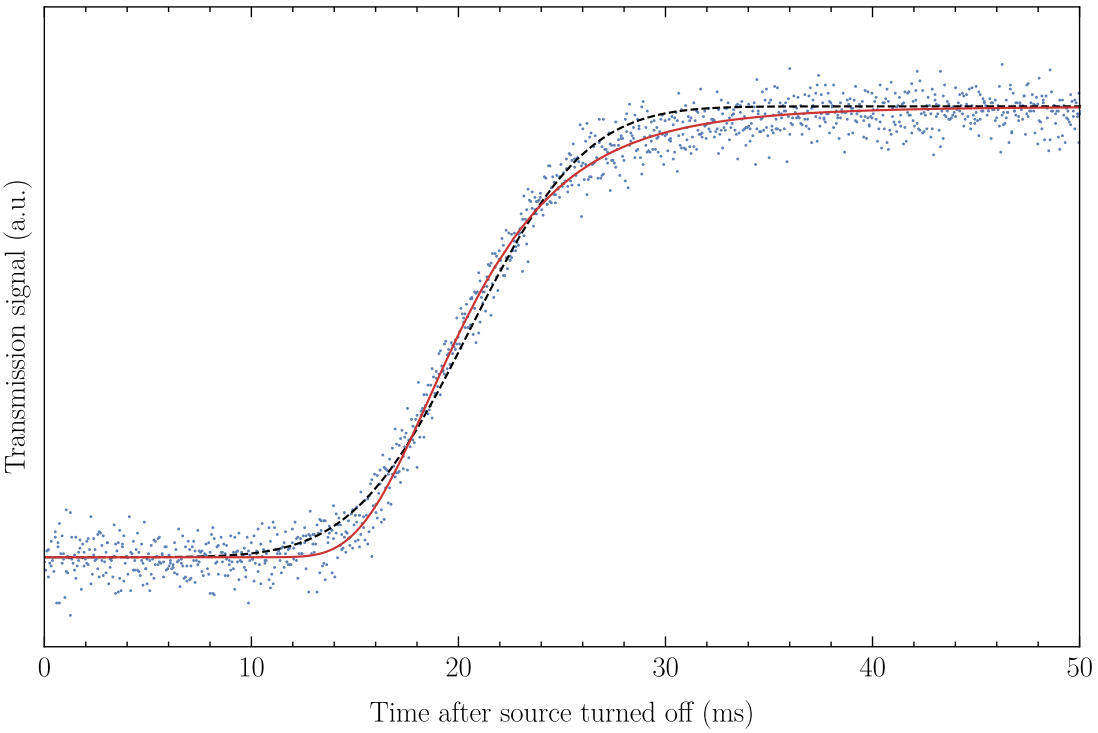


Figure 6.8: An example of a typical transit time signal. A simple $\mathrm{erf}(t)$ model (black, dashed) produced a reasonable fit, however the full model of Eq. 6.19 (red) captured the behaviour significantly better. The time that the MOT was turned off at was measured using a photodiode directed at the pyramid chamber to detect the drop in fluorescence.

chapter), so the standard single-position approach was used. The underestimate should be born in mind when considering the absolute values of the flux.

6.4 Summary

Measurement techniques were developed to allow accurate characterisation of the important parameters of the output flux of the prototype cold-atom source: the divergence, the longitudinal velocity distribution, and the total flux. This required determining the atomic column density profile of the beam, which was achieved by taking absorption measurements using a narrow probe beam at various heights relative to the flux, and for which a measurement apparatus was built that included optical power stabilisation, sensitive differential amplifier circuitry, and a weak magnetic field in order to achieve the high sensitivity demanded. The same apparatus was used to determining the longitudinal velocity profile of the flux, by

using a transit time approach. Ideally the transit time method would have measured the time for the atomic flux to travel between two measurement points, since this would have given a more accurate estimate for the longitudinal velocity, however the weak absorption signals made this impractical and instead the transit time of the atoms from within the source to a single measurement point was used (giving a $10-20\%$ underestimate of the final velocity of the atoms). For both the atomic column density and longitudinal velocity data, analytical models were developed to fit to the data and extract the required parameters. In the following chapter, the resultant flux characterisation from applying these techniques is presented and analysed.

7

Characterisation of the Flux

The primary goal of the characterisation of the new design of pyramid MOT source was to understand the impact of the aperture size on the flux. Although the extremes of very small and large aperture sizes can be straightforwardly understood (see Sec. 3.1), the intermediate regime where all cold-atom sources operate has not previously been investigated. The flux dependence on vapour pressure, aperture size, MOT beam diameter and MOT beam intensity were measured and analysed. In addition, the dependence on the MOT position (the $B = 0$ position of the quadrupole field where a MOT will form in the absence of an exit channel) was investigated by varying the transverse and axial bias fields, which also allowed the robustness of the source to background fields to be quantified.

For each of these dependencies of the flux, only one parameter was changed at a time. The detuning of the MOT light was kept constant at $2\,\Gamma$ throughout all data acquisition because the flux was consistently found to be optimised for that value, and similarly the magnetic field gradient was found to be optimal at 18.2 G/cm (in the axial direction) and therefore kept unchanged.[1] The bias fields (which move the $B = 0$ position) required fine tuning for each new aperture size to optimise the flux (due to small alignment changes from removing the pyramid from the vacuum chamber to change the aperture), but changing the vapour pressure or MOT light characteristics (intensity, diameter) required no adjustment

[1] 18.2 G/cm was the maximum field gradient achieved with the available current supply for the MOT coils, and the gradient could be reduced by 10 – 15% before a reduction in the flux occurred.

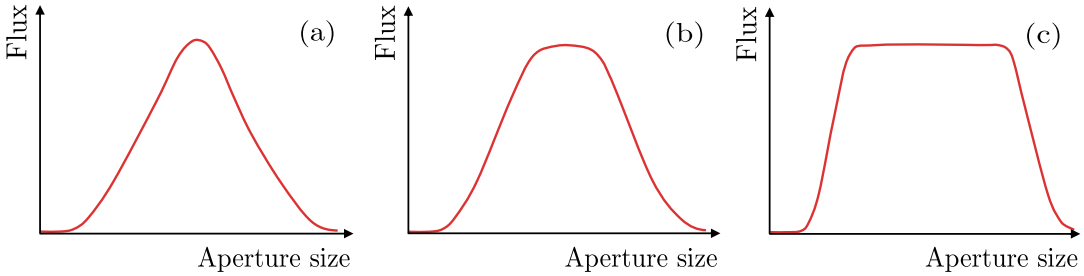


Figure 7.1: Possible forms of the flux dependency on the aperture size. There may be a very strong dependence (a) since the aperture defines the exit channel that couples atoms from the MOT trapping region to the exit aperture, or there may be a saturated dependence (c) if atoms are efficiently 'recycled' in the MOT region, or an intermediate situation with some saturation (b).

of the bias fields to maximise the flux and were hence kept constant for each aperture size.[2]

First, the dependence of the flux on aperture size is focussed on, beginning with the different possible relationships that may be expected, since this was the dependence of greatest interest.

7.1 Flux vs. Vapour Pressure & Aperture Size

It is not a straightforward task to predict how the flux will vary with aperture size. On the one hand, the flux could be expected to depend strongly on the aperture size, since the aperture defines the geometry of the exit channel of the pyramid. In particular, for small apertures the diffraction of the retroreflected light from the aperture closes the exit channel so that atoms at the $B = 0$ position are not channelled towards the aperture (see Sec. 3.1.3), and large apertures both reduce the trapping volume (reducing the capture rate of the MOT source) and result in higher transverse velocities (causing more atoms to escape the exit channel before reaching the aperture – see Sec. 3.1.2), which could result in a sharply peaked dependence similar to that shown in Fig. 7.1(a). On the other hand, it could be argued that the flux should instead be independent of aperture size if the atoms that leave the exit channel prior to the aperture are 'recycled' by the laser cooling and directed back

[2] i.e. as the vapour pressure or MOT beam intensity/diameter were changed, no change was required to the $B = 0$ position (which is where a MOT would form); any changes to the bias fields only reduced the flux.

to the MOT centre, rather than being lost completely. Such 'looped' trajectories have been shown in numerical simulations by Ovchinnikov [87], Lu et al. [99] and Kohel et al. [103], and would produce a saturated dependence, such as Fig. 7.1(c).

The source was characterised over a range of vapour pressures at each aperture size, to mitigate the effect of pressure on the source performance (see Sec. 2.3.1) when determining the maximum flux for each aperture size. Figure 7.2 shows the flux as a function of pressure for multiple aperture sizes (a – f), and the corresponding maximum fluxes at each aperture size (g).[3]

Of the tested aperture sizes, four (b – e) showed the pressure-dependence expected from Eq. 2.1: at low pressures the flux increase was approximately linear, corresponding to the direct proportionality of the MOT loading rate to background atomic density (Eq. 1.44); then the dependence saturated and eventually decreased, which arises from the exponential pressure-dependence of the collisional loss rate. For the 1.27 mm aperture (a), the pressure was not increased sufficiently to see the saturation, and for 0.38 mm (f) the absorption signal was barely detectable, hence only two measurements of the flux were taken. For the 0.71 mm aperture (d), the flux saturated then decreased for 50% lower pressures than the rest. This is likely to be a result of the non-rubidium background pressure being abnormally high, caused by the dispensers being nearly exhausted and operated at higher currents than normal – dispensers have a tendency to release more than just the desired alkali vapour when at the end of their life.

Bearing in mind that the flux for 0.71 mm appeared anomalous, Fig. 7.2(g) shows a very strong dependence of the maximal flux as a function of aperture size. From the lower range of this data, no flux should be expected from an aperture smaller than 0.3 mm, and even for 0.4 mm the flux was too low to be of practical use. The flux then increased approximately linearly up to a 1.0 mm aperture, and showed indications of being saturated above this, however there was insufficient data to be able to assert this with certainty.[4] The strong

[3] Note that the pressure plotted here is the partial pressure of ^{87}Rb. The total partial pressure of rubidium would include that of ^{85}Rb, and would therefore be larger by a factor of 3.6 (since the natural relative abundance of ^{87}Rb is 27.83%).

[4] The apparatus is capable of testing aperture sizes up to 10 mm and will be used to investigate larger

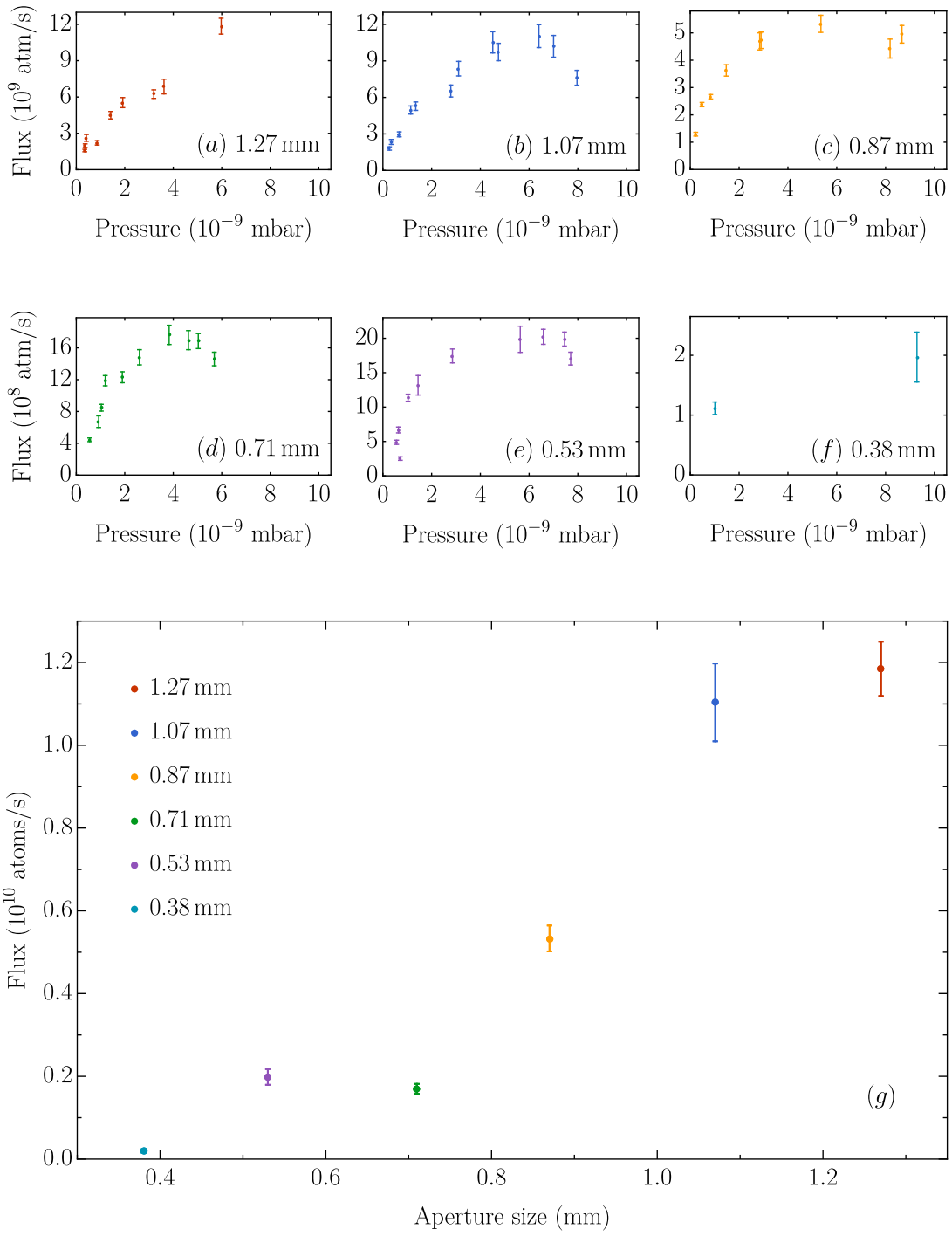


Figure 7.2: The measured dependence of the flux of atoms produced by the prototype pyramid source. The flux was measured as a function of the ^{87}Rb partial pressure for multiple aperture sizes (a) to (f), and the maximum recorded fluxes plotted against aperture size in (g). The green point corresponding to data in (d) is anomalous – see text for discussion. Note that the flux units for (a – c) are an order of magnitude larger than that of (d – f).

dependence of flux on aperture size implies that the recycling mechanism of the MOT source is not transferring all loaded atoms into the output flux.

The reason for this inefficiency is that the time τ that an atom takes to be cooled and directed out of the source increases with the number of recycling events that the atom undergoes. Since the fraction of atoms lost from background collisions is $1-e^{-n\sigma_{\mathrm{col}}\langle v\rangle\tau}$ (from Sec. 2.3.1), the probability of collisional loss increases with τ. For a narrow aperture, a large fraction of atoms will have a sufficiently large transverse velocity when entering the exit channel to leave the channel before reaching the aperture; the funnelling efficiency χ is small. The average number of recycling events is therefore high, such that τ becomes long enough for a high probability of collisional loss within that time. Saturation of the flux for large apertures (>1.0 mm) implies that χ is sufficiently high for τ to remain below the threshold where collisional losses prevent recycling occurring effectively, however this is hypothetical without more data to show saturation clearly.

In addition to aperture size, other parameters affect the properties of the output flux as shown in Fig. 7.3. The beam divergence and the FWHM of the axial velocity showed no noticeable variation as a function of the vapour pressure, and their mean values for each aperture size are plotted in Fig. 7.3(a) and (b) respectively. Neither show any clear dependence on aperture size.

In contrast, the average axial velocity of the output flux showed two dependencies: a slight decrease with increasing pressure (c),[5] and an approximately linear dependence on the aperture size – the minimum and maximum values for each aperture size are shown in Fig. 7.3(d). Increasing the pressure might be expected to increase the average axial velocity instead, since the increasing collisional loss rate would preferentially remove the slowest atoms with longest τ. However, an opposing effect is the increased absorption of the

aperture sizes in the future to establish if the flux is saturating in this region, and at what point the flux starts to decrease. Only time constraints prevented this data being included in this thesis.

[5] Note that the data for the 1.27 mm aperture size (red in Fig. 7.3(c)) did not show any obvious linear trend, so was anomalous compared to the data for other five aperture sizes investigated. This is likely to be because the 1.27 mm aperture size was the first to be characterised, and the data acquisition approach may have been less refined than for subsequent aperture sizes, producing more noise and error that hid the slight linear trend expected.

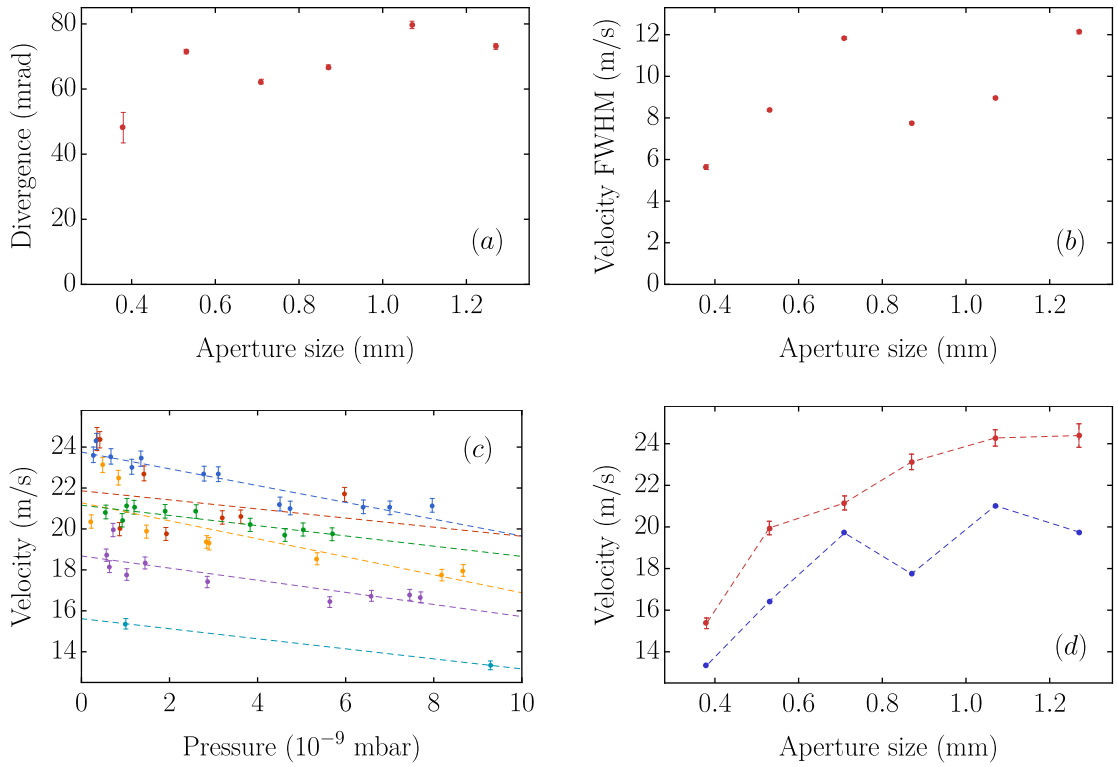


Figure 7.3: The variation with aperture size of: (a) the mean divergence; (b) the mean FWHM of the axial velocities; (c) the axial velocity, shown as a function of pressure where the colours correspond to the same aperture sizes as in Fig. 7.2, and with weighted linear fits applied to illustrate the approximately linear dependence; and (d) the maximum (red) and minimum (blue) axial velocities of the flux. These are the mean/maximum/minimum values observed when measuring the flux at a fixed aperture size over a range of vapour pressures. Note that in (c), the 1.27 mm data (red) does not show any obvious linear trend, and the best fit line (red dashed) is therefore a poor fit, as discussed in footnote 5.

incident MOT light, such that the intensity along the exit channel is reduced; at 10^{-9} mbar of ^{87}Rb the MOT intensity along the axis is reduced by 3% at the aperture, whereas this increases to 29% at 10^{-8} mbar.[6] If the pyramid were mounted in a compact chamber, the former effect would be expected to dominate, however, since for testing it was placed in an existing large chamber that was more than twice as long as required,[7] the absorption of the MOT light was greater. When employed as a compact device, it is likely that instead of the slight reduction in axial velocity with pressure observed here (c), the axial velocity would

[6] Note that this effect arises from keeping the MOT intensity constant as the pressure is increased, and to avoid the decrease in axial velocity with pressure would simply require an increase in the MOT intensity to compensate for the absorption by the background vapour.

[7] The chamber was 9 cm long, and the pyramid aperture was located 26 mm from the rear surface with the differential pumping hole.

increase. This is an avenue for future investigation with a pyramid source in a compact package.

The second dependence of the axial velocity, on aperture size (d), arises from the retroreflected light diffracting from the aperture, as explained in Sec. 3.1.3: for a smaller aperture the diffraction is greater, which results in a larger intensity counterpropagating with the exit channel, that serves to reduce the intensity imbalance and hence the acceleration experienced by the atoms. The axial velocity increase is approximately 7 m/s per mm travelled, which is sufficient that a small aperture size could be a consideration if a particularly low-velocity flux were desired. However, the axial velocities are still well within the typical capture range of a MOT, so no issue arises with the slightly higher velocities associated with large aperture sizes when loading a MOT.

In conclusion, the impact of the aperture size was primarily on the total flux of atoms, which is the most critical parameter to a cold-atom source. There was a strong increase with aperture size, before a possible saturation above about 1.0 mm, and more data will be taken in the future to establish if the flux is saturating in this region, and at what point the flux starts to decrease. Aside from the total flux, the divergence and the axial velocity FWHM showed no significant dependence on the aperture size, albeit with limited data, but the average axial velocity showed an approximately linear increase with the aperture size.

7.2 Flux vs. MOT Beam Diameter

The total flux of a source is predicted to increase with the diameter of the incident laser beam, due to the increasing size of the trapping region (see Sec. 1.4.2). As such, the new pyramid source was designed to be easily scalable. The dependence of the flux characteristics on the MOT beam diameter was investigated for two aperture sizes by using an iris to reduce the beam diameter,[8] and the results are shown in Fig. 7.4. The mean axial velocity (a), axial

[8] Note that the use of an iris to adjust the MOT beam diameter is different to using a beam expander to change the diameter. A beam expander preserves the profile of the beam relative to its width, whereas using an iris just removes the outermost profile of the beam, which for a Gaussian beam is the region of lowest intensity.

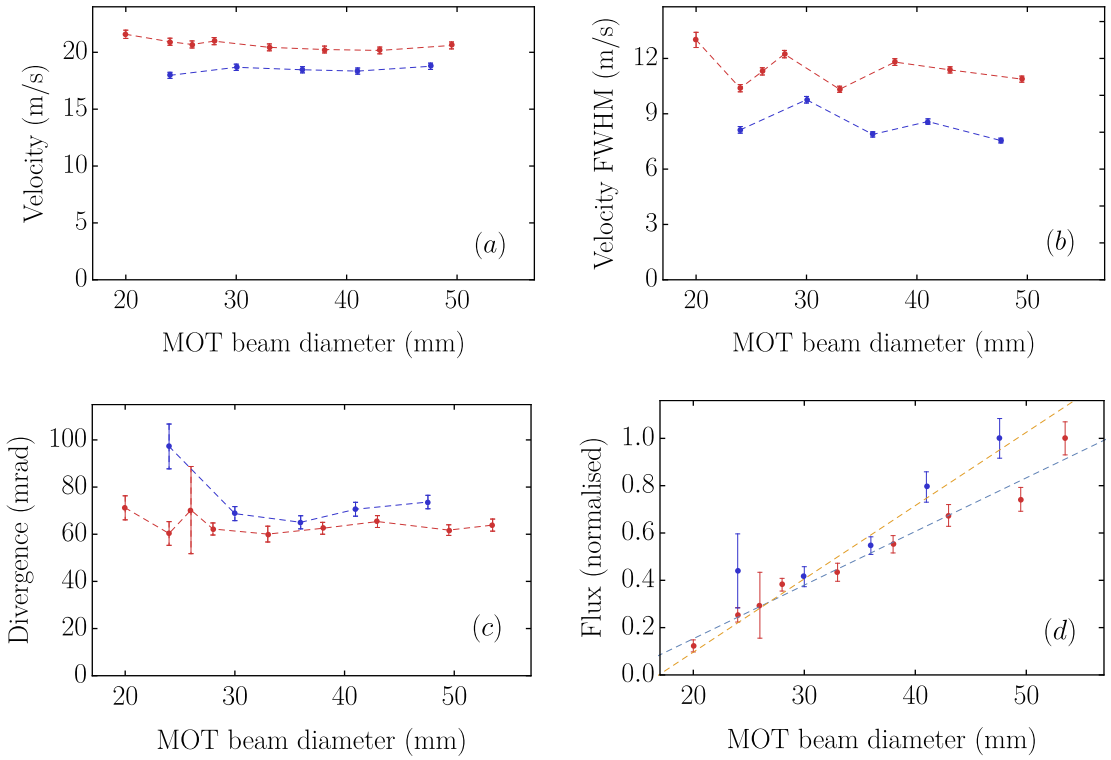


Figure 7.4: The measured dependence on the MOT beam diameter, for aperture sizes of 0.71 mm (red) and 0.53 mm (blue), of: (a) the mean axial velocity; (b) the FWHM of the axial velocity; (c) the divergence of the flux; and (d) the flux, normalised since the vapour pressure was not the same for the two aperture sizes.

velocity FWHM (b), and the divergence (c) all appeared independent of the beam diameter.[9] These characteristics are unchanged since they depend on the dynamics in and around the exit channel, which were unaffected by reducing the beam diameter; the MOT centre was approximately 15 mm from the pyramid aperture, so the optical field is unchanged in the region from the MOT centre to the aperture until the beam diameter reaches 15 mm, but the flux was negligible below 20 mm and so no data could be taken.

In contrast, the flux showed a strong and apparently linear dependence on the beam diameter in Fig. 7.4(d). The simple model of a MOT source in Sec. 2.3.1 predicted a d^4 dependence, however the reality of a pyramid MOT is more complicated. Firstly the model assumes beams of uniform intensity, whereas the use of Gaussian beams (albeit ones expanded beyond the pyramid diameter to be more uniform) means that a reduction of the

[9] The 0.53 mm divergence data at 24 mm beam diameter is an outlier due to the density profile being very noisy for such low fluxes, and hence difficult to accurately fit to.

diameter at the extremes has a smaller effect than the model would expect. Secondly, for atoms entering the trapping region near the outer limits of the pyramid (whether from the background vapour or off the mirror surface), the solid angle over which an atom will have sufficient distance to travel in order to be slowed without colliding with a pyramid mirror is much smaller than those atoms entering the central region of the pyramid. These factors reduce the extent to which the flux depends on the MOT beam diameter, but the relationship in Fig. 7.4(d) is still strong, and crucially shows no sign of saturating. This therefore justifies a scalable design of pyramid source, and the production of larger pyramid sources should be expected to produce greater fluxes of atoms.

7.3 Flux vs. MOT Beam Intensity

Both the aperture size and MOT beam diameter showed generally small or negligible impacts on the velocity and divergence characteristics of the flux. This is because these properties are predominantly determined by the axial intensity imbalance along the exit channel, which is largely unaffected by those parameters. The net intensity determines the number of photons atoms will scatter before reaching the aperture, which sets the velocity of the atoms. If the average axial velocity is v, then the number of photons absorbed is $N = v/v_\mathrm{r}$, where v_r is the recoil velocity from Eq. 1.30. Correspondingly, N photons must also be spontaneously emitted, which causes a random walk in velocity space that determines the divergence and FWHM of axial velocities.

Regarding the divergence in particular, without the effect of these spontaneously emitted photons the expected divergence is much lower. Assuming the exit channel is small compared to the trapping region, atoms entering the exit channel will be at about the Doppler temperature T_D (from Sec. 1.2.2). The velocity associated with T_D is $v_\mathrm{D} = \sqrt{k_B T_\mathrm{D}/M} = 11.8\,\mathrm{cm/s}$ for ^{87}Rb. For an atom accelerated to 20 m/s, this would correspond to a FWHM divergence angle of 13.9 mrad, much smaller than the typical 20 – 50 mrad divergences observed (see Table 2.1). However, there is heating by the photons emitted spontaneously during acceler-

ation that causes a random walk in velocity space, for which the standard deviation of the zero-centred velocity distribution is $\sqrt{\alpha N}$. The constant α depends on the radiation pattern of the atom. For an isotropic radiation pattern, $\alpha = 1/3$, but correct treatment of the atom, and assuming circularly polarised light, gives $\alpha = 3/10$ [199, 200]. Therefore, the FWHM divergence angle from this heating during acceleration is given by[10]

$$\begin{aligned}\theta &= 2\tan^{-1}\left(\frac{\sqrt{2\ln 2}\sqrt{\frac{3}{10}N}}{N}\right) \\ &\approx \sqrt{\frac{5}{3N}}\end{aligned} \tag{7.1}$$

where the small-angle approximation has been made. For $v = 20\,\mathrm{m/s}$ this results in a FWHM divergence angle of 22.1 mrad. Thus this is the primary contribution to the divergence, and scales with $N^{-1/2}$.

The flux characteristics as a function of MOT beam intensity are shown in Fig. 7.5. These observations emphasise the importance of the intensity of the incident cooling beam on the resulting divergence and distribution of axial velocities. The velocity FWHM (a) increased with the intensity and saturated at about $3I_{\mathrm{sat}}$, with no clear dependence on the aperture size. The axial velocity (b) on the other hand tended towards saturation but was still increasing even at $7I_{\mathrm{sat}}$, and the two smallest aperture sizes had notably lower axial velocities, while the other three were broadly similar. This is a consequence of diffraction from the smaller aperture sizes reducing the axial intensity imbalance, as mentioned previously. This also suggests that above $0.7-0.8\,\mathrm{mm}$, the apertures are sufficiently large that diffraction is negligible, however there is not enough data to confirm this hypothesis.

The linear atomic density (c) is shown as normalised, since the vapour pressures were not identical for the different measurement sets. It increased approximately linearly, from a negligible signal below I_{sat} to saturation above $4I_{\mathrm{sat}}$. Since the axial velocity (b) was still varying above $4I_{\mathrm{sat}}$, this raises the prospect of being able to tune the velocity of the output flux with only a small change in the total flux (which is the product of the linear density

[10] Using the fact that the HWHM of a Gaussian distribution with standard deviation σ is $\sqrt{2\ln 2}\,\sigma$.

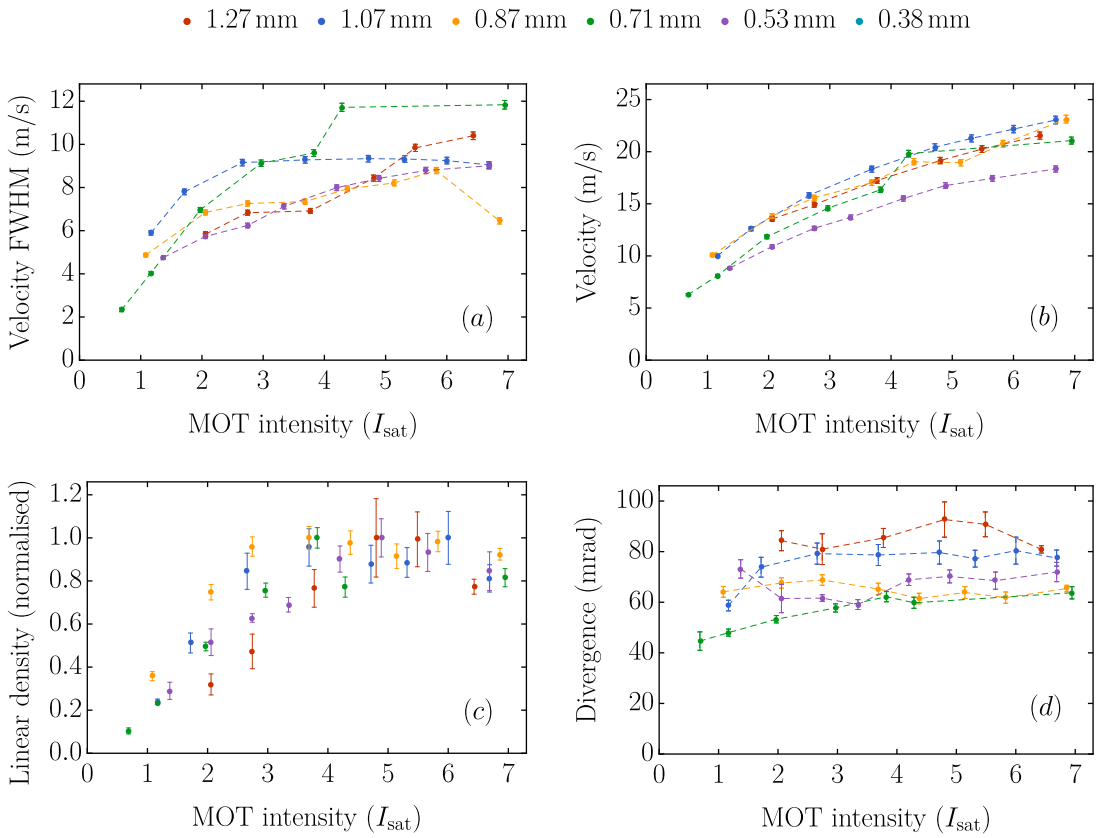


Figure 7.5: The measured dependence on the MOT beam intensity, for a range of aperture sizes, of: (a) the axial velocity FWHM; (b) the mean axial velocity; (c) the linear atomic density, normalised since the vapour pressure was not the same for the different aperture sizes; and (d) the divergence. The intensity plotted was the average intensity of the MOT beam, in units of the saturation intensity I_{sat} for $\sigma^{\pm}$ transitions ($1.669\,\mathrm{mW/cm^2}$).

and velocity, from Eq. 6.3). However, a caveat to these plots is the aforementioned scatter from the mirrors (see Sec. 4.4.1). In the linear density plot (c), above $6I_{sat}$ the density (and hence the flux) fell below the saturation level.[11] The expected behaviour would have been simple saturation, but the issue was that as the intensity increased, the forces on the atoms saturated while the amount of scatter generated from the mirrors increased linearly. Therefore the heating and loss due to the scattered light (which no longer has the requisite polarisation or direction for cooling) continued to increase while the loading rate of the atoms was constant, resulting in a reduction of the flux. This was a clear indication that the scatter from the mirrors had a detrimental impact on the flux. It should also be expected to have

[11] The linear atomic density is shown here rather than the flux in order to make this effect more apparent, rather than obscuring it due to the additional variation in the velocity measurements that are multiplied with the linear densities to give the total atomic flux.

influenced the velocity dependence on the MOT intensity, since scatter will preferentially cause losses of slower atoms, thereby increasing the velocity of the emitted atoms. The lack of saturation in the axial velocity plot (b) should therefore be treated with some caution, in case it would saturate in the absence of scatter from the mirrors.

The effect of scatter may also be apparent in the divergence (d) of the flux. The typical values of 60 – 80 mrad are two to three times larger than those generally observed for similar sources (see Table 2.1). This is likely to be a result of the additional heating caused by the scattered light.

It should also be noted that the data in Fig. 7.2 was acquired with the MOT light intensity at $6.9 I_{\mathrm{sat}}$, for which the flux was observed to be approximately 10% below the maximum due to scatter (from Fig. 7.5(c)). The maximum achievable fluxes should be ∼10% higher than those reported here if the MOT light intensity were reduced to limit the heating and loss due to scatter.

7.4 Flux vs. MOT Position & Magnetic Field

In addition to the characterisation of the source above (with regard to optimising the flux and controlling the various parameters), the robustness of the source to changes in the MOT position (the $B = 0$ position of the magnetic quadrupole field, which is the position where a MOT would form in the absence of an exit channel for the atoms) was investigated. This was performed by varying the transverse and axial bias fields,[12] although the same effect would be achieved by translating the quadrupole coils, so the results below not only indicate how sensitive the flux is to the MOT position, but also how robust the performance of the source is to changes in the magnetic field, either due to changes in the background field or of the position of the coils.

[12] In the transverse direction, the field gradient was 9.1 G/cm, therefore a 1 G bias field corresponded to a displacement of the quadrupole field centre by 1.10 mm. Similarly, in the axial direction the field gradient was 9.1 G/cm, resulting in a sensitivity of the MOT position equal to 0.55 mm/G.

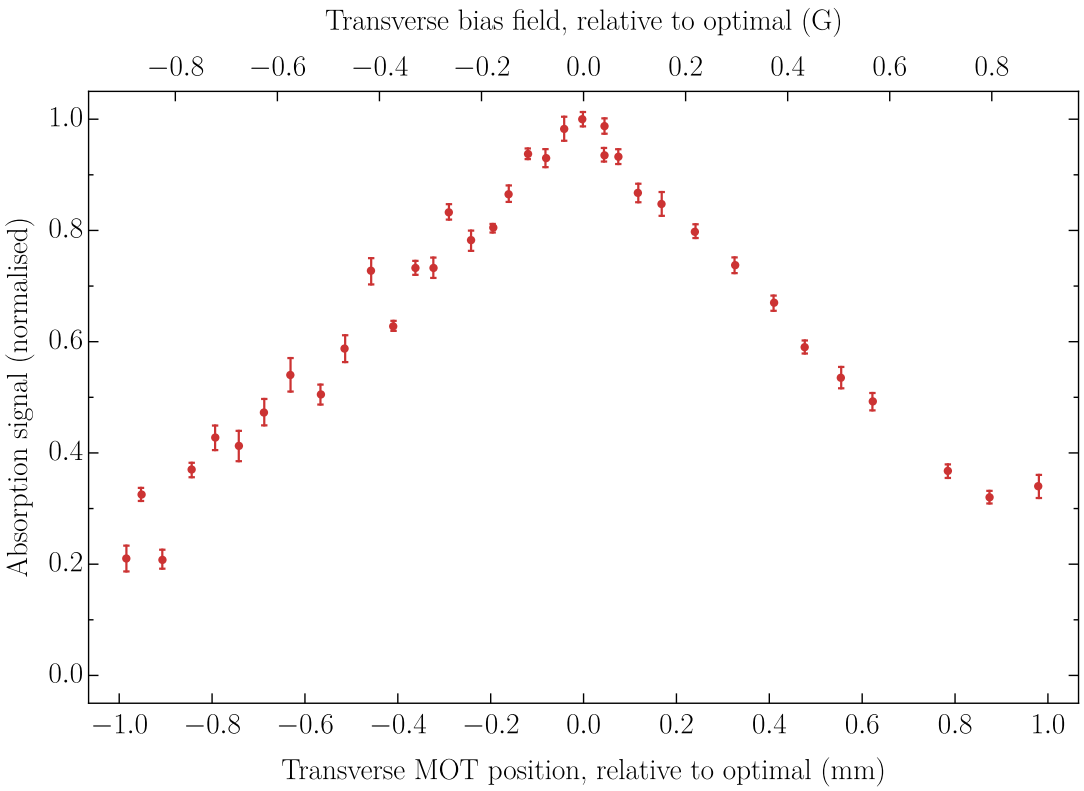


Figure 7.6: The dependence of the absorption signal (normalised against the maximum value) on the transverse MOT position (relative to the optimal position), performed by applying a transverse bias field, with the applied field also shown (relative to the optimal field of 0.79 G). The absorption signal was directly proportional to the total flux, as explained in the text. The sensitivity of the MOT position to the applied transverse bias field was 1.10 mm/G.

7.4.1 Transverse Position

The divergence and axial velocity were found to be independent of transverse changes to the MOT position in the vertical direction. This was as expected, since changing the bias fields to alter the MOT position does not impact the optical fields, which are responsible for these properties of the flux, as described above. This meant that the absorption signal at a single position in the atomic flux was directly proportional to the total flux of atoms.[13] The change in this signal for an aperture size of 0.71 mm is shown in Fig. 7.6. A displacement of less than 100 µm (equivalent to a field of less than 0.1 G) was sufficient to reduce the flux by 10%, and the flux dropped below 50% of its maximum value for displacements equal to

[13] A constant divergence meant that the integral of the density profile (the linear density along the source axis) at the axial measurement position was directly proportional to the density measured at any transverse position, and the constant velocity meant that the flux was directly proportional to the linear density.

the aperture size.

The cause of the flux reduction is that the overlap of the exit channel with the region where atoms congregate reduces as the MOT position is moved off-axis – the funnelling efficiency χ decreases since atoms are less likely to enter the exit channel.[14] For a portable device this sensitivity to small changes in the MOT position are important. Not only does it require the position of the quadrupole coils to be stable to less than 100 µm, but the magnetic field of the Earth is typically $0.25-0.65$ G, which is sufficient that if the the source were to be used in multiple locations or orientations then it may require bias coils to zero the local magnetic field, which would add bulk and additional power requirements. It is suspected that a wider aperture would reduce the sensitivity of the flux to transverse mechanical and magnetic changes (potentially to the point of not requiring bias fields) since, for a given shift in MOT position, the reduction in overlap of the exit channel with the atoms would be smaller for a larger aperture due to the wider exit channel. This will be the subject of future investigations.

7.4.2 Axial Position

The source was far less sensitive to axial variations in the MOT position because the overlap of the exit channel with the atoms does not change substantially, unlike with transverse changes. The axial velocity was found to be unchanged by the axial field, and Fig. 7.7 shows how the divergence (a) and axial velocity spread (b) were mainly independent of the field, except as the field centre was moved close to the pyramid apex. It would seem likely that the cause for these increases was closer proximity to the mirrors and the associated scatter, since atoms move slowest and hence spend a significant amount of time in the vicinity of the field centre, so an increased intensity of scattered light would cause substantial heating.

Away from this region though, the axial velocity and divergence were broadly independent of axial changes, so the normalised absorption signal at one point in the flux was roughly

[14] This was observed visually, with a cloud of trapped atoms becoming apparent and increasing in size as the transverse bias field was moved away from the optimal value.

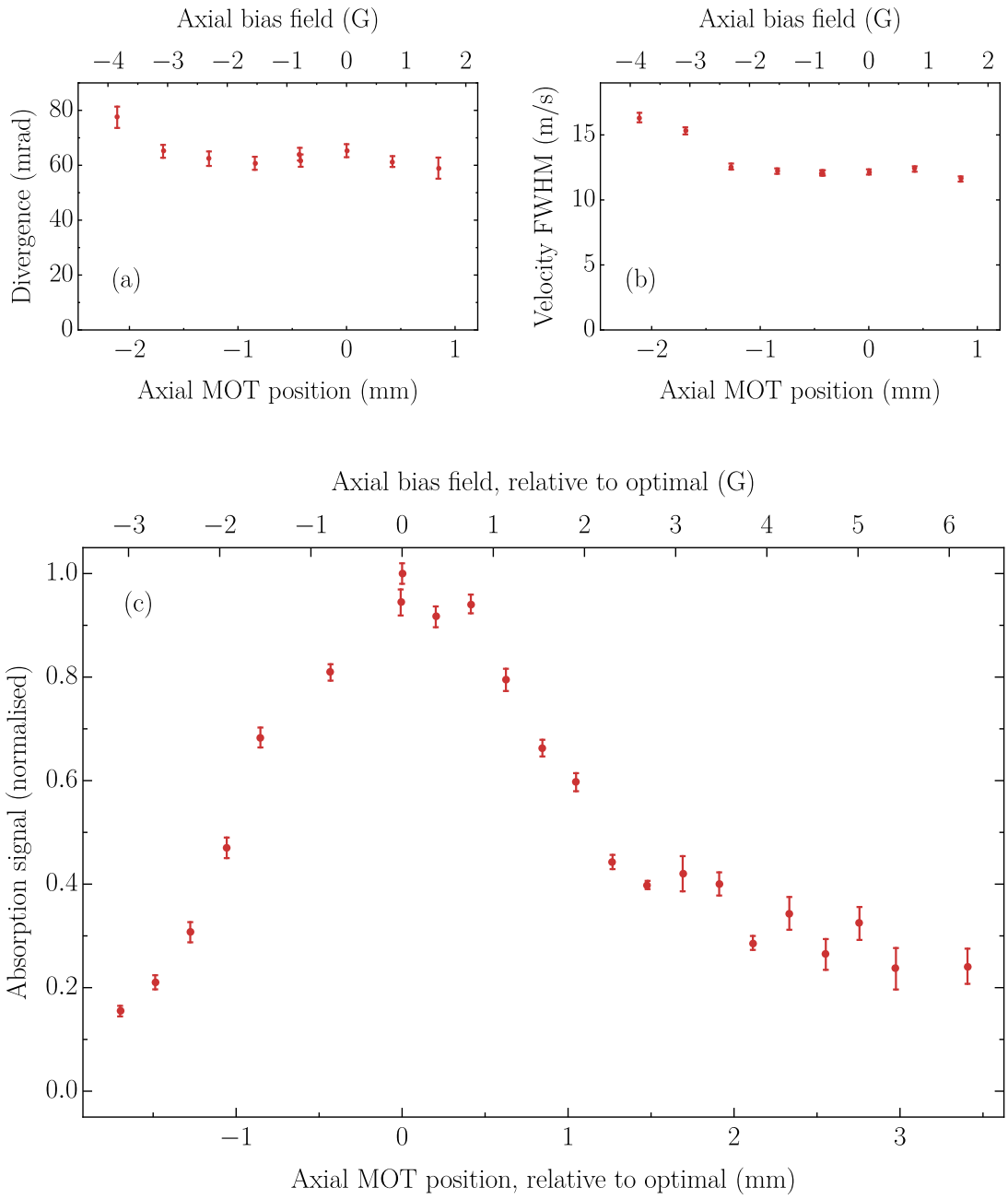


Figure 7.7: The dependence of flux characteristics on the axial MOT position (relative to the optimal position), performed by applying an axial bias field (with the applied field also shown, relative to the optimal field of 8.5 G): (a) the beam divergence; (b) the FWHM of the axial velocity distribution; and (c) the absorption signal (normalised against the maximum value). The absorption signal was approximately directly proportional to the total flux, as explained in the text. The sensitivity of the MOT position to the applied axial bias field was 0.55 mm/G, and negative values of the bias field moved the MOT position towards the pyramid aperture.

proportional to the total flux, and is shown in Fig. 7.7(c). The MOT position could be moved by about 0.5 mm from the optimal value before the flux fell by 10%, five times further than for the transverse shifts. For increasingly positive fields, the MOT position moved further from the aperture and the funnelling efficiency reduced because of: the reduced overlap with the exit channel; a smaller maximum transverse velocity for atoms to successfully travel the length of the exit channel without drifting out; and a reduced intensity imbalance in the exit channel due to a greater impact of the diffraction from the pyramid aperture. The effect was that a large and diffuse cloud of atoms became visible for large positive fields, since the loss rate of atoms into the exit channel was so low. For negative fields the flux reduced more sharply, partly because of the increased intensity of scattered light, and also because moving the field centre away from the centre of the trapping region reduces the capture velocity, and hence the loading rate.

In addition, because the axial field gradient is twice as large as the transverse gradient (from Eq. 1.37), the sensitivity of the MOT position to axial bias fields is halved compared to transverse fields, so that reducing the flux by 10% required a 1 G field. This is significantly above the magnetic field of the Earth, making the performance of the source extremely robust to the typical stray axial fields that would be encountered in different locations and orientations.

7.5 Maximum Pyramid Source Flux

In addition to investigating the impact of aperture size on the flux and characterising the dependence of the flux on the important parameters of the source, it was also important to find the maximum flux the new design of pyramid source could produce. The largest recorded flux produced by this source was $1.18(6) \times 10^{10}$ atoms/s for a 1.27 mm aperture at a 6×10^{-9} mbar partial pressure of ^{87}Rb. The axial velocity distribution had a mean of 21.6(3) m/s and a FWHM of 11.2(2) m/s, and the FWHM divergence of the beam was 86(2) mrad.[15]

[15] The atomic density profile measured for this optimal flux is that shown in Fig. 6.6.

The total flux is the most important parameter for a cold-atom source, and in this respect the prototype pyramid source compares highly favourably to the other sources in the literature (Table 2.1 is reproduced here for convenience as Table 7.1, with the new pyramid source of this thesis included). To the best of our knowledge, the flux recorded is the largest of any pyramid or LVIS source, and within a factor of two of the highest reported flux from a 2D$^+$-MOT [95]. Some 2D-MOT sources have produced up to 6×10^{10} atoms/s, however the absence of axial cooling means typically only a third of atoms are within the capture velocity of a MOT [51]. In contrast, the mean velocity of our source is well within typical MOT capture velocities.

However, the FWHM of the axial velocities appears abnormally large, albeit still within typical capture velocities. In addition, the divergence is more than double that observed from comparable sources, although is still low enough to be satisfactory for MOT loading, particularly for compact devices where the distance from source to MOT is small. Despite these unexpectedly high values posing little issue to the performance of the source for loading MOTs, they are symptomatic of an underperformance of the source due to excess heating of the atoms, which is believed to be due to the scattered light from the mirrors.

Quantifying the impact of this scattered light is not straightforward however. In the case of Kohel et al. [103], their pyramid source suffered from scattered light (off the mirror edges, rather than the entire mirror surface as in this case), and it was found that by placing a mask in front of the pyramid to block the MOT beam from hitting the mirror edges, the output flux increased by an order of magnitude. Expecting this level of improvement for a version of our source without the scattering issues seems unreasonable, since that would make it comparable to Zeeman slowers, however it indicates that with such a source, a significant increase to the flux should be achieved, as well as a reduction in the divergence and axial velocity FWHM. The process of producing such pyramid sources is currently ongoing, but the source described here, despite the scattering, is comparable to the best MOT sources presented in the literature.

Source Type	Institution	Year	Species	Flux (atoms/s)	Velocity (m/s) Mean	Velocity (m/s) FWHM	Divergence, Full Angle (mrad)	Cooling Intensity (mW/cm^2)	Cooling Intensity (I_{sat})	Detuning ($\Gamma/2\pi$)	B-Field Gradient (G/cm)	Aperture Size (mm)	Reference
Zeeman Slower	Havard	2005	^{87}Rb	3.2×10^{12}	45	25	24	–	–	–	3	–	[84]
		2005	^{87}Rb	1.7×10^{12}	120	25	24	–	–	–	3	–	[84]
	Nottingham	2014	^{133}Cs	1×10^{8}	–	–	–	–	–	–	–	–	[85]
		2014	^{6}Li	7×10^{7}	40	–	–	–	–	–	–	–	[85]
	AOSense	2018*	Sr/Ca/Yb	1×10^{11}	40	–	–	–	–	-2	–	–	[86]
Pure 2D-MOT	FOM, Amsterdam	1998	^{87}Rb	6×10^{9}	12	15	46	3	1.8	-1.7	17.7	0.8	[54]
	Stuttgart	2002	^{87}Rb	6×10^{10}	50	75	32	11.2	6.7	-1.9	17	6	[51]
	NPL, London	2005	^{87}Rb	2×10^{8}	–	–	<74	2.5	1.5	-3	6	2	[87]
	JPL, Pasadena	2006	^{133}Cs	1.5×10^{10}	38	22	–	2.1	1.9	-1.4	15	4	[88]
2D-MOT	LKB, Paris	2002	^{87}Rb	1×10^{9}	0.3-3	–	–	4.2	2.5	-3	10	–	[89]
	JPL, Pasadena	2012	^{133}Cs	8×10^{9}	–	–	–	2.3	2.1	-1.4	15	4	[90]
	KRISS, Daejeon	2012	^{87}Rb	4.5×10^{10}	39	2	12	–	–	-2	14	4	[91]
	USTC, Shanghai	2017	^{88}Sr	1×10^{9}	33	15	60	42.5	1.0	-1.5	–	2	[92]
2D$^+$-MOT	FOM, Amsterdam	1998	^{87}Rb	9×10^{9}	8	3.3	43	3	1.8	-3	12.6	0.8	[54]
	Strathclyde	2000	^{85}Rb	7.3×10^{8}	2-8	–	23	5	3.0	–	–	–	[93]
	Harvard	2003	^{87}Rb	8×10^{9}	15	3	12.5	11	6.5	-5	21.5	1.25	[94]
	NPL, London	2005	^{87}Rb	8×10^{9}	11	5	<74	2.5	1.5	-3	6	2	[87]
	TIFR, Mumbai	2006	^{85}Rb	1.9×10^{10}	15	3.5	26	–	–	-2	15	2	[95]
		2006	^{87}Rb	2×10^{10}	17	5	26	–	–	-2	15	2	[95]
	ColdQuanta	2018*	Rb/Cs	1×10^{9}	–	–	–	–	–	–	–	0.75	[96]
3D-MOT	CNRS, Paris	1997	^{133}Cs	1×10^{6}	1.9-5	–	–	–	–	–	–	–	[97]
	INFN, Napoli	2001	^{87}Rb	7×10^{7}	14	–	–	5	3.0	-2.5	15	–	[80]
	LKB, Paris	2001	^{87}Rb	1.3×10^{8}	14	9	20	–	–	-3	15	5	[98]
LVIS	JILA, Boulder	1996	^{87}Rb	5×10^{9}	14	2.7	30	13.2	7.9	-5	5	~ 1	[99]
	FOM, Amsterdam	1998	^{87}Rb	3.2×10^{8}	26	6.3	27	6.8	4.1	-3.3	13.6	0.8	[54]
	NIST, Boulder	2005	^{133}Cs	1×10^{10}	–	–	–	10	9.1	-1.7	7	0.5	[100]
	NPL, London	2005	^{87}Rb	8×10^{9}	8.5	4	<74	2.5	1.5	-3	8	2	[87]
Pyramid MOT	Oxford	1998	^{133}Cs	1.1×10^{9}	11.3	2-3	40	6	5.4	-2	10	1×2	[42]
	Wisconsin	1998	^{39}K	5.3×10^{3}	–	–	–	12.5	7.1	-7	4	2	[101]
		1998	^{40}K	3×10^{-1}	–	–	–	12.5	7.1	-7	4	2	[101]
	Pisa	2001	^{133}Cs	4×10^{9}	10	1.5	26	10	9.1	-2.7	12	1×2	[102]
	JPL, Pasadena	2003	^{133}Cs	2.2×10^{9}	15	–	15	3	2.7	-2.1	–	1	[103]
		2004	^{87}Rb	1×10^{8}	10	–	15	1.2	0.7	-2.3	–	1	[104]
		2004	^{133}Cs	2×10^{8}	–	–	15	0.99	0.9	-2.1	–	1	[104]
	Durham	2008	^{87}Rb	1.8×10^{7}	–	–	–	4.0	2.4	-2.8	10.1	2.4×3.0	[105]
		2008	^{133}Cs	1.3×10^{7}	–	–	–	4.0	3.6	-3.0	8.5	2.4×3.0	[105]
	Oxford	2018	^{87}Rb	1.2×10^{10}	21.6	11.2	86	11.4	6.9	2	18.2	1.27	This work
Grating MOT	AFRL, New Mexico	2017	^{87}Rb	4×10^{8}	16.5	8	–	11	6.5	–	20	1	[106]

Table 7.1: A summary of cold atom sources from the literature, reproduced from Table 2.1 with the newly characterised pyramid source of this work included.

7.6 Summary

Characterisation of the prototype pyramid source allowed the dependence of the flux on the aperture size to be observed, which clearly demonstrated the importance of aperture selection. A strong dependence of the total flux on aperture size was found, with a negligible flux below 0.4 mm and possible saturation above 1.0 mm, although measurements for larger aperture sizes are required to confirm this, and to determine at what aperture size the flux decreases. These aperture sizes are within the capability of the adjustable pyramid design of this thesis (up to 10 mm apertures are achievable), and measurements are ongoing for larger aperture sizes. In addition to impacting the total flux, the aperture size had an influence on the axial velocity of the atomic flux, with a slight linear increase observed.

Measurements of the flux as a function of the MOT beam diameter found that the velocity distribution and divergence were independent of the diameter, whereas the total flux was strongly dependent. This justifies the exploration of larger pyramid sources in the future to obtain higher fluxes. When the flux was investigated as a function of MOT beam intensity, the flux was found to saturate then decrease as the intensity increased, when it should be expected to simply saturate. The cause was the scattered light from the coating of the pyramid mirrors, the intensity of which continues to increase with the incident intensity, while the MOT loading rate saturates, hence reducing the total flux for high incident intensities. The mean and FWHM of the axial velocity distribution were found to increase with intensity before saturating, as expected, and the divergence showed no clear pattern, but was distinctly larger than would be expected of a cold-atom source, which is believed to be another result of the scatter from the mirrors.

The impact of the MOT position was also investigated, and the flux was found to be significantly more sensitive to transverse deviations from the optimal position compared to axial deviations, because transverse shifts cause the overlap of the exit channel with the accumulated atoms to reduce much more than equivalent axial shifts. The MOT position was adjusted by using bias fields, and this allowed the robustness of the source to stray

background fields to be understood; transverse fields of less than 0.1 G were sufficient to reduce the total flux by 10%, whereas 1 G fields in the axial direction were required for the same impact. The velocity distribution and divergence of the flux were largely independent of the MOT position.

The maximum flux produced by the source was comparable to the highest MOT sources in the literature, and given the compact and robust nature of the design, this potentially makes it a commercially viable product with a wide range of applications in the currently expanding quantum technologies market. This led to an industry collaboration with M Squared Lasers which is outlined in Appendix C.

8

Summary & Outlook

In this thesis, I have designed, built and characterised a high-flux cold-atom source, which is summarised here and followed by potential further measurements and improvements, of which several are currently being implemented.

8.1 Project Summary

The goal of this project was to design, manufacture and characterise a compact and robust cold-atom source for use in portable quantum devices as part of the ongoing drive to apply sophisticated techniques developed in research laboratories to real-world situations. The new design used a MOT source with the pyramid geometry, since the use of a single beam reduces the size and complexity of both the vacuum system and optical apparatus, the latter of which reduces the sensitivity to mechanical vibrations and the possibility of misalignments. The majority of previous pyramid designs have been square-profiled, and all recorded MOT sources have used fixed apertures, therefore a novel design was developed that allowed the aperture size to be varied. The symmetry of the design minimises the number of different parts required and renders it easy to manufacture and assemble, with the intention being to move towards achieving commercial viability. The design is subject to an ongoing international patent application, and attracted an industrial collaboration with a leading laser company, M Squared Lasers.

A demanding requirement of the pyramid geometry is to place the optical elements in vacuum, and this was a difficult feature of the manufacturing process. The cracking of the glass mirror substrates when epoxied to metal mounts caused a substantial delay, but extensive testing identified the primary cause as a high surface roughness of the glass surface. The use of optically flat surfaces was shown to prevent cracks forming, and a repeatably successful epoxying procedure was developed. The adjustable-aperture mechanism worked smoothly for the prototype,[1] although the use of a non-UHV material in manufacturing could have degraded the vacuum in the pyramid chamber, and this component certainly showed signs of degradation after prolonged exposure to a rubidium atmosphere. Of greater significance was the high level of scattered light from the multilayer dielectric mirror coating, far higher than that of previous pyramid mirrors with near-identical coatings, and which increased by an order of magnitude after exposure to air following being in a rubidium environment.

Despite these issues, characterisation of the produced prototype was performed in detail and revealed in particular a strong dependence of the total flux on the aperture size below 1.0 mm, which allowed a lower limit of 0.4 mm for usable fluxes to be estimated. The impact of the mirror scatter was apparent in the decrease of the flux at high MOT intensities, and in the abnormally high axial velocity spread and divergence of the output beam. However, these values were not sufficiently extreme to impact the effectiveness of the source for loading a MOT, and the measured total flux of $1.18(6) \times 10^{10}$ atoms/s is comparable to the highest reported values in the literature, while the mean axial velocity of 21.6(3) m/s is such that the entirety of the flux is within the capture range of a standard MOT.

Overall, the novel design of pyramid source has been successfully produced and tested, providing important insights into the crucial role of aperture size on the performance of a cold-atom source, and a high flux was achieved despite some limitations of the manufacturing process.

[1] Although, the cCAS prototype of Appendix C used the same tolerances and the mechanism was stiff, so some refinement is still required.

8.2 Future Directions

There are several avenues to explore in the future of this project, which can be broadly split into better characterisation of the design (and of cold-atom sources in general), and developing the design into a commercially viable compact source.

8.2.1 Further Characterisation

The key unique feature of the pyramid source design is the adjustable aperture, which allowed multiple aperture sizes to be characterised, however the approximately two-week cycle time to remove the pyramid, change the aperture size, return the system to vacuum and perform the characterisation, limited the number of sizes that were tested within the available time. The resultant measurements show that the flux increased throughout the range with possible saturation for the larger aperture sizes, and this is the next regime to explore in order to better understand the mechanism in play for different aperture sizes, and to be able to optimise the flux. Ideally, in-vacuum adjustability would be incorporated, using a custom vacuum chamber, to greatly reduce the cycle time.

In addition, the pyramid prototype showed high sensitivity to transverse magnetic fields when this was explored for a 0.71 mm aperture, and it is expected that this sensitivity would reduce for larger apertures. Verifying this would be an important step in optimising a portable cold-atom source. Another important design parameter to optimise is the pyramid diameter. The flux from the prototype source showed a linear increase with MOT beam diameter without saturation, therefore using larger diameter pyramids is expected to provide higher fluxes. To explore this, a new prototype is currently being fabricated using the same design as the prototype but with an 85.2 mm diameter; a 55% radial increase and 140% increase in cross-sectional area.

The production of a new pyramid will also allow a better estimate of the ultimate performance because the problems with the coating plant vacuum quality have been addressed

since the coating of the prototype mirrors. The use of ion-beam assisted deposition should eliminate the scatter from the mirrors that restricted the performance of the prototype.

8.2.2 Design Refinements

The novel design of pyramid source proved highly successful, and avenues for additional improvements have been identified, particularly regarding compact vacuum packaging and the mirror substrate material.

The prototype pyramid source was housed in a DN100CF chamber with an ion pump an order of magnitude larger than the pyramid itself, which served as a useful system for validating the design but requires replacing for a compact product. The chamber size was reduced for the cCAS prototype of Appendix C, but, by using off-the-shelf ConFlat flanges for convenience, was still far larger than optimal. To package the pyramid design compactly, a collaboration with Torr Scientific Ltd. is under way to produce a tightly-fitting welded chamber with the possibility of incorporating in-vacuum adjustability of the aperture. As a commercial product, the latter would allow the user to fine tune the aperture to control the conductance (expanding it initially for effective pumping, for example) or operate it as a shutter for the source. The use of permanent magnets to reduce the power requirements of the source, the incorporation of a compact optical system (for producing the MOT beam from a fibre input), and the avoidance of requiring active pumping on the pyramid chamber are options being explored to reduce the footprint of the device.

Glass mirror substrates were used for both prototypes, since these are widely used in pyramid MOTs and are able to achieve high surface quality. These successfully enabled the generation of a high flux from the prototype source, but had several drawbacks. Aside from the cracking difficulties encountered, for which a working solution was found, the shaping and polishing of the glass had a long lead time (particularly after the first batch were defective). An alternative approach is to use metal substrates, which are rarely used in the field of cold-atom physics because of the lower surface quality,[2] although are in widespread use in

[2] Generally, the harder the material the better the surface finish that can be achieved. For polishing

the fields of high-power lasers, especially infrared and far-infrared lasers used industrially for cutting.

A significant advantage of using metal is that it is far easier to machine than glass, therefore arbitrary shapes are possible and the majority of the manufacturing can be done in-house. For example, instead of approximating the ideal mirror shape with a segment of a circular blank, as done for the glass substrates of the prototype, the optimal form can be produced and the outer edges chamfered to avoid the additional radial footprint that the thickness of the glass adds. In addition, an all-metal construction will be more robust than one incorporating glass, and be capable of withstanding bake-out temperatures well above the $\sim 250\,^{\circ}\mathrm{C}$ limit imposed by the presence of epoxy with the glass mirror substrates. As a result, an all-metal pyramid is in the process of being produced, replacing the metal-mounted glass with single pieces of polished stainless steel. The typical reflectivity of stainless steel is 60% in the visible spectrum, but dielectric coatings can be applied in the same way as on glass substrates. Therefore, aside from cases where mirrors have stringent flatness requirements, metal mirror substrates are an acceptable alternative to glass, and in the case of the pyramid source provide multiple benefits for a compact and robust source.

8.3 Concluding Remarks

A compact and high-flux design of cold-atom source has been developed, produced and characterised, providing important information about the optimal parameters for such sources. The ultimate performance was restricted by some manufacturing issues, and several routes to improving the design and performance of the source have been identified, making it a project with an exciting and ambitious future.

stainless steel, the 316 grade is preferable, although the softer 304 grade can also be polished. An exception is titanium which, despite being harder than stainless steel, does not polish well because the surface tends to be crystalline, causing different zones to polish at different rates.

Appendices

A

Adjustable-Aperture Design Technical Details

The features and details of the adjustable-aperture pyramid source designs are described here, building on the outline given in Chapter 3.

A.1 Mirror Mounts

The mirror mounts fixed the mirrors at 45° to the vertical axis to produce the square-based pyramid geometry. The surface contacting the glass had side and bottom lips that located the corner of the glass to facilitate precise alignment, and a gap between the two lips allowed excess epoxy to escape. Similarly, the mount did not extend to the edges of the glass so that excess epoxy would not protrude past the boundaries of the mirrors, since that would obstruct the mechanism. The rear surface of the mount was flat and had a blind, tapped hole to facilitate mounting during the mirror coating process (described in Sec. 4.4).

On the bottom of the mount was a rectangular protrusion that slid along the grooves in the rotator plate. The protrusion had a tapped hole to accommodate the bolt that passed through the slots in the base and rotator plates, and which allowed the motion of the mirrors as well as securing the mirror in place when fully tightened. The bolt hole was placed in line

with the centre of mass of the combined mount and mirror system in the horizontal plane. This avoided any torque about the vertical being applied to the mount during operation of the mechanism, which would have caused increased friction and possible seizing.[1] Ideally the centre of mass of the combined mirror, mount and bolt system should be between the rotator and base plates to avoid torque being applied about the horizontal axis, however this was not possible without adding substantial mass to the region of this system below the base plate. An increase in the size and weight of the source is undesirable for quantum technology applications, where the SWAP criteria of Size, Weight and Power are applied.

A.2 Rotator Plate

The grooves in the rotator plate were 0.05 mm wider than the sliding protrusions of the mirror mounts in order to allow for machining tolerances. The top edges of the grooves were chamfered for two purposes: firstly, to allow for any material in the corresponding corner of the mirror mounts not being fully machined out; and secondly, to provide channels for trapped air to escape from the pyramid structure. Trapped pockets of air in a vacuum system, with a low conductance channel to the main volume, will gradually leak and limit the achievable pressure. Such trapped pockets are called *virtual leaks* and can arise from areas of large surface-to-surface contact. For this reason, the bottom face that contacts the base plate was not flat, but instead had a 5 mm wide lip around the circumference to minimise the area of contacting surface, while not being narrow enough to increase the friction to levels that could cause wear.

A.3 Base Plate

The base plate had an upper lip that protruded 4 mm to correctly locate the rotator plate, and which was 0.1 mm larger in diameter than the rotator plate to allow smooth motion. The

[1] Generating a torque requires energy, thus increasing the energy required to operate the mechanism. This could become significant if operating the mechanism using an in-vacuum motor with low power.

height of the base plate had to be sufficient to accommodate the height of the bolt heads, and 1 mm clearance was allowed. The height of the base plate was achieved by a downwards protruding 5 mm wide lip (again using a narrow lip to minimise surface-to-surface contact). The central hole had a lip that protruded downwards so that conductance to the neighbouring chamber was primarily via the pyramid aperture.

The shape of the base plate slots is important to the motion. If the centre of the slots is described in cylindrical polar coordinates, $\mathrm{d}r/\mathrm{d}\theta$ should be minimised such that a small rotation of the plate results in a small movement of the mirrors. This way, any slack in the mechanism is translated to only minor variations in the position of the mirrors, and this is essential to avoid seizing. However, the shape of the slots is limited by the presence of the other slots; for a 90° increase in θ, the radial position must increase by at least the width of the slots to prevent them intersecting. The start and finish positions are also limited since the diameter of the bolt heads restricts how close the bolt centre can approach the inner and outer downwards facing lips.

A.4 Vacuum Fastenings

Bolts in vacuum must be vented to avoid trapped pockets of air forming virtual leaks. Ordinarily there are two methods: *centre venting*, where a through-hole down the centre of the bolt provides conductance; and *slot venting*, where a slot is machined through the thread parallel to the axis of the bolt. The latter is not suitable for the pyramid source design due to the rotator and base plate slots pushing on the bolts to generate motion. If a slot vent were in line with the pushing motion for one bolt, it would not be in contact with the pushing surface while the others were, potentially leading to mirrors colliding and the mechanism seizing due to the tight tolerances. Centre-vented bolts were therefore used.

B

Standard Vacuum Component Sizes

Commercial off-the-shelf UHV vacuum components come in a discrete range of sizes, which are summarised in Table B.1. The outer diameter of flanges are standardised and well-defined, however the internal diameters of components are variable to within a few millimetres, therefore the values shown in the table are typical values only. Larger sizes of vacuum flange are also available but were not relevant to the project of this thesis.

Equivalent Designations		Flange Outer	Typical Inner
European	North American	Diameter (mm)	Diameter (mm)
DN16CF	CF34	34	15.7
DN35CF or DN40CF	CF70	70	34.8
DN63CF	CF114	114	60.2
DN100CF	CF150	150	97.4
DN160CF	CF200	200	148.2

Table B.1: Standard UHV vacuum component sizes. The inner diameters are typical values only.

C

cCAS Project

Although the nature of cold-atom experiments means that there are a wide range of applications for a high-flux source, the most immediate application is atom interferometry. As part of an Innovate UK project designated cCAS (compact Cold-Atom Source), we collaborated with M Squared Lasers (MSL) to explore the application of the new pyramid source design to their quantum gravimeter project.

C.1 Design

The collaboration occurred in parallel with the characterisation of the prototype described in the preceding chapters, and therefore required the construction of a second prototype. Manufacturing of the original prototype included spare mounted mirrors, and the cCAS prototype therefore utilised mirrors produced and coated identically to those in the original prototype.

An importance difference however was the vacuum chamber. The chamber used for testing only had access to the mounting holes from the viewport, which prevented the pyramid from being sized to tightly fill the chamber. For cCAS a new chamber was built. Since the pyramid mirrors had been designed for DN63CF, this was the chamber size chosen, which required redesigning the rotator and base plates, since those were designed for the DN100CF

testing chamber. In addition to reducing the diameter of the plates, the slots in the base plate were redesigned to reduce the change in radial position of the mirrors with angle ($\mathrm{d}r/\mathrm{d}\theta$). Also, the bolts to secure the mirror mounts in place were replaced by threaded studs with nuts. The reason for this was that when the original pyramid mechanism was repeatedly operated, friction would gradually loosen the mounting bolts. The prototype had the bolts tightened after changing the aperture size, but if the mechanism were to be adjusted in-vacuum, then loosening of the bolts would become an issue. The solution was to replace the bolts by threaded studs, tightly fastened into the mirror mounts, then a nut applied to secure them in place. This would allow the nuts to be set at the correct tightness for smooth motion, then application of epoxy or solder could fix the position of the nut relative to the stud, thereby maintaining the requisite tolerances during repeated operation of the mechanism.

Although the use of a DN63CF vacuum chamber tightly packaged the pyramid, the compactness of the cCAS prototype was limited by the preference to use off-the-shelf components for compatibility with the existing MSL vacuum chamber, and to minimise the lead time for the source. Standard UHV components use ConFlat flanges that provide a reliable and repeatable sealing mechanism, but add substantial bulk to the system. A welded chamber for cCAS would have been approximately 60 mm in diameter, whereas the chamber used was 112 mm (see Fig. C.1). In addition, two DN40CF side ports were included; one for the electrical feedthroughs for the rubidium dispensers, and one for an optional pump to be attached. A DN63CF viewport was attached to one end of the chamber,[1] while a zero-length reducer flange (DN63CF to DN16CF) was placed at the opposite end, to which the pyramid was mounted using two M2×15 mm slot-vented bolts. The reducer flange had a 16 mm long 5 mm diameter hole to provide identical differential pumping to the original prototype.

The anti-Helmholtz coils to generate the magnetic quadrupole field were designed to avoid active cooling and to require minimal electrical power, as opposed to the high-current water-cooled coils used for testing the original prototype. Each coil was composed of 140 turns of

[1] The viewport flange used threaded studs and nuts instead of bolts, so that the exposed studs provided a means to mount the MOT optics directly to the chamber.

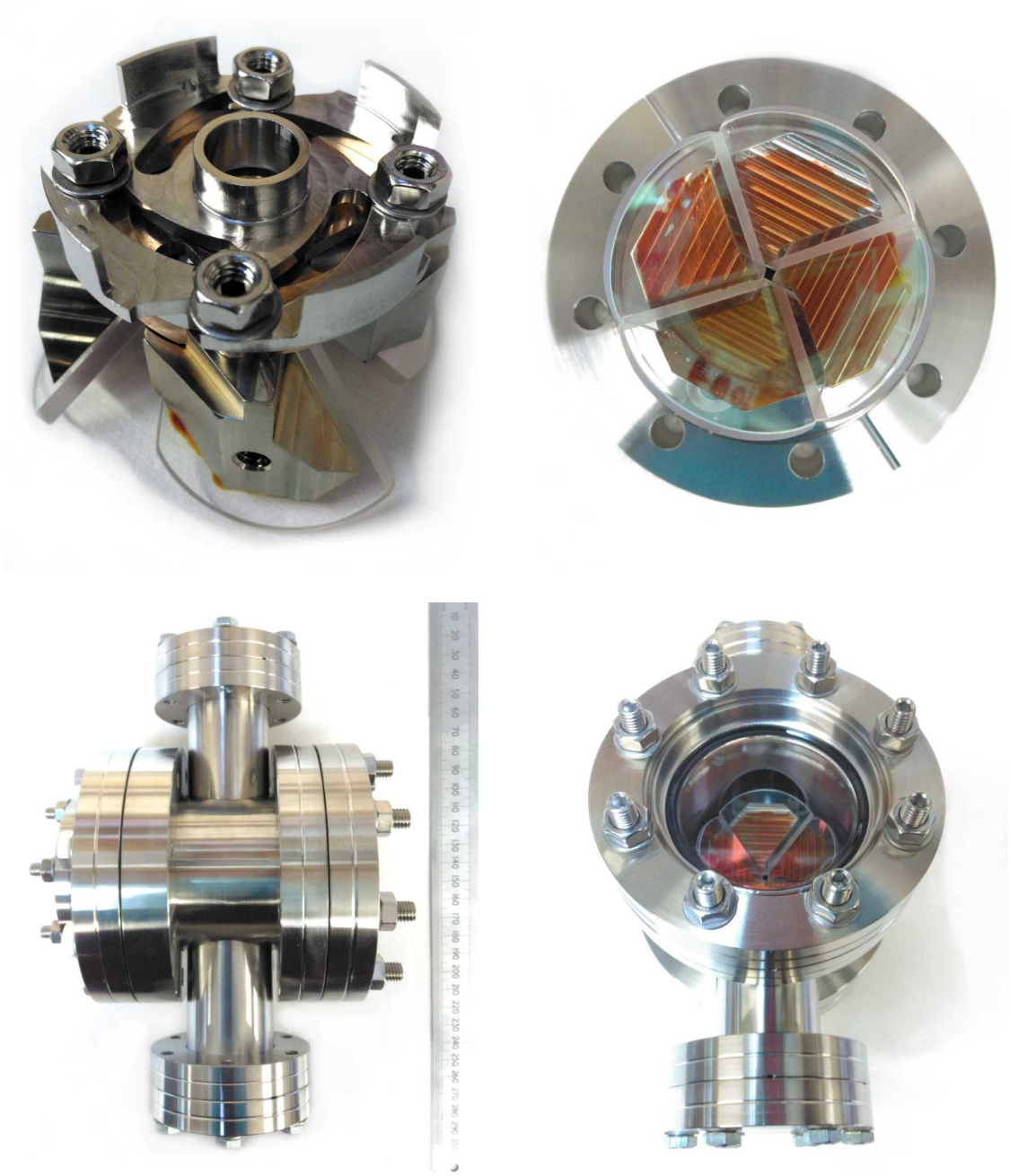


Figure C.1: The prototype source developed for the cCAS project. Top left: the underside of the pyramid with the aperture fully opened. Top right: the pyramid with the aperture closed to 1.5 mm, mounted on a DN63CF to DN16CF zero-length reducer flange. Bottom left: the side view of the DN63CF chamber used to house the cCAS pyramid, with two DN40CF side ports (one for electrical feedthroughs and one for an optional pump) with a ruler for scale. Bottom right: the pyramid mounted inside the chamber. The vast majority of the size and weight of the chamber is from the ConFlat flanges.

1.50 mm ML enamelled copper wire,[2] chosen for its thin insulation layer and temperature limit of 240 °C, which meant that the coils did not limit the maximum bake-out temperature of the source. The coil formers were machined from aluminium to maximise heat transfer, and the estimated radiated power of each coils was 17 W when operated at 5.5 A to produce a gradient of 18 G/cm, which matched that of the original prototype.

C.2 Assembly & Installation

The rotator plate was machined from phosphor bronze, as intended in the original prototype, with identical dimensions for the grooves, however the sliding motion of the mounted mirrors was very stiff. This was despite using the same mounted mirrors that had been tested to slide smoothly in the rotator plate of the original. It may have been that a layer of tarnish on the phosphor bronze (which tarnishes faster than brass) was sufficiently thick to affect the motion, or it could have been that the 0.5 mm additional width of the grooves relative to the protrusions on the mirror mounts is sufficiently marginal that machining variations impact the motion. In either case, further work to understand the optimal tolerances of the mechanism need to be carried out.

Despite this difficulty, the pyramid was assembled using the same cleaning procedures as the original prototype, and mounted in the vacuum chamber as shown in Fig. C.1. The source was then evacuated with a turbo pump and baked at 90 °C using heater tape for a week, after which the pressure was at or below the 5×10^{-9} mbar sensitivity limit of the pressure gauge on the pump-side of the system. The source was then vented with argon, sealed and transported to MSL in Glasgow, where it was installed on a test system for loading a grating MOT. Unfortunately two issues prevented successful operation of the cCAS prototype in Glasgow. Firstly, the vacuum pressure achieved in the test system was 10^{-8} to 10^{-7} mbar, believed to be due to contaminated cleaning solvents, and since all pumping of the pyramid chamber was via the differential pumping hole (rather than having an additional ion pump), this would have limited the pressure in the source to about 10^{-6} to 10^{-5} mbar

[2] Scientific Wire Company ML1500D-500

(using Eq. 3.3). Secondly, since the cCAS mirrors were identical to those of the original pyramid, the substantial scatter was present, and this hindered the MSL engineers from observing MOT fluorescence. As a result, no MOT was observed in the cCAS chamber and this prevented testing of the performance of the source when loading a grating MOT. The collaboration is still ongoing, with new pyramid sources currently being built that should be free from the mirror scatter (see the following chapter).

C.3 Optimal Chamber Length

The chamber for the cCAS pyramid was longer than the minimum length required to fit the pyramid, due to the DN40CF side ports constraints. It is interesting to note that it is not yet decided what the optimum chamber length is. For compactness, clearly a chamber that tightly fits the pyramid is optimal, however the region outside the pyramid volume has axial cooling due to the retroreflected MOT beam, and therefore affects the velocity distribution of atoms entering the pyramid. For a standard 3D quadrupole field, the effects of cooling in this region can be largely neglected since the magnetic field is optimised for the trapping volume of the pyramid, and the field further away just detunes the atoms far from both beams. However, analytic calculations and numerical simulations in Oxford indicate that if the magnetic field outside the pyramid region is controlled and adjusted to have a similar profile to that of a Zeeman slower, then the fraction of atoms entering the pyramid trapping region with velocity below the capture velocity would significantly increase, resulting in an estimated 2 to 5 fold increase in the flux. This would be a novel and moderately straightforward extension to the cold-atom source design presented in this thesis, and will form a part of future work to improve the source performance.

Acronyms

AOI	Angle of incidence
AOM	Acousto-optic modulator
ASE	Amplified spontaneous emission
CTE	Coefficient of thermal expansion
ECDL	External-cavity diode laser
EOM	Electro-optic modulator
FWHM	Full width at half maximum
HV	High vacuum
IBAD	Ion beam assisted deposition
IPA	Isopropyl alcohol
LVIS	Low-velocity intense source
MOT	Magneto-optical trap
MSL	M Squared Lasers
MTS	Modulation transfer spectroscopy
OBEs	Optical Bloch equations
PBS	Polarising beam splitter
TA	Tapered amplifier
Ti:sapphire	Titanium-doped sapphire laser
UHV	Ultra-high vacuum
VCO	Voltage-controlled oscillator

Bibliography

[1] X. Wu et al. "Multiaxis atom interferometry with a single-diode laser and a pyramidal magneto-optical trap". In: *Optica* 4.12 (Dec. 2017), p. 1545. arXiv: 1707.08693. DOI: 10.1364/OPTICA.4.001545 (cit. on pp. 1, 2).

[2] J. Kitching, S. Knappe & E. A. Donley. "Atomic sensors - A review". In: *IEEE Sensors Journal* 11.9 (Sept. 2011), pp. 1749–1758. DOI: 10.1109/JSEN.2011.2157679 (cit. on p. 1).

[3] A. V. Rakholia, H. J. McGuinness & G. W. Biedermann. "Dual-axis high-data-rate atom interferometer via cold ensemble exchange". In: *Physical Review Applied* 2.5 (Nov. 2014), p. 054012. arXiv: 1407.3847. DOI: 10.1103/PhysRevApplied.2.054012 (cit. on pp. 1, 2).

[4] P. Gillot et al. "The LNE-SYRTE cold atom gravimeter". In: *2016 European Frequency and Time Forum (EFTF)*. IEEE, Apr. 2016, pp. 1–3. DOI: 10.1109/EFTF.2016.7477832 (cit. on pp. 1, 2).

[5] N. Poli et al. "Precision measurement of gravity with cold atoms in an optical lattice and comparison with a classical gravimeter". In: *Physical Review Letters* 106.3 (Jan. 2011), p. 038501. arXiv: 1010.2033. DOI: 10.1103/PhysRevLett.106.038501 (cit. on p. 1).

[6] L. Hu et al. "Atom interferometry with the Sr optical clock transition". In: *Physical Review Letters* 119.26 (Dec. 2017), p. 263601. arXiv: 1708.05116. DOI: 10.1103/PhysRevLett.119.263601 (cit. on p. 1).

[7] B. Barrett, I. Chan & A. Kumarakrishnan. "Atom-interferometric techniques for measuring uniform magnetic field gradients and gravitational acceleration". In: *Physical Review A - Atomic, Molecular, and Optical Physics* (2011). arXiv: 1104.4577. DOI: 10.1103/PhysRevA.84.063623 (cit. on p. 1).

[8] Y. Bidel et al. "Compact cold atom gravimeter for field applications". In: *Applied Physics Letters* 102.14 (Apr. 2013), p. 144107. arXiv: 1302.1518. DOI: 10.1063/1.4801756 (cit. on pp. 1, 2).

[9] A. Louchet-Chauvet et al. "The influence of transverse motion within an atomic gravimeter". In: *New Journal of Physics* 13.6 (June 2011), p. 065025. DOI: 10.1088/1367-2630/13/6/065025 (cit. on p. 1).

[10] H. Müller et al. "Atom-interferometry tests of the isotropy of post-Newtonian gravity". In: *Physical Review Letters* 100.3 (Jan. 2008), p. 031101. arXiv: 0710.3768. DOI: 10.1103/PhysRevLett.100.031101 (cit. on p. 1).

[11] B. Elder et al. "Chameleon dark energy and atom interferometry". In: *Physical Review D* 94.4 (Aug. 2016), p. 044051. DOI: 10.1103/PhysRevD.94.044051 (cit. on p. 1).

[12] J. M. Hogan et al. "An atomic gravitational wave interferometric sensor in low earth orbit (AGIS-LEO)". In: *General Relativity and Gravitation* 43.7 (July 2011), pp. 1953–2009. arXiv: 1009.2702. DOI: 10.1007/s10714-011-1182-x (cit. on p. 1).

[13] S. Dimopoulos et al. "General relativistic effects in atom interferometry". In: *Physical Review D* 78.4 (Aug. 2008), p. 042003. arXiv: 0802.4098. DOI: 10.1103/PhysRevD.78.042003 (cit. on p. 1).

[14] C. Burrage, E. J. Copeland & E. A. Hinds. "Probing dark energy with atom interferometry". In: *Journal of Cosmology and Astroparticle Physics* 2015.03 (Mar. 2015), pp. 042–042. arXiv: 1408.1409. DOI: 10.1088/1475-7516/2015/03/042 (cit. on p. 1).

[15] A. D. Ludlow et al. "Optical atomic clocks". In: *Reviews of Modern Physics* 87.2 (June 2015), pp. 637–701. DOI: 10.1103/RevModPhys.87.637 (cit. on p. 1).

[16] G. E. Marti et al. "Imaging optical frequencies with 100 μHz precision and 1.1 μm resolution". In: *Physical Review Letters* 120.10 (Mar. 2018), p. 103201. DOI: 10.1103/PhysRevLett.120.103201 (cit. on p. 1).

[17] M. Schioppo et al. "Ultrastable optical clock with two cold-atom ensembles". In: *Nature Photonics* 11.1 (Jan. 2017), pp. 48–52. arXiv: 1607.06867. DOI: 10.1038/nphoton.2016.231 (cit. on p. 1).

[18] S. Chu et al. "Three-dimensional viscous confinement and cooling of atoms by resonance radiation pressure". In: *Physical Review Letters* 55.1 (July 1985), pp. 48–51. DOI: 10.1103/PhysRevLett.55.48 (cit. on p. 1).

[19] E. L. Raab et al. "Trapping of neutral sodium atoms with radiation pressure". In: *Physical Review Letters* 59.23 (Dec. 1987), pp. 2631–2634. DOI: 10.1103/PhysRevLett.59.2631 (cit. on pp. 2, 47).

[20] H. J. Lewandowski et al. "Simplified system for creating a Bose-Einstein condensate". English. In: *Journal of Low Temperature Physics* 132.5-6 (2003), pp. 309–367. DOI: 10.1023/A:1024800600621 (cit. on p. 2).

[21] A. Hinton et al. "A portable magneto-optical trap with prospects for atom interferometry in civil engineering". In: *Philosophical Transactions of the Royal Society A: Mathematical, Physical and Engineering Sciences* 375.2099 (Aug. 2017), p. 20160238. DOI: 10.1098/rsta.2016.0238 (cit. on pp. 2, 50, 53–55, 69).

[22] V. Ménoret et al. "A transportable cold atom inertial sensor for space applications". In: *International Conference on Space Optics 2010*. Ed. by N. Kadowaki. SPIE, Nov. 2010, p. 110. DOI: 10.1117/12.2309256 (cit. on p. 2).

[23] Z. K. Hu et al. "Demonstration of an ultrahigh-sensitivity atom-interferometry absolute gravimeter". In: *Physical Review A* 88.4 (Oct. 2013), p. 043610. DOI: 10.1103/PhysRevA.88.043610 (cit. on p. 2).

[24] S. Pollock et al. "Integrated magneto-optical traps on a chip using silicon pyramid structures". In: *Optics Express* 17.16 (Aug. 2009), p. 14109. arXiv: 0905.0777. DOI: 10.1364/OE.17.014109 (cit. on p. 2).

[25] S. Kulas et al. "Miniaturized lab system for future cold atom experiments in microgravity". In: *Microgravity Science and Technology* 29.1 (2017), pp. 37–48. DOI: 10.1007/s12217-016-9524-7 (cit. on p. 2).

[26] C. C. Nshii et al. "A surface-patterned chip as a strong source of ultracold atoms for quantum technologies". In: *Nature Nanotechnology* 8.5 (May 2013), pp. 321–324. DOI: 10.1038/nnano.2013.47 (cit. on pp. 2, 46, 51).

[27] H. Müntinga et al. "Interferometry with Bose-Einstein condensates in microgravity". In: *Physical Review Letters* 110.9 (Feb. 2013), p. 093602. arXiv: 1301.5883. DOI: 10.1103/PhysRevLett.110.093602 (cit. on p. 2).

[28] E. A. Salim et al. "Compact, microchip-based systems for practical applications of ultracold atoms". In: *Quantum Information Processing* 10.6 (Dec. 2011), pp. 975–994. DOI: 10.1007/s11128-011-0300-8 (cit. on pp. 2, 3).

[29] F. Esnault et al. "HORACE: A compact cold atom clock for Galileo". In: *Advances in Space Research* 47.5 (Mar. 2011), pp. 854–858. DOI: 10.1016/j.asr.2010.12.012 (cit. on p. 2).

[30] L. Liu et al. "In-orbit operation of an atomic clock based on laser-cooled 87Rb atoms". In: *Nature Communications* 9.1 (Dec. 2018), p. 2760. DOI: 10.1038/s41467-018-05219-z (cit. on p. 2).

[31] C. Freier et al. "Mobile quantum gravity sensor with unprecedented stability". In: *Journal of Physics: Conference Series* 723 (June 2016), p. 012050. DOI: 10.1088/1742-6596/723/1/012050 (cit. on p. 2).

[32] J. Lautier et al. "Hybridizing matter-wave and classical accelerometers". In: *Applied Physics Letters* 105.14 (Oct. 2014), p. 144102. arXiv: 1410.0050. DOI: 10.1063/1.4897358 (cit. on p. 2).

[33] B. Battelier et al. "Development of compact cold-atom sensors for inertial navigation". In: *SPIE Photonics Europe*. Ed. by J. Stuhler & A. J. Shields. Vol. 9900. Apr. 2016, p. 990004. DOI: 10.1117/12.2228351 (cit. on p. 2).

[34] E. R. Elliott et al. "NASA's cold atom lab (CAL): system development and ground test status". In: *npj Microgravity* 4.1 (Dec. 2018), p. 16. DOI: 10.1038/s41526-018-0049-9 (cit. on p. 3).

[35] F. Theron et al. "Frequency-doubled telecom fiber laser for a cold atom interferometer using optical lattices". In: *Optics Communications* 393 (June 2017), pp. 152–155. arXiv: 1610.02830. DOI: 10.1016/j.optcom.2017.02.013 (cit. on p. 3).

[36] Q. Wang et al. "A compact laser system for the cold atom gravimeter". In: *Optics Communications* 358 (Jan. 2016), pp. 82–87. DOI: 10.1016/j.optcom.2015.09.001 (cit. on p. 3).

[37] M. de Angelis et al. "iSense: A portable ultracold-atom-based gravimeter". In: *Procedia Computer Science* 7 (2011), pp. 334–336. DOI: 10.1016/j.procs.2011.09.067 (cit. on p. 3).

[38] J. A. Rushton, M. Aldous & M. D. Himsworth. "Contributed review: The feasibility of a fully miniaturized magneto-optical trap for portable ultracold quantum technology". In: *Review of Scientific Instruments* 85.12 (Dec. 2014), p. 121501. DOI: 10.1063/1.4904066 (cit. on pp. 3, 58, 70).

[39] V. Schkolnik et al. "A compact and robust diode laser system for atom interferometry on a sounding rocket". In: *Applied Physics B* 122.8 (Aug. 2016), p. 217. DOI: 10.1007/s00340-016-6490-0 (cit. on p. 3).

[40] R. Saint et al. "3D-printed components for quantum devices". In: *Scientific Reports* 8.1 (Dec. 2018), p. 8368. DOI: 10.1038/s41598-018-26455-9 (cit. on p. 3).

[41] K. I. Lee et al. "Single-beam atom trap in a pyramidal and conical hollow mirror". In: *Optics Letters* 21.15 (Aug. 1996), p. 1177. DOI: 10.1364/OL.21.001177 (cit. on pp. 4, 49, 53, 54, 63).

[42] J. Arlt et al. "A pyramidal magneto-optical trap as a source of slow atoms". In: *Optics Communications* 157.1-6 (Dec. 1998), pp. 303–309. DOI: 10.1016/S0030-4018(98)00499-4 (cit. on pp. 4, 39, 44, 50, 53, 54, 79, 149).

[43] H. Perrin. *Light-matter interaction / Laser cooling and trapping*. École Prédoctorale de Physique des Houches, 2014. URL: http://www.phlam.univ-lille1.fr/leshouches/leshouches14.html (cit. on pp. 6, 19).

[44] C. Foot. *Atomic physics*. Oxford University Press, 2011. URL: https://global.oup.com/ukhe/product/9780198506966 (cit. on pp. 6, 18).

[45] S. J. Blundell & K. M. Blundell. *Concepts in thermal physics*. 1st ed. Oxford University Press, 2006. URL: https://global.oup.com/academic/product/9780199562107 (cit. on p. 6).

[46] R. Grimm, M. Weidemüller & Y. B. Ovchinnikov. "Optical dipole traps for neutral atoms". In: *Advances in Atomic, Molecular and Optical Physics*. Feb. 2000, pp. 95–170. DOI: 10.1016/S1049-250X(08)60186-X (cit. on p. 14).

[47] C. N. Cohen-Tannoudji & W. D. Phillips. "New mechanisms for laser cooling". In: *Physics Today* 43.10 (Oct. 1990), pp. 33–40. DOI: 10.1063/1.881239 (cit. on p. 17).

[48] M. Kasevich & S. Chu. "Laser cooling below a photon recoil with three-level atoms". In: *Physical Review Letters* 69.12 (Sept. 1992), p. 1741. DOI: 10.1103/PhysRevLett.69.1741 (cit. on p. 19).

[49] A. Aspect et al. "Laser cooling below the one-photon recoil energy by velocity-selective coherent population trapping". In: *Physical Review Letters* 61.7 (Aug. 1988), pp. 826–829. DOI: 10.1103/PhysRevLett.61.826 (cit. on p. 19).

[50] S. Stellmer et al. "Laser cooling to quantum degeneracy". In: *Physical Review Letters* 110.26 (June 2013), p. 263003. arXiv: 1301.4776. DOI: 10.1103/PhysRevLett.110.263003 (cit. on p. 19).

[51] J. Schoser et al. "Intense source of cold Rb atoms from a pure two-dimensional magneto-optical trap". In: *Physical Review A* 66.2 (Aug. 2002), p. 023410. DOI: 10.1103/PhysRevA.66.023410 (cit. on pp. 26, 40, 44, 46–48, 148, 149).

[52] A. Cable, M. Prentiss & N. P. Bigelow. "Observations of sodium atoms in a magnetic molasses trap loaded by a continuous uncooled source". In: *Optics Letters* 15.9 (May 1990), p. 507. DOI: 10.1364/OL.15.000507 (cit. on p. 29).

[53] A. M. Steane, M. Chowdhury & C. J. Foot. "Radiation force in the magneto-optical trap". In: *Journal of the Optical Society of America B* 9.12 (Dec. 1992), p. 2142. DOI: 10.1364/JOSAB.9.002142 (cit. on p. 29).

[54] K. Dieckmann et al. "Two-dimensional magneto-optical trap as a source of slow atoms". In: *Physical Review A* 58.5 (Nov. 1998), pp. 3891–3895. DOI: 10.1103/PhysRevA.58.3891 (cit. on pp. 29, 44, 46, 48, 129, 149).

[55] D. A. Steck. "Rubidium 87 D line data". In: (Jan. 2015). URL: http://steck.us/alkalidata (cit. on pp. 31, 90).

[56] X. Xu et al. "Cooling and trapping of atomic strontium". In: *Journal of the Optical Society of America B* 20.5 (May 2003), p. 968. DOI: 10.1364/JOSAB.20.000968 (cit. on p. 32).

[57] C. G. Townsend et al. "Phase-space density in the magneto-optical trap". In: *Physical Review A* 52.2 (Aug. 1995), pp. 1423–1440. DOI: 10.1103/PhysRevA.52.1423 (cit. on p. 33).

[58] A. M. Steane & C. J. Foot. "Laser cooling below the Doppler limit in a magneto-optical trap". In: *Europhysics Letters (EPL)* 14.3 (Feb. 1991), pp. 231–236. DOI: 10.1209/0295-5075/14/3/008 (cit. on p. 33).

[59] M. Haw et al. "Magneto-optical trap loading rate dependence on trap depth and vapor density". In: *Journal of the Optical Society of America B* 29.3 (Mar. 2012), p. 475. DOI: 10.1364/JOSAB.29.000475 (cit. on p. 34).

[60] K. Lindquist, M. Stephens & C. Wieman. "Experimental and theoretical study of the vapor-cell Zeeman optical trap". In: *Physical Review A* 46.7 (Oct. 1992), pp. 4082–4090. DOI: 10.1103/PhysRevA.46.4082 (cit. on p. 34).

[61] K. E. Gibble, S. Kasapi & S. Chu. "Improved magneto-optic trapping in a vapor cell". In: *Optics Letters* 17.7 (Apr. 1992), p. 526. DOI: 10.1364/OL.17.000526 (cit. on p. 34).

[62] M. Gildemeister. "Trapping ultracold atoms in time-averaged adiabatic potentials". Ph.D. Thesis. University of Oxford, 2010. URL: https://ora.ox.ac.uk/objects/ora:5672 (cit. on p. 36).

[63] J. Léonard et al. "Optical transport and manipulation of an ultracold atomic cloud using focus-tunable lenses". In: *New Journal of Physics* 16.9 (Sept. 2014), p. 093028. arXiv: 1406.2336. DOI: 10.1088/1367-2630/16/9/093028 (cit. on p. 36).

[64] J. Söding et al. "Short-distance atomic beam deceleration with a stimulated light force". In: *Physical Review Letters* 78.8 (Feb. 1997), pp. 1420–1423. DOI: 10.1103/PhysRevLett.78.1420 (cit. on p. 37).

[65] M. R. Williams et al. "Bichromatic force measurements using atomic beam deflections". In: *Physical Review A* 61.2 (Jan. 2000), p. 023408. DOI: 10.1103/PhysRevA.61.023408 (cit. on p. 37).

[66] L. Yatsenko & H. Metcalf. "Dressed-atom description of the bichromatic force". In: *Physical Review A* 70.6 (Dec. 2004), p. 063402. DOI: 10.1103/PhysRevA.70.063402 (cit. on p. 37).

[67] T. C. Liebisch et al. "Atom-number amplification in a magneto-optical trap via stimulated light forces". In: *Physical Review A* 85.1 (Jan. 2012), p. 013407. DOI: 10.1103/PhysRevA.85.013407 (cit. on p. 37).

[68] M. A. Chieda & E. E. Eyler. "Bichromatic slowing of metastable helium". In: *Physical Review A* 86.5 (Nov. 2012), p. 053415. arXiv: 1207.4989. DOI: 10.1103/PhysRevA.86.053415 (cit. on p. 37).

[69] C. Corder et al. "Laser cooling without spontaneous emission using the bichromatic force". In: *Journal of the Optical Society of America B* 32.5 (May 2015), B75. DOI: 10.1364/JOSAB.32.000B75 (cit. on p. 37).

[70] X. Hua, C. Corder & H. Metcalf. "Simulation of laser cooling by the bichromatic force". In: *Physical Review A* 93.6 (June 2016), p. 063410. DOI: 10.1103/PhysRevA.93.063410 (cit. on p. 37).

[71] K. D. Rathod, A. K. Singh & V. Natarajan. "Continuous beam of laser-cooled Yb atoms". In: *EPL (Europhysics Letters)* 102.4 (May 2013), p. 43001. arXiv: 1303.7057. DOI: 10.1209/0295-5075/102/43001 (cit. on pp. 39, 41, 127).

[72] G. Lamporesi et al. "Compact high-flux source of cold sodium atoms". In: *Review of Scientific Instruments* 84.6 (June 2013), p. 063102. arXiv: 1301.6566. DOI: 10.1063/1.4808375 (cit. on pp. 39, 41, 45, 110, 127).

[73] M. Martínez Valado et al. "Atomic transfer between two magneto-optical traps". In: *SPIE 8001, International Conference on Applications of Optics and Photonics*. Ed. by M. F. Costa. May 2011, p. 800118. DOI: 10.1117/12.892169 (cit. on p. 39).

[74] K. H. Kim et al. "Cold atomic beam produced by a conical mirror funnel". In: *Physical Review A* 64.1 (May 2001), p. 013402. DOI: 10.1103/PhysRevA.64.013402 (cit. on p. 39).

[75] S. P. Ram, S. K. Tiwari & S. R. Mishra. "Improved transfer efficiency with pulsed atom transfer between two magneto-optical traps". In: (Mar. 2010). arXiv: 1003.5519 (cit. on p. 39).

[76] S. R. Chanu, K. D. Rathod & V. Natarajan. "Generation of a cold pulsed beam of Rb atoms by transfer from a 3D magneto-optic trap". In: *Physics Letters A* 380.37 (Aug. 2016), pp. 2943–2946. arXiv: 1608.00385. DOI: 10.1016/j.physleta.2016.07.022 (cit. on pp. 39, 46, 48).

[77] K. Gibble, S. Chang & R. Legere. "Direct observation of s-wave atomic collisions". In: *Physical Review Letters* 75.14 (Oct. 1995), pp. 2666–2669. DOI: 10.1103/PhysRevLett.75.2666 (cit. on p. 39).

[78] C. J. Myatt et al. "Multiply loaded magneto-optical trap". In: *Optics Letters* 21.4 (Feb. 1996), p. 290. DOI: 10.1364/OL.21.000290 (cit. on p. 39).

[79] M. Prevedelli et al. "Trapping and cooling of potassium isotopes in a double-magneto-optical-trap apparatus". In: *Physical Review A* 59.1 (Jan. 1999), pp. 886–888. DOI: 10.1103/PhysRevA.59.886 (cit. on p. 39).

[80] L. Cacciapuoti et al. "A continuous cold atomic beam from a magneto-optical trap". In: *The European Physical Journal D* 15.2 (Aug. 2001), pp. 245–249. DOI: 10.1007/s100530170172 (cit. on pp. 39, 44, 48, 110, 149).

[81] T. B. Swanson et al. "Efficient transfer in a double magneto-optical trap system". In: *Journal of the Optical Society of America B* 15.11 (Nov. 1998), p. 2641. DOI: 10.1364/JOSAB.15.002641 (cit. on p. 39).

[82] A. Parsagian & M. Kleinert. "Designing and building a permanent magnet Zeeman slower for calcium atoms using a 3D printer". In: *American Journal of Physics* 83.10 (Oct. 2015), pp. 892–899. DOI: 10.1119/1.4930080 (cit. on p. 40).

[83] C. J. Dedman et al. "Optimum design and construction of a Zeeman slower for use with a magneto-optic trap". In: *Review of Scientific Instruments* 75.12 (Dec. 2004), pp. 5136–5142. DOI: 10.1063/1.1820524 (cit. on p. 40).

[84] C. Slowe, L. Vernac & L. V. Hau. "High flux source of cold rubidium atoms". In: *Review of Scientific Instruments* 76.10 (Oct. 2005), p. 103101. DOI: 10.1063/1.2069651 (cit. on pp. 44, 64, 126, 149).

[85] A. Paris-Mandoki et al. "Versatile cold atom source for multi-species experiments". In: *Review of Scientific Instruments* 85.11 (Nov. 2014), p. 113103. DOI: 10.1063/1.4900577 (cit. on pp. 44, 110, 149).

[86] *Beam-RevC cold atomic beam system*. Tech. rep. AOSense, Inc. URL: https://aosense.com/product/cold-atomic-beam-system/ (cit. on pp. 44, 149).

[87] Y. B. Ovchinnikov. "Compact magneto-optical sources of slow atoms". In: *Optics Communications* 249.4-6 (May 2005), pp. 473–481. DOI: 10.1016/j.optcom.2005.01.047 (cit. on pp. 44, 46, 47, 63, 110, 129, 134, 149).

[88] J. Ramirez-Serrano et al. "Multistage two-dimensional magneto-optical trap as a compact cold atom beam source". In: *Optics Letters* 31.6 (Mar. 2006), p. 682. DOI: 10.1364/OL.31.000682 (cit. on pp. 44, 47, 110, 149).

[89] P. Cren et al. "Loading of a cold atomic beam into a magnetic guide". English. In: *The European Physical Journal D - Atomic, Molecular and Optical Physics* 20.1 (July 2002), pp. 107–116. DOI: 10.1140/epjd/e2002-00106-3 (cit. on pp. 44, 45, 48, 127, 149).

[90] J. R. Kellogg et al. "A compact high-efficiency cold atom beam source". English. In: *Applied Physics B* 109.1 (Oct. 2012), pp. 61–64. arXiv: 1107.5602. DOI: 10.1007/s00340-012-5220-5 (cit. on pp. 44, 45, 48, 110, 149).

[91] S. J. Park, J. Noh & J. Mun. "Cold atomic beam from a two-dimensional magneto-optical trap with two-color pushing laser beams". In: *Optics Communications* 285.19 (Sept. 2012), pp. 3950–3954. DOI: 10.1016/j.optcom.2012.05.041 (cit. on pp. 44–46, 48, 127, 149).

[92] I. Nosske et al. "Two-dimensional magneto-optical trap as a source for cold strontium atoms". In: *Physical Review A* 96.5 (Nov. 2017), p. 053415. arXiv: 1709.00790. DOI: 10.1103/PhysRevA.96.053415 (cit. on pp. 44, 149).

[93] H. Chen & E. Riis. "Cold atomic beam from a rubidium funnel". In: *Applied Physics B* 70.5 (May 2000), pp. 665–670. DOI: 10.1007/s003400050878 (cit. on pp. 44, 48, 149).

[94] R. Conroy et al. "Compact, robust source of cold atoms for efficient loading of a magnetic guide". In: *Optics Communications* 226.1-6 (Oct. 2003), pp. 259–266. DOI: 10.1016/j.optcom.2003.09.012 (cit. on pp. 44, 45, 48, 149).

[95] S. Chaudhuri, S. Roy & C. S. Unnikrishnan. "Realization of an intense cold Rb atomic beam based on a two-dimensional magneto-optical trap: Experiments and comparison with simulations". In: *Physical Review A* 74.2 (Aug. 2006), p. 023406. DOI: 10.1103/PhysRevA.74.023406 (cit. on pp. 44, 46, 48, 126, 148, 149).

[96] *CASC-1000 cold atom source cell*. Tech. rep. ColdQuanta. URL: https://www.coldquanta.com/standard_products/cold-atom-source-cells/ (cit. on pp. 44, 149).

[97] S. Weyers et al. "A continuous beam of cold cesium atoms extracted from a two-dimensional magneto-optical trap". In: *Optics Communications* 143.1-3 (Nov. 1997), pp. 30–34. DOI: 10.1016/S0030-4018(97)00312-X (cit. on pp. 44, 45, 149).

[98] W. Wohlleben et al. "An atom faucet". English. In: *The European Physical Journal D* 15.2 (Aug. 2001), pp. 237–244. DOI: 10.1007/s100530170171 (cit. on pp. 44, 46, 48, 127, 129, 149).

[99] Z. T. Lu et al. "Low-velocity intense source of atoms from a magneto-optical trap". In: *Physical Review Letters* 77.16 (Oct. 1996), pp. 3331–3334. DOI: 10.1103/PhysRevLett.77.3331 (cit. on pp. 44, 46, 54, 129, 134, 149).

[100] E. A. Donley, T. P. Heavner & S. R. Jefferts. "Optical molasses loaded from a low-velocity intense source of atoms: an atom source for improved atomic fountains". In: *IEEE Transactions on Instrumentation and Measurement* 54.5 (Oct. 2005), pp. 1905–1910. DOI: 10.1109/TIM.2005.853218 (cit. on pp. 44, 149).

[101] R. Williamson et al. "A magneto-optical trap loaded from a pyramidal funnel". In: *Optics Express* 3.3 (Aug. 1998), p. 111. DOI: 10.1364/OE.3.000111 (cit. on pp. 44, 50, 53, 63, 149).

[102] A. Camposeo et al. "A cold cesium atomic beam produced out of a pyramidal funnel". In: *Optics Communications* 200.1-6 (Dec. 2001), pp. 231–239. DOI: 10.1016/S0030-4018(01)01643-1 (cit. on pp. 44, 48, 53, 54, 126, 127, 149).

[103] J. M. Kohel et al. "Generation of an intense cold-atom beam from a pyramidal magneto-optical trap: experiment and simulation". In: *Journal of the Optical Society of America B* 20.6 (June 2003), p. 1161. DOI: 10.1364/JOSAB.20.001161 (cit. on pp. 44, 53, 54, 63, 126, 134, 148, 149).

[104] N. Lundblad et al. "Two-species cold atomic beam". In: *Journal of the Optical Society of America B* 21.1 (Jan. 2004), p. 3. DOI: 10.1364/JOSAB.21.000003 (cit. on pp. 44, 110, 149).

[105] M. L. Harris, P. Tierney & S. L. Cornish. "Magnetic trapping of a cold Rb-Cs atomic mixture". In: *Journal of Physics B: Atomic, Molecular and Optical Physics* 41.3 (Feb. 2008), p. 035303. arXiv: 0711.2598. DOI: 10.1088/0953-4075/41/3/035303 (cit. on pp. 44, 64, 149).

[106] E. Imhof et al. "Two-dimensional grating magneto-optical trap". In: *Physical Review A* 96.3 (Sept. 2017), p. 033636. DOI: 10.1103/PhysRevA.96.033636 (cit. on pp. 44, 48, 51, 71, 110, 149).

[107] P. Berthoud, E. Fretel & P. Thomann. "Bright, slow, and continuous beam of laser-cooled cesium atoms". In: *Physical Review A* 60.6 (Dec. 1999), R4241–R4244. DOI: 10.1103/PhysRevA.60.R4241 (cit. on pp. 45, 46).

[108] B. K. Teo, T. Cubel & G. Raithel. "A slow and dark atomic beam". In: *Optics Communications* 212.4-6 (Nov. 2002), pp. 307–315. DOI: 10.1016/S0030-4018(02)02001-1 (cit. on pp. 45, 46, 48).

[109] F. Shimizu, K. Shimizu & H. Takuma. "Four-beam laser trap of neutral atoms". In: *Optics Letters* 16.5 (Mar. 1991), p. 339. DOI: 10.1364/OL.16.000339 (cit. on p. 46).

[110] C. Chesman et al. "Two-and four-beam magneto-optical trapping of neutral atoms". In: *Optics Letters* 19.16 (Aug. 1994), p. 1237. DOI: 10.1364/OL.19.001237 (cit. on p. 46).

[111] J. Reichel, W. Hänsel & T. W. Hänsch. "Atomic micromanipulation with magnetic surface traps". In: *Physical Review Letters* 83.17 (Oct. 1999), pp. 3398–3401. DOI: 10.1103/PhysRevLett.83.3398 (cit. on p. 48).

[112] W. Hänsel et al. "Bose-Einstein condensation on a microelectronic chip". In: *Nature* 413.6855 (Oct. 2001), pp. 498–501. DOI: 10.1038/35097032 (cit. on p. 48).

[113] M. L. Harris. "Realisation of a cold mixture of rubidium and caesium". Ph.D. Thesis. University of Durham, 2008. URL: http://etheses.dur.ac.uk/2300/ (cit. on pp. 48, 52–54, 110).

[114] M. Vangeleyn et al. "Single-laser, one beam, tetrahedral magneto-optical trap". In: *Optics Express* 17.16 (Aug. 2009), p. 13601. DOI: 10.1364/OE.17.013601 (cit. on pp. 49, 50, 55).

[115] J. A. Kim et al. "Atom trap in an axicon mirror". In: *Optics Letters* 22.2 (Jan. 1997), p. 117. DOI: 10.1364/OL.22.000117 (cit. on pp. 49, 63).

[116] V. Shah et al. "A miniature cold-atom frequency standard". In: *arXiv* (2011). arXiv: 1111.5890 (cit. on pp. 49, 69).

[117] D. R. Scherer et al. "Progress on a miniature cold-atom frequency standard". In: *arXiv* (2014). arXiv: 1411.5006v1 (cit. on p. 49).

[118] M. Vangeleyn et al. "Laser cooling with a single laser beam and a planar diffractor". In: *Optics Letters* 35.20 (Oct. 2010), p. 3453. arXiv: 1006.4526. DOI: 10.1364/OL.35.003453 (cit. on p. 51).

[119] J. P. McGilligan et al. "Phase-space properties of magneto-optical traps utilising micro-fabricated gratings". In: *Optics Express* 23.7 (Apr. 2015), p. 8948. arXiv: 1503.01702v1. DOI: 10.1364/OE.23.008948 (cit. on p. 51).

[120] J. G. H. Franssen, M. A. W. van Ninhuijs & O. J. Luiten. "Compact ultracold electron source based on a grating magneto optical trap". In: *arXiv* (June 2018). arXiv: 1806.10504 (cit. on p. 51).

[121] J. P. McGilligan et al. "Grating chips for quantum technologies". In: *Scientific Reports* 7.1 (Dec. 2017), p. 384. DOI: 10.1038/s41598-017-00254-0 (cit. on p. 51).

[122] D. McCarron. "A quantum degenerate mixture of 87Rb and 133Cs". Ph.D. Thesis. University of Durham, 2011. URL: http://etheses.dur.ac.uk/3242/ (cit. on pp. 52–54, 110).

[123] M. Vangeleyn. "Atom trapping in non-trivial geometries for micro-fabrication applications". Ph.D. Thesis. University of Strathclyde, 2011. URL: http://photonics.phys.strath.ac.uk/wp-content/uploads/2013/08/MVAngeleyn_Thesis_final.pdf (cit. on p. 52).

[124] P. Tierney. "Magnetic trapping of an ultracold 87Rb 133Cs atomic mixture". Ph.D. Thesis. University of Durham, Sept. 2009. URL: http://etheses.dur.ac.uk/2039/ (cit. on pp. 53, 54).

[125] A. Harsono. "Dipole trapping and manipulation of ultra-cold atoms". Ph.D. Thesis. University of Oxford, 2006. URL: https://www2.physics.ox.ac.uk/sites/default/files/2013-01-19/andrian_pdf_71380.pdf (cit. on pp. 53, 54, 64, 87).

[126] B. T. Sheard. "Magnetic transport and Bose-Einstein condensation of rubidium atoms". Ph.D. Thesis. University of Oxford, 2010. URL: https://ora.ox.ac.uk/objects/ora:5670 (cit. on pp. 53, 54, 71, 78).

[127] T. Li. "Manipulation of cold atoms using an optical one-way barrier". Ph.D. Thesis. University of Oregon, 2008. URL: http://atomoptics-nas.uoregon.edu/publications/tao-li-dissertation (cit. on p. 54).

[128] B. M. Xu et al. "Realization of a single-beam mini magneto-optical trap: A candidate for compact CPT cold atom-clocks". In: *Optics Communications* 281.23 (Dec. 2008), pp. 5819–5823. DOI: 10.1016/j.optcom.2008.08.012 (cit. on pp. 54, 71).

[129] E. Hecht. *Optics, Global edition*. 5th ed. Pearson Education Limited, 2017. URL: https://catalogue.pearsoned.co.uk/educator/product/9781292096933.page (cit. on pp. 60, 99).

[130] G. Brooker. *Modern classical optics*. Oxford University Press, 2003. URL: https://global.oup.com/academic/product/9780198599654 (cit. on pp. 60, 78, 97).

[131] P. D. D. Schwindt. "Magnetic traps and guides for Bose-Einstein condensates on an atom chip: Progress toward a coherent atom waveguide beamsplitter". Ph.D. Thesis. University of Colorado, 2003. URL: http://jilawww.colorado.edu/bec/CornellGroup/theses/schwindt_thesis.pdf (cit. on p. 64).

[132] J. F. Hulbert et al. "Versatile Rb vapor cells with long lifetimes". In: *Journal of Vacuum Science & Technology A: Vacuum, Surfaces, and Films* 31.3 (May 2013), p. 033001. DOI: 10.1116/1.4795759 (cit. on p. 64).

[133] J. F. O'Hanlon. *A user's guide to vacuum technology*. 3rd ed. Hoboken, NJ, USA: John Wiley & Sons, Inc., June 2003. DOI: 10.1002/0471467162 (cit. on pp. 67, 68, 70, 71).

[134] R. Grinham & D. A. Chew. "A review of outgassing and methods for its reduction". In: *Applied Science and Convergence Technology* 26.5 (Sept. 2017), pp. 95–109. DOI: 10.5757/ASCT.2017.26.5.95 (cit. on p. 67).

[135] J. L. de Segovia. "Physics of outgassing". In: *CERN Accelerator School : Vacuum Technology*. CSIC Madrid. 1999. DOI: 10.5170/CERN-1999-005.99 (cit. on p. 67).

[136] VACOM. *Welding processes*. 2018. URL: https://www.vacom.de/en/home/369-welding-processes (visited on 12/11/2018) (cit. on p. 68).

[137] J. R. Chen, C. H. Lee & Y. C. Liu. "A comparison of thermal outgassing rates of aluminum alloy and stainless steel vacuum chambers". In: *AIP Conference Proceedings*. Vol. 171. AIP, 1988, pp. 244–249. DOI: 10.1063/1.37306 (cit. on pp. 68, 69).

[138] *Cleaning aluminium for vacuum applications*. Tech. rep. Meyer Tool and Manufacturing Inc., 2009. URL: https://www.mtm-inc.com/av-20090309-cleaning-aluminum-for-vacuum-applications (cit. on p. 68).

[139] J. I. Malcolm. "Construction of a portable platform for cold atom interferometry". Ph.D. Thesis. University of Birmingham, 2015. URL: http://etheses.bham.ac.uk/6472/ (cit. on p. 69).

[140] J. Grosse et al. "Design and qualification of an UHV system for operation on sounding rockets". In: *Journal of Vacuum Science & Technology A: Vacuum, Surfaces, and Films* 34.3 (May 2016), p. 031606. DOI: 10.1116/1.4947583 (cit. on p. 69).

[141] A. G. Hinton. "Development of a transportable cold atom gradiometer". Ph.D. Thesis. University of Birmingham, 2016. URL: http://etheses.bham.ac.uk/7120/ (cit. on p. 69).

[142] J. Vovrosh et al. "Additive manufacturing of magnetic shielding and ultra-high vacuum flange for cold atom sensors". In: *Scientific Reports* 8.1 (Dec. 2018), p. 2023. DOI: 10.1038/s41598-018-20352-x (cit. on p. 69).

[143] E. Mimoun et al. "Fast production of ultracold sodium gases using light-induced desorption and optical trapping". In: *Physical Review A* 81.2 (Feb. 2010), p. 023631. arXiv: 0911.5656. DOI: 10.1103/PhysRevA.81.023631 (cit. on p. 69).

[144] M. Minato & Y. Itoh. "Vacuum characteristics of titanium". In: *Journal of Vacuum Science & Technology A: Vacuum, Surfaces, and Films* 13.3 (May 1995), pp. 540–544. DOI: 10.1116/1.579781 (cit. on p. 69).

[145] Y. Morimoto et al. "Outgassing characteristics of titanium with surface treatment of oxidation". In: *Shinku* 45.8 (2002), pp. 665–669. DOI: 10.3131/jvsj.45.665 (cit. on p. 69).

[146] M. Takeda et al. "Hydrogen outgassing mechanism in titanium materials". In: *Applied Surface Science* 258.4 (Dec. 2011), pp. 1405–1411. DOI: 10.1016/j.apsusc.2011.09.092 (cit. on p. 69).

[147] R. A. Rimmer et al. "High-power testing of RF cavities for the PEP-II B factory". In: *Proceedings of the 1997 Particle Accelerator Conference (Cat. No.97CH36167)*. Vol. 3. IEEE, 1997, pp. 3004–3006. DOI: 10.1109/PAC.1997.753089 (cit. on p. 69).

[148] R. Veness et al. "Installation and commissioning of vacuum systems for the LHC particle detectors". In: *Particle Accelerator Conference*. 2009, pp. 372–374. URL: https://cds.cern.ch/record/1199583 (cit. on p. 69).

[149] G. Lee. *Materials for ultra-high vacuum*. Tech. rep. Batavia, IL: Fermi National Accelerator Laboratory, Aug. 1989. DOI: 10.2172/6985168 (cit. on pp. 69, 70).

[150] *Optical glass: Data sheets*. Tech. rep. Schott AG, 2018. URL: https://www.schott.com/d/advanced_optics/ac85c64c-60a0-4113-a9df-23ee1be20428 (cit. on pp. 70, 72).

[151] K. J. Hughes, C. A. Sackett & A. T. Brown. *Helium barrier atom chamber*. 2012. URL: http://www.google.com/patents/US20120258022 (cit. on p. 70).

[152] C. B. Alcock, V. P. Itkin & M. K. Horrigan. "Vapour pressure equations for the metallic elements: 298-2500K". In: *Canadian Metallurgical Quarterly* 23.3 (July 1984), pp. 309–313. DOI: 10.1179/cmq.1984.23.3.309 (cit. on p. 70).

[153] D. Coyne. *LIGO vacuum compatible materials list*. Tech. rep. LIGO, 2014. URL: https://dcc.ligo.org/E960050/public (cit. on p. 70).

[154] *Polymer outgassing & NASA outgassing standards*. Tech. rep. Cova Scientific, 2016. URL: https://www.covascientific.com/blog/outgassing (cit. on p. 71).

[155] P. Chiggiato. *Outgassing*. Tech. rep. CERN, 2006. URL: https://cas.web.cern.ch/sites/cas.web.cern.ch/files/lectures/platjadaro-2006/chiggiato-1.pdf (cit. on p. 71).

[156] *What is an epoxy adhesive?* URL: https://www.masterbond.com/techtips/what-epoxy-adhesive (visited on 12/13/2018) (cit. on p. 71).

[157] *Epoxy adhesive application guide*. Tech. rep. Epoxy Technology, Inc., 2016. URL: http://www.epotek.com/site/files/brochures/pdfs/adhesive_application_guide.pdf (cit. on p. 71).

[158] *EPO-TEK 353ND: Technical data sheet*. Tech. rep. Epoxy Technology, Inc., 2017. URL: http://www.epotek.com/site/administrator/components/com_products/assets/files/Style_Uploads/353ND.pdf (cit. on pp. 71, 76).

[159] D. Z. Anderson & J. G. J. Reichel. *Cold atom system with atom chip wall*. 2004. URL: https://patents.google.com/patent/US7126112B2/un (cit. on pp. 71, 76).

[160] M. Holynski. "Creating a two dimensional cold mixture experiment". Ph.D. Thesis. University of Birmingham, 2012. URL: http://etheses.bham.ac.uk/3807/ (cit. on p. 71).

[161] K. J. Weatherill et al. "A versatile and reliably reusable ultrahigh vacuum viewport". In: *Review of Scientific Instruments* 80.2 (Feb. 2009), p. 026105. arXiv: 0812.1019. DOI: 10.1063/1.3075547 (cit. on p. 71).

[162] S. Du et al. "Atom-chip Bose-Einstein condensation in a portable vacuum cell". In: *Physical Review A* 70.5 (Nov. 2004), p. 053606. DOI: 10.1103/PhysRevA.70.053606 (cit. on p. 71).

[163] N. M. Linke. "Background-free detection and mixed-species crystals in micro- and macroscopic ion-traps for scalable QIP". Ph.D. Thesis. University of Oxford, 2012. URL: https://ora.ox.ac.uk/objects/uuid:a1dd4c65-1a77-472f-b67a-6461afb61e3a (cit. on p. 71).

[164] NASA. *Outgassing data for selecting spacecraft materials online*. 2018. URL: http://outgassing.nasa.gov/ (visited on 11/12/2018) (cit. on pp. 71, 76).

[165] M. B. Squires et al. "Ex vacuo atom chip Bose-Einstein condensate". In: *Applied Physics Letters* 109.26 (Dec. 2016), p. 264101. arXiv: 1608.04787. DOI: 10.1063/1.4971838 (cit. on p. 71).

[166] R. Michaels. *Epoxies and adhesives fit for space*. Tech. rep. Master Bond Inc., 2013. URL: https://www.machinedesign.com/fasteners/epoxies-and-adhesives-fit-space (cit. on p. 71).

[167] *Agilent laser and optics: User's manual, volume I*. Tech. rep. Agilent Technologies, 2007, p. 300. URL: http://www.uzimex.cz/soubory/20080403_laser_optika_cast_1.pdf (cit. on pp. 72, 73, 77).

[168] J. R. Davis, ed. *Metals handbook desk edition*. ASM International, 1998. DOI: 10.31399/asm.hb.mhde2.9781627081993 (cit. on pp. 72–74, 77).

[169] *Stainless steel grade datasheets*. Tech. rep. Atlas Steels, 2013. URL: http://www.atlassteels.com.au/site/pages/stainless-steel-datasheets.php (cit. on p. 72).

[170] A. J. C. Wilson. "The thermal expansion of aluminium from 0° to 650°C". In: *Proceedings of the Physical Society* 53.3 (May 1941), pp. 235–244. DOI: 10.1088/0959-5309/53/3/305 (cit. on p. 73).

[171] *Coefficient of thermal expansion for various materials at different temperatures*. Tech. rep. Bal Seal Engineering, Inc., 2004. URL: https://www.balseal.com/sites/default/files/tr18_020707131421.pdf (cit. on pp. 73, 77).

[172] K. Miyoshi. "Structures and mechanical properties of natural and synthetic diamonds". In: *NASA/TM-1998-107249*. NASA, 1998. Chap. 8. URL: https://ntrs.nasa.gov/search.jsp?R=19980210770 (cit. on p. 74).

[173] *Technical glasses: Physical and technical properties*. Tech. rep. Schott AG, 2010. URL: https://www.schott.com/d/epackaging/2fbc7180-e37c-4209-9eec-617ad9208e51 (cit. on p. 74).

[174] R. L. Lehman & M. G. McLaren. "Materials". In: *The CRC Handbook of Mechanical Engineering*. Ed. by F. Kreith & Y. Goswani. 2nd ed. CRC Press, 2004. Chap. 12. URL: https://www.crcpress.com/9780849308666 (cit. on p. 74).

[175] R. Lehman. *The mechanical properties of glass*. URL: http://glassproperties.com/references/MechPropHandouts.pdf (visited on 12/12/2018) (cit. on p. 74).

[176] *Capillary flow*. URL: https://www.masterbond.com/techtips/capillary-flow (visited on 12/12/2018) (cit. on p. 76).

[177] P. Davies et al. "Influence of adhesive bond line thickness on joint strength". In: *International Journal of Adhesion and Adhesives* 29.7 (Oct. 2009), pp. 724–736. DOI: 10.1016/j.ijadhadh.2009.03.002 (cit. on p. 76).

[178] P. Hidnert & M. G. Blair. "Thermal expansivity and density of indium". In: *Journal of Research of the National Bureau of Standards* 30.6 (June 1943), pp. 427–433. DOI: 10.6028/jres.030.029 (cit. on p. 77).

[179] B. Fletcher. "A rotating optical lattice for ultracold atoms". Ph.D. Thesis. University of Oxford, 2008. URL: https://www2.physics.ox.ac.uk/research/ultracold-quantum-matter/publications/theses (cit. on p. 87).

[180] R. Williams. "Vortex nucleation in a rotating optical lattice of ultracold atoms". Ph.D. Thesis. University of Oxford, 2009. URL: https://www2.physics.ox.ac.uk/research/ultracold-quantum-matter/publications/theses (cit. on p. 87).

[181] T. Arpornthip, C. A. Sackett & K. J. Hughes. "Vacuum-pressure measurement using a magneto-optical trap". In: *Physical Review A* 85.3 (Mar. 2012), p. 033420. arXiv: 1203.0189. DOI: 10.1103/PhysRevA.85.033420 (cit. on p. 89).

[182] R. W. G. Moore et al. "Measurement of vacuum pressure with a magneto-optical trap: A pressure-rise method". In: *Review of Scientific Instruments* 86.9 (Sept. 2015), p. 093108. arXiv: 1401.7949. DOI: 10.1063/1.4928154 (cit. on p. 89).

[183] J. H. Shirley. "Modulation transfer processes in optical heterodyne saturation spectroscopy". In: *Optics Letters* 7.11 (Nov. 1982), p. 537. DOI: 10.1364/OL.7.000537 (cit. on p. 96).

[184] J. Zhang et al. "Characteristics of absorption and dispersion for rubidium D2 lines with the modulation transfer spectrum". In: *Optics Express* 11.11 (June 2003), p. 1338. DOI: 10.1364/OE.11.001338 (cit. on p. 96).

[185] D. J. McCarron, S. A. King & S. L. Cornish. "Modulation transfer spectroscopy in atomic rubidium". In: *Measurement Science and Technology* 19.10 (Oct. 2008), p. 105601. arXiv: 0805.2708. DOI: 10.1088/0957-0233/19/10/105601 (cit. on p. 96).

[186] *CVI Melles Griot technical guide*. CVI Melles Griot, 2009 (cit. on p. 97).

[187] J. C. B. Kangara et al. "Design and construction of cost-effective tapered amplifier systems for laser cooling and trapping experiments". In: *American Journal of Physics* 82.8 (Aug. 2014), pp. 805–817. DOI: 10.1119/1.4867376 (cit. on p. 100).

[188] M. Fuchs. "Development of a high power stabilized diode laser system". Masters Thesis. University of Oregon, 2006. URL: http://atomoptics-nas.uoregon.edu/publications/matthias-fuchs-thesis (cit. on p. 100).

[189] J. Kangara. "Design and construction of tapered amplifier systems for laser cooling and atom trapping experiments". Masters Thesis. Miami University, 2012. URL: http://rave.ohiolink.edu/etdc/view?acc_num=miami1344007693 (cit. on p. 100).

[190] V. Bolpasi & W. von Klitzing. "Double-pass tapered amplifier diode laser with an output power of 1 W for an injection power of only 200 μW". In: *Review of Scientific Instruments* 81.11 (Nov. 2010), p. 113108. DOI: 10.1063/1.3501966 (cit. on pp. 101, 103).

[191] V. M. Valenzuela et al. "Multiple isotope magneto-optical trap from a single diode laser". In: *Journal of the Optical Society of America B* 30.5 (May 2013), p. 1205. arXiv: 1304.3702v1. DOI: 10.1364/JOSAB.30.001205 (cit. on p. 101).

[192] C. E. Rogers & P. L. Gould. "Nanosecond pulse shaping at 780 nm with fiber-based electro-optical modulators and a double-pass tapered amplifier". In: *Optics Express* 24.3 (Feb. 2016), p. 2596. DOI: 10.1364/OE.24.002596 (cit. on p. 101).

[193] D. Trypogeorgos. "Periodically driven atomic systems". Ph.D. Thesis. University of Oxford, 2014. URL: https://ora.ox.ac.uk/objects/ora:11359 (cit. on p. 101).

[194] G. Ritt et al. "Laser frequency offset locking using a side of filter technique". In: *Applied Physics B* 79.3 (Aug. 2004), pp. 363–365. DOI: 10.1007/s00340-004-1559-6 (cit. on pp. 104, 106, 108).

[195] E. Bentine. "Atomic mixtures in radiofrequency dressed potentials". Ph.D. Thesis. University of Oxford, 2018 (cit. on p. 108).

[196] E. A. Donley et al. "Double-pass acousto-optic modulator system". In: *Review of Scientific Instruments* 76.6 (June 2005), p. 063112. DOI: 10.1063/1.1930095 (cit. on p. 108).

[197] C. P. Shillaber. *Photomicrography in theory and practice*. New York: John Wiley and Sons, 1944 (cit. on p. 115).

[198] I. Hughes & T. Hase. *Measurements and their uncertainties: A practical guide to modern error analysis*. Oxford University Press, 2010. URL: https://global.oup.com/academic/product/9780199566334 (cit. on pp. 124, 126).

[199] J. P. Gordon & A. Ashkin. "Motion of atoms in a radiation trap". In: *Physical Review A* 21.5 (May 1980), pp. 1606–1617. DOI: 10.1103/PhysRevA.21.1606 (cit. on p. 141).

[200] V. G. Minogin & V. S. Letokhov. *Laser light pressure on atoms*. Gordon & Breach Science Publishers, 1987. URL: https://www.crcpress.com/9782881240805 (cit. on p. 141).

“I am the Alpha and the Omega,
the First and the Last,
the Beginning and the End.”

Revelation 22:13